Tuning Functional and Catalytic Properties of Materials with Defects, Substitutional Alloying and Pressure: First-principles Studies

A Thesis

Submitted For the Degree of

DOCTOR OF PHILOSOPHY

in the Faculty of Science

by

Suchitra

CHEMISTRY AND PHYSICS OF MATERIALS UNIT
JAWAHARLAL NEHRU CENTRE FOR ADVANCED SCIENTIFIC RESEARCH
Bangalore – 560 064

JUNE 2019

A mi familia

DECLARATION

I hereby declare that the matter embodied in the thesis entitled "**Tuning Functional and Catalytic Properties of Materials with Defects, Substitutional Alloying and Pressure: First-principles Studies**" is the result of investigations carried out by me at the Chemistry and Physics of Materials Unit, Jawaharlal Nehru Centre for Advanced Scientific Research, Bangalore, India under the supervision of Prof. Umesh V. Waghmare and that it has not been submitted elsewhere for the award of any degree or diploma.

In keeping with the general practice in reporting scientific observations, due acknowledgement has been made whenever the work described is based on the findings of other investigators.

Suchitra

CERTIFICATE

I hereby certify that the matter embodied in this thesis entitled "**Tuning Functional and Catalytic Properties of Materials with Defects, Substitutional Alloying and Pressure: First-principles Studies**" has been carried out by Ms. Suchitra at the Chemistry and Physics of Materials Unit, Jawaharlal Nehru Centre for Advanced Scientific Research, Bangalore, India under my supervision and that it has not been submitted elsewhere for the award of any degree or diploma.

Prof. Umesh V. Waghmare
(Research Supervisor)

Acknowledgements

I take this opportunity to express my heartfelt thanks to my thesis advisor Prof. Umesh V. Waghmare to whom I owe the deepest gratitude for his unending support and excellent guidance throughout my graduate study at JNCASR. It was an extreme pleasure working with him with his boundless energy and curiosity in uncovering the mysteries in materials science. An excellent scientist and a brilliant teacher has inspired me to ask the right questions for a given problem. I enjoyed intense scientific discussions which have always motivated me to pursue new scientific ideas, get involved in it actively and solve it efficiently. His valuable comments and instructions in preparing for seminars and writing papers have helped me immensely. I am extremely grateful to Prof. Waghmare for giving me enormous academic freedom during my candidacy. Under his tutelage, I have grown both scientifically and personally. Thank you, Sir.

I am thankful to Prof. C. N. R. Rao for the engaging and fascinating scientific collaborations. Working with him has been very inspiring, and has taught me how to bridge the gap between theory and experiments.

I would also like to express my gratitude to Prof. A. K. Sood, Prof. C. Narayana, Prof. M. Eswaramoorthy, Prof. Sebastian C. Peter and Dr. Nirat Ray for the interesting and fruitful scientific collaborations, support, and insightful suggestions.

I am thankful to Dr. K. Manjunath, Dr. S. R. Lingampalli, Manjeet Chhetri, Anand Roy, Dr. S. Sarkar, Rajkumar Jana, Mohd Monis Ayyub, Dr. S. Maity and Subhadip Das for their fruitful collaborations. I have been greatly benefited from their expertise and learned a lot during discussions.

I thank all the TSU, CPMU and NCU faculty, Prof. S. Narasimhan, Prof. U. V. Waghmare, Prof. G. U. Kulkarni, Prof. S. Balasubramanian, Prof. T. K. Maji, Prof. M. Eswaramoorthy, Prof. R. Ganapathy, Prof. C. Narayana, Prof. K. S. Narayan, Dr. Ranjan Dutta, Prof. S M Shivaprasad, Prof. S. K. Das, Dr. S. Rajaram, Prof. H. Ila, Prof. Vidhyadhiraja N. S., and Prof. A. Chakraborty (IISc.) for their excellent courses which were not only interesting but also enlightening.

I thank Int. Ph.D. conveners Prof. S. Balasubramanian and Prof. T. K. Maji for their support.

I am thankful to the present and past chairmen of CPMU and TSU, Prof. G. U. Kulkarni, Prof. S. Balasubramanian, Prof. C. Narayana, Prof. S. Narasimhan, Prof. U. V. Waghmare and Prof. S. K. Pati for allowing me to use departmental facilities.

I am very thankful to my past and present lab members Sharmila, Summayya, Abhishek, Jayashree, Anjali, Meha, Vinay, Arpita, Koushik, Pawan, Krishnamohan, Shashwat, Sandhya, Harish, Himanshu, Henu, Sweta, Lakshay, Anuja, Bhupalee, Aseem, Raagya, Shivani, Narendra, Koyendrila, Sampath, Prasad, Shashank, and Rajendra for many academic, non-academic and fun interactions at various occasions.

I thank TUE-CMS staff for always giving a helping hand whenever any problem had arisen while making use of the supercomputing resources of Thematic Unit of Excellence-Comptutational Materials Science (TUE-CMS) at JNCASR.

I thank JNCASR for providing me Int. Ph.D. fellowship and acknowledge DST travel grant.

I also thank the complab, Academic, Admin, Library, Dhanvantari, Utility store, Dining Hall and Hostel mess staffs and TSU secretary for all their help.

I am grateful to my Int. Ph.D. batch mates Uttam, Rajib, Abhijit, Sonu, Raaghesh, Pallabi, Krishnendu, Mohini and Susheela for good company in all these years.

I am lucky to have friends like Sweta, Shabnam, Anshu, Mansi, Niharika, Alka, Neha, Ratna and Rashmi who have been by my side through thick and thin since my school and college days.

I express my sincere gratitude to Aruna Ma'am and Kruti for their warm hospitality, affection and support during our group treats.

Above all, I thank my family for the love, affection, and support through all these years.

Synopsis

Technological advances are often enabled by the discovery and development of functional materials. Prediction of the structure of materials, i.e. arrangement of atoms is of great importance in designing of materials with desired properties. With advances in computational modelling and computing resources, it is now possible to predict quantum states of materials using first-principles density functional theory (DFT)-based methods, which provide access to information at atomic and nanometer scales, which may not be readily possible in experiments. The behavior of real materials is deeply affected by defects, atomic substitution, and charge doping, and first-principles calculations allow us to have a precise control over the kind of such factors, and determine their influence on properties systematically. In this thesis, we present a first-principles theoretical analysis of how defects, substitutional alloying, and doping influence the properties of materials that are relevant to their catalytic activity and functionality, and compare my results with the experiment wherever possible.

In chapter 1, we present a brief introduction to the theme of this thesis followed by methods and formalism used in our calculations in chapter 2. The thesis is divided into three parts based on the length-scales relevant to the materials.

In the first part (chapter 3-5), we focus on the effects of anion substitution in bulk oxides (ZnO, TiO_2, CdO) and chalcogenides (CdS, CdSe, CdTe) exploring their properties for photocatalytic applications and tuning the band structure for their use as photocatalysts in the conversion of solar energy for water splitting to produce H_2, a green fuel. In chapter 6, we have studied the pressure-induced structural phase-transition observed in ReO_3. In chapter 7-8 of the **second part** of thesis, we have developed the understanding of the catalytic activity of metallic surfaces (Pd_2Ge and NiCoP) for ethanol oxidation and water splitting reactions on the basis of adsorption energies and the presence of catalytically active sites. We have seen the effect of O-vacancies on the work funcion of the ReO_3 surface in chapter 9 and focus on uncovering the chemical mechanisms that contribute to the SERS shown of Py at ReO_3 surface in chapter 10 of the **second part**

of the thesis. The **third part** (chapter 11) presents the effects of doping on vibrational properties of ReX_2 (X=S, Se). In chapter 12 of the **third part**, we have predicted novel two-dimensional alloys of Si and Ge and have shown that the band gap can be tuned by changing the concentration of Ge.

List of Publications

(1) Suchitra, J. Pan, and U. V. Waghmare, "High tunability of the work function of (001) surface of ReO_3 with O-vacancies: First principles analysis", Journal of Applied Physics **116**, 034304 (2014).

(2) D. V. S. Muthu, Pallavi Teredesai, S. Saha, Suchitra, U. V. Waghmare, A. K. Sood, and C. N. R. Rao, "Pressure-induced structural phase transitions and phonon anomalies in ReO_3: Raman and first-principles study", Phys. Rev. B. **91**, 224308 (2015).

(3) Sumanta Sarkar, Rajkumar Jana, Suchitra, Umesh V. Waghmare, Balamurugan Kuppan, S. Sampath, and Sebastian C. Peter, "Ordered Pd_2Ge intermetallic nanoparticles as highly efficient and robust catalyst for ethanol oxidation", Chem. Mater. **27**, 7459 (2015).

(4) Anand Roy, Suchitra, K. Manjunath, Tokeer Ahmad, Umesh V. Waghmare, and C. N. R. Rao, "Electronic structure and properties of $Cd_4As_2Br_3$ and $Cd_4Sb_2I_3$, analogues of CdSe and CdTe", Solid State Communications **255**, 5 (2017).

(5) Srinivasa Rao Lingampalli, Suchitra Prasad, Krishnappa Manjunath, Mohd Monis Ayyub, Pratap Vishnoi, Umesh V. Waghmare, and C. N. R. Rao, "Effects of substitution of aliovalent N^{3-} and Cl^- ions in place of O^{2-} in ZnO: Properties of $ZnO_{1-x-y}N_xCl_y$ (x,y = 0.0-0.5)", Eur. J. Inorg. Chem. **17**, 2377 (2017).

(6) Anand Roy, Manjeet Chhetri, Suchitra Prasad, Umesh V. Waghmare, and C. N. R. Rao, "Unique features of the photocatalytic reduction of H_2O and CO_2 by new catalysts based on the analogues of CdS, $Cd_4P_2X_3$ (X= Cl, Br, I)", ACS applied materials interfaces **10**, 2526 (2018).

(7) K. Manjunath, Suchitra Prasad, Umesh V. Waghmare, and C. N. R. Rao, "Cd_2NF an analogue of CdO", Dalton Trans. **47**, 9303 (2018).

(8) Mohd Monis Ayyub, Suchitra Prasad, Srinivasa Rao Lingampalli, Krishnappa Manjunath, Umesh V Waghmare, and C. N. R. Rao, "TiNF and related analogues of TiO_2: A Combined Experimental and Theoretical Study", ChemPhysChem **19**, 3410 (2018).

(9) Suchitra, J. Pan and Umesh V. Waghmare, "Chemical mechanism of surface-enhanced Raman scattering of pyridine adsorbed on ReO_3 surface: First-principles Theoretical Analysis", (preprint available).

(10) Sisir Maity, Dheeraj Kumar Singh, Suchitra Prasad, Umesh V. Waghmare, Srinivasan Sampath, and Muthusamy Eswaramoorthy, "High surface area NiCoP nanostructure as an efficient water splitting electrocatalyst for the oxygen evolution reaction", (preprint available).

List of Figures

List of Tables

Contents

Chapter 1

Introduction

Materials have been an integral part of human society since the time immemorial. The various ages of humankind are usually referred to by the materials that were in vogue such as the Stone Age, the Iron Age, and the current Silicon age, etc. The development of many technologies such as biotechnology, nanotechnology, advanced electronics etc.; that make our living comfortable has been intricately associated with the availability of suitable materials. But the challenges of the current world are constantly fuelling the discovery and development of new kinds of materials with desired properties and at the right cost to meet the challenges of the current day world. Advancement in the understanding of a material type is often the forerunner to the stepwise progression of technology.

The physical properties of materials are governed by the arrangement of electrons and atoms in a system and interactions between them. These interactions can be described by the many-body quantum mechanics. However, due to the interactions involved it is quite difficult to solve the Schrodinger's equation exactly. Density functional theory formulated by Kohn-Sham has proven to be a major breakthrough in the field of materials science. With advances in computational resources, simulations and algorithm techniques, it is now possible to accurately predict both microscopic and macroscopic properties of materials in the bulk, surfaces and two-dimensional

materials. It gives access to the atomistic information, which is sometimes challenging to obtain from experiments.

Materials engineering is very important in order to tune/alter the properties of materials. Defects, substitution, external pressures, and electron-doping are some of the ways to tune structural, electronic and vibrational properties of materials. Defects are considered as imperfections in the materials, but defects in the materials may lead to improvement in the performance of an ideal material. Substituting cations/anions with other atoms is another way to tune the electronic properties of materials. Defects and anion substitution affect electronic properties of materials and in some cases lead to enhancement in their catalytic activities. Solid state materials are also known to exhibit phase transition and anharmonic properties under pressure or temperature. The vibrational properties of a material can be tuned by electron/hole doping through the electron-phonon coupling. The topics in this thesis are introduced in the following sub-sections.

1.1 Defects

The law of nature states *nothing is perfect* [1]. In practice, a crystal with a perfectly regular arrangement of atoms cannot exist; imperfections, irregularities, and defects are present to some extent in all crystals. It is crucial to understand the impact of defects on the properties of materials, and synthesizing materials with control over the defect concentration is necessary to tailor the material properties and develop applications with improved functionality and reliability.

All defects and imperfections can conveniently be grouped into four categories, based on their geometry: point defects, line defects (dislocations), planar defects, and volume defects. Impurities in crystal act as a catalyst for the recombination of electrons and holes, by providing a level in the band gap. It acts as a recombination center and controls the lifetime of carriers, and is useful in photocells [2]. It also leads to

enhancement in the photocatalytic activity [3] as it suppresses the charge recombination process. Vacancies in materials tend to tune/change the mechanical and optoelectronic properties [4, 5].

1.2 Anion substitution

The extent of the overlap of the valence orbitals and the electronegativity difference between the cation and anion dictate the band gap of a material. The strong spatial overlap between their orbitals and increase electronegativity difference results in an enhancement in the band gap. It is a common practice to alter electronic and structural properties of materials by substituting cations/anions by suitable ions. The substitution of cations by metal ions brings about marginal changes in the electronic properties. However, anion substitution affects the valence band markedly and hence brings out significant changes in the electronic properties. N substitution in ZnO changes the Raman spectrum markedly and gives enhanced photocatalytic activity [6–9]. Doping of TiO_2 by N leads to the reduction in band gap due to the creation of band above the valence band thereby extending the absorption of TiO_2 to the visible light spectrum [10]. It should be noted that N-doping in oxides favor the creation of O-vacancies.

Cosubstitution of anions in oxides/sulphides shifts the optical absorption band to longer wavelength, making them useful in applications which require visible photoexcitation. It also minimizes the risk of anion vacancies in the system. The anion substituted materials such as P, Cl-CdS are stable up to moderate temperatures and in an aqueous medium, may find its application in the sensor technologies.

1.3 Catalysts for ethanol oxidation and water splitting reactions

Non-renewable resources are the primary source of energy today. With its growing demand and the environmental degradation associated with their use, there is a need to develop alternative clean energy sources. The fuel cell can be used as a device for sustainable energy conversion, starting from hydrogen, methanol, and ethanol as the fuels. Depending on applications, the choice of fuels can be made. Low operating temperatures, sustained operation at high current densities, low weight, compactness, and suitability for discontinuous operation are some of the merits of hydrogen as a fuel in the Proton exchange membrane fuel cells (PEMFCs). The challenges faced by the hydrogen economy are in the production, storage, and transport of hydrogen. The production of hydrogen by water using solar energy as the energy source is one of the clean methods. Electrolysis of water using solar cells, photocatalytic or photoelectrochemical reactions are some of the promising methods of solar hydrogen production.

Ethanol can be used as a fuel, as it can be produced from biomass waste, forestry, and urban residues. The major hindrance in the development of direct ethanol fuel cells (DEFCs) is the relatively sluggish kinetics of the ethanol oxidation reaction (EOR) [11]. Efficient catalysts are needed to overcome this hurdle. Currently, platinum on different supports, and in the form of alloys, bimetallic, and intermetallic compounds are the mostly used electrocatalysts in the low temperature fuel cells.

Efficient catalysts are the prerequisite for the above reaction to proceed successfully. According to the Sabatier principle, the catalysts should not bind too weakly and should be able to activate the reactants, and too strongly and should be able to desorb the products. As a result, there is a volcano-shaped relationship between activity and bond strength as shown in Fig. 1.1. It is of critical importance to understand the reaction mechanism of reactions for the designing of highly efficient

catalysts. In the following section, we give detailed mechanisms of ethanol oxidation reactions and electrocatalytic and photocatalytic water splitting reactions.

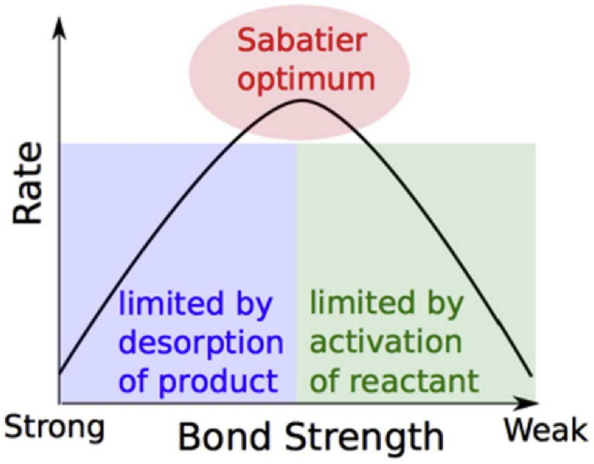

Figure 1.1: Schematic illustration of Sabatier principle. Reprinted with permission from [12]. Copyright (2015) by Elsevier.

1.3.1 Ethanol oxidation reaction

The efficiency of a catalyst is determined by its activity, selectivity, and stability. The commonly accepted mechanism of ethanol oxidation reaction in an acidic medium is a dual-pathway mechanism on noble metals catalyst [13–18] shown in Fig. 1.2. C1 pathway involves the complete oxidation of ethanol to CO_2 or carbonates via $CO_{ads.}$ intermediate by delivering 12 electrons. The C2 pathway involves the partial oxidation of ethanol to acetate transferring four electrons or to acetaldehyde by delivering two electrons without breaking of the C-C bond.

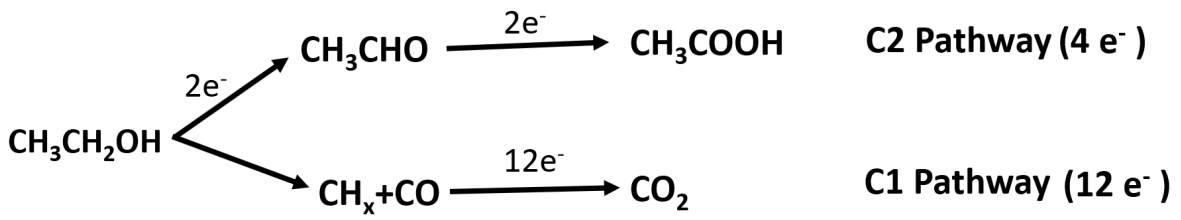

Figure 1.2: Schematic representation of the parallel pathways for ethanol oxidation on noble metal surfaces in acidic medium.

The ethanol oxidation reaction in alkaline medium goes through two pathways: one is through the reactive intermediate pathway and other through poisoning intermediate pathway. Ethanol oxidation reaction in the reactive intermediate pathway is a five steps reactions. In this, M-$(OH)_{ads.}$ ($^*OH$) and M-$(COCH_3)_{ads.}$ ($^*CH_3CO$) intermediates combine to generate acetate ion. The combination of $^*OH$ and $^*CH_3CO$ intermediate states is the rate determining step of the ethanol oxidation reaction. Whereas, in the poisoning-intermediate pathway $^*CH_3CO$ decompose into $^*CO$ and $^*CH_3$ which block the active sites and reduce the efficiency of catalysts [19]. This ethanol oxidation reaction has been shown schematically in Fig. 1.3.

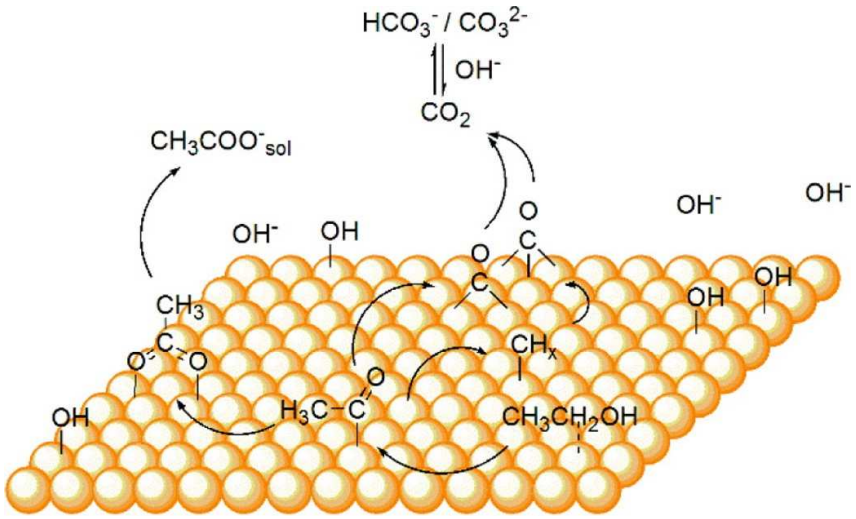

Figure 1.3: Schematic of reaction pathways for interfacial CH_3CH_2OH at metal electrodes in alkaline media. Taken from a Ref. [20].

1.3.2 Water splitting reactions

Water splitting reaction requires energy of 237 kJ/mol to proceed, which can be lowered by the use of suitable catalysts. The splitting of water into hydrogen and oxygen in the ratio 2:1 by the use of appropriate photocatalysts is termed as an overall water splitting reaction.

Phtocatalytic water splitting reactions

Photocatalytic water splitting reaction involves the excitement of electrons from the valence band (VB) to the conduction band (CB) by absorption of a photon of appropriate energy. The generated electron-hole pairs migrate to the surface. The water molecules get reduced to hydrogen by electrons, whereas it is oxidized to give oxygen by holes. The overall water splitting has been shown schematically in Fig. 1.4. One of the important criteria of water splitting reaction is that the conduction band minimum should be more negative than the redox potential of H^+/H_2 (0 V vs. NHE) and the valence band maximum should be more positive than the redox potential of O_2/H_2O (1.23 V). The minimum band gap required for water splitting is thus 1.23 eV.

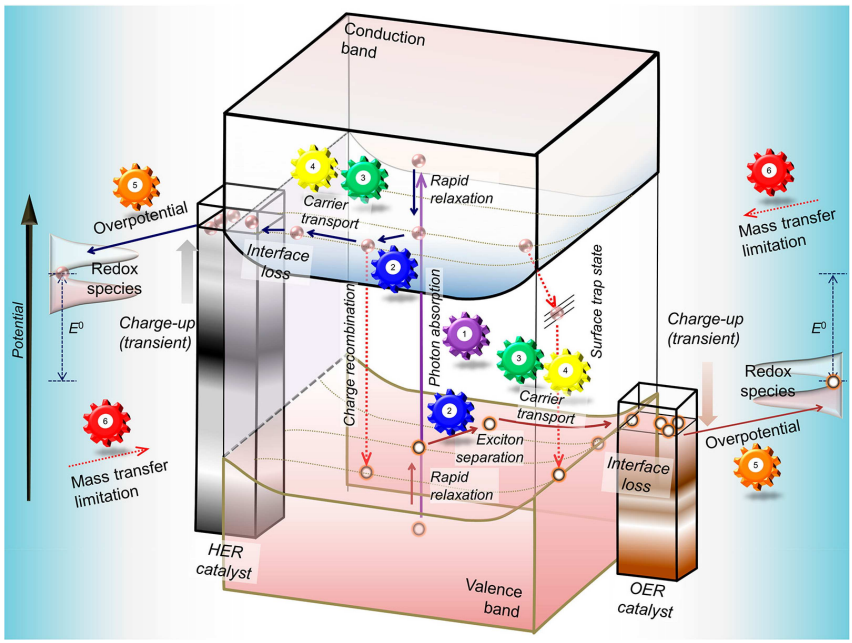

Figure 1.4: Schematic representation of overall water splitting reaction in semiconductor phtocatalysts. The order of photocatalytic process is indicated with numbered gear for overall water splitting. Taken from a Ref. [21].

Electrocatalytic water splitting reactions

Electrocatalytic water splitting reactions requires external electricity input to drive the splitting process. The reaction involves the use of two electrode systems, where hydrogen evolution reaction (HER) or oxidation reduction reaction (ORR) takes place on the cathode, and the oxygen evolution reaction (OER) takes place on the anode. OER requires a high overpotential to overcome the kinetic barrier for OER to occur as it is a four electron-proton coupled reaction as compared to HER which is a two electron-transfer reaction.

Hydrogen evolution reactions

The HER involves two-electron transfer reaction. The adsorption/desorption of a hydrogen intermediate (H^*) through the Volmer-Heyrovsky or the Volmer-Tafel mechanism [22–24] are the accepted pathways for HER in acidic solution:

$$Volmer\ step : H^+ + e^- \rightarrow H^* \tag{1.1}$$

$$Heyrovsky\ step : H^* + H^+ + e^- \rightarrow H_2 \tag{1.2}$$

$$Tafel\ step : H^* + H^* \rightarrow H_2 \tag{1.3}$$

In alkaline medium, the reaction formula for the HER is represented as:

$$Volmer\ step : H_2O + e^- \rightarrow H^* + OH^- \tag{1.4}$$

$$Heyrovsky\ step : H_2O + e^- + H^* \rightarrow H_2 + OH^- \tag{1.5}$$

$$Tafel\ step : H^* + H^* \rightarrow H_2 \tag{1.6}$$

The HER kinetics in alkaline solution is slow as compared to that in the acidic medium. This is because, it involves the dissociation of H_2O molecule in the Volmer

step which provides H* to the following steps by cleaving H-O-H bond, and is considered to be the rate-determining step of the overall reaction. The pathways of HER in both alkaline and the acidic medium has been illustrated schematically in Fig. 1.5.

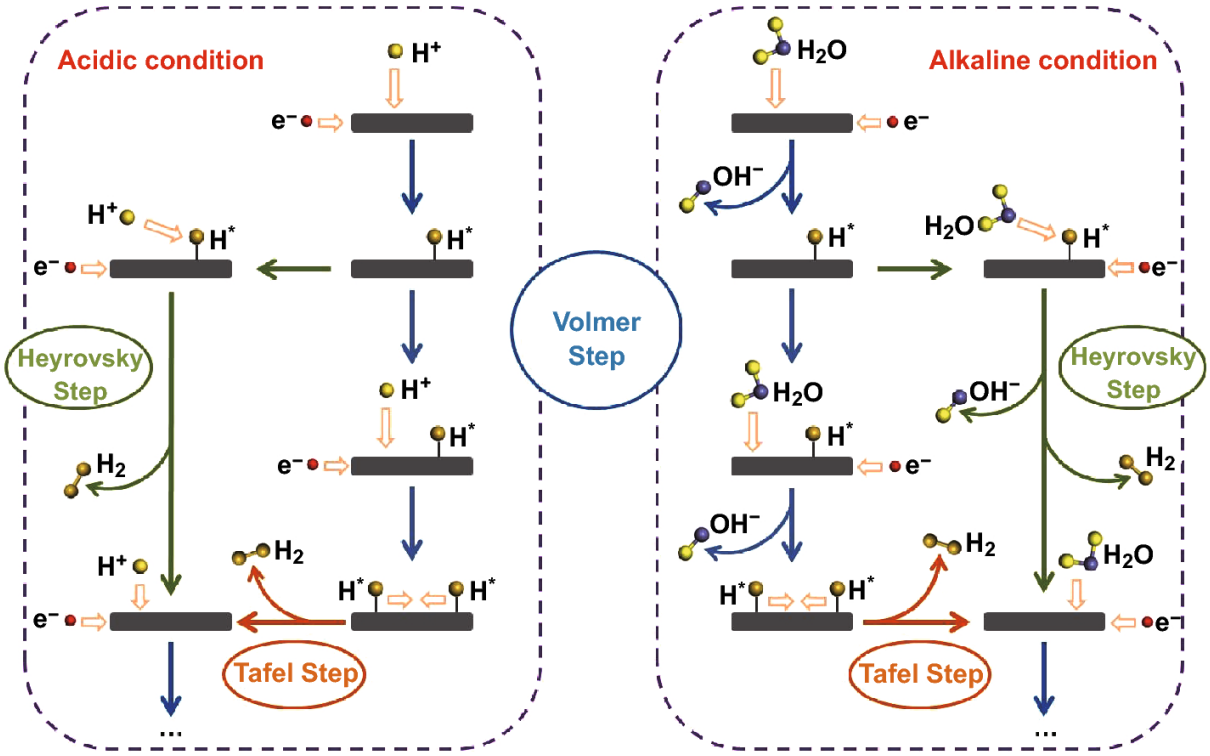

Figure 1.5: Schematic representation of electrocatalytic HER in both alkaline and acidic medium. Taken from Ref. [25].

Oxygen evolution reactions

OER involves four proton-coupled electron transfers from water to form an O_2 molecule which is slow kinetically and greatly affects the efficiency of overall water splitting. The OER in both acidic and alkaline medium involves MOH and MO intermediates. There are two ways in which O_2 can be evolved, one involves the direct combination of MO to evolve $O_{2(g)}$, and other involve the formation of MOOH which eventually decompose to give $O_{2(g)}$. The bonding interactions between adsorbate and surface is crucial for the electrocatalytic efficiency.

Proposed mechanism under acidic conditions [26]:

$$M + H_2O_{(l)} \rightarrow MOH + H + e^- \tag{1.7}$$

$$MOH + OH^- \rightarrow MO + H_2O_{(l)} + e^- \tag{1.8}$$

$$2MO \rightarrow 2M + O_{2(g)} \tag{1.9}$$

$$MO + H_2O_{(l)} \rightarrow MOOH + H^+ + e^- \tag{1.10}$$

$$MOOH + H_2O_{(l)} \rightarrow M + O_{2(g)} + H^+ + e^- \tag{1.11}$$

Reaction steps involved in alkaline medium:

$$M + OH^- \rightarrow MOH \tag{1.12}$$

$$MOH + OH^- \rightarrow MO + H_2O_{(l)} \tag{1.13}$$

$$2MO \rightarrow 2M + O_{2(g)} \tag{1.14}$$

$$MO + OH^- \rightarrow MOOH + e^- \tag{1.15}$$

$$MOOH + OH^- \rightarrow M + O_{2(g)} + H_2O_{(l)} \tag{1.16}$$

Schematic illustration of OER pathways in both alkaline and acidic medium has been illustrated in Fig. 1.6.

1.4 Perovskite oxides

ABO_3 perovskite oxides exhibit a wide range of behavior ranging from metallic and insulating, superconductivity, ferroelectricity, colossal magnetoresistance, etc. They have applications ranging from catalysis, solar cells to electronic devices. Perovskites show temperature dependent structural phase transitions, where single phonon instability connects the high temperature cubic phase to the low temperature low-symmetry phase. The ferroelectric transition is the common type of transition observed in these compounds; it involves off-centering of B or A site cation in BO_6

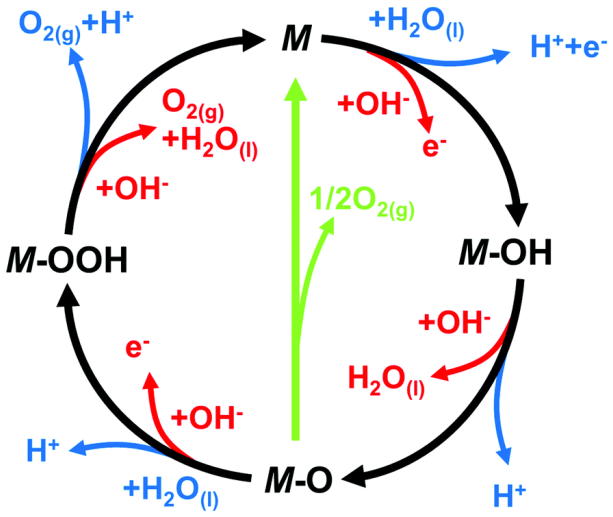

Figure 1.6: Schematic representation of OER in acidic (blue line) and alkaline (red line) medium. The black line shows the formation of a peroxide (MOOH) intermediates for oxygen evolution while other route involves the direct reaction of two adjacent oxo (MO) intermediates (green) to produce. Reprinted with permission from [26]. Copyright (2017) by Royal Society of Chemistry (Great Britain).

octahedra. This off-centering of B cation is because of the vanishing occupation of d orbitals of a transition metal ion. The imaginary phonon modes in their cubic structure indicate the instability and hence the transition.

The second type of phase transition is the antiferrodistortive (AFD) transitions, involving BO_6 octahedral rotations or tilts. The imaginary phonon modes at the M and R points of the Brillouin zone correspond to the octahedral rotations (in-phase and out of phase) leading to these transitions. When the size of the B cation relative to that of the A cation is large, the cubic perovskite structure can be unstable with respect to such octahedral rotational modes, and this can be another factor that leads to cell-doubling structural transitions [27](see Fig. 1.7).

1.5 Two-dimensional materials

With the discovery of graphene, two-dimensional materials have attracted tremendous research interests. They hold great potential to be used in electronics and optoelectronics due to their unique optical, electronic, and mechanical properties.

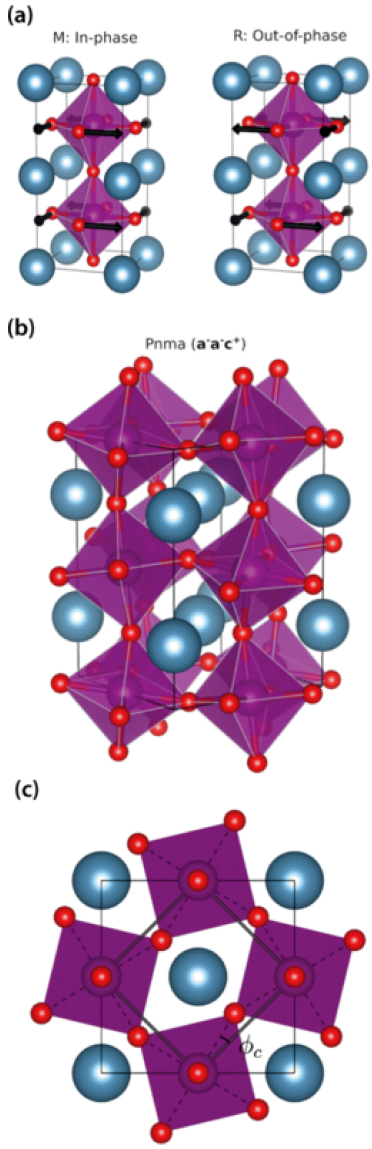

Figure 1.7: (a) Octahedral tilting modes in the cubic perovskite structure. (b) The octahedra are tilted out of phase around the pseudocubic a and b axes and in phase around the c axis in the orthorhombic ground-state structure of ABO_3 (space-group *Pnma*). (c) The definition of the tilt angle φ_c along c-axis. Reprinted with permission from [28]. Copyright (2018) by the American Physical Society (APS).

Graphene is a unique two-dimensional material with many fascinating properties, but its zero band gap hinders its use in various electronic applications. This has triggered the search of 2D-materials beyond graphene with semiconducting character. Transition metal dichalcogenides (TMDCs) possesses semiconducting character, strong spin-orbit coupling and electronic and mechanical properties which make them suitable for applications in high-end electronics, spintronics, optoelectronics, energy

harvesting, flexible electronics, DNA sequencing, and personalized medicine. Hexagonal boron nitride [29], vanadium oxide derivatives, and other chalcogenides including Bi_2Te_3, Sb_2Te_3, and β-FeSe [30, 31] are the other families of solids that have been exfoliated in single layers.

Alloying two-dimensional materials is one way to tune their band gaps. In these TMDCs alloys band gaps can be easily tuned by controlling their composition [32]. Due to the band gap tunability, it can be used in optoelectronics applications [32,33]. Electron/hole doping in the two-dimensional materials can tune the electron-phonon coupling by changing the deformation potential in graphene, phosphorene etc. [34,35]. The electron-phonon coupling tuning by doping may boost electronic properties of graphene based devices. Also, this makes graphene ideal for graphene nanoelectronics.

1.6 Overview of the thesis

The objective of this thesis is to present a first-principles theoretical analysis of how defects, substitutional alloying and doping influence properties of materials that are relevant to their catalytic activity and smart functionality, and connect it with experiment wherever possible. After a brief introduction to the work here, we give an overview of methods and formalism used in our calculations in chapter 2.

The thesis is divided into three parts based on the length-scales relevant to the behavior of materials. **In the first part** (chapter 3-5), we focus on the effects of anion substitution in bulk oxides and chalcogenides on their various properties. In chapter 3, we present a detailed analysis of the effects of N, F substitution (partial as well as complete) in CdO and TiO_2. In chapter 4, we present results of N, Cl substitution in ZnO and show that partial substitution results in the reduction in the band gap of ZnO. Complete anionic substitution of chalcogenides in CdX (X=S, Se, Te) leads to the formation of $Cd_4P_2X_3$ (X=Cl, Br, I), $Cd_4As_2Br_3$ and $Cd_4Sb_2I_3$ compounds with rather different properties compared to their parent compounds. We have studied

the electronic and structural properties of these compounds in chapter 5. In chapters 3-5, we have tried to understand their catalytic activities. In chapter 6, we study the pressure induced structural phase transitions observed in ReO_3 experimentally. We show that the M_3 modes involving ReO_6 octahedral rotation are responsible for its low pressure phase transition.

In the second part of the thesis, we discuss the catalytic activity of metallic surfaces and effects of defects on their properties. Pd_2Ge exhibits better catalytic activity for ethanol oxidation than that of Pd (111) surface. In chapter 7, we demonstrate that a perfect balance between the adsorption energies of CH_3CO and OH on Pd_2Ge surface is responsible for its superior catalytic activity. Pd (111) surface binds quite strongly with CH_3CO leading to surface poisoning, which inhibits the further reactions and hence show poor catalytic activity. In chapter 8, we examine the origins of improved catalytic activity of CoP upon Ni susbtitution towards water splitting reactions. CoP upon Ni substitution neither binds too strongly nor too weakly with the reactive species with free energies of adsorption ΔG close to zero. In contrast, CoP binds strongly with the intermediate species involved in the water splitting reactions and corresponding ΔG's are quite negative. Hence, it exhibits poor catalytic activity compared to Ni substituted CoP. We have shown that the Ni substituted CoP has more catalytically active sites than CoP, which also contributes to its higher catalytic activity.

Defects are known to have a great impact on the properties of materials. In chapter 9, we have shown that the work function of the ReO_3 (001) surface can be tuned from 7 to 3 eV by controlling the oxygen vacancies at the surface. The surface energy is shown to correlate linearly with the work function. ReO_3 is known to undergo pressure-induced structural phase transitions in its bulk as well as in nanocrystalline form, with lower transition pressures in the latter. From the phonon spectrum of ReO_3 surface, we uncover a weak structural instability in the nanocrystalline form due to surface stresses. This is possibly responsible for lower transition pressure in

nanocrystals as compared to the bulk.

ReO_3 in its nanocrystalline form is known to show surface-enhanced Raman scattering (SERS) in pyridine, pyrimidine, and pyrazine. In chapter 10, we investigate Py-ReO_3 interaction within first-principles density functional theory, and focus on uncovering the chemical mechanisms that contribute to the SERS shown of Py at ReO_3 surface.

In the **third part**, we analyze and develop an understanding of properties of two-dimensional materials. In chapter 11, we present the effects of electron doping on vibrational properties in two-dimensional ReX_2 (X=S, Se). We find that due to different electronic structural features of ReS_2 and $ReSe_2$, they behave differently to electron doping even if they possesses the same lattice structure. In chapter 12, we present a predictive analysis of novel two-dimensional $Si_{1-x}Ge_x$ alloys derived from silicene and germanene monolayers, and show how their band gap can be tuned with Ge concentration.

Chapter 2

Methods and Formalism

With advances in quantum mechanics, it is well established that various properties of a material can be explained by the behavior of electrons in the presence of other electrons, nuclei or other perturbation. The Hamiltonian of a system which takes into account electron-electron, electron-nuclear and nuclear-nuclear interactions is given by:

$$\hat{H} = -\frac{\hbar^2}{2m_e}\sum_i \nabla_i^2 - \sum_{i,I}\frac{Z_i e^2}{|\mathbf{r}_i - \mathbf{R}_I|} + \frac{1}{2}\sum_{i\neq j}\frac{e^2}{|\mathbf{r}_i - \mathbf{r}_j|} - \sum_I \frac{\hbar^2}{2M_I}\nabla_I^2 + \frac{1}{2}\sum_{I\neq J}\frac{Z_I Z_J e^2}{|\mathbf{R}_I - \mathbf{R}_J|} \tag{2.1}$$

where electrons are denoted by lowercase subscripts and nuclei, with charge Z_I and mass M_I, denoted by uppercase subscripts. The first term in Equation 2.1 is the kinetic energy of electrons, and the second term represents the interaction between electrons and nuclei (termed as external potential), the third term is the interaction between electrons, the fourth term is the kinetic energy of nuclei, and the fifth term is the interaction between nuclei. The mass of the nucleus is approximately >1836 times larger than that of an electron, and hence its kinetic energy can be neglected. This approximation is called as the **Born-Oppenheimer Approximation**. The

Hamiltonian in Equation 2.1 will then reduce to:

$$\hat{H} = \hat{T} + \hat{V}_{ext} + \hat{V}_{int} + E_{II} \tag{2.2}$$

where $\hat{T}$ is the kinetic energy operator, $\hat{V}_{ext}$ is the potential acting on electrons due to nuclei, $\hat{V}_{int}$ is the electron-electron interaction, and E_{II} is the classical coulomb interaction of nuclei with one another. The properties can be derived by solving the time-independent Schrödinger equation:

$$\hat{H}\Psi(\mathbf{R}, \mathbf{r}) = \varepsilon\mathbf{\Psi}(\mathbf{R}, \mathbf{r}) \tag{2.3}$$

$\mathrm{r} \equiv \{r_1, r_2, r_3, ..., r_N\}$ is the set of N electronic coordinates.

$\mathrm{R} \equiv \{R_1, R_2, R_3, ..., R_P\}$ is the set of P nuclear coordinates.

Where $\varepsilon' s$ are energy eigenvalues and $\Psi(\mathbf{R}, \mathbf{r})' s$ are the corresponding wavefunctions. Ψ is antisymmetric with respect to exchange of electronic coordinates in $\mathbf{r}$.

It is quite difficult to solve Schrödinger's Equation 2.3 accurately. Various approximations have been developed to solve it. Independent electron approximation is the oldest approximation which considers that interaction between the electrons can be ignored. Hartree approximation modified it further by treating the electrons as independent, but interacting only via the mean-field Coulomb potential. Hartree did not consider the asymmetric nature of electronic wavefunctions. Antisymmetric nature of electrons was considered in the Hartree-Fock Approximation. In this framework, asymmetric electronic wavefunction can be written in the form of a Slater determinant such that the wavefunctions are indistinguishable.

Density functional theory is another approach which treats the ground state of many body system accurately, and is efficient to apply. It avoids the problem of functions of 3N-variables (N is the number of electrons and their associated 3 spatial variables) associated with many electron-wave functions with a functional of electron density

which is a function of only 3 spatial variables, and hence has reduced the complexity of many electron problem to a great extent. In other words, it allows one to map exactly the problem of strongly interacting electron gas onto that of a single particle moving in an effective potential arising from the rest.

2.1 Density Functional Theory

2.1.1 Hohenberg-Kohn Theorems

Hohenberg and Kohn proposed that the ground state energy of the system uniquely depends on the electron density in their first theorem. They proved that the ground state energy can be obtained by minimizing the energy of a system according to electron density. Their theorems can be stated as follows:

Theorem I: The external potential $V_{ext}(\mathbf{r})$ of an interacting particle system is uniquely determined by the ground state density $n_o(\mathbf{r})$, within a constant.

Theorem II: The universal energy functional E[n] can be defined in terms of density $n_o(\mathbf{r})$ for any external potential $V_{ext}(\mathbf{r})$. The global minimum of this functional is the ground state energy of the system for given $V_{ext}(\mathbf{r})$. The density $n_o(\mathbf{r})$ that minimizes it is the ground state density $n_o(\mathbf{r})$.

The properties like the kinetic energy, etc., can be determined uniquely if $n(\mathbf{r})$ is specified, then each such property can be viewed as a functional of $n(\mathbf{r})$, including the total energy functional. The total energy functional can be given as:

$$E_{HK}[n] = F_{HK}[n] + \int d^3r V_{ext}(\mathbf{r}) n(\mathbf{r}) + E_{II} \tag{2.4}$$

E_{II} is the interaction energy of nuclei. Functional $F_{HK}[n]$ includes all internal energies,

kinetic energies and potential of interacting electron system and is given by:

$$F_{HK}[n] = T[n] + E_{int}[n] \tag{2.5}$$

$F_{HK}[n]$ is universal by construction since the kinetic energy, and interaction energy of the particles are functionals only of the density.

In order to access the kinetic energy exactly, one practical way is to revert to the usual expression in terms of the set of N single-particle wavefunctions. There is no known explicit functional that maps density directly to the kinetic energy. An approximate approach was suggested by Kohn and Sham (1965). They included the kinetic energy of non-interacting electrons in terms of independent particle wavefunctions, in addition to interaction terms modelled as a functional of the density.

2.1.2 Kohn-Sham Ansatz

The ansatz of Kohn and Sham assumes that the ground state density of the original interacting system is equal to that of some chosen non-interacting system i.e., one can map an interacting problem into a non-interacting problem. This leads to an independent-particle equations for the non-interacting system that can be considered exactly soluble with all difficult many-body terms incorporated into an exchange-correlation functional of the density. The non-interacting system can be described by single-particle equations, and the corresponding Slater determinant is the ground state solution.

Using the Kohn-Sham approach the energy functional can now be written as:

$$E[n(\mathbf{r})] = T_s[n(\mathbf{r})] + \frac{1}{2}\int \frac{n(\mathbf{r})n(\mathbf{r}')d^3r d^3r'}{|\mathbf{r}-\mathbf{r}'|} + \int n(\mathbf{r})V_{ext}(\mathbf{r})dr + E_{xc}[n(\mathbf{r})] \tag{2.6}$$

The first term is the kinetic energy of electrons, the second term is the electrostatic interaction energy between electrons, the third term is the interaction energy of electrons

with external potential and the fourth term is the exchange-correlation interaction between electrons.

The electron density is constructed as:

$$n(\mathbf{r}) = \sum_i |\Psi_i(\mathbf{r})|^2 \tag{2.7}$$

Here i refers to single-particle states and the sum is over all the occupied states. $E_{xc}[n(\mathbf{r})]$ is called the exchange-correlation energy functional. Taking functional derivative $\delta E[n(\mathbf{r})]/\delta\Psi_i^*(\mathbf{r})$ with the constraint that each $\Psi_i(\mathbf{r})$ normalized to unit leads to:

$$\left(-\frac{\hbar^2}{2m}\nabla^2 + V_{KS}(\mathbf{r})\right)\Psi_i(\mathbf{r}) = \varepsilon_i\Psi_i(\mathbf{r}) \tag{2.8}$$

where, V_{KS} is the Kohn-Sham potential for the non-interacting system given as:

$$V_{KS}(\mathbf{r}) = V_{ext}(\mathbf{r}) + \int \frac{n(\mathbf{r}')}{|\mathbf{r}-\mathbf{r}'|}dr + V_{xc}[n(\mathbf{r})] \tag{2.9}$$

where the first term is the external potential, the second term is the Hartree potential. The last term is the exchange-correlation potential defined as:

$$V_{xc}[n(\mathbf{r})] = \frac{\delta E_{xc}[n(\mathbf{r})]}{\delta n(\mathbf{r})} \tag{2.10}$$

2.1.3 Basis Set

Numerical solution of Kohn Sham equations defined in (2.8) requires us to choose a mathematical representation for the one electron orbital i.e, we need a basis to expand the wave functions Ψ_n, and then truncate the basis (so that the calculation time is

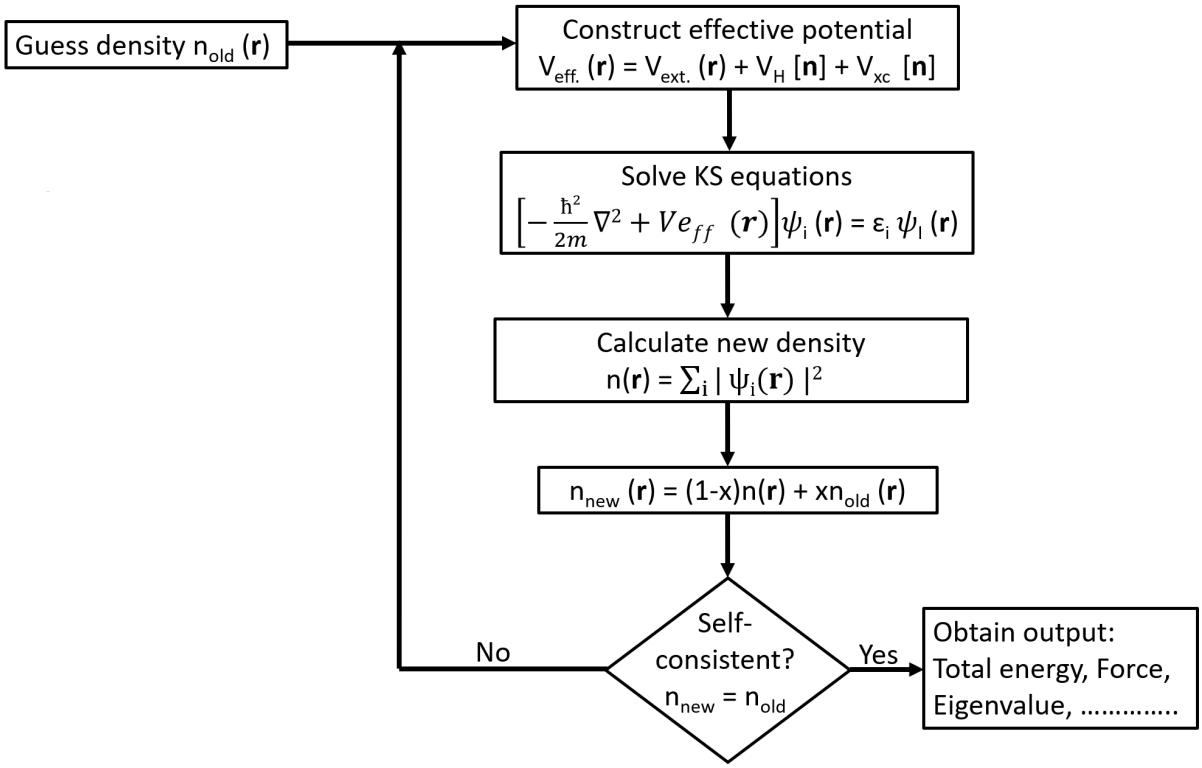

Figure 2.1: Self-consistency loop for the iterative solution of KS equations.

finite). Different types of basis sets are Plane-waves, atomic orbitals and mixed (set of atom centered basis set along with plane waves or other basis sets). For isolated systems such as atoms and molecules, the atomic orbital basis is commonly used. For extended periodic systems, the system is represented by a basis set of mutually orthonormal basis.

Plane-wave basis set required to expand the electronic wave functions is often very large. Considering the infinite system as a repeating array of unit cells allow us to expand the finite number of electronic wave functions. Also, the potential experienced by an electron is invariant under crystal lattice translation i.e, $V_{ext}(\mathbf{r}) = V_{ext}(\mathbf{r}+\mathbf{R})$ where, R is a lattice vector. Bloch's theorem states that in periodic solid each electronic wave functions can be written as the product of a cell-periodic part and a wavelike part:

$$\psi_{jk}(\mathbf{r}) = u_{jk}(\mathbf{r})e^{i\mathbf{k}.\mathbf{r}}. \tag{2.11}$$

Here, u_{jk} is a cell periodic part, and an exponential term is a plane wave. The cell-periodic part can be expanded in terms of a discrete set of plane waves whose wave vectors are reciprocal lattice vectors ($\mathbf{G}$) of the crystal.

$$u_{jk} = \frac{1}{\sqrt{V}} \sum_{G} C_{jk}(\mathbf{G}) e^{i\mathbf{G}.\mathbf{r}} \tag{2.12}$$

Therefore, each electronic Bloch wave function can be written as a sum of plane waves,

$$\psi_{jk} = \frac{1}{\sqrt{V}} \sum_{G} C_{j,k+G} e^{[i(\mathbf{k}+\mathbf{G}).\mathbf{r}]} \tag{2.13}$$

For non-periodic systems like surfaces, some vacuum is added to the repeating crystal slab such that faces of crystal do not interact with each other. Isolated molecules can be also studied in similar fashion, keeping molecule in a box such that the interaction between molecules is negligible.

The kinetic energy of plane waves is given by the following relations:

$$T_{|k+G|} = \frac{\hbar^2 |\mathbf{k}+\mathbf{G}|^2}{2m} \tag{2.14}$$

The plane waves basis with smaller kinetic energy are more relevant to the low energy states. So, plane waves are truncated by using an energy cutoff parameter E_{cut}.

The advantage of the plane wave basis is that they are independent of atomic positions, and they represent all region of space with the same resolution. So, Hellmann-Feynmann theorem can be used readily to evaluate forces. The calculation of energy and its derivative is analytic and quite simple. Also, the quality of the basis is controlled by a single parameter. The main shortcoming of the plane wave basis comes from the fact that the valence wavefunctions oscillate rapidly in the region occupied by the core electrons due to the strong ionic potential in this region. This demands a large basis set, making it computationally expensive. Pseudopotential approximation discussed in this chapter is the solution to this problem.

2.1.4 Exchange-Correlation Energy Functional

Electrons are Fermions, hence the wavefunction of many electron system should be asymmetric under exchange of any two electrons. This produces a spatial separation between the electrons that have the same spin leading to a reduction in the Coulomb energy of the electronic system. The reduction in energy due to antisymmetric nature of wavefunction is called the exchange energy, this is generally referred to as the Hartree-Fock approximation. Coulomb energy of the system is also reduced at the cost of an increase in kinetic energy when the electrons of the same spin are spatially separated. The difference between the many body energy of an electronic system and that calculated in the Hartree-Fock approximation is called the correlation energy. It is quite difficult to determine the exact value of exchange-correlation functional due to electron-electron interactions involved. Kohn Sham replaces many electron problem by single electron equation. The exchange-correlation energy functional Kohn Sham approach can be defined as:

$$E_{xc}[n(\mathbf{r})] = T[n(\mathbf{r})] - T_o[n(\mathbf{r})] + E_{ee}[(\mathbf{r})] - E_H[n(\mathbf{r})] \tag{2.15}$$

Here, $\mathrm{T}_o[n(\mathbf{r})]$ and $\mathrm{E}_{ee}[(\mathbf{r})]$ are exact kinetic and electron-electron interaction energies respectively. Since, exact value of E_{xc} is not known; so various approximations based on electron density have been introduced to describe it. We discuss a few widely used approximations to calculate the correlation energy:

Local density approximation (LDA): The exchange-correlation energy of an electronic system is constructed by assuming that the exchange-correlation energy per electron ($\varepsilon_{xc}(\mathbf{r})$) at a point $\mathbf{r}$ in the electron gas is equal to the exchange-correlation energy per electron of a homogenous electron gas that has the same density as the

electron density at a point **r**. Thus,

$$E_{xc}^{LDA}[n(\mathbf{r})] = \int d^3r n(\mathbf{r})\varepsilon_{xc}(n(\mathbf{r})) \tag{2.16}$$

and

$$\frac{\delta E_{xc}[n(\mathbf{r})]}{\delta n(\mathbf{r})} = \frac{\partial[n(\mathbf{r})\varepsilon_{xc}(\mathbf{r})]}{\partial n(\mathbf{r})} \tag{2.17}$$

with

$$\varepsilon_{xc}^{LDA}(\mathbf{r}) = \varepsilon_{xc}^{hom}[n(\mathbf{r})] \tag{2.18}$$

The local density approximations assumes that the effects of exchange and correlations are local in character. The Perdew-Zunger (PZ), Perdew-Wang (PW), and Vosko-Wilk-Nusair (VWN) functionals are the LDA functionals used commonly in calculations, which interpolate between exact results available at high and low densities n.

Generalized Gradient Approximations (GGA): In a system like molecules where the charge density varies rapidly, GGA has been proved as an improvement over LDA. The exchange-correlation energy is expressed as a sum of contributions from each point in real-space depending only on the density and its gradient at each point and independent of other points

$$E_{xc}^{GGA}[n(\mathbf{r})] = \int d^3r \varepsilon_{xc}(n(\mathbf{r}), \nabla\mathbf{n})n(\mathbf{r}) \tag{2.19}$$

Typically, GGA reduces the magnitude of exchange correlation energy, resulting in partial correction of the overbinding typical of LDA and thus improving the better agreement with experiments. Perdew and Wang (PW91) and Perdew, Burke and

Ernzerhof (PBE) are some of the functional within GGA.

Hybrid functionals: This exchange-correlation energy functional incorporates a portion of exact exchange from Hartree-Fock with the rest of exchange-correlation from other sources. These functionals are the combination of orbital-dependent Hartree-Fock and density functional and hence termed as a hybrid. Hybrid density functionals have further improved upon the GGA results. The inclusion of nondynamical exchange correlations effectively delocalizes the GGA exchange hole leading to the improvement in results. For accurate estimation of band gaps, we have used Heyd-Scuseria-Ernzerhof (HSE) hybrid functionals based on a screened Coulomb operator for the exchange interaction of the form [36],

$$E_{xc}^{\omega PBEh} = aE_x^{HF,SR}(\omega) + (1-a)E_X^{PBE,SR}(\omega) + E_x^{PBE,LR}(\omega) + E_c^{PBE} \tag{2.20}$$

where a = $\frac{1}{4}$, ω is an adjustable parameter which controls the extent of short-range interactions, $E_x^{HF,SR}(\omega)$ is the short-range Hartree-Fock exact functional, $E_x^{PBE,SR}(\omega)$ and $E_x^{PBE,LR}(\omega)$ are respectively the short and long range components of PBE exchange functional and E_c^{PBE} is the PBE correlation functional. The exact exchange mixing is performed only for short-range interactions in both HF and DFT. As a result exchange hole become delocalized among the near neighbors of a reference point, but not beyond.

Hybrid functionals are the most accurate functionals for the calculations of band gaps or excitation energies but are computationally expensive compared to simple LDA and GGA functionals.

2.1.5 Pseudopotential approximation

In solids or molecules, the core electrons are tightly bound to the nucleus and do not take part in bonding. So, core electrons are removed from the calculation, and the

interaction of the valence electrons with the nucleus plus the core states is replaced by an effective screened potential. This is termed as a pseudopotential approximation. The solution of the atomic Schrödinger's equation for the pseudopotential is a pseudo-wave function different from the true wave function. The pseudopotential is constructed in such a way that its scattering properties are similar to those of the all-electron potential. It requires less number of basis functions and hence is computationally efficient, without compromising much on the properties of the system.

Pseudopotentials are constructed using a cutoff radius (r_c) which sort of separates the valence region from the core region. The region beyond r_c is treated as a valence region and within the r_c is core region. The value of r_c is chosen in such a way that the last node of the all electron wavefunction fall inside it. Pseudopotential and all electron wavefunction are identical outside the cutoff radius.

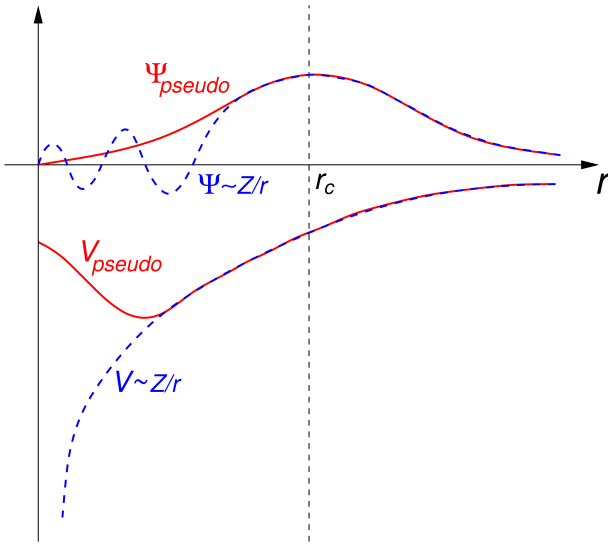

Figure 2.2: Schematic representation of all-electron (dashed lines) and pseudoelectron (solid lines) potentials and their corresponding wavefunctions. The radius at which all-electron and pseudoelectron value matches is designated r_c.

In the norm-conserving pseudopotentials, the norm of all electron wavefunction in the core region (0 to r_c) remains conserved. Atoms like $2p$, $3d$, and $4f$ have highly localized charge densities in the valence shell as well as in the core. The norm-conserving pseudopotential is not much effective in reducing the number of plane waves required

for representation. Another alternative to this is the ultrasoft pseudopotential. The ultrasoft pseudopotential generates the smoother wavefunction and reduces the size of the required plane wave basis set, by increasing the value of r_c without sacrificing transferability.

2.1.6 Linearized Augmented Plane Wave (LAPW) method

The linearized augmented plane wave (LAPW) method is one of the most accurate methods for performing electronic structure calculations for crystals. It is based on the density functional theory for the treatment of exchange and correlation. LAPW [37] derives its idea from Slater's APW method [38, 39]. The LAPW method introduces a basis set for calculating (Kohn-Sham) eigenvalues (energy bands) of a many-electron system (here a crystal) by introducing a basis set. An efficient basis for such solutions is constructed by first partitioning the cell into two parts: spheres around each atom (I), and the remaining interstitial region (II) (marked in Fig. 2.3). The LAPW basis functions are then constructed by connecting plane waves (sinusoidal functions) in the interstitial region to linear combinations of atomic-like functions in the spheres. The basis is thus atomic-like where the solution is atomic-like, and completely general (plane waves) where the solution is not atomic-like and may vary widely from one crystal structure to another. In this formalism the basis function in the interestial region can be written as:

$$\phi(\mathbf{r}) = \frac{1}{\sqrt{V}} \sum_{G} C_G e^{i(\mathbf{k}+G).\mathbf{r}} \tag{2.21}$$

Inside atomic spheres the wave functions can be written as:

$$\phi(\mathbf{r}) = \sum_{lm} (A_{lm} u_l m(\mathbf{r}) + B_{lm} u_l^{'}(\mathbf{r})) Y_{lm}(\mathbf{r}) \tag{2.22}$$

The atomic-like nature of the LAPW basis in the vicinity of the atoms leads to an

efficient representation, while the plane wave nature in the interstitial region allows for highly accurate solutions for any atomic arrangement: close-packed or open, high-symmetry or low, surfaces or bulk.

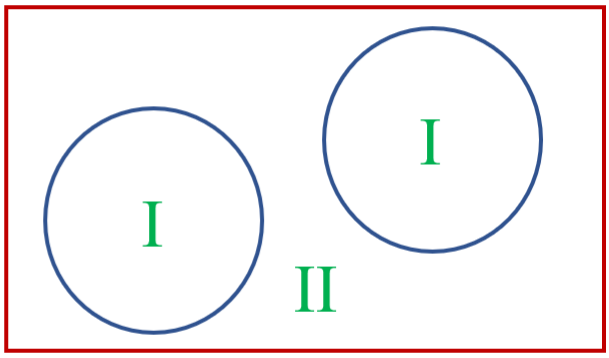

Figure 2.3: Partition of unit cell into atomic spheres (I) and interestitial region (II).

2.1.7 Spin-orbit coupling

The coupling of the intrinsic magnetic moment of electrons (arising due to its spin) with magnetic field seen in its orbital motion around the nucleus leads to the spin-orbit splitting of energy levels. As the nuclear charge increases the spin-orbit coupling becomes stronger, and hence the energy-band structures of solids containing heavy atoms are strongly affected by spin-orbit interaction. In the electronic structure calculation, relativistic effects can be incorporated by solving nonrelativistic Kohn-Sham equations with pseudopotentials tailored to reproduce the solutions of fully relativistic atomic Dirac-like equations. The radial components of the solutions of a fully relativistic atomic Dirac-like equation depend on the total angular momentum j and on the orbital angular momentum l. The non-local part of a pseudopotential in this case includes both scalar relativistic and spin-orbit coupling [40]:

$$V_{NL} = \sum_{l} \sum_{l,j,m_j} E^I_{l,j} \left|\beta^I_{l,j} Y^{I,j,m_j}_{l,\frac{1}{2}}\right\rangle \left\langle\beta^I_{l,j} Y^{I,j,m_j}_{l,\frac{1}{2}}\right| \tag{2.23}$$

where, $Y_{l,\frac{1}{2}}^{I,j,m_j}$ are the two-components spin-angle functions which appear in the solution of the Dirac equation in spherically symmetric potential. $\beta_{l,j}^{I}$ are the radial components of the projector function for each l and j,

2.1.8 Dispersive interaction

A general short-coming of all common GGA functionals, including hybrids, that replace part of the local by nonlocal HF exchange, is that they can not describe long-range electron correlations that are responsible for van der Waals (vdW, dispersive) forces. The vdW interactions between atoms and molecules play an important role in many chemical systems. The methods developed to include dispersion corrections in DFT can be broadly divided into two classes. In one class of method, the dispersion interaction is added as a semi-empirical corrections on top of existing local functionals, and another class of method attempts to develop non-local exchange-correlation energy functionals that can incorporate the London interactions [41, 42]. We have used parametrized DFT-D2 treatment of Grimme [41] for weak interactions between substrate and molecules. This gives a fairly accurate treatment of London dispersion interactions at relatively low computational cost, and we briefly describe the formulation below. The total energy with dispersion correction is given as,

$$E_{DFT-D2} = E_{KS-DFT} + E_{disp} \tag{2.24}$$

where $E_{KS\text{–}DFT}$ is the self consistent Kohn-Sham energy (Eq. 2.6) and E_{disp} is the empirical dispersion correction which is given as,

$$E_{disp.} = -S_6 \sum_{i=1}^{N_{at}-1} \sum_{j=i+1}^{N_{at}} \frac{C_6^{ij}}{R_{ij}^6} f_{dmp}(R_{ij}) \tag{2.25}$$

Here, N_{at} is the number of atoms in the system, C_6^{ij} denotes the dispersion coefficient for a pair of atoms i and j, S_6 is a global scaling factor that depends only on

the approximate functional used, and R_{ij} is an interatomic distance. To avoid the singularities for small R_{ij}, a damping function (f_{dmp}) is used,

$$f_{dmp}(R_{ij}) = \frac{1}{1 + e^{-d(R_{ij}/R_r - 1)}} \tag{2.26}$$

Here, R_r is the sum of atomic van der Waals radii, the parameter d determines the dispersion corrections to the total energy and is fixed to 20 by Grimme to give accurate dispersion energies, but still maintaining negligible energies for typical covalent bonding situations. The dispersion coefficient C_6^{ij} for a given pair of atoms i and j, is written as a geometric mean of the individual coefficients:

$$C_6^{ij} = \sqrt{C_6^i C_6^j} \tag{2.27}$$

2.2 Phonons

Crystal lattice possess long range translational order, and all motions are ceased at absolute zero temperature. At T>0 K the ions vibrate with a certain amplitude that depends on temperature. These thermal lattice vibrations can be considered as a collective motion of ions which can be populated and excited just like electrons. These excitations are phonons. Phonons greatly influence a wide variety of physical properties of materials: specific heats, thermal expansion, heat conduction, the resistivity of metals, superconductivity etc. There are mainly two ways of calculating phonon modes: by displacing the particles according to the desired pattern in a supercell of the required size (*frozen phonons*), and by perturbatively considering the displacements of the atoms in the unit cell and the appropriate vector in the phonon BZ (*linear response*). The linear response makes use of density functional perturbation theory.

2.2.1 Frozen phonons

It is an older way to calculate phonons. In this method, the series of displacements of atoms is performed and the forces exerted on other atoms is evaluated. The elements of force constant matrix Φ is constructed by calculating the forces between the atoms in a crystal [43]:

$$\Phi_{i\alpha,j\beta} = \frac{-\partial F_{j\beta}}{\partial u_{i\alpha}} = \frac{\partial^2 E}{\partial u_{i\alpha} \partial u_{j\beta}} \tag{2.28}$$

Here, i and j are the atoms and α and β are the Cartesian directions, $F_{j\beta}$ is the force on atom j due to a displacement $u_{i\alpha}$ of atom i in direction α. The force constants calculated by this method represents a sum over supercell of forces between one atom and all periodic images, they are not true atom-atom force constants. The Fourier transform of $\Phi_{i\alpha,j\beta}$ at wave vector k gives the dynamical matrix ($D_{i\alpha,j\beta}$) (renormalized by a mass factor). The phonon frequencies are obtained as the square roots of eigenvalues of the dynamical matrix.

One drawback of the frozen-phonon method is that it requires large supercells to calculate the force constant matrix accurately, and hence is computationally expensive. Due to the periodic boundary conditions used in DFT calculations, the displacement of one atom in a small unit cell creates forces not only on all the atoms in the same unit cell, but also on the periodic images of these atoms. This drawback of frozen phonon method is overcome by the density functional perturbation theory.

2.2.2 Density Functional Perturbation Theory

In this method, it is essential to calculate the second-order change in the DFT total energy (δ^2E) within the framework of density functional theory. The perturbation is induced by small displacement δR of ion from its equilibrium positions. This results in change in the external potential V_{ext}, which changes Ψ in the KS equation, and hence the charge density. The interatomic force constants (IFCs) are obtained using

second order derivatives of ground state energy with respect to perturbation, i.e. ionic displacement [44, 45],

$$K_{IJ} = \frac{\partial^2 E(\{\mathbf{R}\})}{\partial \mathbf{R}_I \partial \mathbf{R}_J} = \int \frac{\partial n(\mathbf{r})}{\partial \mathbf{R}_J} \frac{\partial V_{[R]}(\mathbf{r})}{\partial \mathbf{R}_I} d\mathbf{r} + \delta_{IJ} \int n(\mathbf{r}) \frac{\partial^2 V_{[\mathbf{R}]}(\mathbf{r})}{\partial \mathbf{R}_I \partial \mathbf{R}_J} d\mathbf{r} + \frac{\partial^2 E_N(\{\mathbf{R}\})}{\partial \mathbf{R}_I \partial \mathbf{R}_J} \tag{2.29}$$

The IFC depends on ground state charge density and its linear response to displacement of ion ($\frac{\partial n(r)}{\partial R_I}$). In the perturbation theory, Kohn-Sham equation is given as:

$$(H^{(0)}_{SCF} - \epsilon^{(0)}_i)|\phi^{(1)}_i\rangle + (V^{(1)}_{SCF} - \epsilon^{(1)}_i)|\phi^{(0)}_i\rangle = 0 \tag{2.30}$$

Here, $H^{(0)}_{SCF}$ is unperturbed Kohn-Sham Hamiltonian. $\epsilon^{(0)}_i$ and $\phi^{(0)}_i$ are the eigenvalues and eigenvectors of this Hamiltonian. The self-consistent Kohn-Sham effective potential is given at first order by:

$$V^{(1)}_{SCF}(\mathbf{r}) = V^{(1)}_{ext}(\mathbf{r}) + e^2 \int \frac{n^{(1)}(\mathbf{r}')dr'}{|\mathbf{r} - \mathbf{r}'|} + \int d\mathbf{r}' \frac{dV_{XC}(\mathbf{r})}{dn(\mathbf{r}')} \,|_{n^{(0)}(\mathbf{r})}\, n^{(1)}(\mathbf{r}') \tag{2.31}$$

By solving the equations 2.30 and 2.31, the change in charge density can be evaluated using:

$$\frac{\partial n(\mathbf{r})}{\partial \mathbf{R}_I} = 4Re \sum_{n=1}^{N/2} \psi^*_n(\mathbf{r}) \frac{\partial \psi_n(\mathbf{r})}{\partial \mathbf{R}_I} \tag{2.32}$$

Δn is used to evaluate the second derivative of total energy using equation 2.29.

References

1. M. C. Payne, M. P. Teter, D. C. Allan, T. A. Arias and J. D. Joannopoulos, Iterative minimization technique for *ab initio* total-energy calculations: molecular dynamics and conjugate gradients, *Rev. Mod. Phys. 64, 1045-1097*

2. Richard M. Martin, *Electronic Structure: Basic Theory and Practical Methods*, Cambridge University Press, 2004

3. Jorge Kohanoff, *Electronic Structure Calculations For Solids and Molecues*, Cambridge University Press, 2006

Part I

Metal Oxides and Chalcogenides

Chapter 3

TiNF and Cd_2NF: The Analogues of TiO_2 and CdO

3.1 Introduction

Aliovalent anion substitution in inorganic compounds has a profound effect on the material properties [46]. For example, substitution of N^{3-} and F^- in metal oxides changes the electronic properties significantly [47]. N-doping alone in oxides creates oxygen vacancies in the lattice which is avoided by codoping with F. Co-doping with N and F is therefore an important way to alter the electronic as well as optical properties of oxides. It has been found recently that substitution of N^{3-} and F^- in ZnO affects the band gap in an interesting manner, [48, 49] first decreasing significantly followed by an increase with higher content of N^{3-} and F^- [46]. Especially important is the discovery [50] of Zn_2NF in which entire O^{2-} in ZnO is substituted by N^{3-} and F^- equally. Aliovalent anion substitution is also found to have an effect on the electronic structure of the metal sulphides [46, 51]. Theoretical studies on the band structure of N, F-cosubstituted oxides show that an isolated band appears at the top of the valence band which could be attributed to the *N-2p* states whereas *F-2p* states lie low in energy [49]. A decrease in the band gap is observed by the substitution of N in

oxides thereby rendering the oxides active in the visible spectrum whereas F doping although less explored does not affect the band structure significantly, but enhances the photocatalytic activity by creating surface oxygen vacancies [52, 53]

TiO_2, an important oxide occurs in three structural forms: rutile, anatase, and brookite, and has the potential for use in a wide variety of applications such as a photocatalysis [54–58], solar cells [59, 60], in Li-ion batteries [61] etc. As the anatase phase of TiO_2 is a semiconductor with a wide band gap of 3.2 eV, its electrons can be excited only by ultraviolet (UV) light. Several efforts have been focussed on reducing the band gap of TiO_2 so that it can be photo-excited by visible light, for example by substitution of N and Nd [62,63]. Prof. C. N. R Rao's group* synthesized N, F-doped anatase TiO_2 which is colored. They have also synthesized TiNF both in rutile and anatase phase by completely substituting O atoms with N and F. Cd_2NF is another interesting compound synthesized by them by completely replacing O atoms of CdO by N and F atoms.

In this chapter, we present a detailed analysis of the structural and electronic properties of TiNF in both the rutile and anatase structure. We have also tried to understand the vibrational properties of TiNF and N, F-doped anatase TiO_2. Aligning the valence and conduction bands of anatase TiNF relative to the standard hydrogen electrode (SHE) potential, we assess its potential as a photocatalyst for water splitting reaction.

3.2 TiNF and N, F-doped TiO_2 †

3.2.1 Computational details

Our first-principles calculations are based on density functional theory (DFT) as implemented in the Quantum ESPRESSO (QE) package [65]. We have used a local

*New Chemistry Unit, Jawaharlal Nehru Centre for Advanced Scientific Research, Bangalore-560064

†This work has been published in ChemPhysChem **19**, 3410 (2018) [64]. Reproduced with permission from the John Wiley and Sons.

density approximation (LDA) to treat the exchange-correlation energy of electrons, and norm-conserving pseudopotentials to represent the interaction between ionic cores and valence electrons. We employ an energy cut-off of 85 Ry to truncate the plane-wave basis set used in the representation of Kohn-Sham wavefunctions. The structures were relaxed to minimize total energy until the Hellmann-Feynmann force on each atom is less than the 0.01 eV/Å. We used uniform meshes of 4×4×4, 6×6×8, and 4×4×2 k-vectors to sample integrations over Brillouin Zones (BZ) of TiNF in anatase (primitive unit cell), rutile and N, F-doped TiO_2 respectively. We used the Heyd-Scuseria-Ernzerhof (HSE-06) hybrid functional of exchange-correlation energy [36] to obtain accurate estimates of band gaps, with 2×2×2 mesh of k-points in the evaluation of Hartree-Fock exchange energy. Phonon dispersion was determined with Fourier interpolation of the dynamical matrices obtained at q-points on a uniform 2×2×2 mesh with DFT linear response technique as implemented in QE. We have carried out some of the calculations with LDA ultrasoft pseudopotentials (USPPs) for benchmarking through comparison with results of Ref. 14.

We constructed 2×2×2 supercells of the most stable chemically ordered configuration of TiNF in both anatase and rutile forms and introduced a F-vacancy by removing one F atom in the supercell. We performed LDA+U calculations using U=3.0 eV in order to include on-site correlations of Ti-*3d* orbitals. Structures were internally relaxed maintaining the lattice constant obtained with U=0 eV. For a better comparison of the structures with F-vacancy and pristine TiNF, we repeated the calculations of pristine TiNF including the U correction. To probe the optical properties of N, F-doped TiO_2, we obtained the imaginary part of dielectric tensors as a function of frequency.

3.2.2 Structural Properties

Anatase TiNF crystallizes in the body-centered tetragonal (BCT) crystal structure. Since all its anion sites are symmetry equivalent, N and F atoms can be arranged in the three symmetry inequivalent configurations of the conventional unit cell ($Ti_4N_4F_4$). In the first configuration, alternating (001) planes are occupied entirely by N atoms and F atoms (the configuration I, Fig. 3.1 (a)). In the second, N and F atoms occupy the alternate atomic sites (configuration II, Fig. 3.1(b)), and in the third, N and F atoms occupy alternate sites only in (001) plane such that the diagonally opposite sites of the unit cell are occupied by the same species (configuration III, Fig. 3.1(c)). Matar [66] has reported results for electronic and structural properties of TiNF using first-principles calculations, considering the configurations I and II. As our estimates of lattice constants (Table 3.1) and the reported values obtained using USPP are different, we performed structural relaxation of configurations I and II using USPP.

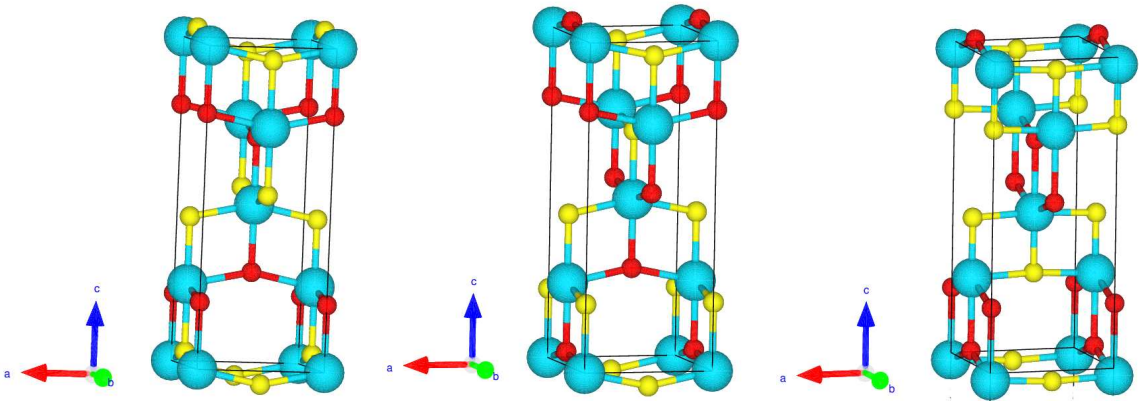

(a) (b) (c)

Figure 3.1: Different realisation of chemical ordering of N and F atoms in anatase structure of TiNF. (a) Configuration I, (b) Configuration II, and (c) Configuration III. Ti, N, and F atoms are represented by blue, yellow, and red spheres respectively.

We find that the calculated lattice constants are indeed in close agreement with the results in Ref. [66] (Table 3.2). In TiNF in the rutile structure, N and F atoms can be arranged in two symmetry inequivalent configurations. In one, N and F atoms occupy sites in alternating (001) planes (the configuration I, Fig. 3.2(a)), while in

Table 3.1: Lattice constants (Å) and bond lengths (Å) of anatase TiNF in the three configurations (see Fig. 3.1).

Structural Parameters	Exp. [67]	Config. I	Config. II	Config. III	Config. III (distorted)
a/b	3.79	3.84	3.81	3.86/3.80	3.81/3.82
c	9.50	9.33	9.57	9.40	9.49
Ti-N (‖)	1.9354	1.97	2.00	1.93	1.92
Ti-N (⊥)	1.9760	1.87	1.79	1.82	1.83
Ti-F (‖)	-	1.93	1.90	1.99	2.05/1.96
Ti-F (⊥)	-	2.10	2.42	2.18	2.16

configuration II, N and F occupy the alternate atomic sites (Fig. 3.2(b)). The lattice constants and bond angles of these configurations have been shown in Table 3.3. The complete substitution of O by N and F leads to the elongation of lattice constants. Since the structure is disordered, we do not get γ=90^o in the configuration I and structure is orthorhombic for configuration II. For configuration II we get a lattice constants a=4.55 $\mathring{A}$, b=4.68 $\mathring{A}$, considering the disorderness in the system we have given its average in Table 3.3.

Table 3.2: Lattice constants (Å) and bond lengths (Å) of TiNF in the two configurations of TiNF in anatase structure obtained using calculations based on LDA-USPPs. For benchmarking we compare with results of similar calculations in Ref. [14].

Structural Parameters	Config. I	Config. I [66]	Config. II	Config. II [66]
a/b	3.84	3.851	3.81	3.81
c	9.50	9.547	9.69	9.66
Ti-N (‖)	1.98	1.98	2.01	1.94
Ti-N (⊥)	1.89	1.90	1.78	2.04
Ti-F (‖)	1.93	1.94	1.91	1.91
Ti-F (⊥)	2.15	2.14	2.52	2.27/2.50

We also considered the various chemical ordering of N and F atoms substituted in TiO_2 by substituting two O atoms by one N and one F atoms in the conventional unit cell of anatase TiO_2. Using site occupancy disorder (SOD) [68] technique we obtained seven inequivalent configurations of $TiO_{\frac{6}{4}}N_{\frac{1}{4}}F_{\frac{1}{4}}$ (see Fig. 3.3). Energies of

Table 3.3: Lattice constants (Å) and bond lengths (Å) of TiNF of the two configurations of TiNF in rutile structure.

Configurations	Lattice constants	Bond angles (^{o})
I	a=b=4.61, c=2.98	α=β=90, γ=86
II	<a>=4.62, c=2.99	α=β=γ=90

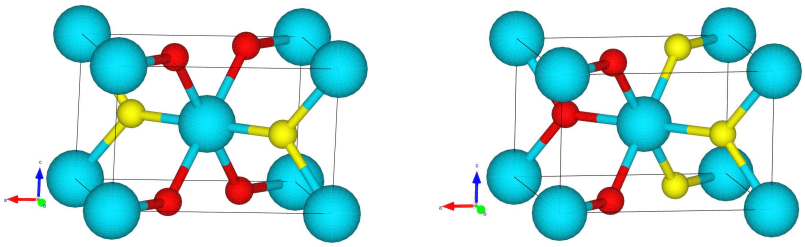

(a) (b)

Figure 3.2: Various chemically ordered states of N and F in rutile structure of TiNF (a) configuration I and, (b) configuration II discussed in the text. Ti, N and F atoms are represented by blue, yellow, and red spheres respectively.

these configurations show that the stable configuration is the one in which one plane is completely occupied by N atoms and an other plane is occupied by F atoms (shown in Fig. 3.3(g)) such that N-Ti-F bonding occurs along (001) direction. The lattice constants and band gaps of these configurations have been tabulated in Table 3.4. The substitution of N and F for oxygen results in expansion of the lattice of TiO_2.

Table 3.4: Relative energies (ΔE=E$_n$-E$_7$), lattice constants and associated band gaps (obtained using LDA-NC) of various chemical ordering of N and F atoms in anatase $TiO_{\frac{6}{4}}N_{\frac{1}{4}}F_{\frac{1}{4}}$. Configurations 1 to 7 have been shown in Figs. 3(a)-(g) respectively.

Configurations	ΔE (meV/f.u.)	Lattice constants (Å)	Band gaps (eV)
1	68	a=3.75, b=3.80, c=9.26	0.95
2	47	a=3.78, b=3.79, c=9.22	0.92
3	6	a=3.74, b=3.78, c=9.27	1.80
4	60	a=3.75, b=3.81, c=9.24	0.96
5	3	a=3.75, b=3.78, c=9.32	1.38
6	17	a=3.74, b=3.79, c=9.26	1.45
7	0	a=3.79, b=3.78, c=9.22	1.01

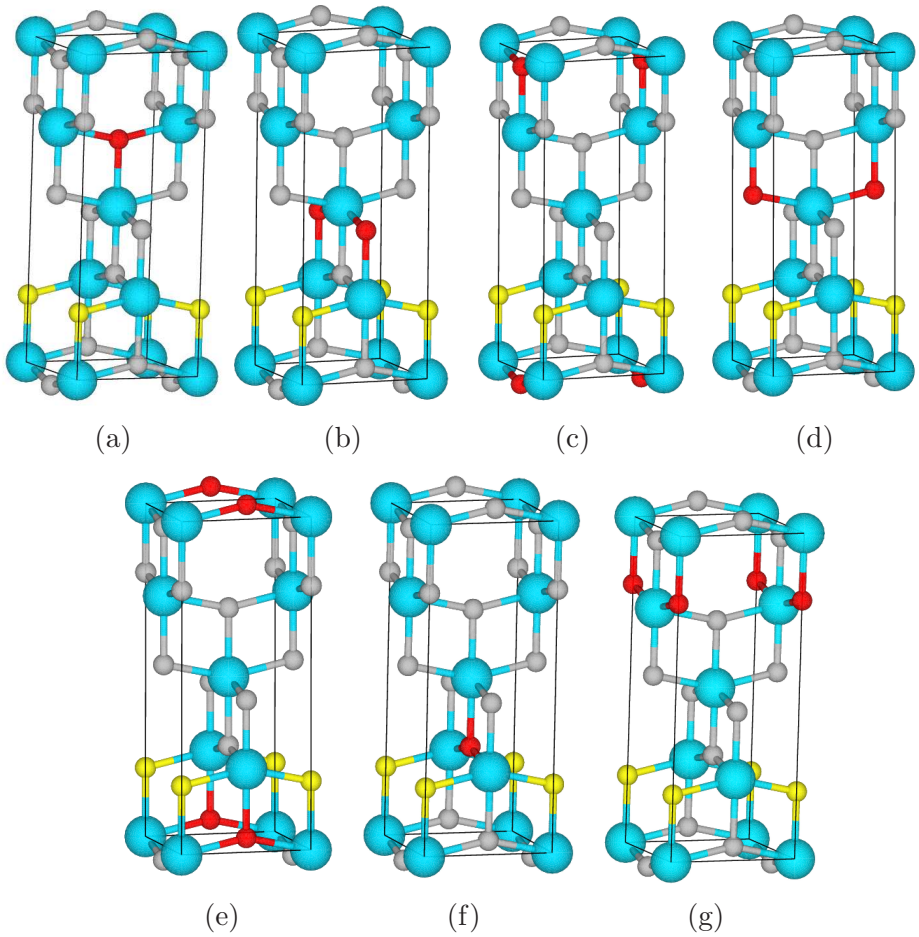

Figure 3.3: Various chemically ordered states of N and F substituted anatase structure of TiO_2 ($TiO_{\frac{6}{4}}N_{\frac{1}{4}}F_{\frac{1}{4}}$) (a)-(g). Ti, N, F and O atoms are represented by blue, yellow, red, and grey spheres respectively.

We obtained formation energies of different configurations of TiNF using the relation $E_{Ti_2N_2F_2}$-E^{Ti}_{hcp}-E_{N_2}-E_{F_2}, where $E_{Ti_2N_2F_2}$, E^{Ti}_{hcp}, E_{N_2} and E_{F_2} are the energies of bulk TiNF, hexagonal close packing (hcp) Ti crystal, isolated N_2, and F_2 molecules respectively. We find that the configuration III of anatase TiNF is energetically favorable of all the considered configurations (Fig. 3.1(c)). In TiNF in the rutile structure, configuration II with N and F atoms occupying the alternate sites is the most stable of all (Fig. 3.2(b)). TiNF in its rutile structure is energetically favorable by 0.13 eV/f.u. than its anatase structure. In the calculation of formation energies of $TiO_{\frac{6}{4}}N_{\frac{1}{4}}F_{\frac{1}{4}}$ configurations we used $E_{Ti_{\frac{6}{4}}N_{\frac{1}{4}}F_{\frac{1}{4}}}$-$2E^{Ti}_{hcp}$-$\frac{1}{2}E_{N_2}$-$\frac{1}{2}E_{F_2}$-$3E_{O_2}$. E_{O_2} is the energy of gaseous oxygen molecule. The formation energy of the stable configuration

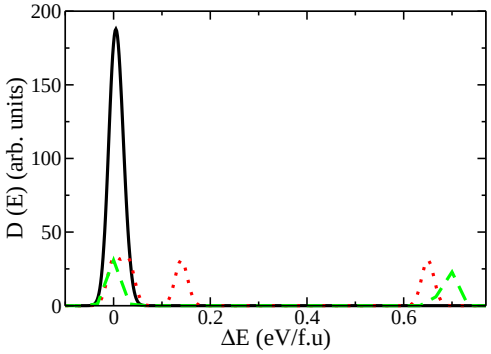

Figure 3.4: Distribution of formation energies of TiNF in rutile (dotted red line) and anatase (dashed green line) structures, and N, F-doped anatase TiO_2 (solid black line). The lowest fomation energy has been taken at zero.

(configuration VII) of $E_{TiO_{\frac{6}{4}}N_{\frac{1}{4}}F_{\frac{1}{4}}}$ is -10.57 eV/f.u, indicating its formation is more favorable than that of TiNF (-7.51 eV/f.u), as expected from the generically greater stability of oxides. We find that $E_{TiO_{\frac{6}{4}}N_{\frac{1}{4}}F_{\frac{1}{4}}} > \frac{3}{2}E_{Ti_2O_4}+\frac{1}{2}E_{Ti_2N_2F_2}$ by 0.1 eV/Ti atom indicating the formation of TiNF and TiO_2 more favorable compared to $TiO_{\frac{6}{4}}N_{\frac{1}{4}}F_{\frac{1}{4}}$. The distribution of formations enrgies for all the considered systems have been shown in Fig. 3.4.

3.2.3 Electronic structure

We now examine the electronic structure of three chemically ordered configurations of anatase TiNF along high symmetry lines of the BZ of the primitive unit cell of BCT (Fig. 3.5). It is clear that different ordering of N and F in the lattice influences its band gaps (see band gaps of these configurations in Table 3.5). As expected, the most stable of the configurations has the widest band gap. Our LDA-based estimate of the band gap of configuration I is 0.68 eV, which was predicted to be metallic by Matar [66]. In this work, the author determined the electronic nature of the configuration I on the basis of the projected density of states (PDOS). In a calculation based on LDA-USPP, the band gap of configuration I is 0.12 eV which can be missed in the PDOS through use of broadening of the δ function. We find an indirect band gap of 1.92 eV for configuration II, which is quite close to the estimate

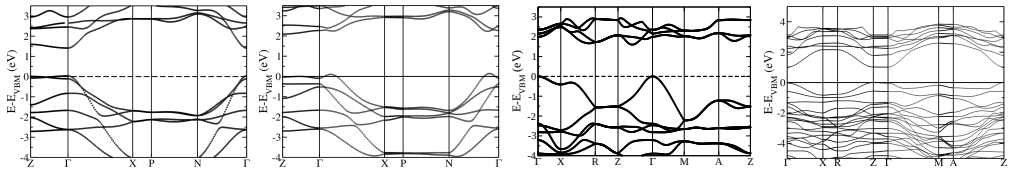

(a) (b) (c) (d)

Figure 3.5: Electronic structure of anatase TiNF in (a) configuration III, (b) distorted configuration III, (c) rutile TiNF and (d) anatase $TiO_{1.50}N_{0.25}F_{0.25}$.

of 2.0 eV by Matar [66]. Since LDA underestimates the band gaps, we used hybrid functionals in calculations to determine the band gaps accurately (see Table 3.5). We now present the detailed analysis of stable configurations of TiNF and N, F-doped anatase TiO_2.

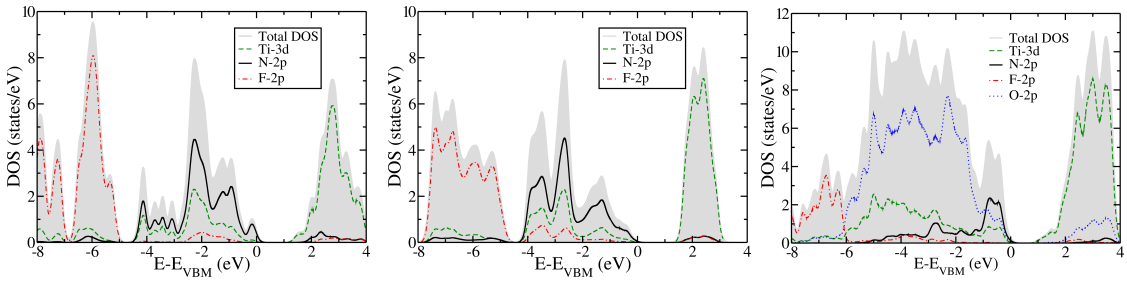

(a) (b) (c)

Figure 3.6: Projected density of states of (a) anatase TiNF (configuration III), (b) rutile TiNF, and (c) $TiO_{1.50}N_{0.25}F_{0.25}$ in anatase structure.

Configuration III of the anatase structure is energetically most stable having lowest energy of all. In configuration III, we find a direct band gap of 1.36 eV at Γ-point (Fig. 3.5(a)) and an indirect band gap of 2.73 eV using hybrid functional based calculations (see Table 3.5). From the PDOS, it is clear that the states near valence band maximum (VBM) have a predominant contribution from 2p orbitals of N, with a slight mixing with Ti-3d states. Lower energy (∼-6 eV) valence bands are constituted primarily of F-2p orbitals. The states at the conduction band minimum (CBM) have a predominant contribution from Ti-3d orbitals (Fig. 3.6(a)), similar to that of TiO_2, confirming the idea of valence band engineering of oxides with anion substitution [46]. Configuration II represents the most stable chemical ordering of N and F in TiNF in the rutile structure. We find an indirect band gap of 1.64 eV using LDA-NC (Fig.

3.5(c)) and 2.70 eV using HSE calculations. Similar to TiNF in the anatase structure, we have a dominant contribution of Ti-3d orbitals in conduction bands and of N-2p orbitals in valence bands(Fig. 3.6(b)).

In $TiO_{\frac{6}{4}}N_{\frac{1}{4}}F_{\frac{1}{4}}$, we find an indirect band gap of 1.01 eV (Fig. 3.5(d)) in the electronic structure obtained with LDA calculations. In the HSE band structure, the band gap is 2.37 eV in close agreement with the experimental band gap of 2.60 eV. Complete substitution of O with N and F in TiO_2 increases the band gap significantly, with states at VBM having a dominant contribution from N-2p orbitals and states near the CBM mostly comprising of Ti-3d states (Fig. 3.6(c)).

3.2.4 Phonons

In the phonon spectrum calculated along high symmetry lines in the BZ of configuration III of TiNF in the anatase structure, we find some modes with imaginary frequencies along Z-Γ-X lines (Fig. 3.7(a)). The mode with an imaginary frequency of 255i cm^{-1} at Γ-point involves the in-plane displacements of N atoms in opposite directions. We distorted the structure by freezing these modes through displacements of atoms by 0.03 Å, and obtained a new lower energy structure upon relaxation (will be termed as the distorted structure). Lattice constants of the distorted configu-

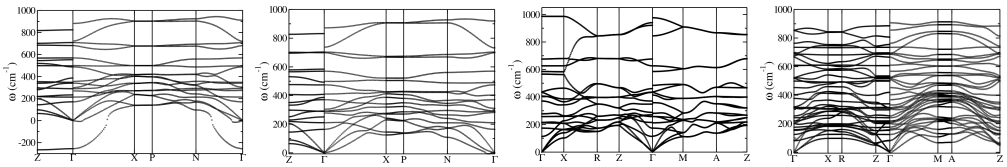

(a) (b) (c) (d)

Figure 3.7: Phonon spectra of configuration III of TiNF in (a) undistorted and, (b) distorted anatase structure, in (c) Rutile structure and (d) N, F-doped TiO_2 in anatse structure.

ration III after freezing the mode are (a=3.81 Å, b=3.82 Å, and c=9.49 Å), in even better agreement with the experimental values (see changes in bond lengths in Table 3.1). The energy of the relaxed structure reduces by 0.024 eV/f.u relative to

Table 3.5: Electronic band gaps and relative energies (ΔE) of the three configurations of anatase TiNF estimated within LDA and HSE calculations. The electronic band gaps and ΔE of TiNF in its rutile structure have been given in parentheses.

	Band gaps (eV)		ΔE (eV/f.u.)
	LDA-NC	HSE	
I	0.68 (0.28)	2.17 (1.89)	0.65 (0.68)
II	1.92 (1.64)	3.46 (2.70)	0.14 (0.00)
III	1.36	2.73	0.024
III (distorted)	2.10	3.35	0.00

the undistorted one and its band gap changes from a direct to an indirect type and with an enhancement to 2.1 eV (LDA estimate) (Fig. 3.5(b)). Calculations with the HSE functional yields an estimate of the band gap of 3.35 eV, while the rest of the electronic structure remain qualitatively similar. We find no unstable modes ($\omega^2 < 0$) in the phonon dispersion of distorted structure (Fig. 3.7(b)), confirming its local stability (as an energy minimum). Phonon spectrum of TiNF in the rutile structure has no imaginary frequencies indicating its local stability (Fig. 3.7(c)). Phonon bands are more dispersed in the rutile structure compared to the anatase structure. Phonon spectrum of TiNF in its rutile structure has a gap around 500 cm^{-1} (see the vibrational density of states, Fig. 3.8(a)). We see a higher density of modes at 670 cm^{-1} in the rutile structure whereas, it is at 400 cm^{-1} in the rutile structure (Fig. 3.8(a)). Configuration VII of N, F-doped anatase TiO_2, has no unstable modes indicating its stability (Fig. 3.7(d)). Also, we have a high density of modes around 735 cm^{-1} (Fig. 3.8(b)). The polar character of the phonons of TiNF (both rutile and anatase) and N, F-doped anatase TiO_2 is clearly evident in the LO-TO splitting in their phonon spectra (Fig. 3.7). We have tabulated the Raman and infrared active modes of TiNF and N, F-doped anatase TiO_2 in Table 3.6, which constitute spectral signatures of the three materials analyzed here.

Table 3.6: Frequencies (cm^{-1}) of Raman and infrared active phonons of TiNF and N, F-doped TiO_2.

TiNF				N, F-doped	
Anatase		Rutile		TiO_2	(anatase)
Raman active	Infrared active	Raman active	Infrared active	Raman active	Infrared active
164	251	114	213	126	156
290	303	213	215	156	298
292	403	215	349	177	310
371	490	370	370	201	314
474	584	433	586	204	340
570	737	461	676	211	403
699		586		220	453
703		627		242	499
		940		254	516
				309	535
				403	607
				453	609
				499	
				516	
				519	
				524	
				607	
				609	
				666	
				688	
				690	
				696	
				735	
				763	
				855	

Table 3.7: Born effective charges of atoms in TiNF in the anatase structure (distorted configuration III).

Atoms	Z^*_{xx}	Z^*_{yy}	Z^*_{yz}	Z^*_{zy}	Z^*_{zz}
Ti	6.88	3.00	0.008	0.067	3.53
N	-5.53	-0.99	-0.07	-0.11	-1.83
F	-0.91	-2.02	0.06	0.047	-1.70

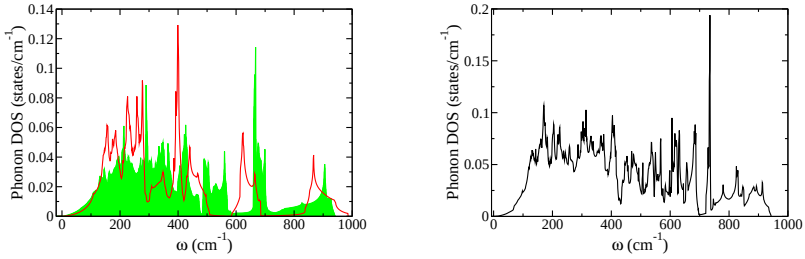

(a) (b)

Figure 3.8: Vibrational density of states of (a) TiNF in rutile (red line) and anatase structural forms (green shaded line), and (b) N, F-doped anatase TiO_2.

3.2.5 Born effective charges

The Born effective charges (Z^*) are the measure of the electric polarization response arising from atomic displacements at zero electric field, or equivalently of the forces exerted on an atom by an electric field. We find unusual Born effective charges for Ti, N and F atoms in TiNF (Table 3.7), which notably deviate from the nominal charges of +4, -3, and -1. The xx-component of Z^* of Ti, N [Z^*_{xx} (Ti) = 6.80, Z^*_{xx} (N) = -5.53], and the yy-component of Z^* of F [Z^*_{yy} (F) = -2.02] are quite anomalous. Z^*_{xx} (N) component is larger than the other components (yy, zz, yz and zy) of the anatase structure. The diagonal elements of Z^* tensors are not all equal due to low crystal symmetry, reflected in different in-plane and out-of-plane Ti-X bond lengths (Ti-N and Ti-F). Substitution and ordering of N and F in TiNF lower the structural symmetry, and the off-diagonal elements of Z^* are also non-zero (Table 3.7). Such large Z^* are because of the strong covalent interaction between Ti and anions [69]. We note that the Z^* is larger along the Ti-N and Ti-F in-plane bonding axis. In its rutile structure, yy and zz-component of Z^* of Ti [Z^*_{yy} (Ti) = 5.99, Z^*_{zz} (Ti) = 6.87] is larger than any other components (see Table 3.8). We see an anomalous charges of Ti in N, F-doped anatase TiO_2, particularly of the Ti atom connected to two N or F atoms (Table 3.9). The yy-component of Z^* of Ti (Ti_3) connected to two N atoms is 8.06 and zz-component of Ti (Ti_4) connected to two F atoms is 7.03. These values of Ti are larger than any other components of Z^* of Ti. This may be attributed to

Table 3.8: Born effective charges of atoms in TiNF in the rutile structure (configuration II).

Atoms	Z^*_{xx}	Z^*_{xy}	Z^*_{yx}	Z^*_{yy}	Z^*_{zz}
Ti	3.33	0.56	0.68	5.99	6.87
N	-1.54	-0.71	-2.08	-4.47	-5.15
F	-1.80	-0.85	0.70	-1.53	-1.73

the stronger covalent interaction between Ti-N/F compared to Ti-O. We also see an anamolous trends in Z^* of N, F and O atoms of N, F-doped anatase TiO_2 (Table 3.9). The LO-TO splitting observed in the phonon spectrum of these systems is attributed to the large Z^* values of Ti, N, F and O atoms. Similar anomalous effective charges of Ti have been found in the anatase phase of TiO_2 and perovskite compounds [70, 71].

3.2.6 Dielectric constants

We have obtained electronic and static dielectric constants of TiNF and $TiO_{\frac{6}{4}}N_{\frac{1}{4}}F_{\frac{1}{4}}$. The electronic dielectric constant (ε^{∞}) along y and z-direction is larger in the rutile structure of TiNF compared to that of the anatase structure (Table 3.10). This may be attributed to the lower band gap of TiNF in the rutile structure. Electronic dielectric tensor components of N, F-doped anatase TiO_2 have been tabulated in Table 3.11. We note that the electronic dielectric constant of N, F-doped anatase TiO_2 is greater than the TiNF in anatase structure along the y-direction.

We obtained the static dielectric constant using dynamical matrices and Born effective charges. We see that the static dielectric tensor of TiNF in rutile structure along y and z-direction is larger than that of TiNF in the anatase structure. From our calculations of the static dielectric constant tensors of TiNF, we find that the major contribution to dielectric constant [$\varepsilon^0_{xx} = 23$] comes from the infrared active mode at 584 cm^{-1} which involves the in-plane vibrations of N atoms along y-direction (Fig. 3.9(a)). As the high frequency mode at 584 cm^{-1} dominates the ε^0, we expect the static

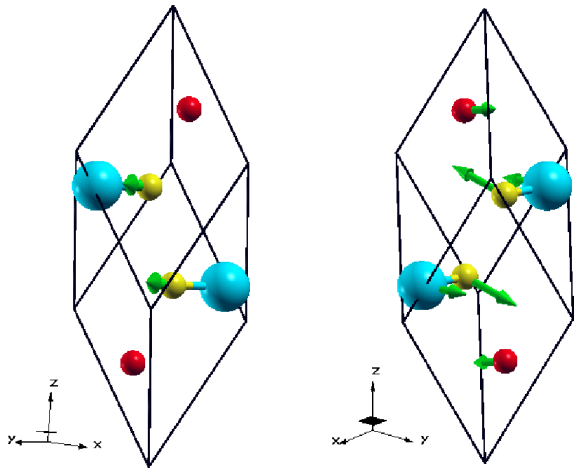

(a) (b)

Figure 3.9: Phonon modes of frequencies 584 cm^{-1} and 164 cm^{-1} contributing dominantly to (a) xx-component, and (b) yy, zz-components, of the static dielectric tensor of TiNF in the anatase structure respectively.

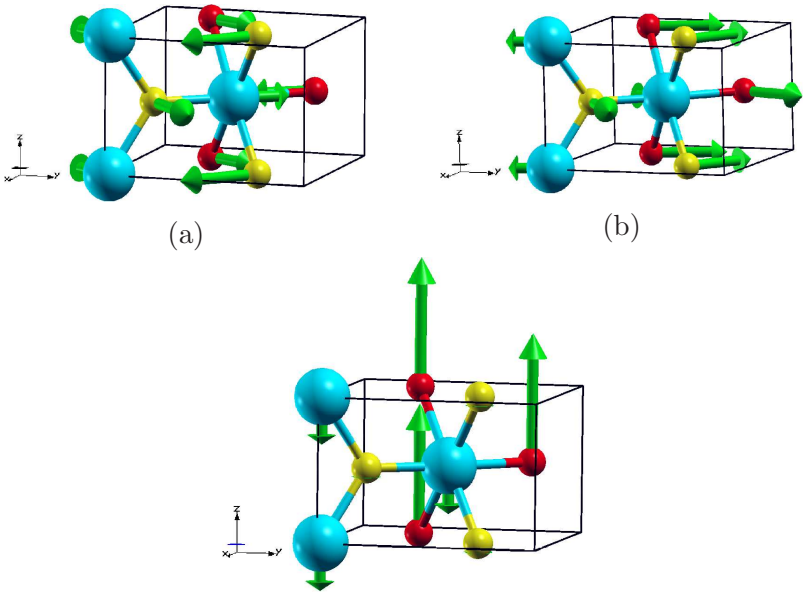

(a) (b)

(c)

Figure 3.10: Phonon modes of frequencies 349 cm^{-1}, 215 cm^{-1} and 213 cm^{-1} contributing dominantly to (a) xx-component, (b) yy-component, and (c) zz-component of the static dielectric tensor of rutile TiNF respectively.

dielectric constants (like ε^0_{xx}) of TiNF to be relatively independent of temperatures or pressures. In contrast, yy and zz-components are dominated by the Raman active mode of 164 cm^{-1} mode (Fig. 3.9(b)), and off-diagonal elements are dominated by the infrared active mode of frequency 302 cm^{-1}. The values of ε^0 components and

Table 3.9: Born effective charges of Ti, O, N and F atoms in N, F-doped anatase TiO_2 (configuration VII).

Atoms	Z^*_{xx}	Z^*_{yy}	Z^*_{zz}
Ti_1	3.79	6.18	4.29
Ti_2	6.74	5.45	5.41
Ti_3	5.14	8.06	4.26
Ti_4	4.23	6.93	7.03
N	-1.07	-6.82	-2.80
F	-2.82	-0.080	-1.35
O_1	-1.05	-5.53	-2.51
O_2	-5.41	-1.20	-2.42
O_3	-2.98	-1.33	-3.95
O_4	-1.22	-4.53	-3.14
O_5	-1.11	-5.36	-1.92
O_6	-4.38	-1.37	-2.91

the modes responsible for it have been tabulated in Table 3.10. In the rutile TiNF, infrared active mode of 349 cm^{-1} contributes most significantly to ε^0_{xx}, and both infrared and Raman active mode at 215 cm^{-1} significantly contributes to ε^0_{yy}. Both of these modes (349 cm^{-1} and 215 cm^{-1}) involve the in-plane movement of N and F atoms (Figs. 3.10(a) and 3.10(b)). The mode at frequency 213 cm^{-1}, which is both infrared and Raman active makes a significant contribution to the zz-component of static dielectric tensor. This mode involves the out-of-plane movement of F and Ti atoms (Fig. 3.10(c)). The ε^0_{yy} of N, F-doped TiO_2 is larger than all dielectric tensor components of TiNF in both structures (Table 3.11). Weakly Raman and infrared active mode at ω=81 cm^{-1}, and both infrared and Raman active mode of frequency 607 cm^{-1} contribute equally to ε^0_{yy}. Both the modes involve in-plane vibrations of N and F atoms. Infrared active mode at ω=535 cm^{-1} and both infrared and Raman active mode of frequency 403 cm^{-1} contribute significantly to ε^0_{xx} and ε^0_{zz} respectively (atomic displacements of these modes have been shown in Fig. 3.11).

Table 3.10: Electronic (ε^{∞}) and static dielectric constants (ε^{0}) of TiNF in the rutile and anatase structure, along with frequencies of phonon modes that dominate the static dielectric tensor components.

	ε^{∞}		ε^{0}		Modes (cm^{-1})	
	Anatase	Rutile	Anatase	Rutile	Anatase	Rutile
xx	8.55	4.08	23.22	9.20	584	349
yy	3.32	8.05	6.00	34.84	164	215
yz	0.10	0.00	0.65	0.00	302	-
zy	0.10	0.00	0.65	0.00	302	-
zz	4.35	8.63	8.21	30.98	164	213

Table 3.11: Electronic and static dielectric constants of N, F-doped anatase TiO_2 along with frequencies of the modes that dominate the static response.

	ε^{∞}	ε^{0}	Modes (cm^{-1})
xx	5.14	17.32	535
yy	7.82	36.43	81, 607
zz	5.85	16.41	403

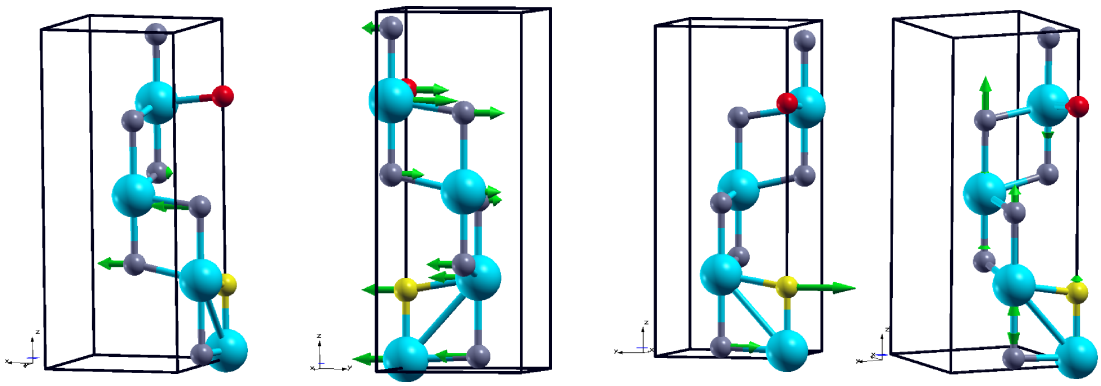

(a) (b) (c) (d)

Figure 3.11: Phonon modes of frequencies 535 cm^{-1}, 81 cm^{-1}, 607 cm^{-1}, 403 cm^{-1} contributing dominantly to (a) xx, (b), (c) yy, and (d) zz components of the static dielectric tensor of N, F-doped anatase $TiO_{1.50}N_{0.25}F_{0.25}$ respectively.

3.2.7 Band edges

TiNF is isolectronic to TiO_2, which is known to exhibit good photocatalytic activity [57]. As $2p$ orbitals of N and F are similar to $2p$ orbitals of O, we probed the photocatalytic activity by aligning its VBM and CBM with respect to the vacuum potential (see Fig. 3.12). To connect with vacuum potential, we constructed a slab

with the (001) surfaces of TiNF (using relaxed bulk coordinates) and used it in a supercell with a vacuum of 15 Å along the z-direction. We determined the difference

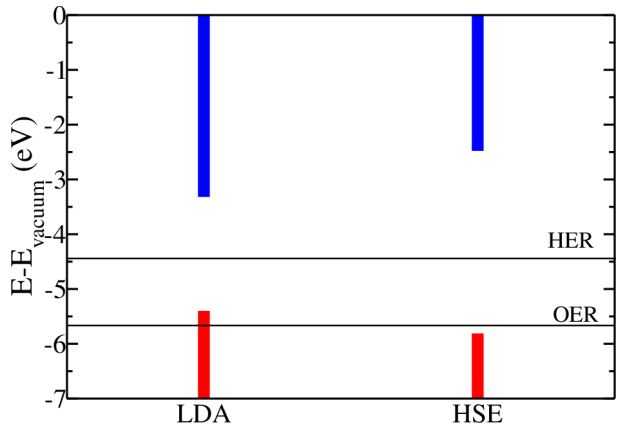

Figure 3.12: Valence band and conduction band edges of anatase TiNF (configuration III) determined with LDA and HSE calculations, aligned with respect to vacuum potential at 0 along with the redox potentials of hydrogen evolution reaction (HER) and oxygen evolution reaction (OER).

ΔV between the potentials in the vacuum and deep inside the bulk, and find that ΔV value does not change with the number of unit cells (the difference between ΔV obtained with slabs of 1 and 2 unit cells being $\sim$0.01 eV). Hence, we proceed further with the TiNF (001) slab consisting of just 1 unit of TiNF. We obtain the energies of bulk VBM and CBM bands relative to its macroscopic average potential in the vacuum (ΔV), and then align the bulk band edges with respect to ΔV as shown in Fig. 3.12. It is clear that the VBM and CBM edges (obtained with HSE calculations) straddle the hydrogen evolution reaction (HER) and oxygen evolution reaction (OER) potentials, and we thus expect anatase TiNF to be suitable for photocatalysis of water splitting reaction.

3.2.8 F-vacancies in TiNF and N, F-doped TiO_2

To understand the dark color of the anatase and rutile phases of TiNF observed experimentally, we introduced Ti^{3+} defects in the rutile and anatase phases by creating a F-vacancy in the supercell. We calculated the formation energy (E_v) of F-vacancy

simulated with 2×2×2 supercells of TiNF in anatase and rutile phase using:

$$E_v = E^v_{TiNF} - (E_{TiNF} - \frac{1}{2}E_{F2}) \tag{3.1}$$

where E^v_{TiNF}, E_{TiNF}, and E_{F2} are the energies of TiNF supercell with vacancy F, pristine TiNF, and gaseous F_2 molecule respectively. E_v of TiNF in the rutile and anatase phases are 3.17 eV and 4.81 eV respectively, which are comparable to anion vacancy formation energies [72–75], making them quite feasible in samples. As a result of vacancy formation, we noticed an increase in the Ti-N (‖) bond length from 1.94 Å to 2.03 Å in the anatase form. This change in the bond length is close to the difference in atomic radii of Ti atoms in Ti^{3+} and Ti^{4+} oxidation states. There is a slight change in Ti-N bond length along z-direction (see Table 3.12). Ti-F (‖) bond length increases from 2.04 Å to 2.76 Å as a result of F-vacancy formation (tabulated in Table 3.12) in the anatase form. In case of rutile TiNF, F is connected to the three Ti atoms. As a result of F-vacancy, we noticed an increase in Ti-N bond length from 1.99 Å to 2.09 Å. There is a small change in the Ti-F bond lengths (see Table 3.12). The other two of the Ti atoms form Ti-Ti bond of length 2.93 Å, and so we do not see comparably large changes in Ti-N/F bond lengths. In the anatase form of TiNF,

Table 3.12: Bond lengths of TiNF in rutile and anatase forms. The bond lengths have been obtained with U correction in both the systems.

Bond lengths (Å)	Pristine	F-vacancy
Anatase phase		
Ti-N (‖)	1.94	2.03
Ti-N (⊥)	1.93	1.92
Ti-F (‖)	2.04/1.98	2.76/vacancy
Ti-F (⊥)	2.12	2.19
Rutile phase		
Ti-N (‖)	1.99	2.09
Ti-N (⊥)	1.91	1.94
Ti-F (‖)	2.09	vacancy
Ti-F (⊥)	2.17	2.18

F is connected to two Ti atoms, and in its rutile form, it is connected to the three Ti atoms. So, we notice a comparatively small change in the Ti-N/F bond length in its rutile form than that in its anatase form.

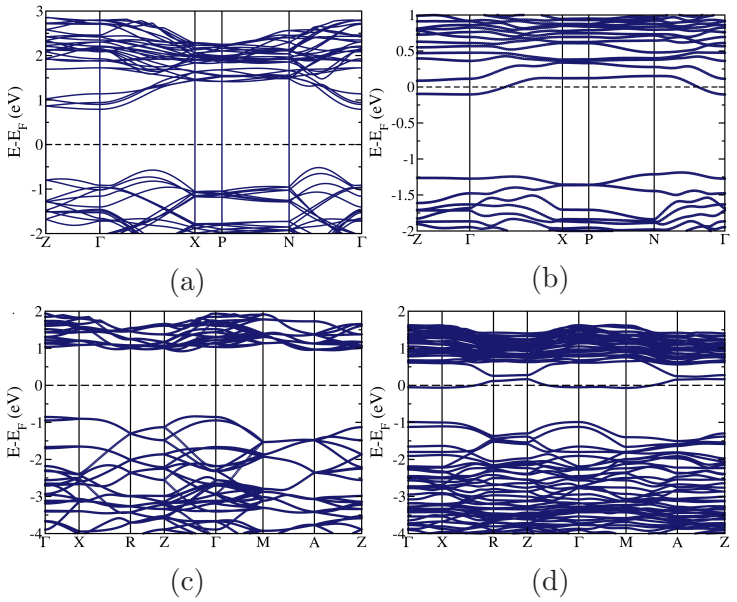

Figure 3.13: Electronic structure of (a) pristine anatase TiNF, (b) with F-vacancy anatase TiNF, (c) rutile TiNF, and (d) rutile TiNF with F-vacancy.

From the calculated electronic structures, it is clearly evident that the band gap reduced from 1.60 eV to 1.1 eV upon introduction of F-vacancy in anatase TiNF. Similarly, there is a change in band gap from 1.75 eV to 0.92 eV due to F-vacancy in the rutile TiNF. Electronic structures (see Fig.3.13(b) and (d)) clearly show an isolated defect band just below the conduction band in both the phases of TiNF. From the projected density of states (Fig. 3.14), it is seen that these defect states are comprised of Ti-3d orbitals. Valence band maximum constitutes primarily of N-2p states in both the phases. The transition from N-2p states to Ti^{3+} defect band is very likely responsible for its black color. We notice an F-2p peak around -6 eV due to F vacancy in anatase TiNF. Assuming that the hybrid functionals give similar increments in the band gap as in pristine TiNF, we predict the HSE band gaps of anatase and rutile TiNF with F-vacancy to be about 2.35 eV and 1.98 eV respectively, which belong to the green and orange-red regions of the visible light

spectrum respectively giving the sample its dark or blackish color.

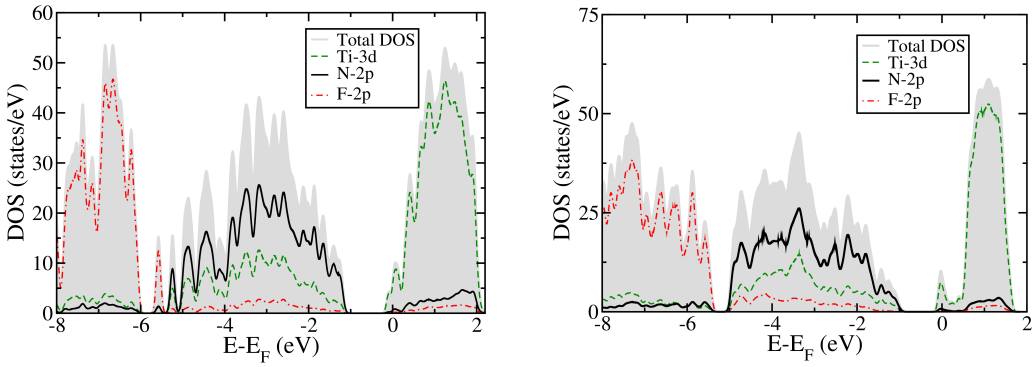

Figure 3.14: Projected density of states of (a) anatase TiNF, and (b) rutile TiNF with F-vacancies.

We obtained frequency dependent imaginary part of the dielectric tensor of the most stable configuration of N, F-doped anatase TiO_2 (shown in Fig. 3.15), which contains information on the absorption properties. Due to the anisotropy of the specific configuration of N, F-doping in the TiO_2 we get three components of the imaginary part of dielectric tensor. As a result of doping, peaks are shifted to lower energies (consistent with a reduction in the band gap) compared to TiO_2, and there are many absorbance peaks. The HSE band gap of N, F-doped TiO_2 is 2.37 eV, which is in the blue region of the visible light spectrum.

3.3 Conclusions

We show that the electronic structure of TiNF is sensitively dependent on the chemical ordering of N and F at anion sites. The energetically favorable configuration of anatase TiNF involves N and F atoms in alternating anionic sites, with diagonal sites occupied by the same elements. The configuration with N and F occupying the alternating atomic sites is energetically favorable in its rutile structure. TiNF (both rutile and anatase) and N, F-doped anatase TiO_2 are the indirect band gap semiconductors. We find anamolous Born charges (Z^*) in TiNF, which show a strong

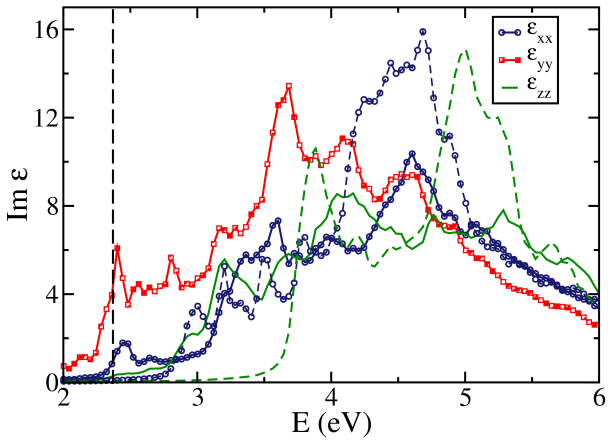

Figure 3.15: Imaginary part of dielectric tensor as a function of frequency of TiO_2 and N, F doped TiO_2. Dotted line: TiO_2 and solid line: N, F-doped TiO_2. xx and yy components are degenerate in case of TiO_2. HSE band gap of 2.37 eV of N, F-doped TiO_2 has been marked by dashed line on an energy axis

covalent p-d interaction between anions and Ti. The dependence of static dielectric constants ε^0 on relatively high frequency modes suggest that they are expected to be weakly dependent on temperature and pressure. Based on the analysis of conduction and valence band edges, we predict TiNF to be suitable for photocatalytic water splitting reaction. N, F substitution in TiO_2 reduces its band gap from 2.35 eV to 1.01 eV. The dark or black color of TiNF is due to the transition from N-2p in valence band maximum to defect band associated with F-vacancies, occurring just below the conduction band. This band is composed of 3d orbitals of Ti, meaning that Ti^{3+} is responsible for the observed color. The band gaps of anatase and rutile TiNF with F-vacancies lie respectively in the green, and orange-red regions of the visible light spectrum. The band gap of N, F-doped anatase TiO_2 lies in the blue region of the visible light spectrum.

3.4 Cd_2NF ‡

Cd_2NF crystallizes in the cubic lattice with the space group of *Fm3m* (no. 225) and a unit cell parameter of a = 4.7052 Å. In the structure, each Cd atom is coordinated

‡This work has been published in Dalton Trans. **47**, 9303 (2018) [76].

with six N/F atoms.

3.4.1 Computational details

Our first-principles calculations are based on density functional theory (DFT) as implemented in the Quantum ESPRESSO (QE) package [65], with a local density approximation (LDA) to treat the exchange-correlation energy of electrons. We used ultrasoft pseudopotentials to represent the interaction between ionic cores and valence electrons, and an energy cut-off of 45 Ry (450 Ry) to truncate the plane- wave basis for the representation of Kohn-Sham wave functions (density). Crystal structures were relaxed to minimize total energy with respect to atomic positions until the Hellmann-Feynmann forces on each atom are less than the 0.01 eV/Å. We used the Heyd-Scuseria-Ernzerhof (HSE-06) [36] hybrid functional (that mixes short range exact exchange energy) to obtain accurate estimates of electronic band gaps. We considered anionic disorder through various configurations of N and F decorating anionic sites.

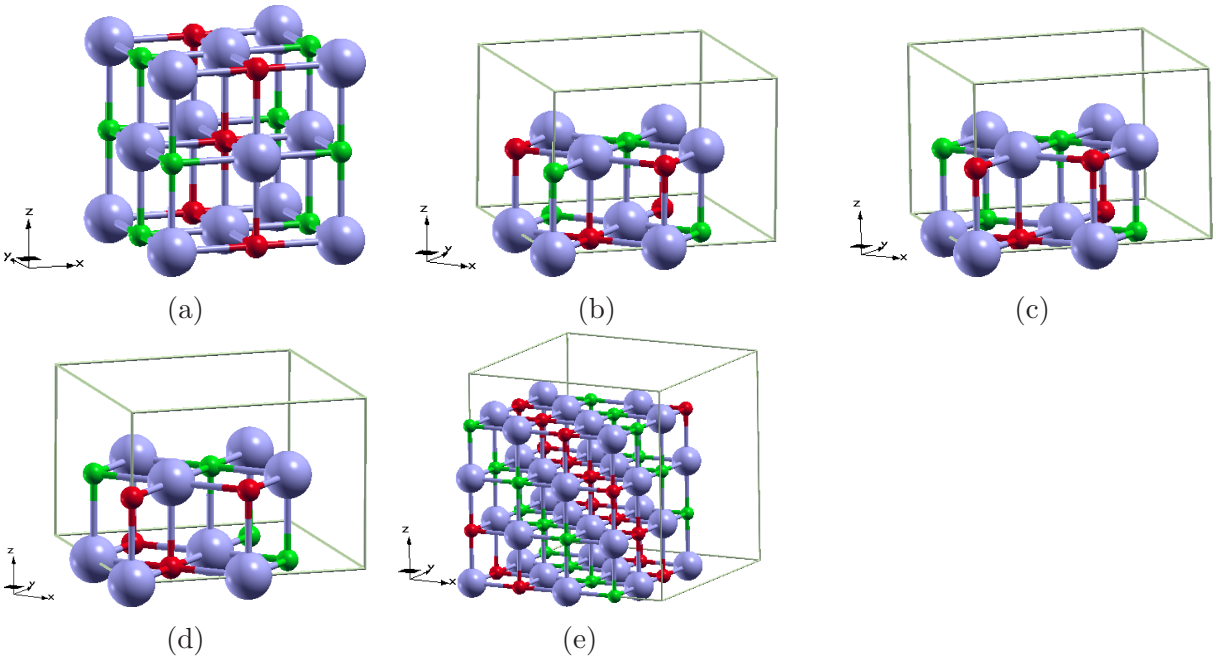

Figure 3.16: Configurations of different chemical orderings of N and F in Cd_2NF with (a) 1×1×1, (b)-(d) $\sqrt{2} \times \sqrt{2} \times 1$, and (e) 2×2×2 supercells. Cd, N and F are represented by purple, red and green spheres respectively.

3.4.2 Structural Properties

As Cd_2NF crystallizes in the cubic rocksalt structure, we simulated disorder in site occupancy by N and F by constructing the 1×1×1, $\sqrt{2}\times\sqrt{2}\times 1$ and 2×2×2 periodic supercells (shown in Fig. 3.16), where $1\times 1\times 1$ supercell corresponds to conventional cubic cells with four Cd sites. In the 1×1×1 configuration shown in Fig. 3.16(a), each Cd is connected to the four N/(F) atoms and two F/(N) atoms. As a result of such N and F ordering, there is a contraction in the lattice constant a and expansion in the b and c. The Cd-N/F bond lengths are 2.26 Å and 2.41 Å. In the $\sqrt{2}\times\sqrt{2}\times 1$ supercell of Cd_2NF, we considered three symmetry inequivalent configurations (Fig. 3.16(b)-(d)).

Table 3.13: Relative energies of various chemically ordered configurations of N and F atoms in $\sqrt{2}\times\sqrt{2}\times 1$ supercell of Cd_2NF. Configurations I, II, and III have been shown in Fig. 3.16(b)-3.16(d) respectively.

Configurations	E_n-E_{III} (eV/unit cell)	lattice constants (Å)
I	0.53	a=b=4.67, c=4.82
II	0.42	a=b=4.79, c=4.65
III	0.00	a=b=4.95, c=4.40

The relative energies of these configurations and their associated lattice constants have been tabulated in Table 3.13. From the energies of these configurations in the $\sqrt{2}\times\sqrt{2}\times 1$ supercell of Cd_2NF (see Table 3.13), it is clear that the configuration III (shown in Fig. 3.16(d)) is the most stable. In this, lattice constants a and b expand, whereas c contracts. The in-plane Cd-N (Cd-F) bond lengths are 2.41 Å and 2.24 Å (2.92 Å and 2.39 Å), and the out-of-plane Cd-N (Cd-F) bond lengths are 2.22 Å (2.29 Å). We have constructed 2×2×2 supercell and arranged N and F atoms in such a way that three N and three F atoms are close to each other in a cis-position (see Fig. 3.16(e)). In this configuration, there is a contraction in the three lattice constants. Cd-N and Cd-F bond lengths are 2.28 Å and 2.50 Å respectively. In this, the Cd atoms come closer to each other forming a long Cd-Cd bond of length 3.03 Å. See structural parameters of these configurations in Table 3.14. In the further analysis, we have considered three different arrangements of N and F atoms obtained

Table 3.14: Lattice constants and Cd-X bond lengths of Cd_2NF in various configurations of anionic chemical ordering in Cd_2NF.

Supercell	Lattice constants (Å)	Bond lengths (Å)
$1 \times 1 \times 1$	a=4.51 and b=c=4.82	Cd-N/F: 2.26 and 2.41
$\sqrt{2} \times \sqrt{2} \times 1$	a=b=4.95 and c=4.40	Cd-N: 2.41, 2.24 (in - plane) and 2.22 (out of plane) Cd-F: 2.92, 2.39 (in- plane) and 2.29 (out of plane)
$2 \times 2 \times 2$	a=b=c=4.71	Cd-N: 2.28 Cd-F: 2.50

by constructing 1×1×1, $\sqrt{2} \times \sqrt{2} \times 1$ (configuration III being an energetically low structure), and 2×2×2 supercells. The coordination of the Cd atom in all these three configurations has been shown in Fig. 3.17.

Table 3.15: Theoretical lattice constants and CdX (X = N, F) bond lengths of Cd_2NF in various configurations of anionic chemical ordering in Cd_2NF using PAW pseudopotentials.

Supercell	Lattice constants (Å)	Bond lengths (Å)
$1 \times 1 \times 1$	a=4.68 and b=c=4.99	Cd-N/F: 2.50 and 2.34
$\sqrt{2} \times \sqrt{2} \times 1$	a = b = 5.10 and c = 4.59	Cd–N: 2.47, 2.31 (in-plane) and 2.32 (out of plane) Cd–F: 2.99, 2.48 (in-plane) and 2.38 (out of plane)
$2 \times 2 \times 1$	a = b = c = 4.95	Cd–N: 2.35, Cd–F: 2.61

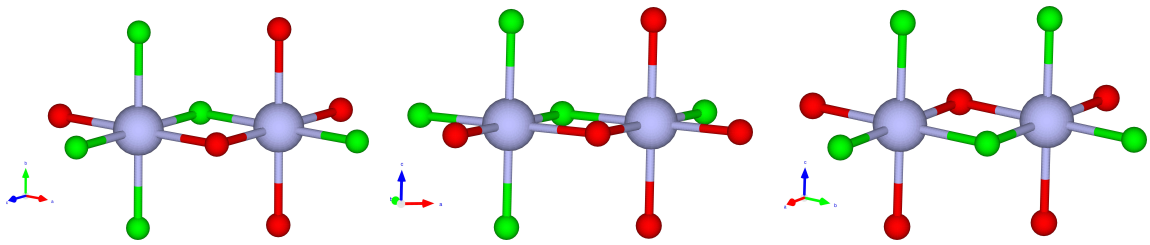

(a) (b) (c)

Figure 3.17: Coordination of Cd atoms in configurations with (a) 1×1×1, (b) $\sqrt{2}\times\sqrt{2}\times1$, and (c) $2 \times 2 \times 2$ supercells of Cd_2NF. Cd, N, and F atoms are represented by purple, red, and green spheres respectively.

3.4.3 Electronic Properties

We obtained the electronic structure of the three configurations along high symmetry lines of the Brillouin zone (Fig. 3.18). It is clearly seen that the different chemical ordering of N and F in Cd_2NF greatly affect its electronic properties. The configuration of Cd_2NF with $1 \times 1 \times 1$ unit cell exhibits a metallic character (Fig. 3.18(a)). Similarly, the configurations of Cd_2NF in $\sqrt{2} \times \sqrt{2} \times 1$ supercell also have the electronic structure with the bands crossing the Fermi level indicating their metallic nature. We note that there is a gap along Z-R-A-Z directions (Fig. 3.18(b)) giving rise to a pseudogap in its electronic structure. We find that Cd_2NF in 2×2×2 supercell also has an electronic structure with bands crossing the Fermi level (Fig. 3.18(c)). From the projected density of electronic states (PDOS), we note N-*2p* orbitals dominating the states at E_F of Cd_2NF in $1 \times 1 \times 1$ and $2 \times 2 \times 2$ supercells (Figs. 3.19(a) and 3.19(c)). In contrast, we do not find a significant contribution of N-*2p* orbitals to the states at Fermi level of Cd_2NF configuration in the $\sqrt{2} \times \sqrt{2} \times 1$ supercells (Fig. 3.19(b)).

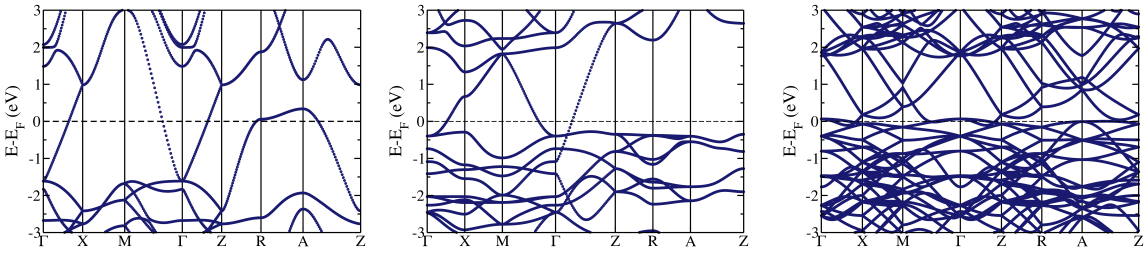

Figure 3.18: Electronic structures of chemically ordered configurations of N and F atoms in (a) $1 \times 1 \times 1$, (b) $\sqrt{2} \times \sqrt{2} \times 1$, and (c) $2 \times 2 \times 2$ unit cells of Cd_2NF.

While Cd_2NF is a semiconductor as observed experimentally, our DFT calculations predict it to be metallic. We performed electronic structure calculations with projected augmented wave (PAW) [77] using VASP [78]. We still get a metallic character in all the configurations considered (shown in Fig. 3.20). The structural parameters obtained using this method has been tabulated in Table 3.15. As we get tetragonal

structures upon relaxation of Cd_2NF configurations in $1 \times 1 \times 1$ and $\sqrt{2} \times \sqrt{2} \times 1$ supercells, in contrast to the cubic structure observed experimentally, we also studied the effects of variation in lattice constants. In all these simulations, we found Cd_2NF to be weakly metallic.

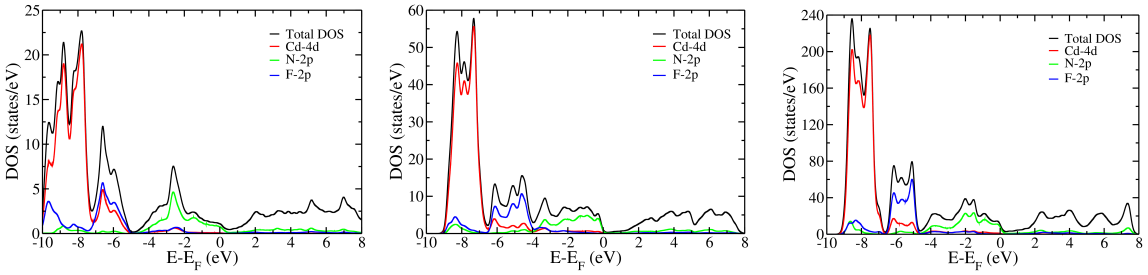

(a) (b) (c)

Figure 3.19: Projected density of states of configurations of Cd_2NF with varied N and F ordering in (a) $1 \times 1 \times 1$, (b) $\sqrt{2} \times \sqrt{2} \times 1$, and (c) $2 \times 2 \times 2$ supercells.

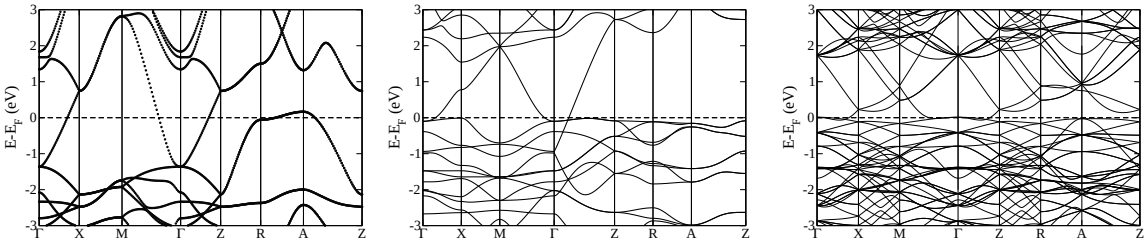

(a) (b) (c)

Figure 3.20: Electronic structure of various ordering of N and F atoms in (a) 1×1×1 (b) $\sqrt{2} \times \sqrt{2} \times 1$, and (c) 2×2×2 supercells of Cd_2NF, obtained from calculations based on PAW.

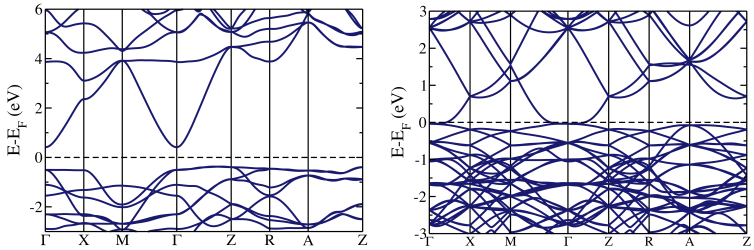

(a) (b)

Figure 3.21: Electronic structure of various ordered configurations of N and F atoms in (a) $\sqrt{2} \times \sqrt{2} \times 1$, and (b) 2×2×2 supercells of Cd_2NF, obtained from calculations based on hybrid functional.

In all the arrangements of N and F atoms obtained using 1×1×1, $\sqrt{2} \times \sqrt{2} \times 1$ and

2×2×2 supercells we find configuration III of $\sqrt{2} \times \sqrt{2} \times 1$ supercell to be energetically stable (see Table 3.16). For more accurate determination of band structures, we performed hybrid functional calculations as implemented in the Vienna ab initio simulation package (VASP) [78] with the projected augmented wave method (PAW) [77]. In the Cd_2NF configurations with $\sqrt{2} \times \sqrt{2} \times 1$ supercells with the experimental lattice constants, we relaxed the structure internally maintaining the cubic lattice

Table 3.16: Energetics of various ordering of N and F atoms in 1×1×1, $\sqrt{2} \times \sqrt{2} \times 1$ (configuration III has been considered here), and 2×2×2 supercell of Cd_2NF obtained using LDA ultrasoft pseudopotentials (LDA-USPPs) and PAW.

Supercells	E (eV/u.c)	
	LDA-USPPs	PAW
1×1×1	0.533	0.51
$\sqrt{2} \times \sqrt{2} \times 1$	0	0.00
2×2×2	0.530	0.28

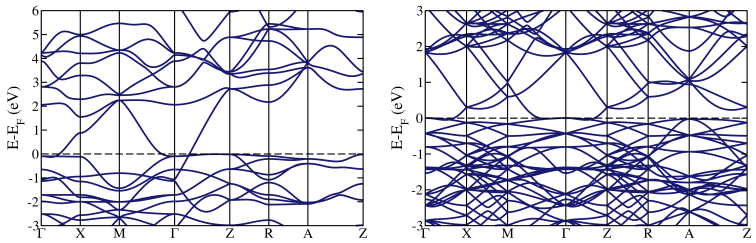

(a) (b)

Figure 3.22: Electronic structure of different chemical ordering of N and F in (a) $\sqrt{2} \times \sqrt{2} \times 1$, and (b) 2×2×2 supercells of Cd_2NF, obtained from calculations that include on-site electron correlations.

constants. We get an indirect band gap of 0.79 eV (Fig. 3.21(a)), which is close to the experimental band gap (0.84–0.90 eV) of CdO [79]. The direct band gap in electronic structure (Fig. 3.21(a)) of Cd_2NF is 0.92 eV at Γ-point. The electronic structure of Cd_2NF configurations with 2×2×2 supercell with theoretical lattice constants exhibits bands crossing the Fermi level indicating metallic nature of Cd_2NF (Fig. 3.21(b)). We also performed LDA+U calculations taking U=3 eV to estimate the effects of onsite correlations on the electronic structure using VASP and PAW potentials. The U correction does not open up a gap in $\sqrt{2} \times \sqrt{2} \times 1$; we have bands

crossing the Fermi level (Fig. 3.22(a)). In the configurations with $2 \times 2 \times 2$ supercells of Cd_2NF, we find a band splitting at the Γ-point (Fig. 3.22(b)), accompanied by a band just below Fermi level shifting closer to it, than that obtained from simulations based on HSE functional.

3.4.4 Conclusions

The electronic structure of Cd_2NF is greatly affected by the arrangement of N and F atoms in an unit cell. The DFT calculations predict the weakly metallic character of Cd_2NF, and a small gap opens in the electronic structure of Cd_2NF configuration with $\sqrt{2} \times \sqrt{2} \times 1$ supercells obtained using hybrid functional calculations. We find that the stable configuration is the one in which Cd is connected to four N atoms and two F atoms (other Cd to two N atoms and four F atoms). The inclusion of the Hubbard U correction did not open up a gap in the electronic structure of Cd_2NF configurations in $\sqrt{2} \times \sqrt{2} \times 1$ and $2 \times 2 \times 2$ supercells.

Chapter 4

Tailoring the Electronic and Structural Properties of ZnO by N^{3-} and Cl^{-} Substitution *

4.1 Introduction

Substitution of aliovalent anions in inorganic materials brings about major changes in the electronic structure and properties [46,48–51,53,81]. Thus, substitution of N and F in ZnO or P and Cl in CdS affect the band gaps significantly and impart photochemical activity in them [48,49,51]. The need to substitute a trivalent as well as a monovalent anion is to avoid the formation of defects. For example, substitution of N^{3-} alone gives rise to changes in the optical spectrum and band gap of ZnO and other oxides, but the products contain a large concentration of oxygen vacancies [82–84]. On the other hand, N, F cosubstituted oxides such as ZnO are devoid of vacancies [48]. N and F cosubstitution in oxides drastically decreases the band gap, and increases the dielectric constant and the extent of decrease in band gap depends on the concentration of N in

*This work has been published in Eur. J. Inorg. Chem. **2017**, 2377 (2017) [80]. Reproduced with permission from the John Wiley and Sons.

them [50,53,85]. Recent theoretical studies on N and F cosubstituted ZnO and P, and Cl cosubstituted CdS show that the decrease in the band gap is due to the presence of an isolated band at the top of the valence band originating from the p-orbitals of trivalent anions, N^{3-} and P^{3-} [46].

Prof. C. N. R. Rao's group[†] synthesized ZnO substituted with N and Cl. Substitution of N and Cl in ZnO causes a drastic decrease in the band gap of ZnO and gives rise to visible-light induced activity to the material. In this chapter, we try to understand here the effect of N and Cl cosubstitution on electronic and structural properties of ZnO at the atomistic level. We have also examined the properties of Zn_2NCl synthesized by the complete substitution of O by N and Cl [86] (synthesized by Prof. C. N. R Rao's group)

4.2 Computational details

Our calculations are based on first-principles density functional theory (DFT) as implemented in the Quantum ESPRESSO package [65]. We have used norm-conserving pseudopotentials to model the interaction between valence electrons and ionic cores. The exchange-correlation energy has been treated within a local density approximation (LDA) [87]. We have used 6×6×4, 6×5×6 and 6×6×6 uniform meshes of k-vectors to sample integrations of Brillouin zone of ZnO, Zn_2NCl and N, Cl substituted ZnO. We represented Kohn-Sham wave functions using a plane wave basis truncated at kinetic energy cut-off of 90 Ry. All structures have been relaxed until the Hellman-Feynman forces on each atom is less than 0.02 eV/Å. For accurate estimation of band gaps, the Heyd–Scuseria–Ernzerhof (HSE-06) hybrid functional has been employed [36].

[†]New Chemistry Unit, Jawaharlal Nehru Centre for Advanced Scientific Research, Bangalore-560064.

Table 4.1: Comparison of theoretical lattice constants with experimental values. The values of lattice constants of configuration II have been shown in parentheses.

	Lattice constants Å	
	Experimental	LDA-NC
ZnO	a=3.248	a=3.22
	c=5.203	c=5.19
Zn_6O_4NCl	a=3.257	a=3.32 (3.29)
	c=5.217	c=5.37 (5.42)
	a=6.1241	a=6.06
Zn_2NCl	b=7.3885	b=7.19
	c=5.9362	c=5.84

4.3 Structure and stability

Our estimates of lattice constants of the wurtzite structure of ZnO are in good agreement with experiment (Table 4.1) and earlier theoretical results [48, 50]. We considered $\sqrt{3} \times \sqrt{3} \times 1$ supercell of ZnO to model substitution of N and Cl, replacing two of the O atoms with a N and a Cl atom each. Using symmetry of the lattice, we get two inequivalent configurations. In one of the configurations, N and Cl are at in-plane neighboring anion sites (the configuration I in Fig. 4.1(a)) and in another, N and Cl are at out-of-plane neighboring anion sites (configuration II in Fig. 4.1(b)). In both of these configurations, N and Cl are bonded to the same Zn atom. To obtain the relative stability of these configurations, we determined their cohesive energies ($E_{coh.}$) using:

$$E_{coh.} = \frac{E_{Zn_6O_4NCl} - (aE_{zn} + bE_O + cE_N + dE_{Cl})}{N} \tag{4.1}$$

Where, $E_{Zn_6O_4NCl}$ is the energy of Zn_6O_4NCl, E_{Zn}, E_O, E_N, and E_{Cl} are the energies of free atoms in the isolated gaseous phase. Here, a, b, c, and d are the total number of Zn, O, N, and Cl atoms respectively, N being the total number of atoms in the system. The cohesive energies of configurations I and II are -4.79 eV/atom and -4.78 eV/atom respectively, which implies that both the configurations are quite comparable in stability, the configuration I being slightly more stable. The introduction of N and

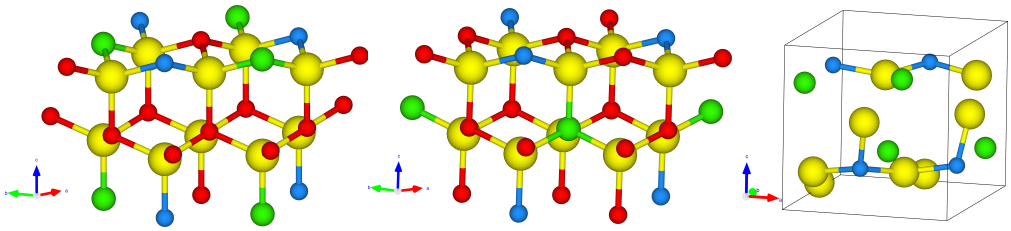

(a) (b) (c)

Figure 4.1: Configuration I (a) and II (b) of Zn_6O_4NCl modelled with $\sqrt{3}\times\sqrt{3}\times1$ supercell of wurtzite ZnO and (c) crystal structure of Zn_2NCl. The yellow spheres represent Zn, red spheres represent O, blue spheres represent N and green spheres represent Cl atoms.

Cl in ZnO leads to an increase in the lattice parameters (Table 4.1). Calculated expansion of the lattice is greater than the experimental measurements probably due to the higher concentration of N and Cl used in our simulations. In the configuration I, Zn-N and Zn-Cl bond lengths are 1.88 Å and 2.45 Å respectively. Whereas, Zn-N and Zn-Cl respectively forms a bond of length 1.91 Å and 2.50 Å in configuration II. N and Cl substitution results in contraction and elongation of Zn-O bonds by 4% and 25% respectively in the configuration I compared to Zn-O bond of 1.96 Å in ZnO. In configuration II, Zn-O bonds contract by 3% and elongate by 27%. This trend is similar to the trend in changes in bond lengths seen in $ZnO_{1-x}N_{\frac{x}{2}}F_{\frac{x}{2}}$ [48].

Zn_2NCl crystallizes in the orthorhombic system with the space group of $Pna2_1$. Each Zn is coordinated with two N and two Cl atoms. Our theoretical estimates of its lattice constants are (a=6.06 Å, b= 7.19 Å, and c=5.84 Å), in fair agreement with the experimental values within the typical errors of LDA (Table 4.1). Its cohesive energy is -4.19 eV/atom signifying somewhat weaker binding than the pristine and N, Cl substituted ZnO. Zn_2NCl and ZnO are the end-members of $ZnO_{1-x}N_{\frac{x}{2}}Cl_{\frac{x}{2}}$, and we now analyze their relative energetics. The total cohesive energy of Zn_6O_4NCl is -57.48 eV, whereas total energy of the combination of Zn_2NCl and 4(ZnO) are -58.12 eV. Thus, the end-members ZnO and Zn_2NCl are relatively more stable than the (N, Cl) substituted ZnO based solid solution. The latter is thus probably stabilized kinetically at low concentration of N and Cl in an experiment.

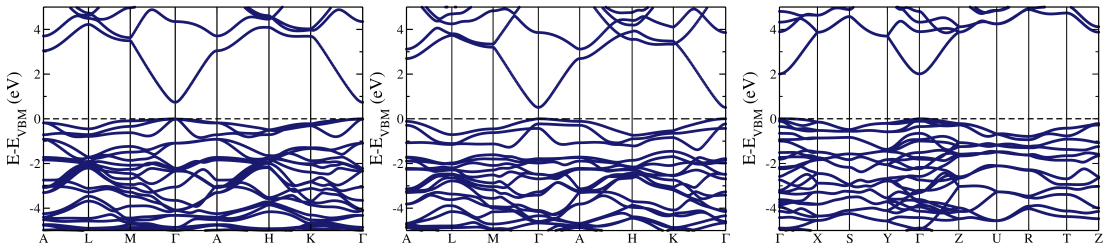

(a) (b) (c)

Figure 4.2: Electronic structures of configuration I (a) and II (b) of Zn_6O_4NCl and Zn_2NCl (c); obtained from LDA calculations.

4.4 Electronic structure

Electronic structure (obtained with LDA) along high symmetry paths show direct band gaps at Γ-point of both ZnO and Zn_6O_4NCl (Fig. 4.2). The estimated band gaps of ZnO and configuration I and II of Zn_6O_4NCl are 0.71 eV, 0.74 eV and 0.51 eV respectively. For improved estimates of band gaps, we employed hybrid functional in our calculations. Underestimation of band gaps is a well-known limitation of local density functional theory, and hybrid functionals typically improve the band gap estimates by mixing exact exchange energy functional with the local one. This treatment leads to a shift in the VBM to lower energy and an increase in the band gaps. HSE band gaps of ZnO and configuration I and II of Zn_6O_4NCl are 2.37 eV, 2.23 eV, and 1.95 eV respectively (Table 4.2). We note that accurate estimation of the band gap of ZnO is particularly challenging [88, 89]. The theoretical band gap of ZnO is underestimated even with HSE/GW calculations due to the strong interaction between the Zn-3d and O-2p orbitals (bands of which are close in energy), and associated issues of convergence with respect to a subspace of unoccupied states. As a result of the substitution of N and Cl, the band gap of ZnO undergoes reduction. As the reduction in the band gap of configuration II is more comparable to experiment, we present further analysis of the configuration II of Zn_6O_4NCl below.

We note an isolated band just above VBM in the gap of Zn_6O_4NCl is responsible for the reduction in band gap by 0.42 eV. To better understand the nature of this isolated

Table 4.2: Electronic band gaps obtained from calculations with HSE and LDA functionals. Band gaps of configuration II of ZN_6O_4NCl are shown in parentheses.

	Band gaps (eV)		
	LDA-NC	HSE	Exp.
ZnO	0.71	2.37	3.20
Zn_6O_4NCl	0.74	2.23	1.93
	(0.51)	(1.95)	
Zn_2NCl	2.01	3.40	3.70

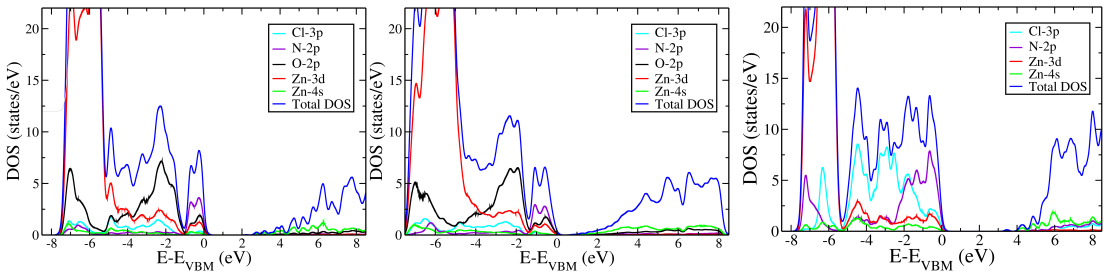

(a) (b) (c)

Figure 4.3: Projected density of states of (a) ZnO, (b) Zn_6O_4NCl (configuration II), and (c) Zn_2NCl, obtained using HSE calculations.

band, we analyze the electronic density of states obtained using HSE calculations of ZnO and Zn_6O_4NCl (Fig. 4.3). In ZnO, the VBM primarily consists of O-2p orbitals and slight contribution from Zn-3d states while the CBM has a predominant character of Zn-4s orbitals (Fig. 4.3(a)). The peaks in the density of states broaden as a result of the substitution of N and Cl in ZnO (Fig. 4.3(b)). The uppermost valence band consists primarily of N-2p states, with a slight mixing with O-2p and Zn-3d orbitals, while the bands associated with Cl-3p states lie below valence band. While the co-substitution of N and Cl facilitates stability, the 2p states of N are responsible for the reduction in the band gap, as reported earlier [48, 50]. The CBM has a predominant contribution from Zn-4s states, which is unaltered upon substitution.

Zn_2NCl exhibits a direct band gap of 2.01 eV (LDA estimate) at Γ-point (Fig. 4.2(c)). The band gap obtained with HSE calculation is 3.40 eV which is closer to the experimental value of 3.50 eV. Liu *et al.* [86] have predicted the band gap to be 3.70 eV

using HSE with projector-augmented-wave (PAW) pseudopotential while our calculations are based on HSE with pseudopotentials. Different choices of pseudopotentials are known to cause a small variation in the estimated band gaps as seen here. The projected density of states (PDOS) of Zn_2NCl, reveals that the VBM is primarily constituted of N-2p states. We notice a mixing or hybridization of Zn-3d and Cl-3p states in bands near the VBM and the CBM has a contribution mainly from Zn-4s orbitals (Fig. 4.3(c)). We note that even the conduction band of (Fig. 4.2(c)) Zn_2NCl is notably different from that of Zn_6O_4NCl. The origin of this can be traced to the changes in Zn-X bonding and hybridization: Short Zn-N bonds cause stronger hybridization as evident in the broader peak of N-2p bands (see Fig. 4.3(c)), and the conduction bands with antibonding character are also consequently affected. This results in the enhanced stability and band gap of Zn_2NCl.

4.5 Conclusions

Our calculations of the electronic structure corroborate the observed reduction in band gap of ZnO as a result of N and Cl substitution. This reduction in the band gap is primarily due to the sub-band of N-2p states at VBM in Zn_6O_4NCl. The occupation of N and Cl at neighboring in-plane and out-of-plane anionic sites have comparable stability. While Zn-N bonds are slightly shorter, Zn-Cl bonds are considerably longer than the Zn-O bonds. Both Zn_2NCl and Zn_6O_4NCl exhibit direct band gaps at Γ-point.

Chapter 5

Effects of Substitution of Aliovalent Anions in Place of Chalcogenides in CdX (X = S, Se, Te)

5.1 Introduction

Substitution of aliovalent anions in metal oxides and chalcogenides significantly affects the electronic structure and properties of the materials. Among the metal chalcogenides, Cd-based chalcogenides (CdS, CdSe, CdTe) are known for several applications [90–94]. Aliovalent anionic substitution in CdS has been shown to be an effective means of tuning their electronic properties and stability [46]. Thus, the substitution of S by P and Cl in CdS, results in a drastic decrease in the band gap, giving rise to noticeable changes in the photocatalytic properties [**?**]. Substitution of S by either P or Cl alone also affects the optoelectronic properties of CdS but is accompanied by the creation of defects [95, 96]. Anionic substitution in CdSe has been reported to have a greater effect on its electronic and optical properties [97]. Co-doping of arsenic and chlorine in CdTe is known to modulate its photovoltaic efficiencies [98]. The doping of Sb in CdTe solar cells results in its improved performance [99, 100]. In

all these cases the dopant concentration varies in the range of 2–15%. Prof. C. N. R Rao's group* synthesized $Cd_4As_2Br_3$ and $Cd_4Sb_2I_3$, wherein the anions in CdSe and CdTe are substituted by As, Br and Sb, I respectively. These compounds are found to possess band gaps in the 1.80–1.93 eV range exhibiting a photoluminescence band in the visible region. $Cd_4As_2Br_3$ and $Cd_4Sb_2I_3$ are both capable of producing hydrogen under visible-light irradiation.

In metal sulphides like CdS, there is a problem of photocorrosion wherein photogenerated holes oxidize the S^{2-} ions leading to the elution of Cd^{2+} [101], and it also requires sacrificial agents for hydrogen evolution reaction (HER). In order to overcome these drawbacks, Prof. C. N. R Rao's group synthesized a family of catalysts of the formula $Cd_4P_2X_3$ (X =Cl, Br, I), obtained by the complete aliovalent substitution of the sulfide ions in CdS by P and X (X = Cl, Br, I). $Cd_4P_2X_3$ photocatalysts show excellent activity and stability, for water splitting as well as for CO_2 reduction without a sacrificial agent or a cocatalyst under artificial or direct sunlight irradiation. In this work, we have tried to understand the electronic and catalytic properties of $Cd_4As_2Br_3$, $Cd_4Sb_2I_3$ and $Cd_4P_2X_3$ (X = Cl, Br, I) using first-principles calculations.

5.2 $Cd_4As_2Br_3$ and $Cd_4Sb_2I_3$ †

5.2.1 Crystal structures

$Cd_4As_2Br_3$ and $Cd_4Sb_2I_3$ crystallize in the cubic structure (Pa–3) with lattice parameters of 12.61 and 13.48 Å respectively. The structure has two independent Cd and As atoms labelled as Cd(1), Cd(2) and As(1), As(2) (Fig. 5.1(a)). Bonding of the As and Br atoms around the Cd centers give rise to a tetrahedral environment wherein Cd(1) is surrounded by two As and two Br atoms whereas Cd(2) is surrounded by one As

*New Chemistry Unit, Jawaharlal Nehru Centre for Advanced Scientific Research, Bangalore.

†This work has been published in Solid State Communications **255**, 5 (2017) [102]. Reproduced with permission from the Elsevier .

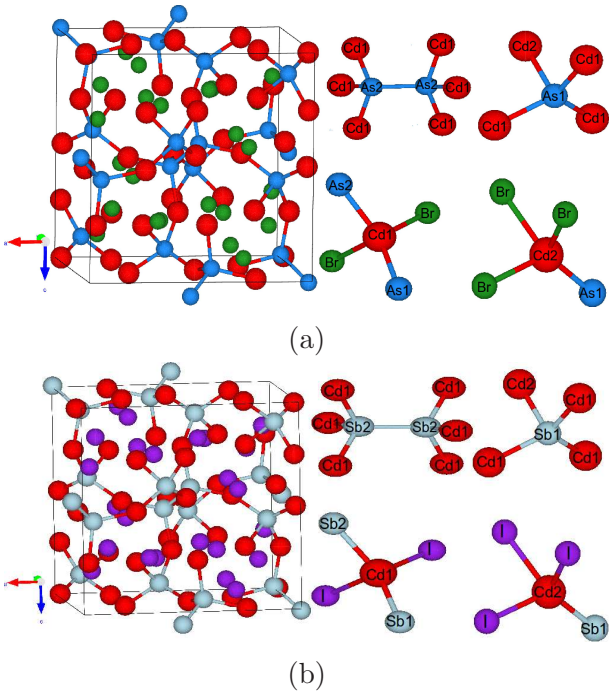

Figure 5.1: Crystal structures of (a) $Cd_4As_2Br_3$ and (b) $Cd_4Sb_2I_3$. The coordination of As, Cd and Sb is shown on the right side of the figure.

and three Br atoms respectively. As(1) possessing 3^- charge forms $AsCd_4$ tetrahedra, whereas As(2) with 2^- charge forms As_2Cd_6 octahedra with a As(2)-As(2) dumbbells in the center (As-As bond length, 2.390 Å). These two polyhedra give rise to the three-dimensional structure to $Cd_4As_2Br_3$, which is linked with the Br located in the voids of the three-dimensional structure (Fig. 5.1(b)). $Cd_4Sb_2I_3$ is isostructural with $Cd_4As_2Br_3$ wherein the Cd(1) atoms are coordinated by two Sb and two I atoms and Cd(2) atoms are coordinated by three I atoms and one Sb atom. Sb (1) (3^- charge) forms Cd_4Sb units and Sb(2) (2^- charge) is part of the Sb_2Cd_6 polyhedra wherein Sb(2)-Sb(2) bond exist (Sb(2)-Sb(2) bond length 2.83 Å) (Fig. 5.1(b)).

5.2.2 Computational details

Our first-principles calculations based on density functional theory (DFT) have been performed using Quantum ESPRESSO package [65], treating exchange-correlation energy within a Generalized Gradient approximation parameterized by Perdew Burke

Ernzerhof (PBE) [103] ultrasoft pseudopotentials. The kinetic energy cut off of 55 Ry is used to truncate the plane wave basis. Uniform mesh of 4×4×4 k-points is used for sampling integration of the Brillouin Zone. The structures have been relaxed to minimize energy until the Hellmann-Feynmann forces on each atom are less than 0.02 eV/Å. For accurate estimation of the band gap we have used the screened hybrid functional of Heyd, Scuseria, and Ernzerhof (HSE) [36], as implemented in the Vienna ab initio simulation package (VASP) [78] with a projector augmented wave method (PAW) [77].

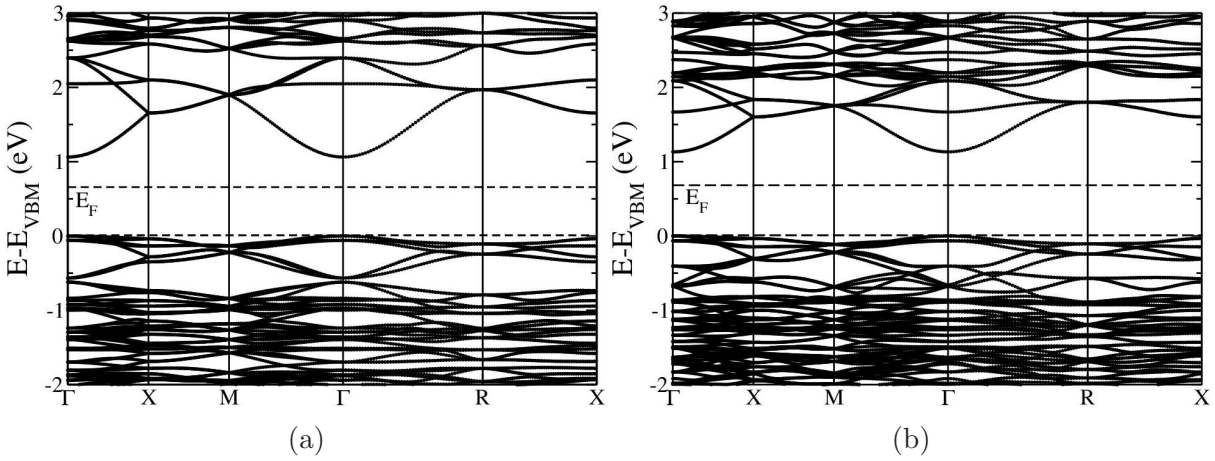

Figure 5.2: Electronic structures of (a) $Cd_4As_2Br_3$ and (b) $Cd_4Sb_2I_3$.

5.2.3 Results and Discussion

$Cd_4As_2Br_3$ and $Cd_4Sb_2I_3$ crystallize in the cubic structure, and our theoretical estimates of their lattice constants are 12.92 Å and 13.85 Å respectively, which are within the typical errors of GGA calculations. Electronic structure of $Cd_4As_2Br_3$ (shown in Fig. 5.2(a)) has a direct band gap of 1.06 eV at Γ-point, which is underestimated with respect to the experimental gap of 1.93 eV. Our HSE calculations predict a band gap of 1.72 eV, which is closer to the experimental value. From the projected density of states (Fig. 5.3(a)), it is evident that the states at VBM and CBM are predominantly comprised of As-4p and Cd-5s orbitals respectively. The maximum contribution to the valence band is from As^{2-} forming As-As (denoted by As2) bond. As^{3-} (denoted

by As1) constitutes the higher energy valence band states. $Cd_4Sb_2I_3$ also has a direct band gap of 1.13 eV (Fig. 5.2(b)), with Cd-5s orbitals contributing to the states near CBM and Sb-5p contributing to the states near VBM (Fig. 5.3(b)). Here also, Sb^{2-} (denoted by Sb2) contributes to the VBM and high energy valence band state has a major contribution from Sb^{3-} (denoted by Sb1).

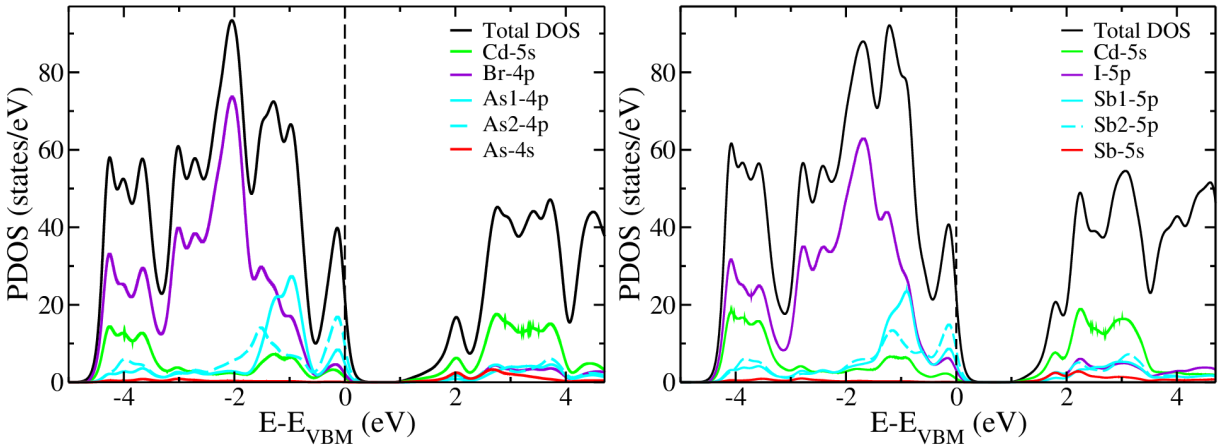

(a) (b)

Figure 5.3: Density of states of (a) $Cd_4As_2Br_3$ and (b) $Cd_4Sb_2I_3$, projected on various atomic orbitals.

From HSE calculations, the band gap of $Cd_4Sb_2I_3$ is expected to be around 1.79 eV, assuming a similar change in the gap with HSE calculations. We noticed that the theoretical estimates of the band gaps of $Cd_4As_2Br_3$ and $Cd_4Sb_2I_3$ obtained using VASP in combination with the PBE functional are 0.98 eV and 1.13 eV respectively, which agree fairly well with the estimates of 1.06 eV and 1.13 eV obtained using QUANTUM Espresso calculations. We have used XCrySDen to visualize HOMO-LUMO of the bulk configuration obtained from Quantum ESPRESSO calculations. Visualization of the wave functions state near the band gap at Γ-point show that the VBM has a major contribution from As-4p orbitals (Fig. 5.4(a)) and CBM has a contribution from s orbitals of Cd, As and Br (Fig. 5.4(b)). In $Cd_4Sb_2I_3$, Sb-5p orbitals constitute the VBM (Fig. 5.4(c)), and the CBM is contributed from s orbitals of Cd, Sb and I (Fig. 5.4(d)).

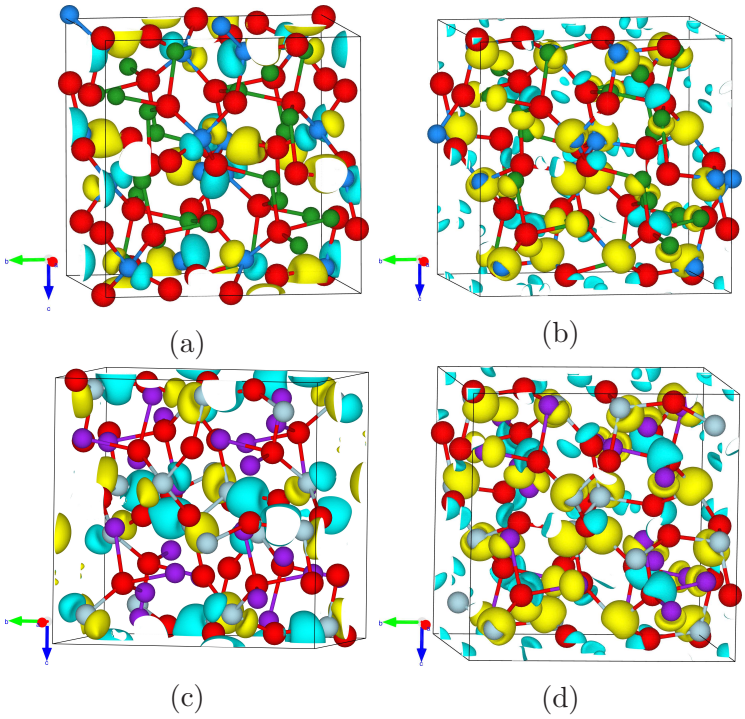

Figure 5.4: Visualization of wavefunctions of (a) HOMO, and (b) LUMO at Γ-point of $Cd_4As_2Br_3$ and (c) HOMO, (d) LUMO at Γ-point of $Cd_4Sb_2I_3$. Yellow and cyan colors of the isosurfaces of wavefunctions indicate positive and negative signs respectively. Cd: Red, As: Blue, Br: Green, Sb: cyan and I: purple.

To assess the potential of $Cd_4As_2Br_3$ and $Cd_4Sb_2I_3$ as photocatalysts for the hydrogen evolution reaction (HER), we have aligned their valence and conduction band edges with respect to vacuum potential. Their positions relative to hydrogen redox potential allow us to discuss their suitability for catalytic behavior. Since it is not straightforward to assign the vacuum potential in calculations of bulk compounds, we performed calculations on (001) slabs consisting of two unit cells of $Cd_4As_2Br_3$ and $Cd_4Sb_2I_3$ amounting to a thickness of 26 Å and 28 Å respectively. The structure of the slab has been constructed using the relaxed bulk positions of the compounds. The bulk band edge energies are aligned with respect to vacuum using ΔV, defined as the difference between the potential in a vacuum and macroscopically averaged potential deep inside the slab. We also simulated slabs with five unit cells thickness and found that the bulk-vacuum potential difference of the two unit-cell thick slab is within 5 meV of that obtained with the thicker slab.

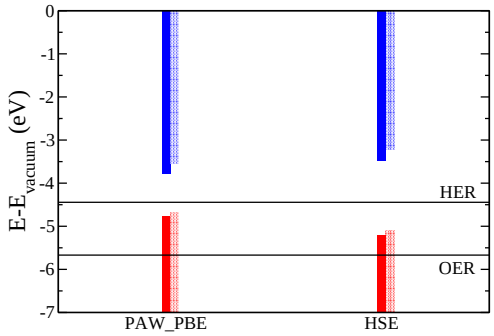

Figure 5.5: Alignment of valence and conduction bands obtained with PAW-PBE and HSE calculations. Solid and shaded bars show the VBM and CBM positions of $Cd_4As_2Br_3$ and $Cd_4Sb_2I_3$ respectively.

For catalyzing the hydrogen evolution reaction, the CBM of semiconductors should ideally be above the HER potential. The band alignment of these compounds (Fig. 5.5) clearly suggests their suitability for photocatalysis of HER. Since their VBMs are above the oxygen evolution reaction (OER) potential, they are not suitable for the OER. As the CBM of $Cd_4As_2Br_3$ is closer to the HER potential than that of $Cd_4Sb_2I_3$, and hence we expect $Cd_4As_2Br_3$ to be more active. The conduction band in $Cd_4As_2Br_3$ is more dispersed along Γ-M than in $Cd_4Sb_2I_3$ (see Fig. 5.2), indicating its lower electronic effective mass and higher mobility. This could be another reason for its higher catalytic activity towards the HER.

5.2.4 Conclusions

$Cd_4As_2Br_3$ and $Cd_4Sb_2I_3$ are the direct band gap semiconductors, with their conduction bands aligned favorably with respect to the redox potential of HER, and hence can be useful in photocatalysis of HER. Secondly, the lower electron mobility of $Cd_4Sb_2I_3$ is partly responsible for its relatively lower HER activity. The top of valence bands of $Cd_4As_2Br_3$ and $Cd_4Sb_2I_3$ consists of As-4p and Sb-5p orbitals respectively.

5.3 $Cd_4P_2X_3$ (X=Cl, Br, I) ‡

5.3.1 Crystal strutcure

$Cd_4P_2Cl_3$ and $Cd_4P_2Br_3$ crystallize in the cubic structure (Pa–3) with lattice parameters of 12.13 and 12.36 Å (Fig. 5.6(a) and (b)), whereas $Cd_4P_2I_3$ crystallizes in the orthorhombic structure (Pcab) with a = 12.85 Å, b= 12.69 Å, and c = 12.62 Å (Fig. 5.6(c)).

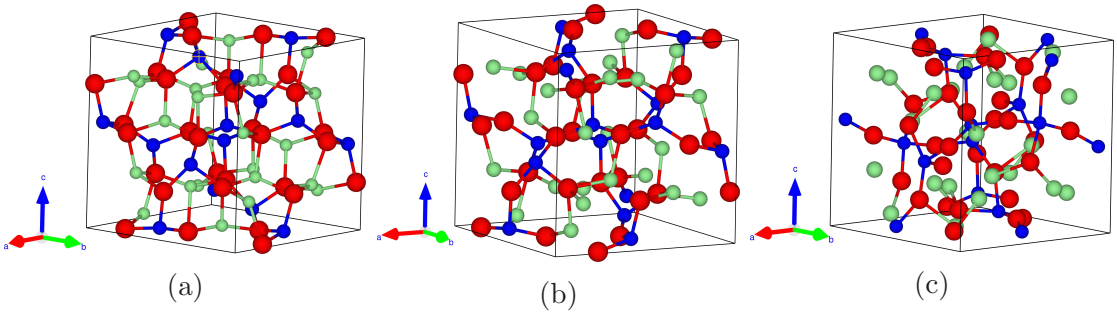

Figure 5.6: Crystal structures of (a) $Cd_4P_2Cl_3$, (b) $Cd_4P_2Br_3$ and (b) $Cd_4P_2I_3$. Cd, P, and X (X = Cl, Br, I) atoms are represented by red, blue and green spheres respectively.

5.3.2 Computational details

We used the Quantum ESPRESSO package [65] in our first-principles calculations carried out within density functional theory (DFT), with ultrasoft pseudopotentials (USPP) to model the interaction between ionic cores and valence electrons. We treated the exchange-correlation energy within a generalized-gradient approximation (GGA) and functional parametrized by Perdew, Burke, and Ernzerhof [103]. We used plane-wave basis truncated with a kinetic energy cut-off of 55 Ry in the representation of Kohn-Sham wavefunctions, and 4×4×4 uniform mesh of k-points for sampling the integrations over the Brillouin zone (BZ). Since DFT calculations underestimate band gaps, we used Heyd-Scuseria-Ernzerhof (HSE) [36] hybrid functional based on a

‡This work has been published in ACS Applied Materials and Interfaces **10**, 2526 (2018) [104]. Reproduced with permission from the American Chemical Society.

screened Coulomb potential in Hartree-Fock exchange interaction in the estimation of gaps. Crystal structures were internally relaxed to minimize total energy maintaining the experimental lattice constants until the Hellman-Feynman forces on each atom are less than 0.02 eV/Å. For alignment of energies of band edges (e.g., the energy of the conduction band minimum (CBM)), we simulated a slab of crystals with (001) orientation and thickness of two units separated by a vacuum of about 15 Å along the z-direction in the periodic supercell. Brillouin zone integrations in these slab calculations were sampled on a 4×x4×1 mesh of k-points.

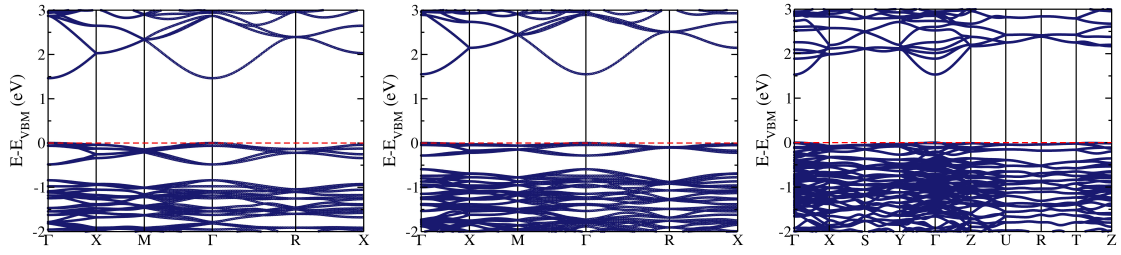

(a) (b) (c)

Figure 5.7: Electronic structures of (a) $Cd_4P_2Cl_3$, (b) $Cd_4P_2Br_3$, and (c) $Cd_4P_2I_3$ along high symmetry lines in the Brillouin Zone.

5.3.3 Results and discussion

We present an analysis of the photocatalytic activity of $Cd_4P_2X_3$ (X=Cl, Br, I) for hydrogen evolution reaction (HER) and CO_2 reduction using first-principles calculation. Their photocatalytic activity is in the order $Cd_4P_2Br_3 > Cd_4P_2Cl_3 > Cd_4P_2I_3$. The electronic structure along high symmetry lines in the Brillouin Zone exhibit a direct band gap at Γ-point for each of $Cd_4P_2X_3$ (X = Cl, Br, I) compounds (Fig. 5.7). From the theoretical estimates and experimentally measured band gaps (see Table 5.1), it is clear that the band gaps estimated with hybrid functional-based calculations are quite close to their experimental values. From the projected density of states (see Figs. 5.8(a), 5.8(b)), it is clear that the electronic bands near the valence band maximum (VBM) have a dominant contribution from $3p$ orbitals of P, with a

slight mixing with $3p$ orbitals of Cl (or $4p$ orbitals of Br) and $5s$ orbitals of Cd in $Cd_4P_2Cl_3$ ($Cd_4P_2Br_3$). The dominant contribution to the states near the conduction band minimum (CBM) comes from $5s$ orbitals of Cd and with a slight mixing with $3p$ orbitals of P, and $3p$ orbitals of Cl (or $4p$ orbitals of Br) is also seen in $Cd_4P_2Cl_3$ ($Cd_4P_2Br_3$) (refer to Fig. 5.8(a), 5.8(b)). In contrast, the states near the VBM of $Cd_4P_2I_3$ have comparable contributions from $5p$ orbitals of I and $3p$ orbitals of P, with a slight mixing with $5s$ orbitals of Cd. $5s$ orbitals of Cd are the dominant contributors to the CBM with a small component of $3p$ orbitals of P and $5p$ orbitals of I (see Fig. 5.8(c)).

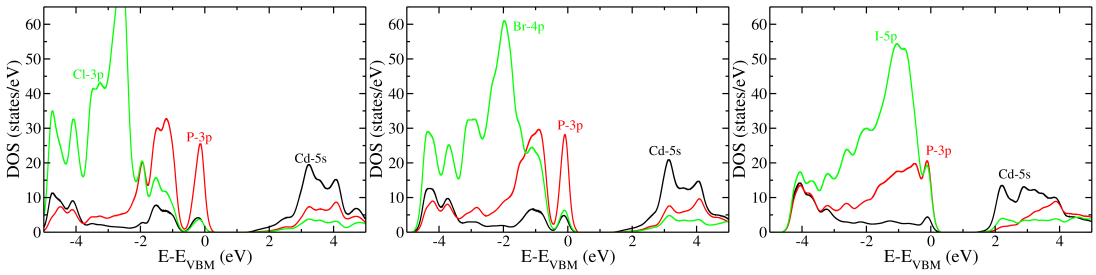

(a) (b) (c)

Figure 5.8: Density of electronic states of (a) $Cd_4P_2Cl_3$, (b) $Cd_4P_2Br_3$, and (c) $Cd_4P_2I_3$ projected onto atomic orbitals.

Table 5.1: Electronic band gaps obtained from calculations based on GGA and HSE functionals and their comparison with experimental values.

Systems	Band gaps (eV)		
	GGA-USPPs	HSE	Exp.
$Cd_4P_2Cl_3$	1.46	2.31	2.21
$Cd_4P_2Br_3$	1.55	2.39	2.24
$Cd_4P_2I_3$	1.53	2.30	2.20

To assess the suitability of the electronic structure of these compounds for photocatalysis, we align their CBMs relative to vacuum and then to the standard hydrogen electrode potential. For this, we determine ΔV, the difference between potentials in the vacuum and deep inside the bulk from simulations of slabs. We obtain the energies of VBM and CBM of the bulk relative to its macroscopic average potential.

We then align the bulk bands with respect to vacuum using ΔV. It is clear that the CBM edge of these compounds is above the HER potential. Hence, $Cd_4P_2X_3$ (X=Cl, Br, I) are suitable for HER (Fig. 5.9). For better photocatalytic activity, the CBM

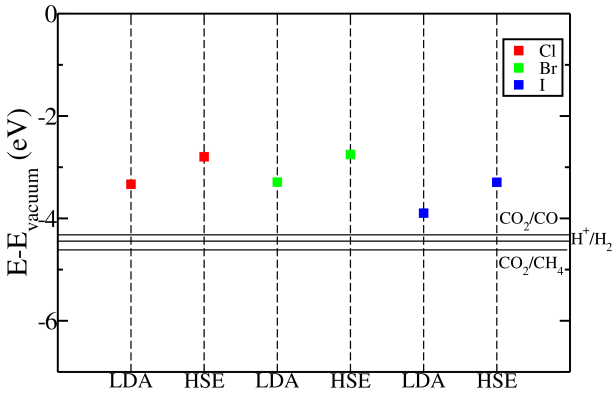

Figure 5.9: Energy of the conduction band minimum (CBM) of $Cd_4P_2X_3$ (X=Cl, Br, I) aligned with respect to the vacuum potential, along with the redox potentials of CO_2 reduction reactions and hydrogen evolution reaction marked in solid lines.

should be closer to the HER potential. Based on this, the ordering of their photocatalytic activity (towards HER) is $Cd_4P_2I_3 > Cd_4P_2Cl_3 > Cd_4P_2Br_3$. To understand the observed trend in their activity, we now consider effects of vacancies, which are known to be common and responsible for enhancing the photocatalytic activity of semiconductors by acting as an electron/hole traps, inhibiting the electron-hole recombination [105, 106]. We introduced 4.2% of X vacancies in $Cd_4P_2X_3$ (X = Cl, Br, I) using supercells, and estimated the vacancy formation energy ($E_{vac.}$) using:

$$E_{vac.} = E_{Cd_4P_2X_{3-\delta}} - (E_{Cd_4P_2X_3} - \frac{1}{2}E_{X2}) \tag{5.1}$$

Here, $E_{Cd_4P_2X_{3-\delta}}$ is the energy of $Cd_4P_2X_3$ with X vacancies, $E_{Cd_4P_2X_3}$ is the energy of pristine crystal and E_{X_2} is the energy of isolated gaseous X_2 molecule. From the vacancy formation energies (see Table 5.2), we find that it is easier to introduce I vacancy and comparatively difficult to introduce Cl vacancy. As a result of the Cl vacancy, we identify a new (defect-related) peak in its VBM (Fig. 5.10(a)). The peak has a contribution mainly from P-3p. and Cd-5s. We find a new peak in the CBM

Table 5.2: Energy of vacancy formation ($E_{vac.}$) in $Cd_4P_2X_3$ (X=Cl, Br, I)

Systems	Evac. (eV)
$Cd_4P_2Cl_3$	3.04
$Cd_4P_2Br_3$	2.83
$Cd_4P_2I_3$	1.95

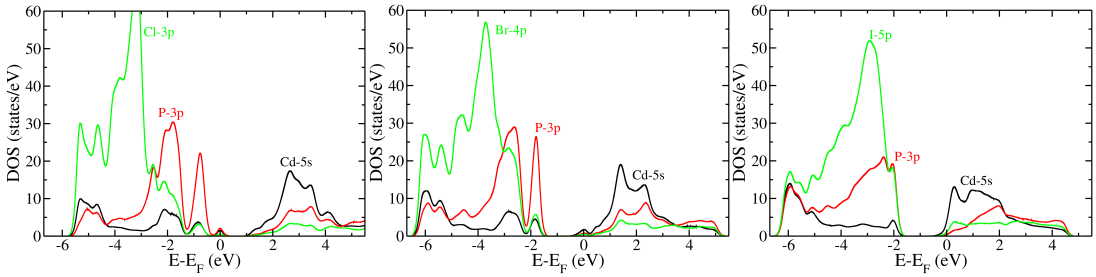

(a) (b) (c)

Figure 5.10: Electronic density of states of (a) $Cd_4P_2Cl_3$, (b) $Cd_4P_2Br_3$, and (c) $Cd_4P_2I_3$, with Cl, Br and I vacancies respectively projected onto atomic orbitals.

due to Br vacancy in $Cd_4P_2Br_3$ (Fig. 5.10(b)). The defect peak has a dominant contribution from $5s$ orbitals of Cd. In $Cd_4P_2Cl_3$, we see that the two Cd atoms come closer and form a bond of length 3.2 Å near the Cl vacancy site. There are no such structural changes in $Cd_4P_2Br_3$ upon introduction of Br vacancy. We find defect peaks near the VBM and CBM of $Cd_4P_2Cl_3$ and $Cd_4P_2Br_3$ respectively. In contrast, $Cd_4P_2I_3$ does not show any new peak in the gap (Fig. 5.10(c)). Consequently, the CBM moves up by 0.16 eV and down by 0.3 eV with respect to that of the pristine compound due to Cl and Br vacancies in $Cd_4P_2Cl_3$ and $Cd_4P_2Br_3$ respectively. This makes $Cd_4P_2Br_3$ more suitable for the photocatalytic water splitting HER reaction compared to $Cd_4P_2Cl_3$. The new defect states in $Cd_4P_2Cl_3$ and $Cd_4P_2Br_3$ acts as a hole and electron traps respectively. This inhibits the electron-hole recombination leading to their good photocatalytic activity [105,106] compared to $Cd_4P_2I_3$. Based on the redox potentials of reactions involved in CO_2 reduction (see Fig. 5.9), we expect $Cd_4P_2X_3$ (X = Cl, Br, I) compounds to be suitable for catalytic CO_2 reduction as well.

5.3.4 Conclusions

Our theoretical analysis of the electronic structure of $Cd_4P_2X_3$ (X=Cl, Br, I) show that these compounds are direct band gap semiconductors with gaps of about 2.2 eV. Secondly, their CBMs are suitably located relative to the redox potentials of HER and CO_2 reduction. Hence, we expect these compounds to be suitable as photocatalysts for these reactions. Cl and Br vacancies in $Cd_4P_2Cl_3$ and $Cd_4P_2Br_3$ give rise to defect peaks in the gap and inhibit the electron-hole recombination leading to a better photocatalytic HER activity than that of $Cd_4P_2I_3$.

Chapter 6

Pressure-induced Structural Phase Transitions and Phonon Anomalies in ReO_3 *

6.1 Introduction

ABO_3 perovskite oxides exhibit a diverse range of phenomena ranging from magnetoresistance, superconductivity to ferroelectricity [27]. Typically, the insulating perovskite oxides, such as $BaTiO_3$, are known to commonly exhibit temperature (T)-induced structural phase transitions in which the vanishing occupation of d orbitals of a transition-metal ion at the B site is a key to its off-centering as well as to the symmetry lowering structural instability. In contrast, T-dependent structural transitions are not common in metallic perovskite oxides, which typically have the d orbitals of their transition metal partially occupied by electrons. Competing structural instabilities in a perovskite involve rotations of the BO_6 octahedra, which are not excluded by the partial occupancy of d orbitals of the B cation [108]. When the

*This work has been published in Phys. Rev. B **91**, 224308 (2015) [107]. Reproduced with permission from the American Physical Society.

size of the B cation relative to that of the A cation is large, the cubic perovskite structure can be unstable with respect to such octahedral rotational modes, and this can be another factor that can lead to structural transitions [27] and be used to understand fundamentally interesting structural transitions in metallic perovskite oxides. From this angle, ReO_3 is a rather interesting metallic perovskite oxide having conductivity within a factor of 6 of that of copper at room temperature and ∼100% reflectivity below the plasma edge at 2.1 eV. Here, the A cation is completely missing, and four pressure-dependent (but interestingly no temperature-dependent) structural transitions are observed.

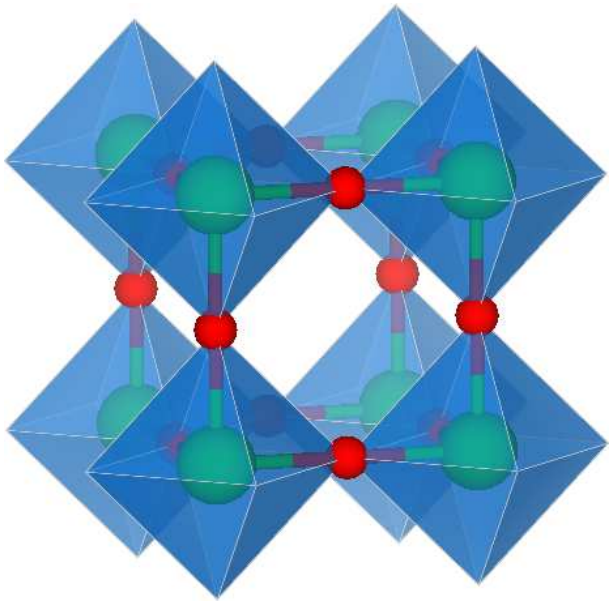

Figure 6.1: Crystal structure of ReO_3 showing corner-linked ReO_6 octahedra.

At ambient pressure, the structure of ReO_3 is cubic (space group *Pm3m*) consisting of corner-linked ReO_6 octahedra and linear Re-O-Re bonds (Fig. 6.1). The empty A cation site in ReO_3 promotes structural instabilities involving rotations of the rigid ReO_6 octahedra. The early interest in ReO_3 was triggered by an observation of a supposedly continuous phase transition at ∼0.5 GPa at room temperature with the compressibility being an order of magnitude higher in the high-pressure phase [109] (and hence termed as compressibility collapse transition). Early neutron-diffraction measurements showed that the high-pressure phase is tetragonal (*P4/mbm*), which

transforms at a slightly higher pressure of 0.72 GPa to the cubic II (*Im3*) phase [110]. However, recent neutron-diffraction studies do not find any evidence of the tetragonal (*P4/mbm*) intermediate phase between the two cubic structures [111]. The softening of the M_3 phonon mode was suggested to be the driving force behind the *Pm3m* to *Im3* pressure transition. X-ray diffraction at high pressures by Jorgensen *et al.* [112] showed three other phase transitions; a cubic II (*Im3*) phase to a monoclinic MnF_3 related phase at 3 GPa to the rhombohedral VF_3 related phase (rhombohedral I) at 12 GPa and to another rhombohedral phase (rhombohedral II) at 38 GPa. Subsequent high-pressure X-ray diffraction studies by Suzuki *et al.* [113] did not observe the monoclinic phase and showed that the cubic phase and rhombohedral I phase coexist in the pressure range of 8–18 GPa. Biswas *et al.* [114] have reported pressure-induced phase transitions in nanocrystalline ReO_3 using synchrotron X-ray diffraction. They have shown that the ambient pressure cubic I phase (*Pm3m*) changes to the monoclinic phase (*C2/c*) at ∼0.3 GPa and from the monoclinic to a rhombohedral I phase (*R3c*) at ∼6.7 GPa and finally to a rhombohedral II phase at ∼20.3 GPa.

Purans *et al.* [115] have carried out Raman measurements at room temperature and ambient pressure. The high-pressure Raman measurement upto 26.9 GPa (performed by Prof. A. K. Sood's group[†]) carried out on a single crystal of ReO_3 shows three phase transitions at 0.6, 3, and 12.5 GPa (see Fig. 6.2) and the low-pressure phase transition is quite intriguing.

First-principles calculations of the electronic structure have been useful in the analysis of electronic properties of ReO_3 revealing that it is a normal Fermi-liquid-type metal [116]. DFT-based calculations also help to understand the relation between the electronic and the structural properties of ReO_3 and related oxides [117]. Recently, lattice dynamics and negative thermal expansion exhibited by ReO_3 at low temperature have been modelled by treating results of the DFT calculations within a quasiharmonic approximation [118]. Although the zone-center phonon frequencies

[†]Department of Physics, Indian Institute of Science, Bangalore-560012.

determined in Refs. [117,118] confirmed the stability of ReO_3 with respect to uniform structural distortions in contrast to that of WO_3 , the large discrepancy between the calculated and experimental frequencies is quite striking. We have employed various flavors and methods of DFT calculations to sort this out and discuss the possible reasons for the discrepancy in terms of electron-phonon coupling and anharmonicity. We determine complete phonon dispersion and two-phonon density of states (DOS) to assign the observed Raman bands in the cubic phase. Finally, we focus on the low-pressure structural phase transition and corroborate experimental observations through determination of pressure-dependent phonon frequencies of the *Pm3m* and *Im3* phases. Our theoretical analysis suggests that the transition between these two phases is a weakly first-order (and not the second-order) transition and highlights the marginal thermal stability of the cubic structure of ReO_3.

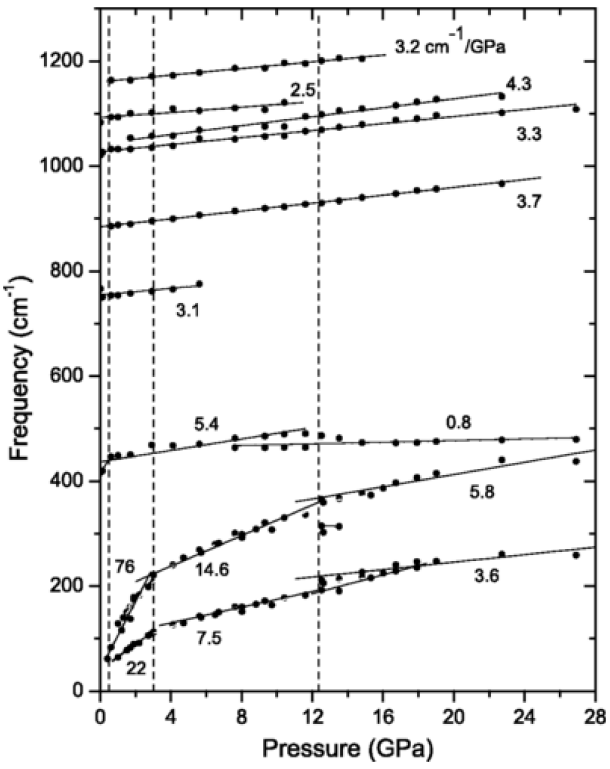

Figure 6.2: Pressure dependence of the frequencies of various Raman modes. The vertical dashed lines represent the phase-transition pressures marked at 0.6, 3, and 12.5 GPa with dotted lines

6.2 Computational details

Our first-principles calculations are based on Quantum ESPRESSO [65] implementation of the DFT at different levels of approximations to the functional description of the exchange-correlation energy: local density approximation (LDA), generalized gradient corrected approximation (GGA), and LDA with an on-site correlation term with a Hubbard U parameter (LDA + U). We have used ultrasoft [119] as well as optimized norm-conserving (NC) pseudopotentials [120] to represent the interaction between the ions and the valence electrons. Nonlinear core corrections were included to capture the effects of the exchange-correlation interaction between valence and core electrons. To validate the results obtained from our calculations based on pseudopotentials, we determined the structure and zone-center phonon frequencies using the frozen phonon method with all-electron calculations with WIEN2K [121] interfaced with the PHONOPY program [122]. For the *Im3* phase of ReO_3, the crystal structure was determined through minimization of total energy using Hellmann-Feynman forces on atoms within the Broyden-Fletcher-Goldfarb-Shanno algorithm. Vibrational frequencies and related dynamical properties were determined using the pseudopotential framework of the density functional perturbation theory as implemented in Quantum ESPRESSO [65].

6.3 Results and Discussion

6.3.1 Zone-center phonons of the cubic structure

As mentioned before, the cubic *Pm3m* structure of ReO_3 has $2F_{1u}(IR)+F_{2u}$ optical phonons at the Γ-point. Our results for frequencies of the infrared-active phonons obtained with different exchange-correlation approximations and pseudopotentials are given in Table 6.1. We note that: (a) Our results obtained with the NC pseudopotential-based DFT calculations are close to the experimental values but differ from those

obtained with full potential linear muffin-tin orbital (LMTO) calculations [117], and (b) the change in pseudopotentials results in a relatively large change in the highest-frequency infrared-active mode.

Table 6.1: Calculated zone-center phonons frequencies (in cm^{-1}) of the cubic ReO_3.

NC LDA	USPP LDA	USPP LDA+U=1 eV	USPP GGA	WIEN2K LDA	Catlow LDA [115]	Experiment [123]
359	378	383	358 (IR)	373	215 (IR)	315 (IR)
393 (IR)	386 (IR)	384 (IR)	375 (IR)	384 (IR)	433	
898 (IR)	759 (IR)	725 (IR)	702 (IR)	755 (IR)	760 (IR)	905 (IR)

The discrepancy between the experimental values [123] and our estimates of phonon frequencies as well as those from earlier calculations [117, 118] is larger than the typical DFT results. Based on our results (Table 6.1), use of different DFT functionals (LDA versus GGA) or inclusion of stronger correlations (LDA versus LDA + U) is unlikely to explain such a large difference. It is found that the highest-frequency mode is quite sensitive to the choice of (norm-conserving versus ultrasoft) pseudopotential (and demonstrated later that it is also very sensitive to pressure). In order to benchmark pseudopotential-based calculations, we have performed full potential calculations using WIEN2K within the LDA and obtained a theoretical lattice constant of 3.73 Å by fitting the Murnaghan equation of state to the energy versus volume curve. At this lattice constant, we determined the zone-center phonon frequencies of ReO_3 using atomic forces calculated with WIEN2K for configurations generated by displacing each of the atoms by 0.01 Å at a time and a frozen phonon method to obtain force constant matrix with a code PHONOPY. The phonon frequencies obtained using full potential and LDA ultrasoft pseudopotential (LDA USPP) calculations are in quite good agreement (Table 6.1). Our estimates of the highest-frequency IR-active mode obtained using LDA USPP and WIEN2K LDA (Table 6.1) are also close to those obtained with full potential LMTO calculations [117]. Although LDA with NC pseudopotential-based calculations seem to yield phonon properties closer to the experiment, it may be spurious because the pseudopotential-based calculations should

ideally be consistent with all-electron calculations (e.g., WIEN2K) for the same flavor of exchange-correlation energy. As other properties are well explained within the LDA by USPP, we have carried out the rest of the calculations within the LDA using USPP at the theoretical lattice constant (a) of 3.72 Å which is close to the experimental value of 3.75 Å.

6.3.2 Phonon dispersion and the two-phonon density of states

Using DFT linear response, we have obtained dynamical matrices at Bloch wave vectors corresponding to high-symmetry points in the Brillouin zone (Γ, X, M, and R) and used Fourier interpolation to determine the dynamical matrices at an arbitrary Bloch vector. The phonon dispersion curves determined here from first principles are qualitatively similar to those computed empirically [123]. Our results for phonon dispersion (see Fig. 6.3(a)) reveal that the softest optical modes are at the zone boundary: M, R, and X. The former two correspond to the rotational modes of the oxygen octahedra. The mode M_3 involves rotation of the ReO_6 octahedron around the z-axis for M = $(110)\frac{\pi}{a}$ and is triply degenerate with M_3 modes at other M points [$(011)\frac{\pi}{a}$ and $(101)\frac{\pi}{a}$] that involve rotation around the x and y-axes, respectively. The R_{25} mode is a triply degenerate mode involving rotations of ReO_6 around each of the Cartesian axes. When one of these modes is unstable (negative values of the square of frequencies), the structure distorts through rotation of ReO_6 octahedra resulting in a cell-doubling structural transition. Mode X_5 is doubly degenerate and does not seem to be directly relevant to any of the observed transitions in ReO_3. Note that there is a gap in the phonon frequencies from 508 to 708 cm^{-1}. High-frequency phonons involve stretching of the Re-O bonds and are isolated from the rest. The modes at the R point (R_2 at 1037 cm^{-1} and R_{12} at 829 cm^{-1}) have the highest frequencies as they involve stretching and compression of Re-O bonds in alternate unit cells. These are significantly higher than in insulating perovskite oxides [108].

Lastly, the acoustic modes of ReO_3 are quite interesting: (a) the transverse acoustic (TA) phonons are much softer than the longitudinal acoustic (LA) phonons, implying that ReO_3 has a large bulk modulus but a rather low shear modulus, and (b) the branches of phonons containing rotational modes M_3 and R_{25} involve a strong mixing with branches of both LA and TA modes. Thus, we expect a strong dependence of M_3 and R_{25} modes on the isotropic and shear strains, and hence they should be quite relevant to pressure-induced structural phase transitions in ReO_3.

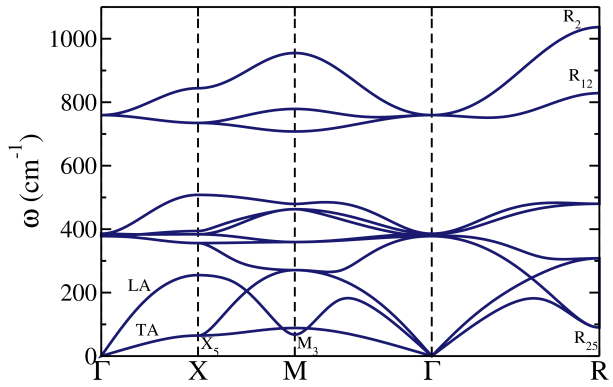

(a)

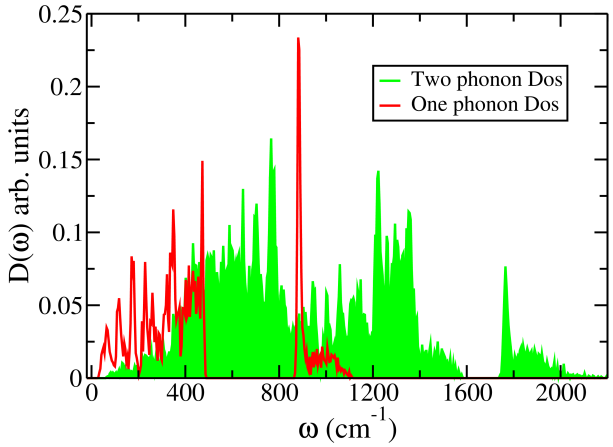

(b)

Figure 6.3: (a) Phonon dispersion and (b) One- and two-phonon density of states of cubic ReO_3.

Since there is no Raman-active mode at the zone center, the bands observed in Raman spectra are clearly second-order Raman modes. From the one-phonon and two-phonon density of states (Fig. 6.3(b)), we attempt to assign overtones using the selection rules [123] (allowing for some errors as was evident in the Γ-point phonons) and

information about various overtones available from the two-phonon DOS obtained by including only the overtones (Fig. 6.3(b)): 259 cm^{-1}: 2×M_3 at 99 cm^{-1}; 350 cm^{-1}: two phonons along the Σ line; 418 cm^{-1}: along the M to X or Σ lines; 600 cm^{-1}: 2 × X_1; 677 cm^{-1}: 2 × Γ_{25} or 2 × X_5 ; 768 cm^{-1}: 2 × X_5; 1026 cm^{-1}: 2 × X_1 or 2 × R_{15}; 1085 cm^{-1}: 2 × X_1 or 2 × R_{15}.

6.3.3 Pressure dependence of phonon frequencies

To understand the observed pressure-dependent structural transitions in ReO_3, we first determine the pressure dependence of phonons at high-symmetry points in the Brillouin zone of the cubic (*Pm3m*) phase. At each wave vector, we find that the high-frequency phonons harden and lower-frequency phonons soften with pressure. At the Γ-point (Fig. 6.4), only the highest energy Γ_{15} phonon is strongly dependent on pressure exhibiting an increase in frequency, and the rate of change of frequency with pressure is 6.2 cm^{-1}/GPa. This is similar to the pressure dependence of polar phonons in ferroelectric oxides [124]. In contrast, the lower-energy phonons of Γ_{25} symmetry exhibit gradual softening with pressure. The strong P dependence of the high-frequency Γ_{15} mode reflects its anharmonic coupling particularly with strain or the LA modes, which is very likely responsible for its T dependence and therefore may explain the discrepancy between its zero temperature calculated and observed frequencies (at room temperature).

The softest mode at the X point having X_5 symmetry softens further with pressure but remains stable. The M_3 and R_{25} phonons involving rotation of ReO_6 octahedra, which are the softest modes in the phonon spectrum of cubic ReO_3 , soften further with a strong dependence on pressure similar to the one reported by Wdowik *et al.* [118]. Although most modes at the M point are weakly dependent on pressure (Fig. 6.4), the M_3 mode is found to exhibit the strongest and anomalous dependence on pressure and becomes unstable for an applied pressure of > 3 GPa. This is the mode (along

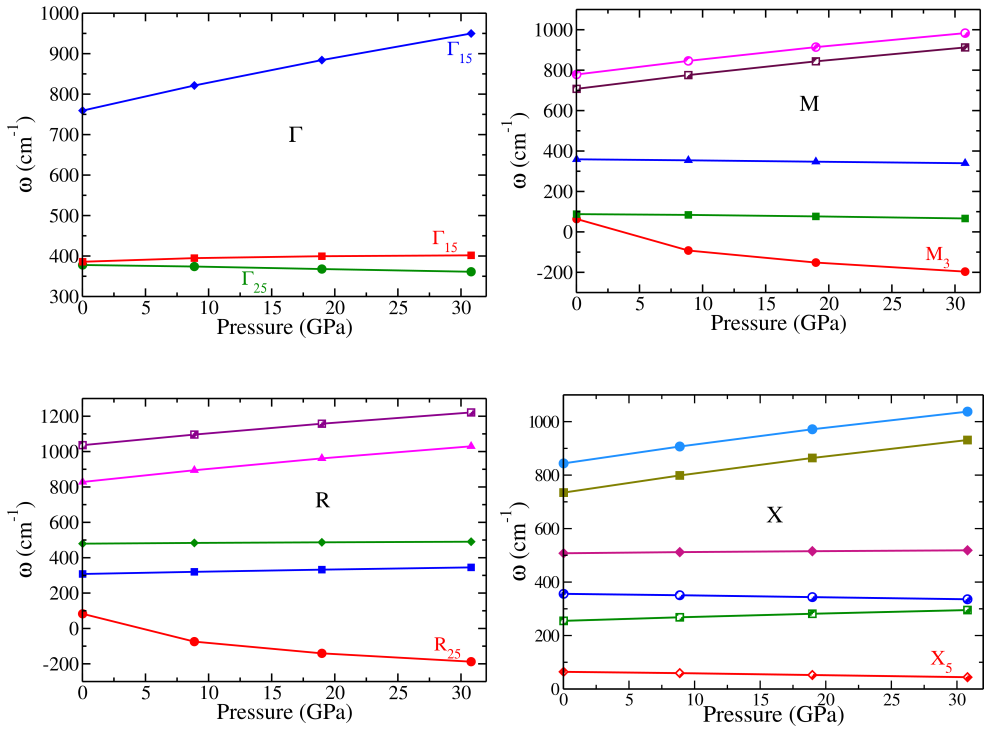

Figure 6.4: Pressure dependence of frequencies of phonons at high-symmetry k points (Γ, X, M, and R) in the Brillouin zone of cubic ReO_3.

with its symmetry-related modes at other M points) that is expected to be relevant to structural phase transition from cubic I to cubic II in ReO_3 . Likewise, the R_{25} mode is found to be sensitive to pressure and becomes unstable at pressures above 5 GPa. Although M_3 is the first mode that becomes unstable as pressure is applied, our estimate of the pressure required for this instability to set in is significantly higher than the observed pressure at which the first structural transition occurs. As we will analyze later, this is because the transition is weakly first order and occurs through a third-order coupling with acoustic modes.

We have determined the pressure dependence of zone-center phonons of ReO_3 in the *Im3* cubic II structure. The *Im3* structure has a unit cell with 8 formula units, and Brillouin-zone folding gives the correspondence of its zone-center phonons with the phonons at Γ, X, M, and R points of the cubic structure. Clearly, they also exhibit a gap between about 505 and 724 cm^{-1}. The softest ones at 57, 62, 63, 88, and 92 cm^{-1}

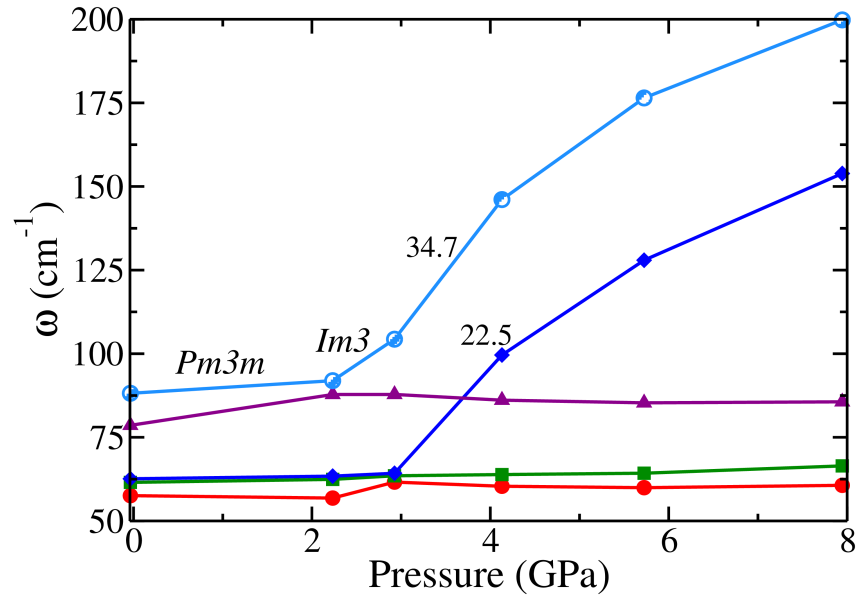

(a)

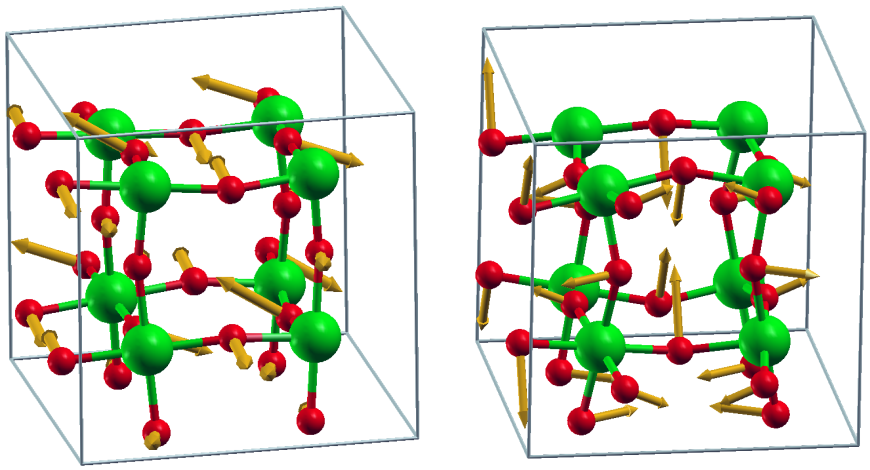

(b) 104 cm^{-1} (5.7 GPa) (c) 128 cm^{-1} (2.9 GPa)

Figure 6.5: (a) Low-frequency phonons of ReO_3 as a function of pressure as it goes through a phase transition from the *Pm3m* to the *Im3* phase and atomic displacements at high and low pressures in (b) and (c), respectively. The large (green) spheres represent Re atoms whereas the O atoms are indicated by small (dark red) spheres.

correspond to mixed modes involving ReO_6 rotations and TA modes of the *Pm3m* structure and are rather sensitive to pressure as expected [see Fig. 6.5(a)]. We notice a sudden change in the frequency at 2.2 GPa which may be attributed to the phase transition from the cubic *Pm3m* to the *Im3* phase. The rate of change in frequencies (cm^{-1}/GPa) is marked in Fig. 6.5(a). Clearly, the theoretical estimates of the rate of change in phonon frequency with pressure [marked in Fig. 6.5(a)], although very

high, are somewhat smaller than the observed values (76 and 22 cm^{-1}/GPa), thereby highlighting the role of thermal fluctuations and anharmonic effects. Nevertheless, our analysis brings out the phonons in the parent high-symmetry *Pm3m* structure

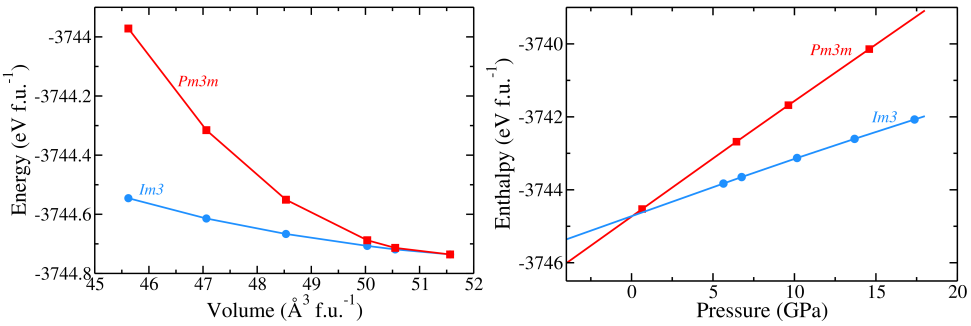

(a) (b)

Figure 6.6: (a) Total energy curve of the *Pm3m* and the *Im3* phases of ReO_3 and (b) their enthalpy change with pressure, calculated using pseudopotentials with the Quantum ESPRESSO package.

of ReO_3 that are relevant to the structural transitions. From visualization of the eigenvectors of these modes of the *Im3* phase, we find that they involve octahedral rotations at high as well as at low pressures [see Figs. 6.5(b) and 6.5(c)]. At P ∼2.2 GPa, there is a striking change in the slope of the pressure dependence of frequencies of these modes, consistent with our experimental observations. The point of drastic change in the slope of ω as a function of pressure gives a rough estimate of transition pressure of the first phase transition. To precisely locate the transition pressure, we determined the enthalpy of the *Pm3m* and *Im3* structures. From the energy as a function of volume [Fig. 6.6(a)] of the *Pm3m* and *Im3* phases of ReO_3, it is clear that the *Im3* phase becomes energetically more favorable as the volume decreases. Using the fit obtained with the Murnaghan equation of state to the energy versus volume curves, we determined the enthalpy as a function of volume. Our estimate of the transition pressure (the point at which the enthalpies of the two phases are equal [Fig. 6.6(b)]) for the *Pm3m* to the *Im3* phase transition is 0.1 GPa, which is smaller than the experimental value of 0.6 GPa. Errors of such magnitude are typical of DFT calculations due to its under estimation of bond lengths or lattice

constants. We carried out all-electron full potential linearized augmented plane-wave calculations using WIEN2K to eliminate the errors in the structure and bond lengths arising from the use of pseudopotentials. Our estimate of the transition pressure from the enthalpy versus pressure curve (Fig. 6.7) obtained using WIEN2K is 0.5 ± 0.1 GPa, quite close to the experiment.

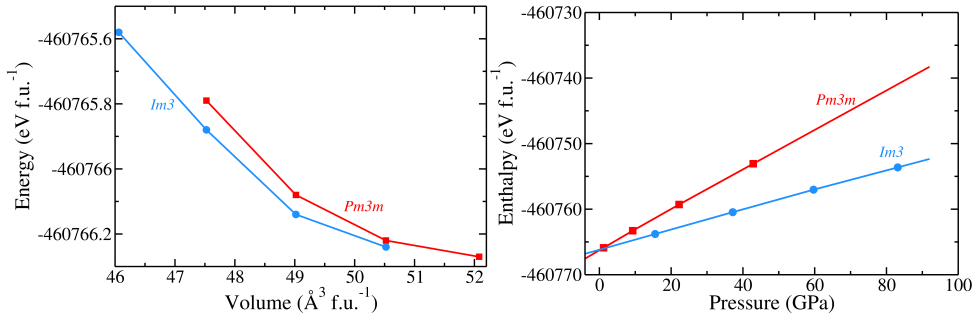

(a) (b)

Figure 6.7: (a) Total energy curve of the *Pm3m* and the *Im3* phases of ReO_3 and (b) their enthalpy change with pressure, obtained from all-electron calculations carried out with WIEN2K.

Our finding that this pressure is clearly lower than the one at which M_3 modes become unstable shows that: (a) the M_3 modes are not the only modes relevant to this transition and (b) that their anharmonic coupling with the TA and LA modes is important. Finally, we comment on the nature of the *Pm3m* to *Im3* phase transition. From our analysis of phonons, we note that the transition from the *Pm3m* to the *Im3* structure is driven by the instability of M_3 phonons. As seen in Fig. 6.4, M_3 phonons become unstable for P > 3 GPa. However, based on the analysis of enthalpy of these structures as a function of P, we find that the transition occurs at a much lower pressure of P = 0.5 GPa. This is depicted in the sketch (see Fig. 6.8) of the frequency of the M phonon with pressure near the transition. We note that: (a) there is a discontinuous change in the slope of ω_M^2 (P) at the transition pressure, and (b) the phonon frequency does not drop to zero at the transition. Based on this, we conclude that the transition is weakly first order as the frequency of the relevant phonon M_3 is quite low (64 cm^{-1}) just below the transition pressure. Although we

cannot rule out an intermediate tetragonal phase, our analysis supports that it is a weakly first-order transition, driven by the third-order couplings between M_3 and acoustic modes as evident in Fig. 6.4. We further note that our calculations bring out clearly that phonon dispersion of the cubic *Pm3m* phase exhibits no unstable modes at pressures above the transition pressure. Thus, the *Pm3m* phase remains metastable even above the transition pressure and can coexist with the *Im3* phase, which means the transition is of the first order.

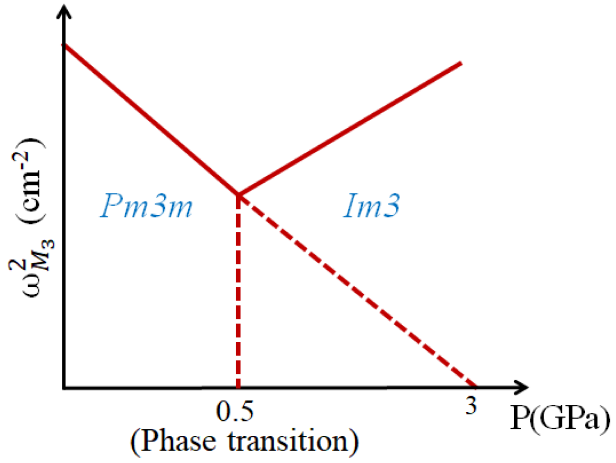

Figure 6.8: Sketch of pressure dependence of frequency of the M phonon near the phase transition.

6.3.4 Electron-phonon coupling

To assess the role of electron-phonon coupling to understand the underestimation of frequencies of the IR-active modes, we estimated the electron-phonon coupling for modes at the high-symmetry wave vectors using DFT linear-response calculations. We find that modes Γ_{25}, X_5, and M_3 exhibit notable electron-phonon couplings of λ = 0.016, 0.06, and 0.01 respectively. All the modes at the R point have vanishingly small λ. This can be understood from the nature of the Fermi surface [117], which exhibits nesting with wave vectors at only X and M points. It is interesting to note that: (a) phonons M_3 and R_{25} relevant to structural transitions exhibit negligible coupling with electrons, (b) the highest-frequency modes do not couple strongly with

electrons, so the dynamical corrections to their adiabatic frequencies would be small and would not explain the discrepancy between theory and experiment, and (c) only the modes that involve bond bending along the Re-O-Re chains (deviation of the Re-O-Re angle from 180^o) couple strongly with electrons.

6.3.5 Why ReO_3 does not exhibit transitions as a function of temperature?

As evident in its phonon dispersion [Fig. 6.3], ReO_3 in the cubic structure does not exhibit any structural instabilities at ambient pressure and 0 K. Its pressure-dependent transition involves unstable modes corresponding to rotations of ReO_6 octahedra. These modes harden with an increase in volume [see Fig. 6.4]. Although ReO_3 exhibits negative thermal expansion at low temperatures, this is not strong enough to make the M_3 mode unstable. As a result, the cubic structure remains stable at elevated temperatures at ambient pressure. We note that its negative thermal expansion involves the anharmonic coupling [118] that is similar to what causes the low-pressure phase transition to be weakly first order.

6.4 Conclusions

We note that the softening and anharmonicity of the M_3 phonon mode are relevant to the low-pressure phase transitions in ReO_3. Our estimate of the transition pressure for the low-pressure transition from the *Pm3m* to the *Im3* structure is 0.1 GPa, lower than the pressure at which M_3 modes become unstable. Thus, the transition has a weakly first-order character and arises from third-order anharmonic coupling between M_3 and acoustic modes.

Part II

Surface and Catalytic Properties of Metallic Surfaces

Chapter 7

Catalytic Oxidation of Ethanol Using Ordered Pd_2Ge Nanoparticles *

7.1 Introduction

Fuel cells have emerged as one of the most prominent options for alternative energy conversion and have been applied for various electrochemical reactions. Currently, platinum on different supports [126, 127] and in the form of alloys [128], bimetallic [129], and intermetallic compounds [130] are the most widely used electrocatalysts in the low temperature fuel cells. A few examples are Pt_3Pb nanoparticles showed high efficiency for formic acid oxidation [131], $PtCu_3$ nanocages were proved to be highly efficient in methanol oxidation [132], and PtRu bilayer coreshell nanoparticles are very good CO tolerant electrocatalyst [133]. Direct alcohol fuel cells (DAFCs) have drawn great attention because they are considered as promising future power sources for electric vehicles and small portable electronics. On the basis of the electrolyte

*This work has been published in Chem. Mater. **27**, 7459 (2015) [125]. Reproduced with permission from the American Chemical Society.

membrane used, DAFCs can be divided into two types: acid- and alkaline-membrane DAFCs. Over the past few decades, extensive attention has been paid to the acid-type DAFCs, and significant progress has been made in their development. However, the commercialization of acid-type DAFCs still remains a challenge because, in acidic media, the expensive Pt or Pt-based electrocatalysts are usually required. In addition, the kinetics of alcohol oxidation on Pt-based electrocatalysts is rather sluggish in acidic media. Recently, increasing attention has been paid to the alkaline-type DAFCs because, in alkaline media, less expensive Pd-based catalysts have comparable or even better electrocatalytic activities than Pt-based catalysts for alcohol oxidation, especially for ethanol oxidation. Xu *et al.* prepared a series of oxide nanocrystal promoted-Pd/C electrocatalysts which were markedly superior to those of Pt-based electrocatalysts in terms of alcohol oxidation activity and poison tolerance in alkaline media [134]. Although Pd proved to be as a suitable electrocatalyst for the ethanol oxidation reaction (EOR) in alkaline media, more effort is needed to further improve the electrocatalytic performance of Pd-based catalysts. Ethanol is relatively less studied than methanol; the reason could be because the C–C bond cleavage in ethanol requires very high dissociating energy (∼350 kJ/mol) [135]. However, the use of ethanol is advantageous over methanol because it is less toxic, highly abundant, low cost, and results in 12 electrons per molecule when it is completely oxidized to CO_2 and H_2O. Some of the catalysts which have been used for electrochemical oxidation of ethanol are SnO_2/PtSn alloys [136], Ni supported/PtRu alloys [137], and Pt/C on other oxides like CeO_2 and NiO [134]. In alkaline medium, it has been shown that the reaction catalyzed by Pt is sluggish as compared to Pd. Hence, Pd on various support materials along with its alloys has been highly studied during the past two decades. A few examples of this class are Pd on TiO_2/C [138], Al_2O_3/C, VO_x/C [139], CeO_2/C [140], Co_3O_4/C [141], MnO_2/C [142], NiO/C, In_2O_3/C [143], CNTs (both SWCNT and MWCNT) [142,144], and the alloys PdNi [145], PdPt [146], PdAu [147], and PdRu [148]. It is experimentally proven that the presence of another metal or

support highly enhances the catalytic activity of Pd nanoparticles by the synergistic effect between Pd and the support.

Apart from the systems mentioned above, several catalysts have been reported in the recent literature for the electrooxidation of ethanol applying different strategies to improve both the activity and the durability of the catalyst. For example, both PtSn [149] and PdSn [150] based alloy nanoparticles are considered as superior catalysts in ethanol electrooxidation because of their high activity and durability in acidic and alkaline media, respectively, but these two classes of compounds do not form ordered intermetallic phases under the normal reaction conditions. In the same manner, $TaPt_3$ ordered intermetallic nanoparticles [151] were reported to show far better activity than Pt_3Sn nanoparticles. However, the ordered phase of $TaPt_3$ was only obtained after the postsynthetic heating at a very high temperature (1000 ^{o}C). PtRh alloy nanocubes supported on graphene [152] were shown to have high activity toward ethanol electrooxidation; however, both the constituents are costly. PdAu nanowires [153] were synthesized in the presence of Br^- and PVP as a shape-directing and stabilizing agent. The presence of an additive on the catalyst surface is detrimental to its catalytic activity as these polymer molecules significantly reduce the effective coverage of ethanol molecules. Motivated by the incredible catalytic activity of PdSn based alloy nanoparticles, Prof. Sebastian C. Peter's group[†] has synthesized the ordered intermetallic compound Pd_2Ge in nanodimension. The electrochemical oxidation of ethanol in an alkaline medium using Pd_2Ge as a catalyst synthesized over a reaction times of 24 h (Pd_2Ge_24) and 36 h (Pd_2Ge_36) of synthesis was studied. The order of activity toward electrochemical oxidation of ethanol is Pd_2Ge_36 > Pd2Ge_24 > Pd/C. The presence of Ge deficiency in the Pd_2Ge_24 sample showed an immense effect on the catalytic activity of the compound

The ethanol oxidation reaction in alkaline medium goes through two pathways: one

[†]New Chemistry Unit, Jawaharlal Nehru Centre for Advanced Scientific Research, Bangalore

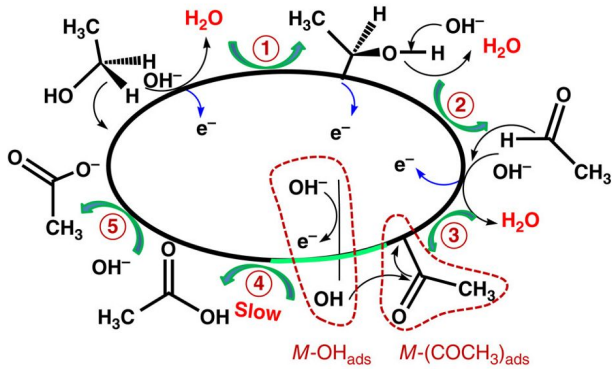

Figure 7.1: Schematic of ethanol oxidation process in an alkaline medium. Taken from the Ref. [19].

is through the reactive intermediate pathway and other through poisoning intermediate pathway. Ethanol oxidation reaction in the reactive intermediate pathway is the five steps reactions. In this, M-$(OH)_{ads.}$ ($^*OH$) and M-$(COCH_3)_{ads.}$ ($^*CH_3CO$) intermediates combine to generate acetate ion. The combination of $^*OH$ and $^*CH_3CO$ intermediate states is the rate determining step of the ethanol oxidation reaction. Whereas, in the poisoning-intermediate pathway $^*CH_3CO$ decompose into $^*CO$ and $^*CH_3$ which block the active sites and reduces the efficiency of the catalysts [19] The ethanol oxidation reaction has been shown schematically in Fig. 7.1. In this chapter, our aim is to understand the experimentally observed catalytic activity of Pd_2Ge in terms of the combined effect of adsorption energies of CH_3CO and OH radical, *d*-band center model, and work function of the corresponding catalyst surfaces.

7.2 Crystal structure

Pd_2Ge crystallizes in the hexagonal Fe_2P structure type ($P\bar{6}2c$ space group), which is a vacancy ordered variant of the AlB_2 prototype (see Fig. 7.2). Among the four different crystallographic sites, two are occupied by the Pd atoms (Wyck. no. 3f and 3g) and the other two are occupied by the Ge atoms (Wyck. no. 2a and 1b). The coordination environments of the catalytically active palladium sites are shown in Fig. 7.2(b) and (c). The open circle represents the deficiency at the Ge atoms.

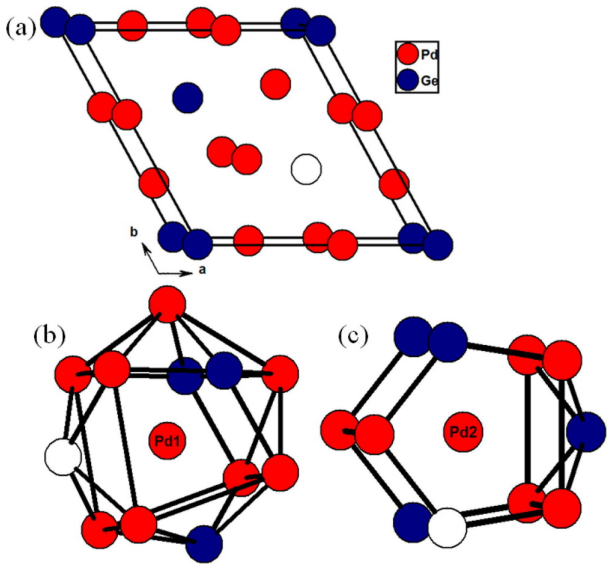

Figure 7.2: (a) Crystal structure of Pd_2Ge. The white atom represents a vacant site at the Ge position for the sample Pd_2Ge_24. Coordination spheres of (b) Pd1 and (c) Pd2.

7.3 Computational details

The first-principles calculations are performed on the density functional theory as implemented in the Quantum ESPRESSO package [65]. The exchange-correlation energy of electrons is treated with a local density approximation with the Perdew–Zunger parametrized form [154]. We employ periodic boundary conditions with 4×4 and 3×3 supercells of Pd (111) and Pd_2Ge (0001) surfaces, respectively, and include a vacuum of about 14 Å along z-direction to keep interaction between periodic images low. We have used a kinetic energy cutoff of 35 Ry to truncate the plane-wave basis. We use uniform meshes of 3×3×1 and 3×3×2 k-points for Pd and Pd_2Ge surfaces, respectively, in sampling integration over the Brillouin zone. We use different orientations of OH and CH_3CO on the surface and relax the system until the Hellmann–Feynman forces on each atom are less than 0.03 eV/Å. We have considered Pd_2Ge_24 as a Ge-deficient surface and Pd_2Ge_36 as a pristine Pd_2Ge phase throughout our calculation.

7.4 Results and discussion

Most catalytic reactions are governed by the Sabatier principle, which states that catalytic activity will be optimum when binding of reactive intermediates with a catalytic surface has intermediate free energies of adsorption (binding energies) [155]. We used this principle as a basis to rationalize the catalytic activity of Pd_2Ge. The ethanol electrooxidation reaction in the alkaline medium on the metal surface involves five steps and intermediates, among which the formation of CH_3COOH (shown below) is the rate determining step [156]:

$$(M - CH_3CO)_{ads.} + M - (OH)_{ads.} \xrightarrow{rds.} M - CH_3COOH + M \tag{7.1}$$

The main intermediate species during ethanol electrooxidation are CH_3CO and OH [156]; the latter helps in cleaning the surface of the catalyst through oxidizing the carbonaceous species. We have used various initial configurations of CH_3CO and OH on Pd_2Ge (0001) and Pd (111) surfaces.

The most favorable binding configurations of CH_3CO and OH adsorbed on Pd_2Ge and Pd(111) are determined through minimization of energy (see Figs. 7.3 and 7.4). OH adsorbs at a minimum distance of 1.2, 1.1, and 1.2 Å from the surface atoms on Pd (111), Pd2Ge_24, and Pd2Ge_36 surfaces, respectively. OH prefers to adsorb on the hollow site of Pd(111) surface and forms three Pd-O bonds of length 2.1 Å (Fig. 7.3(a)). On Pd_2Ge surface with Ge-deficiency (Pd_2Ge_24), OH gets adsorbed on the hollow site of the surface forming three Pd-O bonds of length 2.2 Å (Fig. 7.3(b)). In case of Pd_2Ge_36, OH prefers to adsorb on Pd-Ge bridge and forms a bond with Ge and Pd, such that the Ge-O and Pd-O bond lengths are 1.89 Å and 2.20 Å respectively (Fig. 7.3(c)). The binding energies of OH adsorption on Pd and Pd_2Ge surfaces have been tabulated in Table 7.1.

CH_3CO adsorbs at a minimum distance of 1.79, 1.49, and 1.79 Å from the surface

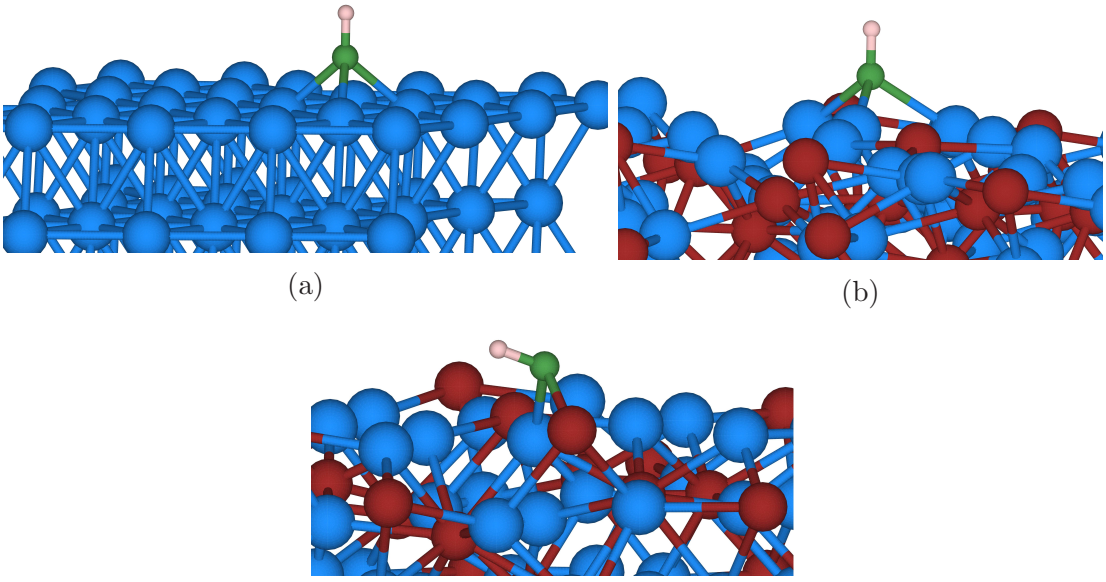

(a) (b) (c)

Figure 7.3: Stable binding geometries of OH on (a) Pd (111), (b) Pd_2Ge_24 and (c) Pd_2Ge_36 surfaces. Pd, Ge, O and H are represented by blue, red, green and pink spheres respectively.

atoms on Pd (111), Pd_2Ge_24, and Pd_2Ge_36 surfaces, respectively. CH_3CO get adsorbed on Pd (111) such that it forms a Pd-C and Pd-O bonds of length 1.92 Å and 2.12 Å respectively (Fig. 7.4(a)). The stable binding geometry of CH_3CO on Pd_2Ge_24 is the one in which it forms two Pd-C bonds and Pd-O bond of length 2.11 Å and 2.17 Å respectively (Fig. 7.4(b)). On Pd_2Ge_36 surface CH_3CO adsorbed by forming a bond Pd-C and Pd-O of lengths 1.96 Å and 2.19 Å respectively (Fig. 7.4(c)). The binding energies of these stable geometries of CH_3CO adsorption on various surfaces have been tabulated in Table 7.1.

On the basis of adsorption energies, it can be clearly seen that OH binds quite strongly with Pd_2Ge surfaces compared to the Pd (111) surface. After OH adsorption, the Pd_2Ge surface undergoes strong relaxation of about 0.2 Å compared to ∼0.1 Å in the case of the Pd surface. This strong relaxation of Pd_2Ge surfaces show the strong interaction between the surface and the adsorbate and hence stronger binding of OH compared to the Pd (111) surface. This is also evident in the density of states, as shown in Fig. 7.5. OH binds strongly to Pd_2Ge_24 surface as compared to Pd_2Ge_36.

Also, Pd_2Ge binds strongly to CH_3CO, followed by Pd (111) and Pd_2Ge_36. To get a better insight into it, we applied the *d*-band model proposed by Hammer and Nørskov [157]. According to this model, the higher the d-band center, the greater the binding and, hence, the catalytic activity. The *d*-band center (ε_d) is given by the following relation in this model:

$$\varepsilon_d = \frac{\int_{-\infty}^{E_F} E\rho_d(E)dE}{\int_{-\infty}^{E_F} \rho_d(E)dE} \tag{7.2}$$

where ρ_d is the projected density of *d*-states of surface atoms, E is the energy, and E_F is the Fermi level. We have obtained the average *d*-band center for CH_3CO and OH

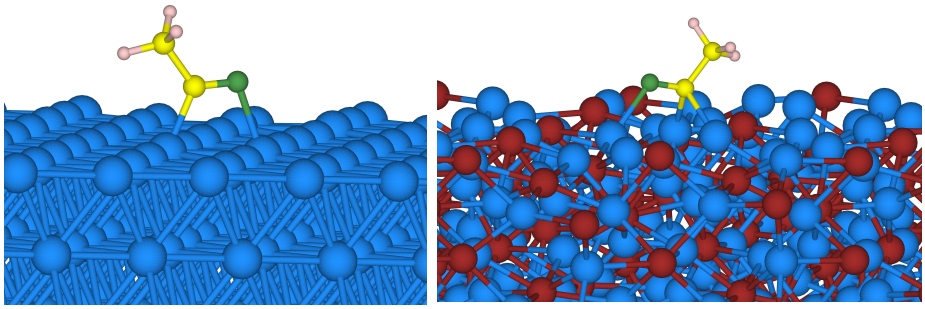

(a) (b)

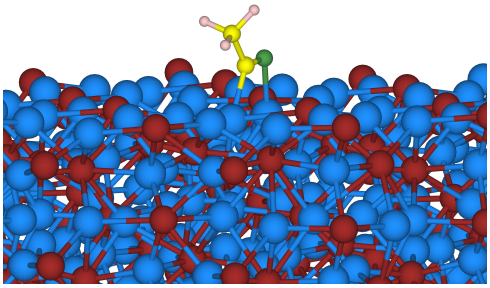

(c)

Figure 7.4: Stable binding geometries of CH_3CO on (a) Pd (111), (b) Pd_2Ge_24 and (c) Pd_2Ge_36 surfaces. Pd, Ge, O, H and C are represented by blue, red, green, pink and yellow spheres respectively.

adsorbed on the surface atoms (see Table 7.1). The *d*-band model fails for Pd (111) and Pd_2Ge_24 surfaces, but the value of the *d*-band center of Pd_2Ge_36 correlates well with its binding energy. Pd_2Ge_36 has a fairly high value of the *d*-band center

and hence can bind strongly with OH. In the case of CH_3CO adsorption, the *d*-band center lies below the Fermi level and hence binds weakly with the Pd_2Ge_36 surface. Pd_2Ge_24 is Ge-deficient and hence possesses vacant Ge sites on its surface, which have two important consequences on the binding ability with the adsorbate: first, these vacant sites themselves act as active adsorption sites [158] and, second, Ge vacancies will expose Pd sites to both CH_3CO and OH radicals (which also act as a catalyst poison at higher adsorption energy) to a greater extent, leading to a decreased coordination number, [159] and high adsorption energy (see Table 7.1). Thus, the strong binding of adsorbate will poison the catalyst surface by decreasing the effective coverage of incoming CH_3CH_2OH molecules. Also, a good catalyst for ethanol oxidation should bind strongly with OH and weakly with CH_3CO; these two criteria are well satisfied by Pd_2Ge_36. Hence, Pd_2Ge_24 shows the intermediate catalytic activity between Pd (111) and Pd_2Ge_36.

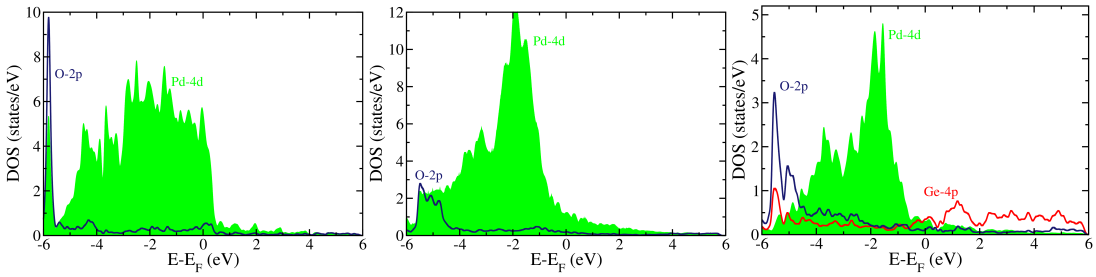

Figure 7.5: Projected density of states as a result of OH adsorption on (a) Pd (111), (b) Pd_2Ge_24 and (c) Pd_2Ge_36 surfaces.

Table 7.1: Adsorption energies (kJ/mol) for CH_3CO and OH radical on different catalyst surfaces. Average value of *d*-band centers (eV) of CH_3CO and OH adsorbed surface atoms are shown in the parentheses.

Catalysts	CH_3CO	OH
Pd (111)	-335.00 (-2.50)	-388.10 (-2.24)
Pd_2Ge_24	-368.78 (-2.73)	-489.53 (-2.40)
Pd_2Ge_36	-288.00 (-2.90)	-436.42 (-2.33)

We converted the potentials required for ethanol oxidation using the relation, E(NHE) = E(Hg/HgO) + 0.108 V [160] to the NHE scale. On the NHE scale, the minimum

potential required for ethanol oxidation is around 4.5 eV. We obtained the work function (ϕ_s) (see Table 7.2) using the following relation:

$$\phi_s = V_{vacuum} - V_{Fermi} \tag{7.3}$$

Here, V_{vacuum} and V_{Fermi} are the potentials in the vacuum and at the Fermi level. The ϕ_s values clearly show that the Pd (111) lies below on the potential scale of ethanol oxidation compared to Pd_2Ge surfaces (see Table 7.2). This also confirms the strong catalytic activity of Pd_2Ge surfaces in comparison to the Pd (111) surface.

Table 7.2: Work functions of different catalyst surfaces.

Catalysts	ϕ_s(eV)
Pd (111)	5.7
Pd_2Ge_24	5.0
Pd_2Ge_36	4.9

7.5 Conclusions

We find that OH prefers to bind on the Pd-Ge bridge of Pd_2Ge_36, whereas it prefers to bind on the hollow sites in case of Pd (111) and Pd_2Ge_24 surfaces. A perfect balance between the adsorption energies of CH_3CO and OH on the catalyst surface dictates its electrocatalytic activity, and the presence of vacancies in the inactive sites undoubtedly affects the course of reactivity. Als, the work function of Pd_2Ge surfaces lie close to the potential of ethanol oxidation leading to its superior catalytic activity as compared to Pd (111) surface.

Chapter 8

Metal Phosphides, $Ni_{0.2}Co_{0.8}P$: An Efficient Catalyst for the Water Splitting

8.1 Introduction

Electrochemical water splitting is an attractive sustainable technology for tapping renewable energy resources with negligible carbon footprints [161–163]. However, the high cost and low earth abundance of the best performing oxygen evolution reaction (OER) and hydrogen evolution reaction (HER) catalysts (RuO_2, IrO_2 etc. for OER and Pt based catalysts for HER) limit their widespread applications [164–167]. Practical prototypes surpassing industrial threshold for water splitting demands not only effective but also earth-abundant electrocatalysts to carry out hydrogen and oxygen generation at opposite electrodes efficiently [168]. The sluggish electron transfer kinetics associated with OER is the major impediment which needs to overcome with the earth abundant catalysts before we realize water splitting as the source of renewable energy [169–171]. Several transition metal oxides [172–175], hydroxides [176–178], sulfides [167, 179–181], selenides [182–184], nitrides [185–187], phosphides [188–195]

etc. are being explored in this direction as monofunctional/bifunctional electrocatalysts for HER and OER studies. Among them; Mo, Fe, Ni, and Co based transition metal phosphides are emerging as a new class of electrocatalysts for OER owing to their good electrical conductivity [90, 192], as compared to their oxide counterparts and excellent stability under a wide range of pH [168]. Furthermore, their ability to show proton and hydride acceptor properties over metal and phosphorus sites respectively aids their performance in HER activity [90, 168, 195–197]. Nevertheless, still a lot of improvement in terms of their structure and composition is required to match their performance with RuO_2, IrO_2 and Pt based catalysts in their respective OER and HER reactions [168].

For example, in comparison to one and two dimensional structures, three dimensional nanoporous architectures of CoP_3 nanoneedles facilitate mass transport dynamics and efficient charge-transfer kinetics at electrode-electrolyte interfaces which in turn enhances their electrocatalytic activity [90]. Furthermore, the presence of hetero-metals in close proximity is known to tune the local electronic environment significantly leading to unusual OER and HER activities [198, 199]. Therefore, a synergistically designed catalysts having balanced pore architecture along with optimally tailored electronic structures is expected to further boost their performance in electrochemical reactions.

Herein, Prof. M. Eswarmoorthy's group* has synthesized a self-supported, (three-dimensional nanoporous NiCoP) catalysts having lattice structure which mainly consists of CoP phase (orthorhombic). It is shown to exhibit excellent performance in catalysing oxygen evolution reaction (OER) in alkaline condition experimentally. It also shows good activity for hydrogen evolution reaction (HER) under both alkaline and acidic conditions. In this chapter, we try to understand the superior catalytic activity of NiCoP as compared to Ni_2P (hexagonal structure) and CoP (orthorhombic

*Chemistry and Physics of Materials Unit, Jawaharlal Nehru Centre for Advanced Research, Bangalore-560064.

structure).

8.2 Computational details

Our first-principles calculations are based on the density functional theory (DFT) as implemented in the Quantum ESPRESSO package [65]. We have used a kinetic energy cut-off of 60 Ry to truncate plane-wave basis set used in the representation of Kohn-Sham wavefunctions. The interaction between valence electrons and ionic cores has been modelled using ultrasoft pseudopotentials. Exchange-correlation energy is treated within a generalized gradient approximation. We have considered CoP (211) and Ni_2P (0001) surfaces of thickness four unit cells. We substituted one Co atom with Ni on each surface of the slab amounting to the composition of $Ni_{0.13}Co_{0.87}P$, which is close to the composition of the experimental sample of $Ni_{0.2}Co_{0.8}P$. The interaction between the periodic images of the slab is kept weak by introducing a vacuum of about 15 Å thickness separating them. We used 4×5×1, 4×5×1, and 6×6×1 meshes of k-points to sample integrations over the Brillouin zones of surfaces of CoP, Ni substituted CoP and Ni_2P respectively. We estimated the Gibbs free energy using:

$$\triangle G = \triangle E + \triangle ZPE - T \triangle S \tag{8.1}$$

Where △E is the DFT energy of binding H, OH, O and OOH to a surface obtained using H_2O and H_2 as a reference, △ZPE and △S are the changes in zero-point energy and entropy of the intermediate species. We have sourced the values of △ ZPE-T△S of H^*, OH^*, O^*, and OOH^* from references [200, 201].

8.3 Results and discussion

According to the Sabatier principle, an intermediate reactive species should not bind too weakly or too strongly to the surface of a catalyst, such that the maximum free energy differences or barriers are small, and the reaction occurs at a faster rate [155]. We used structural optimization to minimum energy of H adsorbed at various sites on the (211) surface of CoP, Ni substituted CoP, and (0001) surface of Ni_2P in the analysis of their activity towards hydrogen evolution reaction (HER). These crystallographic planes are relevant to the surfaces of catalysts investigated in experiments here. The ideal site for H adsorption is on the top of P for both CoP, and Ni substituted CoP (Fig. 8.1(a) and (b)). In contrast, H preferentially adsorbs at a hollow site forming

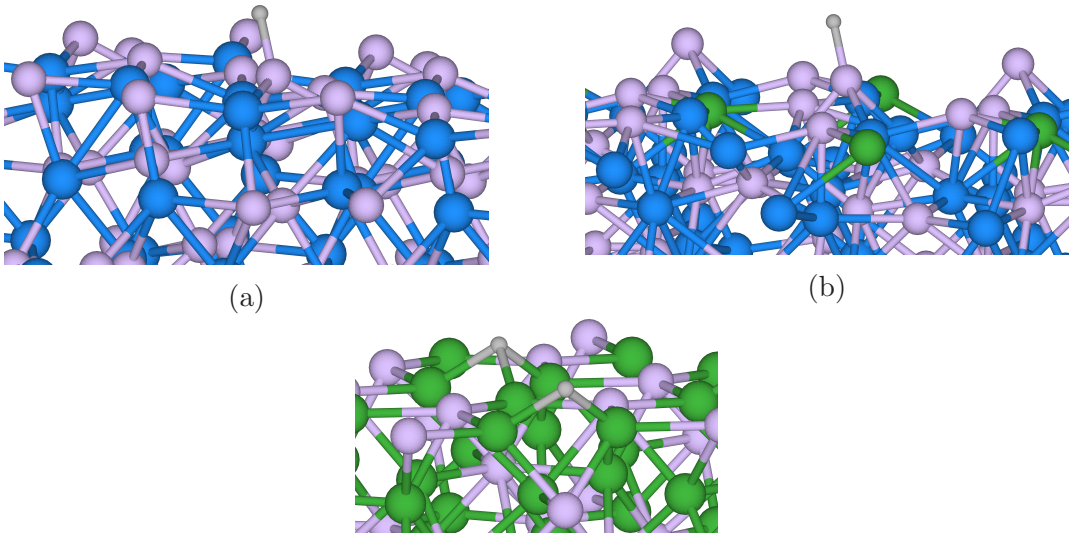

(a) (b) (c)

Figure 8.1: Stable binding configurations of H on (a) CoP, (b) Ni substituted CoP, and (c) Ni_2P surfaces. Co, Ni, P, and H atoms are represented by blue, green, pink and grey spheres respectively.

bonds with three Ni atoms of Ni_2P (Fig. 8.1(c)). From the stable configurations of H adsorption on the three surfaces considered here (shown in Fig. 8.1) and their corresponding bond lengths and binding energies (Table 8.1), it is clear that H binds with Ni substituted CoP most optimally, and its binding to Ni_2P and CoP is much stronger. From Fig. 8.2, we note that ΔG of H adsorption on Ni substituted CoP

Table 8.1: Binding energies and bond lengths of stable configuration of H on various surfaces.

Surfaces	$E_{ads.}$ (eV)	Bond lengths (Å)
CoP	-0.99	P-H: 1.44
Ni substituted CoP	-0.11	P-H: 1.43
Ni_2P	-0.53	Ni-H: 1.79, 1.80, 1.80

Table 8.2: Binding energies and bond lengths of stable configuration of OH on various surfaces.

Surfaces	$E_{ads.}$ (eV)	Bond lengths (Å)
CoP	-0.65	Co-O: 1.94, Co-O: 2.00; O-H: 0.99
Ni substituted CoP	-0.25	P-O: 1.63; O-H: 0.98
Ni_2P	-0.23	Ni-O: 2.04, 2.04, 2.04; O-H: 0.97

is close to zero, and it is most negative for H adsorption on CoP. Hence, the high catalytic activity of Ni substituted CoP is attributed to the optimal binding of H atom to its surface due to change in surface chemistry by Ni substitution as reflected in the competition between P and hollow the sites of adsorption.

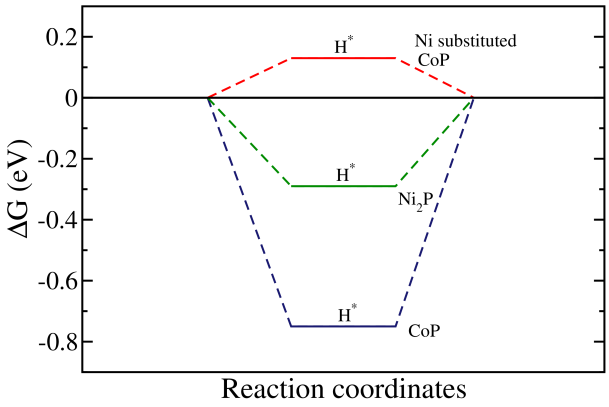

Figure 8.2: Free energy diagram of HER

To analyse the catalytic activity towards oxygen evolution reaction (OER), we simulated adsorption of OH at different sites on the surfaces of CoP, Ni substituted CoP and Ni_2P. OH binds preferentially to the Co-Co bridging site of CoP, in contrast to get adsorbed at a site on top of P atom upon Ni substitution in CoP (Figs. 8.3(a) and (b)). OH prefers to bind on the hollow site of Ni_2P (Fig. 8.3(c)). Binding energies of

OH adsorbed on CoP, Ni substituted CoP and Ni_2P are -0.65 eV, -0.25 eV and -0.23 eV respectively (Table 8.2). OH binds strongly with CoP, correlating with a weaker catalytic activity of CoP than that of Ni substituted CoP and Ni_2P (Table 8.2). The projected density of states (PDOS) of OH and surface atoms reveal a covalency in bonding between the adsorbed molecule and the surface (Fig. 8.4), associated with broadening of PDOS of OH orbitals bands upon interaction with the Ni substituted surface (see Fig. 8.4(b)).

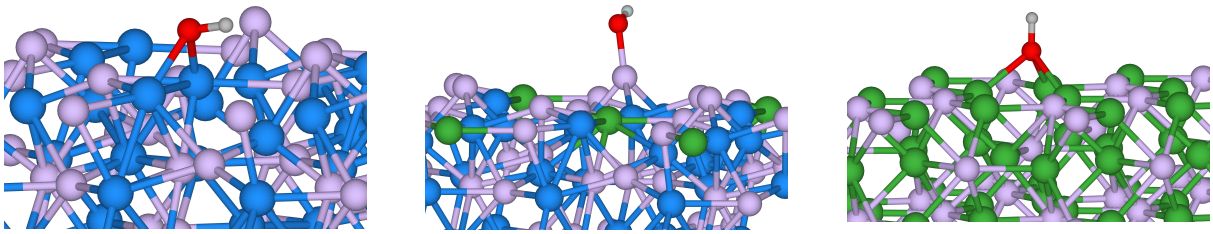

(a) (b) (c)

Figure 8.3: Stable binding geometries of OH on (a) CoP, (b) Ni substituted CoP, (c) Ni_2P surfaces. Co, Ni, P, O and H atoms are represented by blue, green, pink, red and grey spheres respectively.

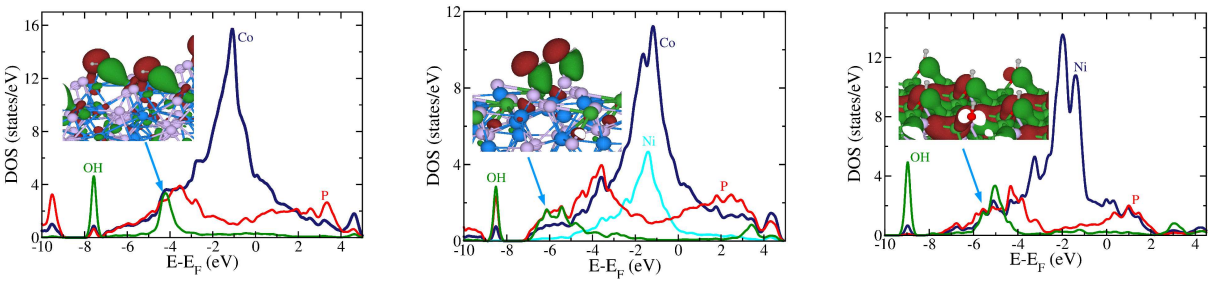

(a) (b) (c)

Figure 8.4: Projected density of states of surface atoms and OH molecule of (a) CoP, (b) Ni substituted CoP, (c) Ni_2P surfaces. Charge density associated with the states marked with arrow is shown in the inset.

Löwdin charge analysis reveals that 0.60 e^- charge is transferred from P atom to O of OH in the Ni substituted CoP. On the other hand, O is bonded to three Ni atoms, and 0.15 e^- is transferred from each Ni atom to the adsorbed O atom. Such electronic charge transfer from the surface to molecule facilitates its reduction and contributes to the observed high catalytic activity. To simulate lower coverages of OH on the surface,

we used 2×2 surface unit cells of Ni_2P, CoP and Ni substituted CoP, considering the adsorption sites found to be favorable from our analysis of adsorption at higher coverage of adsorption of OH (with 1×1 unit cells). As expected, the magnitude of binding energies reduce by 0.47 eV, 0.16 eV, and 0.17 eV respectively for CoP, Ni substituted CoP and Ni_2P surfaces at lower coverage. From the adsorption of O*,

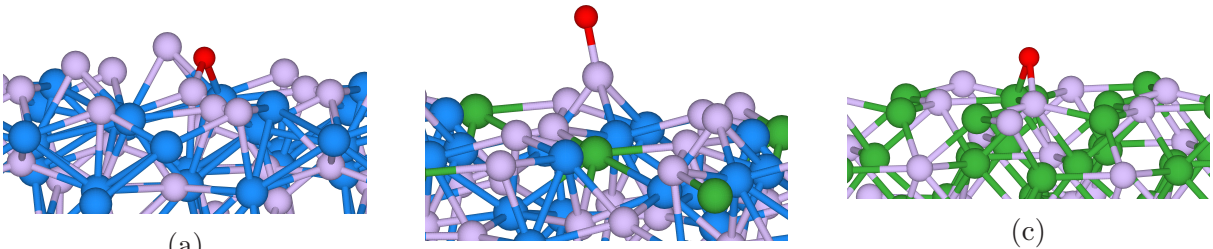

(a) (b) (c)

Figure 8.5: Stable geometry of adsorption of O on (a) CoP, (b) Ni substituted CoP, (c) Ni_2P surfaces. Co, Ni, P, and O are represented by blue, green, pink, and red spheres respectively.

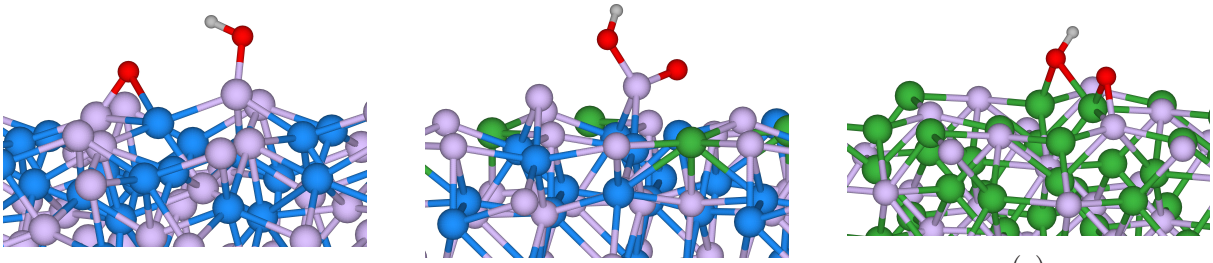

(a) (b) (c)

Figure 8.6: Favorable orientations of OOH on (a) CoP, (b) Ni substituted CoP, (c) Ni_2P surfaces. Co, Ni, P, O and H atoms are represented by blue, green, pink, red and grey spheres respectively.

OH*, and OOH* at various sites, we obtained free energy diagrams relevant to the OER mechanism (see Fig. 8.7). From the binding energies and bond lengths (Figs. 8.5 and 8.6), we note that binding of O and OOH to CoP is quite strong (ΔG is below zero) (tabulated in Table 8.3 and 8.4). CoP forms a strong and stable complex with O. Upon substitution of Ni in CoP, adsorption of O, OOH becomes weak and optimal for catalysis with our estimation of ΔG being close to zero, indicating its high catalytic activity. ΔG of adsorption of O and OOH on Ni_2P surface is weakly

Table 8.3: Adsorption energies and bond lengths of various surfaces after O adsorption.

Surfaces	$E_{ads.}$ (eV)	Bond lengths (Å)
CoP	-1.00	P-O: 1.57
Ni substituted CoP	-0.032	P-O: 1.49
Ni_2P	0.49	Ni-O: 2.12 and P-O: 1.76

Table 8.4: Binding energies and bond lengths of stable configurations after OOH adsorption on various surfaces.

Surfaces	$E_{ads.}$ (eV)	Bond lengths (Å)
CoP	-1.38	P-O: 1.56, 1.64, Co-O: 2.05, O-H: 0.98
Ni substituted CoP	-0.27	P-O: 1.63, 1.51; O-H: 0.98
Ni_2P	0.62	Ni-O: 2.00, 1.91; P-O: 1.56; O-H: 0.98

positive, consistent with its higher catalytic activity than CoP, but weaker than that of Ni substituted CoP.

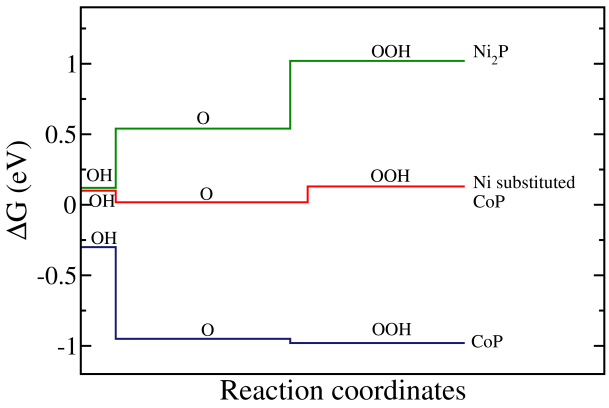

Figure 8.7: Free energy diagram of OER

Relatively weaker binding of intermediate species on the Ni substituted CoP surface than on CoP surface can be explained with the *p*-band model and *d*-band model [157]. As a result of Ni substitution in CoP, the *d*-band center of surface Co atoms shifts from -1.36 eV to -1.41 eV, and *p*-band center of P (at which all the adsorbing species get adsorbed) moves from -1.97 eV to -1.55 eV (see Fig. 8.8). This favors bonding of the adsorbing species with P atoms, with the weaker binding of adsorbing species in Ni substituted CoP. Distribution of binding energies (Fig. 8.9) of the intermediate species with Ni substituted CoP surface cover a small energy window indicating more

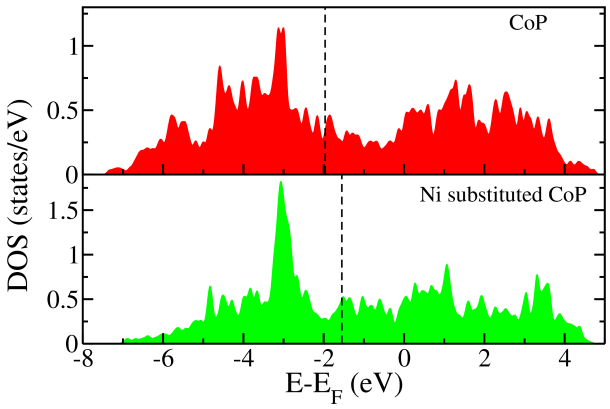

Figure 8.8: Projected density of states of P-3p, the one at which adsorbing species get adsorbed in Ni substituted surfaces. p-band center is shown by a vertical dashed line.

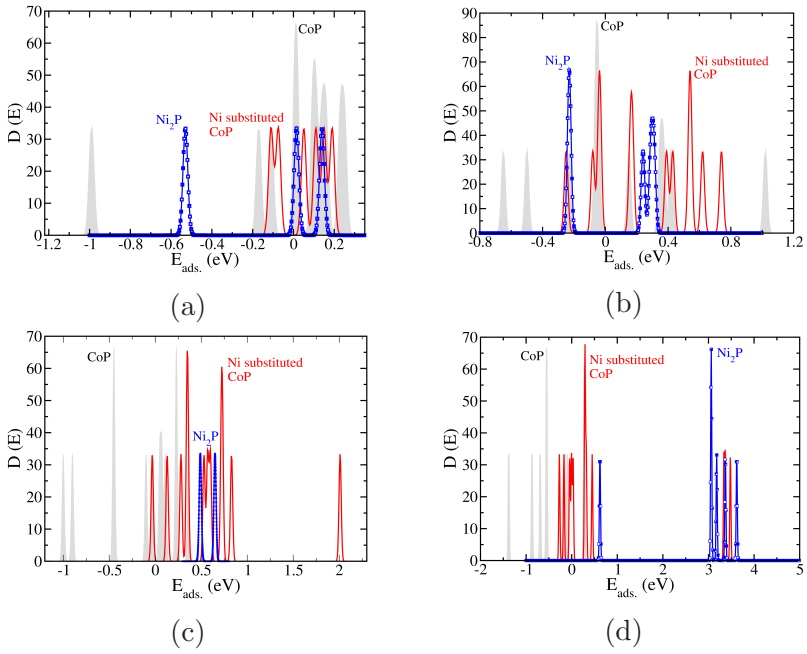

Figure 8.9: Distribution of binding energies of (a) H, (b) OH, (c) O, and (d) OOH at various sites on CoP, Ni substituted CoP and Ni_2P surfaces.

than one catalytically active sites (Fig. 8.9). In contrast, their energies of binding at various sites of CoP cover a wide energy window, indicating fewer catalytically active sites in comparison with Ni substituted CoP surface. Its electrochemical activity is superior due to the small difference in the ΔG values of the intermediate species, with a mechanism involving electronic charge transfer from the surface to adsorbing species.

8.4 Conclusions

We find that all the intermediate species of water-splitting reactions adsorbed on P atom of Ni substituted CoP. It exhibits improved electrochemical catalytic activity due to the small difference in ΔG values of intermediate species, accompanied by a charge transfer from the surface to a molecule. Also, it has more than one catalytically active site and hence is also responsible for its superior catalytic activity.

Chapter 9

High Tunability of the Work Function of (001) Surface of ReO_3 with O-vacancies *

9.1 Introduction

Transition metal oxides exhibit a rich variety of properties such as ferroelectricity, magnetism, superconductivity, and have applications ranging from a catalyst, solar cells to electronic devices. The growth of their films can be controlled well [203], and they are considered as the materials for future electronic devices that can withstand high electric fields and power [204–208]. Interfaces between two oxides are important not only in controlling the flow of charge but are also known to give rise to exotic phenomena. For example, a two-dimensional electron gas is observed at the interface between two insulating oxides [209] with different polar structure, such as $LaAlO_3$ (LAO) and $SrTiO_3$ (STO), which essentially originates from the polar discontinuity at the interface [210]. The coexistence of superconductivity and magnetism (known

*This work has been published in J. Appl. Phys. **116**, 034304 (2014) [202]. Reproduced with permission from the AIP Publishing.

to be mutually exclusive) is reported to exist at such an interface [211].

Oxygen vacancies are quite common in transition metal oxides and have a remarkable influence on their properties. For example, oxygen vacancies occurring preferentially at the surface render magnetoelectric properties to nanocrystals of $BaTiO_3$ [212]. Experimental and theoretical studies have shown that oxygen vacancies in the (001) STO substrate, trapped during the growth of LAO layers on top, are responsible for a high mobility of carriers in the 2-D electron gas forming at the interface. This can not be explained based on the polar catastrophe mechanism alone [213–215]. Oxygen vacancies tune the work function of surfaces of transition metal oxides [216], can also lead to changes in the band offsets [217] relevant to charge transfer between electrode and oxygen vacancies.

Rhenium trioxide (ReO_3) is an unusual transition metal oxide, which exhibits excellent electrical conductivity that is comparable to a good metal like Cu. It occurs in the cubic perovskite ABO_3-type structure with a missing cation at A site and rhenium (Re) atom at the B site coordinated octahedrally by oxygen (O) atoms. It is an excellent candidate as a metallic oxide to be used as an electrode in oxide electronics. ReO_3 single crystal acts as a catalyst for the metathesis reaction of olefins [218], and supported rhenium oxide acts as a catalyst for the selective oxidation of methanol [219]. Sanliang *et al.* [220] have theoretically shown that the molecular methanol adsorbed on ReO_3 surface can be easily dissociated, as seen in experiments [219]. Work function of ReO_3 surface is important to both classes of its applications: electronics and catalysis.

ReO_3 nanocrystal has been effectively used in the surface-enhanced Raman scattering (SERS) of adsorption of pyridine, pyrimidine, and pyrazine [114]. Its metallicity permits electromagnetic field enhancement and oxide chemistry gives chemical bonding with these molecules. ReO_3 is stable at fairly high temperatures at atmospheric pressure but shows pressure-induced structural phase transitions (at 3 GPa in the bulk form, and at 0.3 GPa in its nanocrystalline form) [113, 221–225]. Such a reduction

in the transition pressure in nanocrystals can arise from the surface stresses, and it is important to understand the structure and electronic properties of ReO_3 surfaces. Tsukada *et al.* [226] used discrete-variational X_α method to study clusters of ReO_3 as models of the ReO_3 (001) surface, but a detailed study of vibrational spectra, electronic and structural properties of an extended surface are necessary to understand its properties relevant to electronics, catalysis, and SERS.

In this chapter, we present a detailed analysis of the structure and electronic properties of ReO_3 (001) surface with atomically different terminations (O-terminated and ReO_2-terminated), and discuss their stability. In the nominal ionic state of Re^{6+} in ReO_3 has one electron in the *d*-orbital, hence we explore the possibility of magnetism at its surface. We obtain insight into the mechanisms of pressure-induced structural phase transitions of bulk and nanocrystals of ReO_3 through determination of phonon dispersion. We show that the work function of (001) surface of ReO_3 correlates with its surface energy, and can be tuned remarkably through the introduction of oxygen vacancies at the surface.

9.2 Computational details

Our calculations are based on density functional theory (DFT) with ultrasoft pseudopotential [119] for oxygen core and a norm-conserving pseudopotential [120] for rhenium core as implemented in Quantum ESPRESSO code [65].We model surfaces with a periodic supercell consisting of an infinite slab and vacuum separating them. We consider symmetric slabs (O-terminated and ReO_2-terminated) and an asymmetric slab (mixed O and ReO_2 terminated) terminated with (001) surfaces of ReO_3 shown in Fig. 9.1. ReO_2-terminated, O-terminated, and asymmetric surfaces consist of 6.5, 4.5, and 4 unit layers (of thickness) respectively. The exchange-correlation energy of electrons is approximated with a local-density approximated (LDA) functional as parametrized by Perdew-Zunger [154]. Kohn-Sham wave functions are expanded in

plane wave basis truncated with a kinetic energy cutoff of 30 Ry, and charge density with a cutoff of 200 Ry. We used $12 \times 12 \times 1$ uniform mesh of k-points for sampling integration of Brillouin zone (BZ) (of the surface supercells). We simulate different concentration of O-vacancies by considering the supercell $\sqrt{2} \times \sqrt{2}$ and 2×2 in the ab-plane of symmetric O-terminated slab and the corresponding k-points mesh for sampling Brillouin-zone integration are $9 \times 9 \times 1$ and $6 \times 6 \times 1$ respectively. Here, an equal number of O-vacancies at the two surfaces of the O-terminated slab have been introduced. Self-consistency in Kohn-Sham calculations is achieved self-consistently till the total energies are converged within 10^{-6} Ry/cell. Atomic positions are optimized until the magnitude of a Hellmann-Feynman force on an atom is less than 0.03 eV/Å. The optimized lattice parameter of bulk ReO_3 is 3.77 Å, in reasonable agreement with its experimental value (3.75 Å) [109]. To avoid interaction between the periodic images of slabs and surfaces, we include a vacuum of 10 Å in the supercell. We include dipole correction [227] to simulate an asymmetric slab with periodic boundary conditions. We include results for the asymmetric slab simulated with and without dipole correction, to clearly understand its significance. Since other systems studied here (ReO_2-terminated slab and O-terminated slab with and without O-vacancies) have a symmetry of horizontal plane of reflection, we do not apply dipole correction to them. For the calculation of density of states, we have used a fine mesh of $48 \times 48 \times 2$ k-points with smearing width of 0.005 Ry in the Fermi-Dirac distribution function for occupation numbers. We have computed dynamical matrices at high symmetry wave vectors (Γ, X, M) in the BZ using DFT linear response.

9.3 Structure of (001) surfaces

From the relaxed structures of the three models of slabs, it is clear that the structural relaxation is most pronounced at the surfaces, as expected. Relaxation (seen as changes in the Re-O bond lengths w.r.t. the bulk bond length) is more pronounced

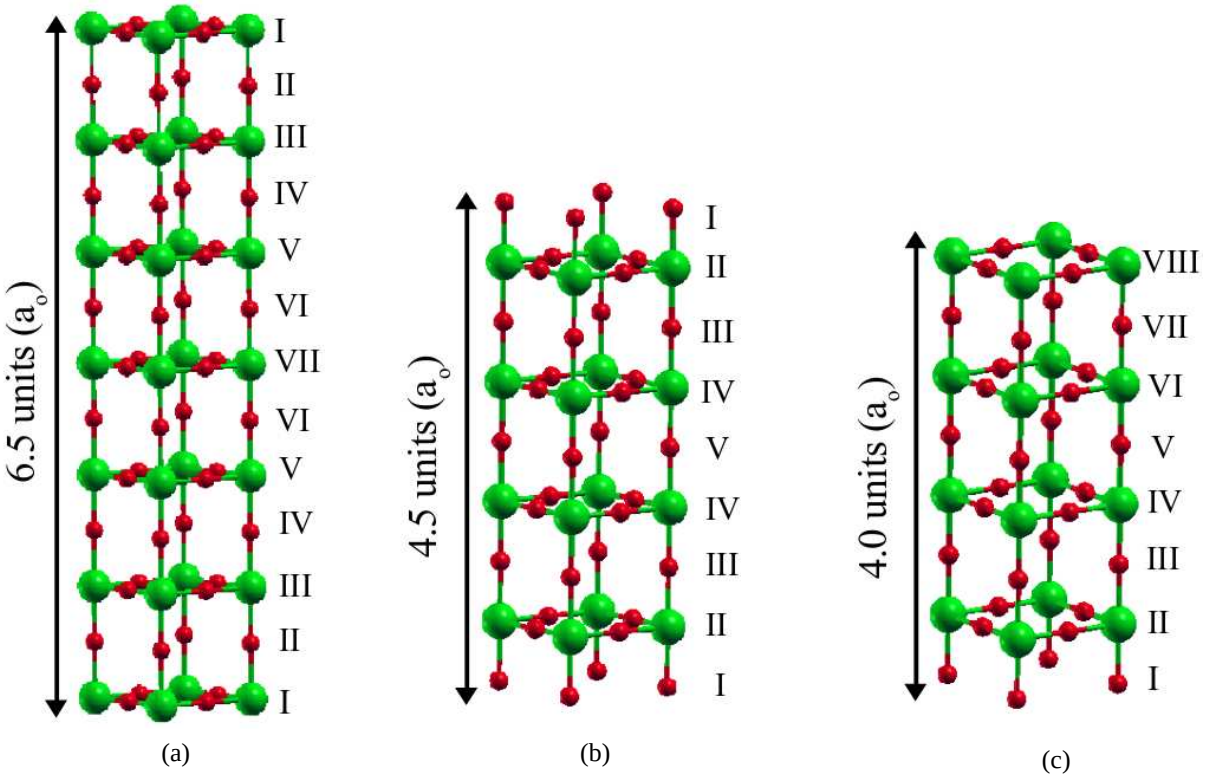

Figure 9.1: Configurations of slabs of ReO_3 with (a) ReO_2-termination, (b) O-termination, and (c) mixed O and ReO_2-termination (asymmetric). Red and green balls are oxygen and rhenium atoms respectively.

for the O-terminated surface in comparison with that near the ReO_2-terminated surface. The Re-O bond length decreases by 7.50% for the O-terminated surface, while it decreases only by 2.64% for ReO_2-terminated surface. Reduction in the Re-O bond length at the surfaces of ReO_2-terminated and O-terminated slabs is a result of movement of atoms present at the surface and in the sub-surface planes in opposite directions. The asymmetric slab shows a mixed effect, i.e. for ReO_2-terminated surface Re-O bond length contracts by 3.13% while it is 7.45% for O-terminated surface. Due to lack of reflection symmetry, it undergoes different structural changes at the two sides: both surface and sub-surface atoms move in the same direction (towards the bulk or away from the vacuum) at ReO_2-terminated surface, and the movement of atoms (at the surface and sub-surface) is opposite in direction at the O-terminated surface. We find that the dipole correction leads to significant changes in structural relaxation w.r.t. asymmetric slab simulated without dipole correction. The relaxation

of surface and the movement of atoms has been shown schematically in Fig. 9.2. We have not shown the inner atomic planes of symmetric surfaces in Fig. 9.2, as the changes there are not significant.

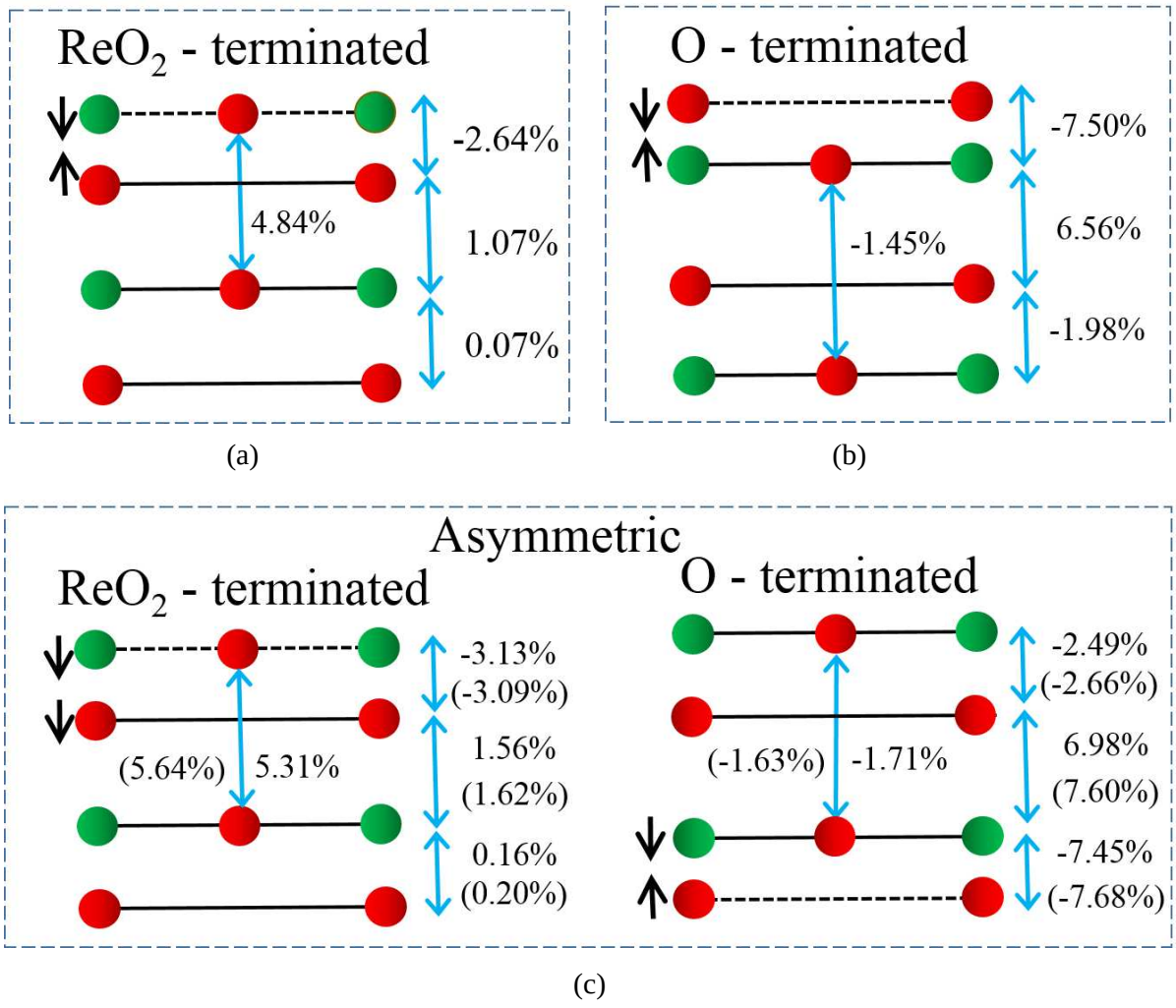

Figure 9.2: Schematic representation of changes in bond lengths and distance between atoms present along central axis in (a) ReO_2-terminated, (b) O-terminated, and (c) mixed O and ReO_2-terminated (asymmetric) surfaces. The changes in bond lengths in asymmetric slab with dipole correction has been shown in parentheses. Direction of arrows shows the movement of atoms and dashed line indicates the surface plane

Reduction in the Re-O bond length at the surface causes elongation of the bond length between the next set of atomic planes away from the surface. Similar behavior was reported for the surfaces of $CaTiO_3$, $SrTiO_3$, and $BaTiO_3$ [228–230]. At the surface atomic plane with ReO_2-termination, Re atoms move towards the bulk (into the slab) and O atoms move outwards (towards the vacuum). O atom at the surface

of O-terminated and asymmetric slabs move towards the bulk. Re-O bonds parallel to the surface undergo a weak elongation of 0.75%, 0.96% and 0.89% at the ReO_2-terminated, asymmetric surface with and without dipole correction respectively, and such changes are not significant in the sub-surface and inner atomic planes. We do not see contraction for the Re-O bonds parallel to the surface.

9.4 Surface energy (γ_s) and work function (ϕ)

The surface energy is defined as the energy required to create a new surface, by cleaving a bulk crystal or as the excess energy due to the breaking of bonds at the surface relative to the bulk. We determine the surface energies of the three slab configurations using equations 9.1, 9.2, and 9.3 for ReO_2-terminated, O-terminated, and asymmetric surfaces respectively:

$$\gamma_s = \frac{1}{2a^2}(E_{slab} - 7E_{bulk} + 0.5E_{O_2}) \tag{9.1}$$

$$\gamma_s = \frac{1}{2a^2}(E_{slab} - 4E_{bulk} - 0.5E_{O_2}) \tag{9.2}$$

$$\gamma_s = \frac{1}{2a^2}(E_{slab} - E_{bulk}) \tag{9.3}$$

where, E_{slab}, E_{bulk}, and E_{O_2} are the total energies of the slab, bulk ReO_3, and an oxygen molecule, a is the lattice constant and $\frac{1}{2}$ accounts for the two surfaces created in the slab configuration. The O-terminated surface has the lowest surface energy of 0.86 J/m^2, indicating its high stability. In contrast, the ReO_2 surface has the highest surface energy of 4.77 J/m^2, and hence is the least stable. γ_s of the asymmetric surface is energetically close to the average of those in ReO_2-terminated and O-terminated surfaces, with a surface energy of 2.50 J/m^2. With the inclusion of the dipole correction in the simulation of the asymmetric slab, our estimate of the surface energy is 2.52 J/m^2.

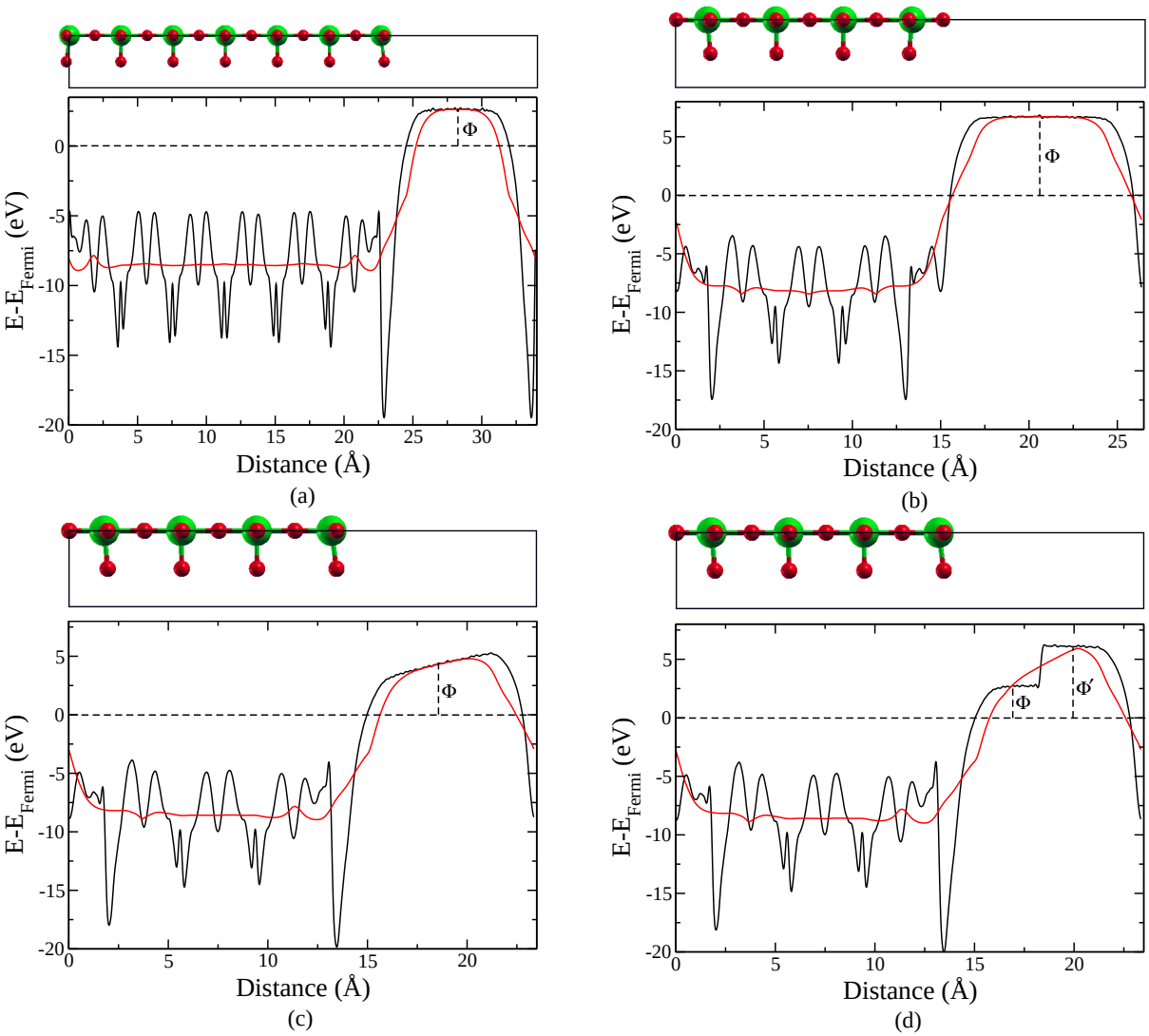

Figure 9.3: Variation in potential along the direction perpendicular to (a) ReO_2-terminated surface, (b) O-terminated surface, (c) asymmetric surface without dipole correction, and (d) with dipole correction. Red and green circles are oxygen and rhenium atoms respectively.

The work function of a material is the minimum energy required to remove an electron from the Fermi level of a metal to a point in vacuum at infinity and has been obtained using the following expression:

$$\phi = V_{vacuum} - E_{Fermi} \tag{9.4}$$

where, V_{vacuum} is the average potential in the vacuum region, and E_{Fermi} is the Fermi level. Here, the potential includes bare nuclear, Hartree and exchange-correlations potentials. From the variation in potential along the direction perpendicular to surfaces of ReO_3 (Figs. 9.3(a)-9.3(c)), estimates of the work function of ReO_2-terminated, O-terminated and asymmetric surfaces are 2.6 eV, 6.8 eV, and 4.4 eV respectively. The work functions anti-correlate with the surface energies i.e., the surface with lowest surface energy has the highest work function; the work function correlates with the stability of the surface. For a ready comparison, we have tabulated γ_s and ϕ in Table 9.1.

Table 9.1: Surface energies and work functions of ReO_3

Surfaces	Surface energy (J/m^2)	Work Function (eV)
ReO_2-terminated	4.77	2.60
O-terminated	0.86	6.80
Asymmetric (without dipole correction)	2.50	4.40
Asymmetric (with dipole correction)	2.52	2.70, 6.03

The electrostatic potential in a vacuum away from the asymmetric slab has a non-zero slope (Fig. 9.3(c)), indicating that it is polar in nature and there is an electric field of -4.52×10^9 V/m. A linear fit of the dependence of this electric field on vacuum thickness yields the following expression:

$$E_d(d_v) = \frac{1}{0.28d_v - 0.061} \tag{9.5}$$

Here, d_v is the vacuum thickness in nm and E is an electric field in V/nm. Equation

(5) shows that the electric field vanishes as the vacuum thickness becomes infinitely large. So, the slope in Fig. 9.3(c) will tend to zero as vacuum thickness approaches infinity.

As a result of dipole correction in the simulation of the asymmetric slab, the two distinct vacuum levels can be clearly seen in Fig. 9.3(d). The work functions of O and ReO_2 surfaces are 2.70 eV and 6.03 eV respectively (see Table 9.1). The average of these work functions is 4.37 eV, which is close to the work function of the asymmetric slab estimated without dipole correction.

Oxygen vacancies are commonly present in transition metal oxides, we now investigate the work function as a function of oxygen vacancies on the most stable (oxygen terminated slab) surface. We note that the ReO_2-terminated surface corresponds to 100% oxygen vacancies in the O-terminated slab. We find a significant decrease in the work function with an increase in the concentration of oxygen vacancies at the surface (see Fig. 9.4). Such decrease in the work function is due to (a) reduction in the oxidation state of Re due to oxygen, and (b) formation of electric dipoles at the surface. Indeed, oxygen vacancies have an energy cost, and hence result in an increase in the surface energy. The stability of (001) surface of ReO_3 thus reduces with oxygen vacancies, and the correlation of work function with stability of a surface is quite clear in our results (see Fig. 9.4). The work function directly influences the energy barriers at interfaces, and in the case of ReO_3, Schottky barrier at a metal-semiconductor interface can thus be tuned with oxygen vacancies. These results thus have remarkable relevance to electronics based on the 2-D electron gas forming at the interface of two insulating oxides. In particular, our work highlights drastic changes that can occur in the work function of a perovskite oxide due to oxygen vacancies and provides a mechanism to understand the sensitivity of the 2-D electron gas to growth conditions.

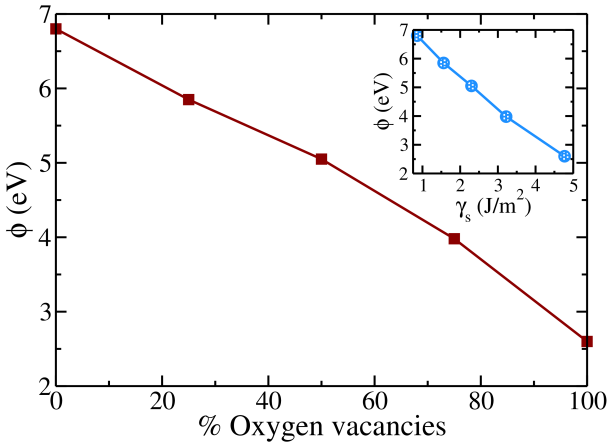

Figure 9.4: Variation of work function with different concentration of oxygen vacancies. Inset shows the trend of change in work function as a function of surface energy.

9.5 Electronic structure and Density of States

Electronic structure of bulk ReO_3 (Fig. 9.5(a)) exhibits flat bands in the lower part of the conduction band in the Γ-X region and in the valence band minima ranging along X-M segment. The most striking feature in the electronic structure of surfaces shown in Figs. 9.5(b)-9.5(d) is the presence of many flat bands, and so the wavefunctions are expected to be localized at the surface. Previous studies on the electronic structure of surfaces have reported the presence of flat bands. For e.g., the lowest conduction band of $SrTiO_3$ (100) surface is flat between Γ and X points [231]. In the case of (001) surface of cubic $BaMnO_3$, the highest energy valence band is flat between Γ and X points [232].

Partial density of states (PDOS) of bulk ReO_3 (Fig. 9.6) and the layerwise PDOS of three surfaces (Fig. 9.7) show that their valence band is mainly constituted of O-*2p* orbitals and the conduction band has a character of Re-*5d* staes. PDOS of bulk ReO_3 (Fig. 9.6) shows that the O-*2p* orbital (p_z) pointing towards the metal form σ-bond while those perpendicular to M-O-M forms π-bond. The hybridization between metal and oxygen is of bonding type in valence bands, whereas it is of anti-bonding character in the conduction band. A similar analysis for bulk ReO_3 was given by Cora [233] and Stachiotti [234]. The widths of conduction and valence bands of bulk ReO_3 are

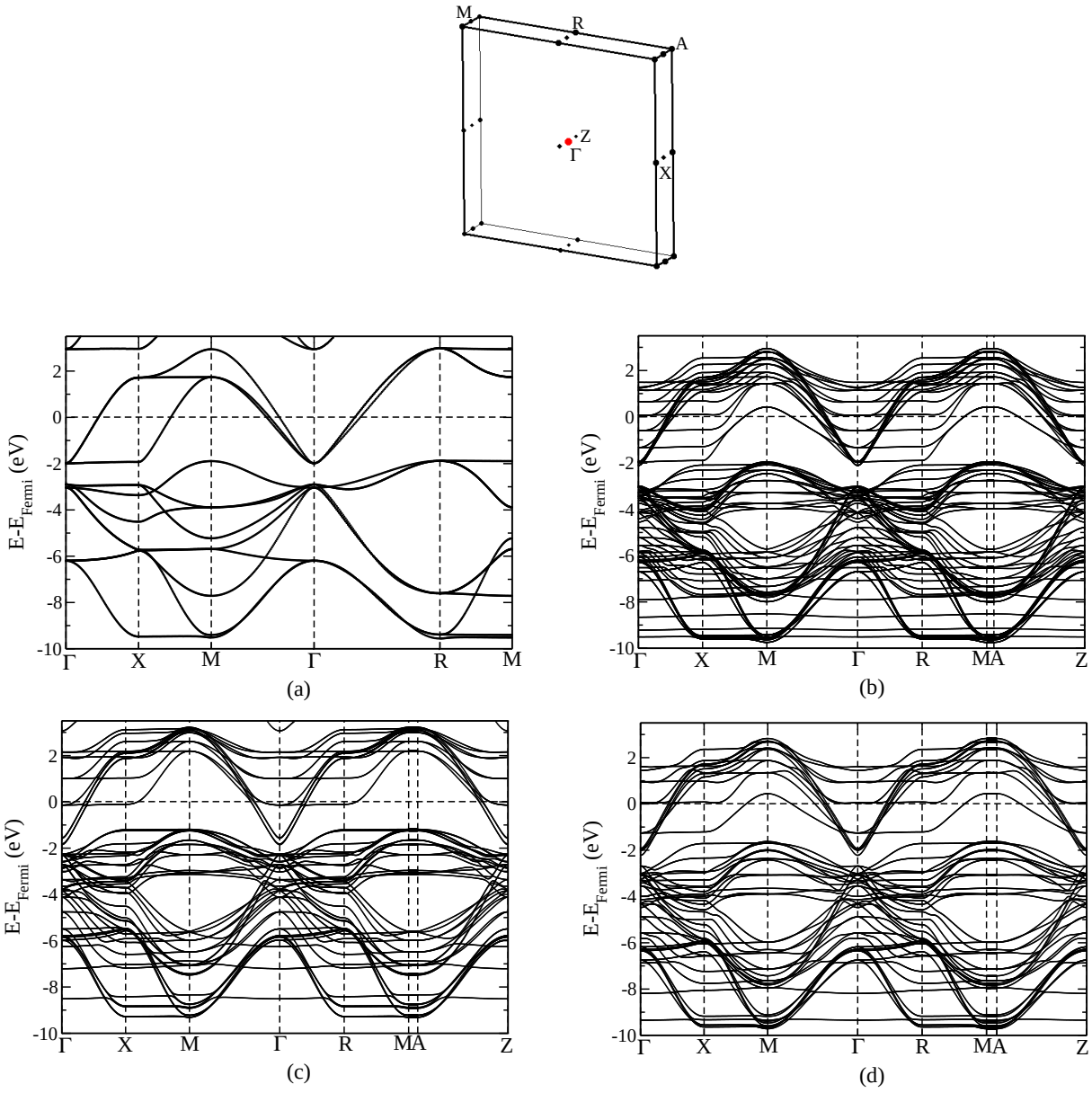

Figure 9.5: Electronic structure of (a) bulk, (b) ReO_2-terminated surface, (c) O-terminated surface, and (d) asymmetric surface. Brillouin zone of slab is given at the top.

about 4.7 eV and 8.3 eV respectively. Previously reported values for the width of conduction and valence bands are 5.0 eV and 8.4 eV respectively [233, 234]; so our results are in good agreement with their results. Due to the lowering of symmetry at the surface, O-*2p* and Re-*5d* orbitals are no longer degenerate. It is evident from Figs. 9.7(a)-9.7(c) that the PDOS peaks of p_x, p_y, and p_z orbitals of the oxygen atoms coincide with those of the PDOS peaks of Re-*5d* orbitals indicating a strong hybridization between these orbitals. This leads to the lowering of the energy of e_g orbitals relative to t_{2g}, opposite to that expected in octahedral crystal field splitting. The same is seen for bulk ReO_3 (Fig. 9.6) and has been discussed by Stachiotti *et al.* [234] and attributed to a strong hybridization.

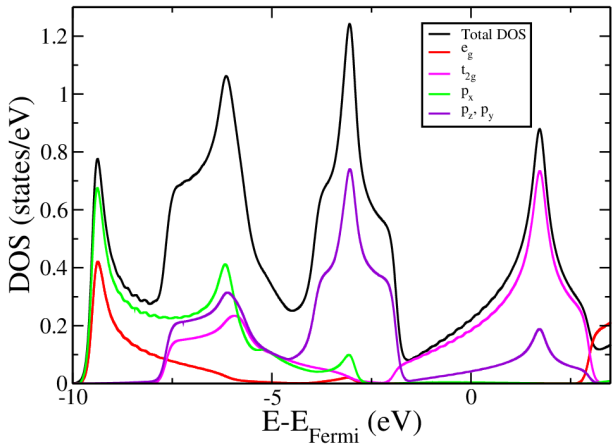

Figure 9.6: Total and projected density of states of bulk ReO_3.

The PDOS of bulk ReO_3 shows the contribution of t_{2g} orbitals at the Fermi level (Fig. 9.6). In contrast, the PDOS of surfaces (Fig. 9.7) shows that t_{2g} and d_z^2 orbitals of Re in the surface layer of ReO_2-terminated surface dominate near the Fermi level, while d_{xy} orbitals of Re in the sub-surface plane dominate the Fermi level in O-terminated surface. The asymmetric slab shows mixed properties of O-terminated and ReO_2-terminated surfaces, so the layers close to ReO_2-plane at the surface show the behavior of ReO_2-terminated surface, while those near to O-plane at surface shows the behavior of O-terminated surface. Unoccupied states comprising of e_g orbitals are at higher energy in bulk ReO_3 (Fig. 9.6), but it is found at a slightly lower energy

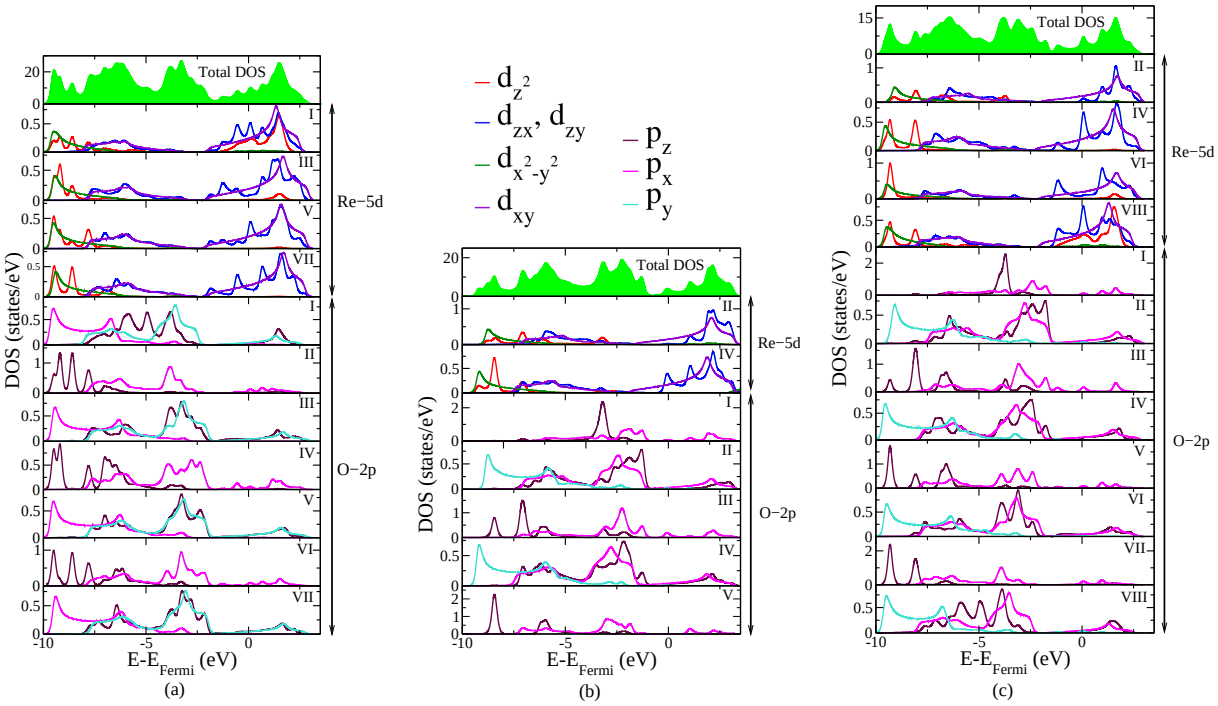

Figure 9.7: Total and projected density of states of (a) ReO_2-terminated surface, (b) O-terminated surface, and (c) asymmetric surface. Note: O-*2p* orbitals in layers II, IV, VI for figure (a), I, III, V for figure (b) and I, III, V and VII for figure (c) have degenerate p_x and p_y states.

in the surface layers (Figs. 9.7(a) and 9.7(c)). This is responsible for the energy cost of creating a surface. Removal of oxygen at the surface causes an increase in the nuclear field which leads to the lowering of energy of Re-*6s* states above Fermi level as compared to those in bulk ReO_3 and in the sub-surface atomic planes.

The contribution of Re-*5d* states to bands at the Fermi level is dominant (Figs. 9.7(a)-9.7(c)), and hence the work function of ReO_2-terminated surface is low in comparison with that of the O-terminated surface as O-*2p* states are below the Fermi level. Kanishka *et al.* [235] reported that the ReO_3 nanocrystal shows weakly paramagnetic behavior at room temperature and magnetic hysteresis at low temperatures when the size of the particle is small, noting that Re in ReO_3 has one electron in d-orbital and may show some magnetization. We explored a possible magnetization, and find that the ReO_2-terminated surface indeed exhibits weak magnetization, whereas we find no magnetization in the O-terminated surface as it lacks any Re at the surface. The

imbalance or difference in the occupancy of up-spin and down-spin in Re atoms at the surface leads to weak magnetization at the surface. The same is evident in spin density distribution, where spins are essentially localized near the Re atoms at the surface (Fig. 9.8). The asymmetric slab does not exhibit any magnetization, which is probably due to its polarity and the presence of an O-terminated surface at one of its ends. We note that the introduction of dipole correction in asymmetric slab does not alter the electronic properties.

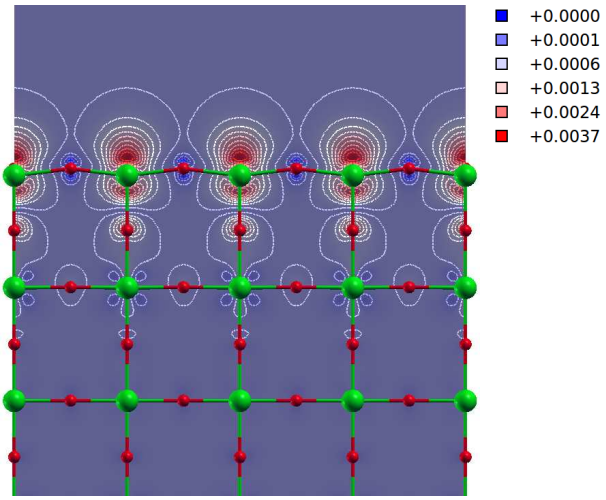

Figure 9.8: Spin density distribution of ReO_3 slab with ReO_2-termination.

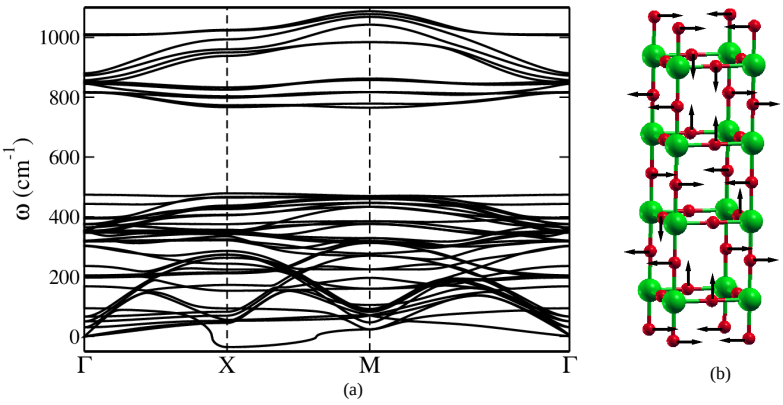

Figure 9.9: (a) Phonon dispersion along high symmetry lines of the Brillouin zone, and (b) atomic displacements associated with unstable mode at X-point of O-terminated slab.

9.6 Phonons

We now determine the effects of a surface on structural instabilities of ReO_3 and identify vibrational signatures, by obtaining phonon dispersion of the most stable slab configuration (O-terminated) (Fig. 9.9(a)). We find modes with imaginary frequencies of 36.7i cm^{-1} at (100) $\frac{\pi}{a}$ (X-point), suggesting that the structure is weakly unstable at nano-scale. The bulk ReO_3 undergoes pressure-induced phase transitions through cubic (0-3 GPa), monoclinic (3-12 GPa), VF_3-type structure (above 12 GPa) and extremely hard rhombohedral phase (above 38 GPa) [222]. Experimentally, ReO_3 nanocrystal exhibits pressure-induced phase transition from cubic I structure (*Pm3m*) at the ambient pressure to a monoclinic structure (*C2/c*) around 0.3 GPa, and it transforms to rhombohedral I structure (*R3c*) around 6.7 GPa and to rhombohedral II structure around 20.3 GPa [221]. Thus, transition pressures are lower in nanocrystals than in the bulk. The unstable mode around X-point in the phonon dispersion (Fig. 9.9(a)) of the slab are relevant to pressure-induced phase transition in nanocrystals of ReO_3. The unstable mode involves the in-plane and out-of-plane displacement of oxygen atoms present in both ReO_2 and O-planes (Fig. 9.9(b)) amounting to ReO_6 rotation; the same ReO_6 octahedral rotations are also known to be relevant to the phase transitions in the bulk ReO_3, where they correspond to M_3 phonons (at wave vector (110)$\frac{\pi}{a}$). Here, these instabilities are strengthened by the structural changes at the surface, and should cause structural transitions at lower pressure in nanocrystals of ReO_3 [221]. Such size dependence of pressure-induced phase transitions can also be understood in terms of the stress created at the surface as a result of lower coordination of O and shorter Re-O bond lengths. This mimics compressive normal stress, which offsets (lower) the transition pressures in nanocrystals as seen in the experiment [221].

9.7 Conclusions

We have considered three different slab configurations (ReO_2-terminated, O-terminated and asymmetric) in the study of (001) surfaces of ReO_3. Contraction of about 7.50% and 2.64% in Re-O bond length results at the O-terminated surface and ReO_2-terminated surface respectively. The asymmetric slab is polar in nature, and the electric field associated with it goes to zero as the vacuum thickness tends to infinity. Electronic structure of ReO_3 surfaces contains many flat bands and are associated with electronic states localized at the surface. Re-*5d* orbitals dominate the states at the Fermi level and result in a weak magnetization found at the ReO_2-terminated (001) surface. Structural instabilities involving ReO_6 rotations are further strengthened by the stresses created at the surface, and provide a possible explanation for the observed reduction in transition pressure in nanocrystals relative to bulk.

Based on the surface energies, O-terminated surface is the most stable (001) surface of ReO_3. We find that the surface with the lowest surface energy (greatest stability) has the highest work function. We have demonstrated that the work function of ReO_3 (001) surface can be tuned remarkably by controlling the concentration of oxygen vacancies at its surface. Our work highlights the relevance of oxygen vacancies to oxide heterostructures, and provide a mechanism in terms of work function to understand the sensitivity of their interfacial properties to oxygen vacancies, and hence the growth conditions such as oxygen pressure. Finally, we note that inclusion of dipole corrections permit an unambiguous determination of work functions of the two surfaces of an asymmetric slab simulated within periodic boundary conditions.

Chapter 10

Chemical Mechanism of Surface-Enhanced Raman Scattering of Pyridine Adsorbed on ReO_3 Surface: First-principles Theoretical Analysis

10.1 Introduction

ReO_3, an unusual transition metal oxide with good metallic conductivity, shows surface plasmon resonance in response to an exciting laser light. Its plasmon band maximum is in the range of 500-550 nm which is in the visible region [114]. Secondly, the absorption peak of ReO_3 nanoparticle is relatively broad, giving resonance over a broad range of wavelengths. Biswas *et al.* [114] demonstrated the SERS of pyridine (Py) when adsorbed on ReO_3 nanocrystal (using an exciting laser light of wavelength 632.8 nm) with a sizeable enhancement factor of order 10^5-10^6. Being an

oxide, ReO_3 surface is expected to interact strongly (chemically) with an adsorbate. Thus, SERS of a molecule at the surface of an oxide like ReO_3 is expected to give interesting information on the nature of chemical interaction in addition to its vibrational spectral information. For example, Biswas and Rao suggested that Py may be in a "flat-on"configuration or make a small angle with respect to the surface, based on the observed frequency shifts.

There are broadly two mechanisms responsible for SERS: one involves enhancement of electric field in the vicinity of a molecule due to excitation of a plasmon at the metallic surface (electromagnetic enhancement) [236–238], and the other involves chemical interaction such as charge transfer between the molecule and the surface [239, 240]. A combination of electromagnetic and chemical enhancements is typically responsible for most instances of SERS. While electromagnetic enhancement is often dominant, chemical enhancement is typically of the order of 10^2-10^3 [241–243]. Because of this, it is not readily possible to isolate and estimate the contribution of the chemical mechanism to SERS, and theoretical analysis is expected to be effective in obtaining insights.

While first-principles calculations have been quite useful in studies of adsorbate molecule-surface interaction, not many works have attempted to connect it to the SERS. In this chapter, we investigate Py-ReO_3 interaction within first-principles density functional theory, and focus on uncovering the chemical mechanisms that contribute to the SERS shown of Py at ReO_3 surface. We show that Py adsorbs by forming bonds with atoms at the surface, and consequent elongation of C-N bond of Py results in softening (red shifts) of some of its phonon modes, while the same leads to blue shifts in the ring stretching and asymmetric ring breathing modes.

10.2 Computational Details

Our first-principles calculations are based on density functional theory (DFT) as implemented in the Quantum ESPRESSO package [65]. We have treated exchange-correlation energy of electrons within (i) a local density approximation (LDA) with a functional form parameterized by Perdew and Zunger [154] and (ii) generalized gradient approximation (GGA) with functional of Perdew and Wang [244]. We employ periodic boundary conditions with supercell containing 3×3×5 units of ReO_3 and include a vacuum of 15 Å, in the direction perpendicular to ReO_3 slab (along z-direction) to keep interactions between the periodic images low. We have used a kinetic energy cutoff of 30 Ry to truncate the plane-wave basis sets. We use a uniform mesh of 4×4×1 k-points in sampling integrations over its Brillouin Zone, and smear occupation numbers of electronic states using Fermi-Dirac distribution with smearing width (k_BT) of 0.014 eV. We relax the structure to minimum energy until the magnitude of Hellmann-Feynman force on each atom is less than 0.03 eV/Å, in magnitude. Our simulations of adsorption of Py on ReO_3 include van der Waals (vdW) interaction within the Grimme scheme [245], and we also present results of simulations without including vdW for comparison. We have used density functional perturbation theory to obtain phonon spectra of Py in an isolated (free) form, and in the structure, it takes in the adsorbed configuration to estimate the effects of its adsorptive interaction with ReO_3 surface.

10.3 Results

10.3.1 Pyridine-ReO_3 interaction

We consider various modes of adsorption simulated with different initial configurations of Py on ReO_3 surface (with O and ReO_2 terminations) used in structural relaxation, and find the corresponding minimum energy, stable structural state of adsorption of

Py on ReO_3 surface (see Fig. 10.1). We estimate the strength of interaction between Py molecule and ReO_3 surface with adsorption energy (E_A):

$$E_A = E_{ReO_3-Py} - E_{ReO_3} - E_{Py}, \tag{10.1}$$

where; E_{ReO_3-Py}, E_{ReO_3}, and E_{Py} are the total energies of the ReO_3-Py adsorbed complex, ReO_3 slab and free Py molecule respectively.

10.3.2 Possibility of dissociative adsorption

Py dissociates through its interaction with an O-terminated ReO_3 surface when it is initially aligned horizontally at a *rather short* distance of approximately 1.00 Å from the surface (see Fig. 10.1(a)). During this process, one of the surface O atoms etches out, and Py binds quite strongly to the surface with the binding energy of -4.63 eV obtained using LDA. In contrast, it relaxes and gets aligned parallel to the surface at a distance of 2.2 Å (slightly tilted) when Py is kept at a farther distance of 1.26 Å from the surface however. In this configuration, Py has a weak interaction with the O-terminated surface, and its binding energy is -0.51 eV (Table 10.1). We determined the energy barrier associated with dissociation of Py by considering configurations along the path joining the dissociated and undissociated Py states (in the latter optimized structure of the physiosorbed state). These configurations defining the transition path were constructed using the following relation:

$$\vec{d}^{\mu}_{\alpha} = \vec{d}^{\mu}_{i} + (\alpha - 1)\frac{\vec{d}^{\mu}_{f} - \vec{d}^{\mu}_{i}}{6} \tag{10.2}$$

where μ is any atom, α is an integer ranging from 1 to 7 that discretizes (parametrizes) the transition path, i (α=1) and f (α=7) being the initial and final states respectively.

From the energy along this path (Fig. 10.2), it is clear that Py needs to cross an energy

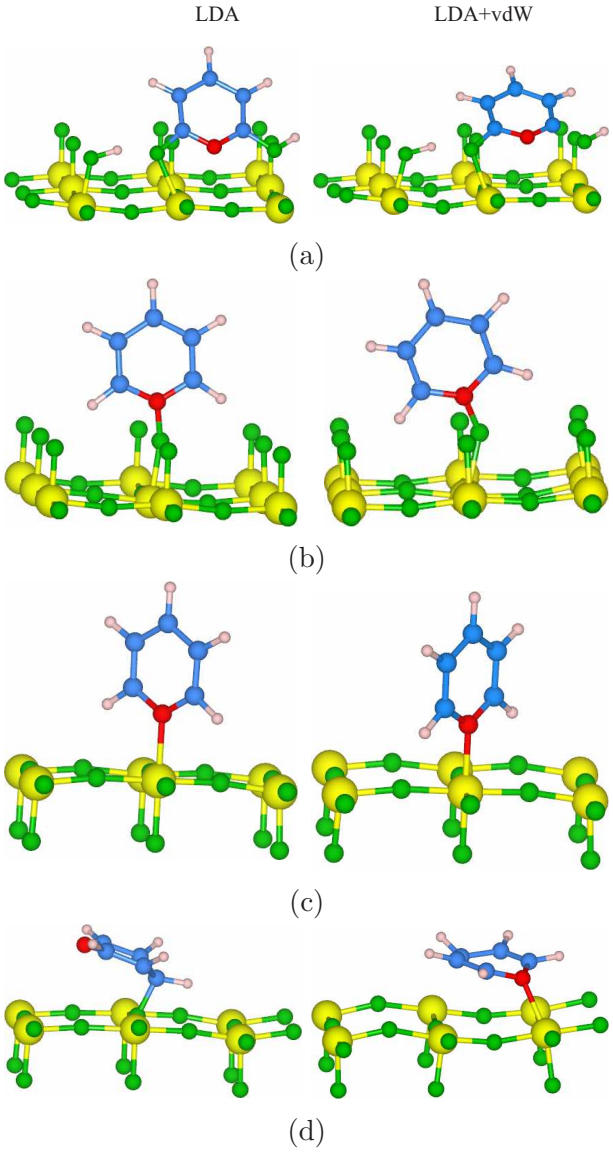

Figure 10.1: Structures of Py-ReO_3 adsorption complex simulated with DFT-LDA (left) and DFT-LDA with vdW interaction (right) (a) dissociated Py when kept parallel to O-terminated surface at 1 Å in the initial configuration. Vertically oriented Py bonded to the surface O atom on (b) O-terminated and Re atoms through N on (c) ReO_2-terminated surface and (d) the structure of Py when kept parallel to the ReO_2-terminated surface at a distance of 1 Å in an initial configuration.

barrier (E_b) of 0.1 eV before dissociation. Under normal temperature and pressure (NTP) conditions, the average velocity of water molecules is 590 m/s. Renormalizing this with the molecular weight of Py, we find that the kinetic energy of the Py molecule in a liquid state is about 0.03 eV. Thus, it is with a low probability that Py may dissociate because the average thermal kinetic energy of Py is too small to cross the

barrier and get too close to the ReO_3 surface needed for its dissociation.

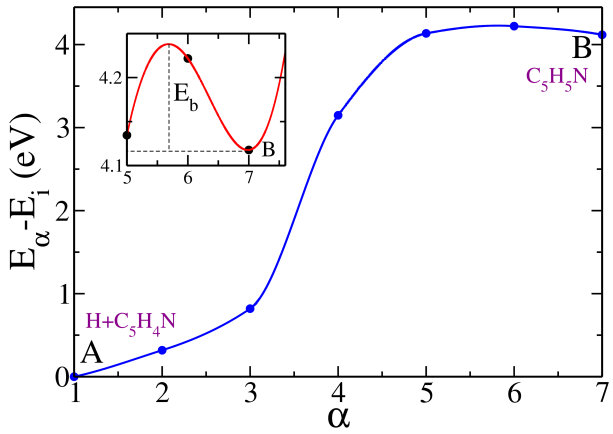

Figure 10.2: Energy of Py-ReO_3 complex along a path connecting dissociatively chemisorbed state (A) with physisorbed states (B), with barrier height shown in the inset. α is an integer ranging from 1 to 7 that determines the transition path from initial to final state.

We find that Py dissociation occurs only when it adsorbs on an O-terminated surface and not on a ReO_2-terminated surface in any of the configurations we considered. This is probably because of the low coordination number of surface O atoms and matching of Py size with O-sublattice. As a result, surface bonds on O-terminated surface undergo large relaxation and reconstruct themselves easily. In contrast, an atom on ReO_2-terminated surface has a high coordination number and its oxygen is saturated, and hence it is chemically less active and is unlikely to break the molecular bonds of Py through a strong adsorptive bonding interaction.

10.3.3 Non-dissociative adsorption

We now present an analysis of different configurations of Py on ReO_3 surfaces, in which it maintains a relatively longer distance from the surface and does not dissociate. In its adsorption on an O-terminated surface, the most stable configuration is the one in which Py remains in a vertical orientation, with its N atom bonded to O atom at the surface (Fig. 10.1(b)). The N-O bond length is 1.31 Å and Re-O bond at the surface stretches by 6.2 % upon the formation of a bond with Py. On ReO_2-terminated surface

too, Py remains vertical after adsorption with N binding to Re atom at the surface (Fig. 10.1(c)), with a Re-N bond length of 2.05 Å. As a result of this interaction, Re atom raises above the surface by 0.15 Å leading to relatively weaker elongation of Re-O bond length by 2.9 %. This is consistent withi the stronger binding of Py with ReO_2-terminated surface than the O-terminated surface as reflected in energetics (Table 10.1).

Table 10.1: Binding energies of Py adsorbed on ReO_3 (001) surfaces in horizontal and vertical alignments obtained using LDA, LDA-vdW and GGA-vdW.

Surfaces	Alignments	Binding energies (eV)		
		LDA	LDA-vdW	GGA-vdW
O-terminated/Py	Horizontal (Py dissociates)	-4.63	-5.67	-
	Horizontal	-0.51	-1.21	-0.60
	Vertical	-1.95	-2.79	-1.99
ReO_2-terminated/Py	Horizontal (Py dissociates)	-0.22	-2.91	-
	Horizontal	-1.59	-2.91	-2.21
	Vertical	-2.24	-2.96	-2.28

10.3.4 Effect of van der Waal interaction on adsorption energies

We now quantify the effect of vdW interaction on the structure and energies of adsorption complexes. Since vdW forces are attractive in nature, their inclusion enhances the strength of bonding. For the Py aligned *parallel* to ReO_2-terminated surface at a distance of 1 Å in the initial configuration, the inclusion of vdW involves the qualitative changes in the geometrical structure. Py binds to the surface through the C-O bond of length 1.48 Å in a simulation not including vdW interaction, and after its inclusion it binds through the Re-N bond of length 2.13 Å (see Fig. 10.1(d)). As a result of which the adsorption energy significantly increases from -0.22 to -2.91 eV. We will discuss the effect of vdW on the structures in which Py is vertically aligned to the surface as it is the stable binding geometry.

For the *vertically* aligned Py, we find that the inclusion of vdW interaction leads to small changes in bond lengths. Re-N bond on ReO_2-terminated surface contracts by 0.01 Å due to vdW interaction. Due to this, Re rises above the surface by 0.07 Å along z-direction giving rise to the elongation of Re-O bond by 1.52 %. The adsorption energy increases in magnitude from -2.24 eV to -2.96 eV. On the O-terminated surface, the vdW interaction causes elongation of N-O bond from 1.31 Å to 1.32 Å and Py tilts a bit towards the surface (Fig. 10.1(b)). The interaction between Py and surface leads to elongation of Re-O bond by 7.62 %. We notice that the vdW interaction causes an increase in adsorption energy from -1.95 eV to -2.70 eV (Table 10.1). We estimate the van der Waal contribution to adsorption energy (E_A^v) using:

$$E_A^v = E_{ReO_3-Py}^v - E_{ReO_3}^v - E_{Py}^v \tag{10.3}$$

where $E_{ReO_3-Py}^v$, $E_{ReO_3}^v$ and E_{Py}^v are the energies due to dispersion correction (vdW contributions) of the ReO_3-Py complex, ReO_3 slab, and isolated Py molecule respectively. We notice that the vdW contribution to the adsorption of Py on the ReO_2-terminated surface is larger than that on the O-terminated surface. Since a large contact area leads to stronger vdW interaction, Py aligns parallel to the surface experiencing more vdW forces compared to other configurations.

GGA proved to be more accurate in determining the binding energy of molecules over LDA. In this part, we compare our results obtained using LDA–vdW with GGA–vdW. Py aligned vertically on O-terminated surface forming N-O bond of length 1.36 Å is the most stable configuration of all (see Fig. 10.3(b) and Table 10.1). The effect of GGA-vdW is more noticeable when Py is aligned parallel to the surface. Py gets adsorbed at a larger distance of 1.5 Å from the surface than 0.73 Å(in LDA). For this configuration, the binding energy is -0.60 eV compared to -1.21 eV obtained using LDA-vdW. In case of Py adsorption on ReO_2-terminated surface the stable geometry is the one in which surface Re atom forms a Re-N bond of length 2.07 Å (Fig. 10.3(d))

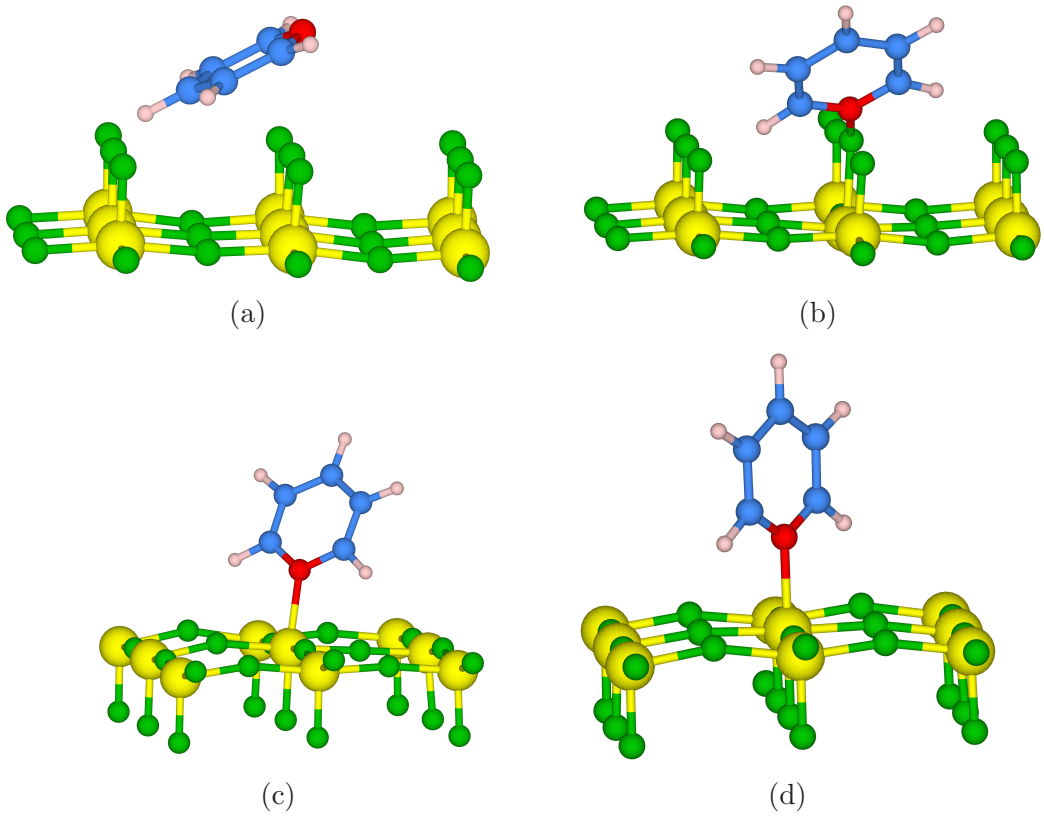

Figure 10.3: Pyridine aligned horizontally and vertically on (a), (b) O-terminated surface and (c), (d) on ReO_2-terminated surface. These structures are simulated with GGA-vdW.

and corresponding binding energy is -2.28 eV. We notice that the GGA-vdW predicts weaker binding of Py to ReO_3 surfaces than LDA-vdW. Also, Py tilts more towards the surface in simulation based on GGA-vdW calculations.

10.3.5 Effect of O-vacancies on the binding geometry of Py

O-vacancies are the most common defect found in metal oxides. We introduce O-vacancies by removing one O atom from both ReO_2 and O-terminated surface. We have considered two initial configurations: one in which Py is aligned horizontally placed above the defect on the surface and the second in which Py is aligned vertically over the surface defect. The vertically aligned Py is the most stable configuration, in this Py forms a Re-N bond of length 2.20 Å obtained using LDA-vdW on O-terminated surface (Fig. 10.4(a)). The binding energy of this configuration is -3.37

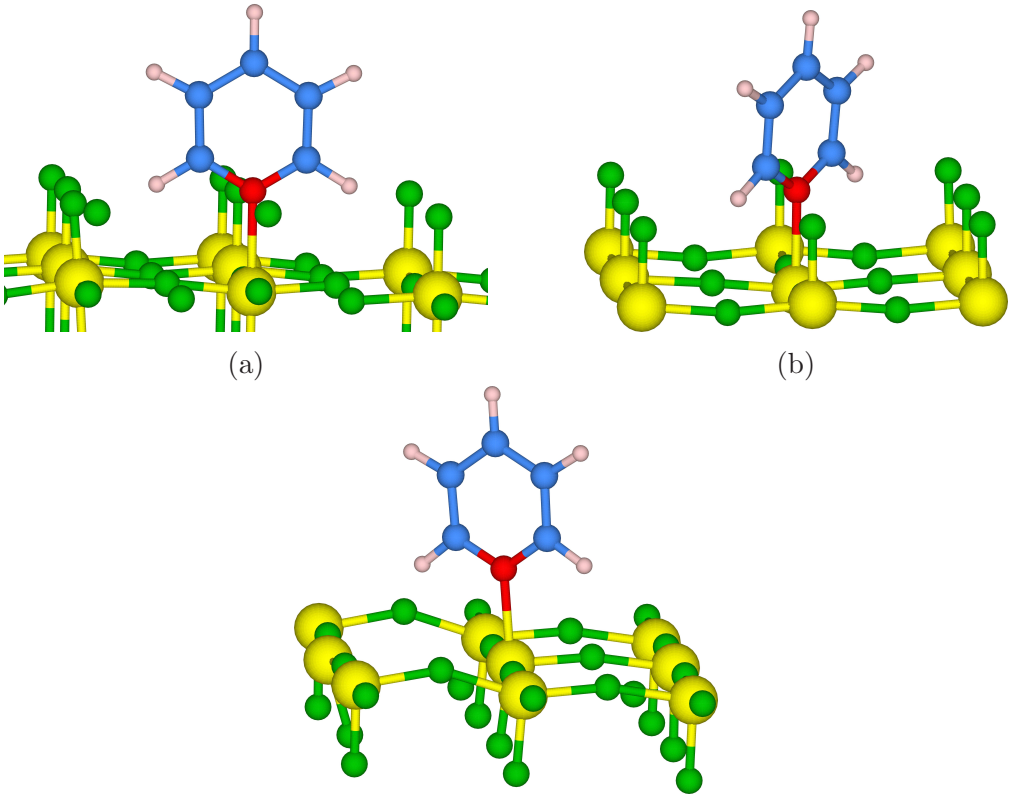

Figure 10.4: Stable binding geometries of Py adsorbed on O-terminated surface with O-vacancies simulated with (a) LDA-vdW and (b) GGA-vdW. (c) Lowest energy configuration of Py on ReO_2-terminated surface with O-vacancies simulated with GGA-vdW.

eV. Using GGA-vdW, we find vertically aligned Py placed above the defect to be the most stable configuration on the O-terminated surface (Fig. 10.4(b)). In this configuration, N of Py forms a bond with Re atom of length 2.20 Å with the binding energy of -2.60 eV (Table 10.2). Re atom forming Re-N bond of length 2.11 Å with the binding energy of -1.93 eV is the most stable configuration of Py on ReO_2-terminated surface. As a result of the defect on O-terminated surface, Py binds quite strongly. Whereas, defects on ReO_2-terminated surface weakens the interaction between Py and surface. Both GGA-vdW and LDA-vdW predict the vertically aligned Py with strong chemical interaction between the molecule and surface to be the most stable configuration.

Table 10.2: Binding energies of Py on O-terminated surface with O-vacancies.

Alignments	Binding energies (eV)	
	LDA-vdW	GGA-vdW
Horizontal	-2.23	-1.09
Vertical	-3.37	-2.60

10.4 Phonons

Raman spectra obtained experimentally [114] show that the ring stretching mode of Py at 1582 cm^{-1} (ν_{8a}) shifts to a higher frequency of 1628 cm^{-1}after adsorption on ReO_3. The greater red shifts from 1068 cm^{-1} to 1027 cm^{-1} and 991 cm^{-1} (ν_1, A_1) to 962 cm^{-1} of the Raman modes are observed in ν_{18a}, A_1 (nomenclature adopted for this modes in papers like [114,246,247]) and symmetric ring breathing modes respectively. We obtained phonons of Py before and after adsorption (vertically aligned), and our results confirm qualitatively the trends seen in the experiment (Fig. 10.5(a) and (c)). Our estimates represent a red shift in frequency for symmetric ring breathing, (ν_1) from 986 cm^{-1} to 976 cm^{-1} and 971 cm^{-1} on O-terminated and ReO_2-terminated surfaces respectively. The ring stretching mode (ν_{8a}) blue shifts from 1591 cm^{-1} to 1604 cm^{-1} and 1600 cm^{-1} upon adsorption on O-terminated (Fig. 10.5(a)) and ReO_2-terminated surfaces respectively (Fig. 10.5(c)). The shifts in the frequencies are smaller than the observed values, and this difference between theory and experiment is probably because we have removed (decoupled) the ReO_3 slab from the calculation of vibrational modes of the adsorbed complex, and seem to lower shifts in mode frequencies with origin the change in molecular structure. The exception to this is the C-H in-plane deformation mode (ν_{9a}, A_1), for which the observed frequency shift is from 1217 cm^{-1} to 1204 cm^{-1}, while our estimates of its shift are from 1199 cm^{-1} to 1167 cm^{-1} and 1174 cm^{-1} due to adsorption on O and ReO_2-terminated surfaces respectively. For Py aligned vertically above the defect on O-terminated surface, we noticed an almost the same shift in frequencies after adsorption. The introduction of defects on the O-terminated surface do not change $\Delta\omega$ significantly (Fig. 10.5(b)).

Similarly, using GGA-vdW we obtained the phonon of Py (vertically aligned) before and after adsorption. The shift in frequencies of Py as a result of adsorption on O-terminated surface agrees qualitatively well with the experimentally observed results (Fig. 10.5(a)). The shift in the frequencies is quite small. We notice that there is no change in the frequency of asymmetric ring breathing mode (591 cm^{-1}) after Py adsorption on ReO_2-terminated surface (Fig. 10.5(c)). In a configuration with Py aligned vertically on the O-terminated surface and placed directly above the defect, there is no shift in frequencies for trigonal ring breathing mode (1030 cm^{-1}).

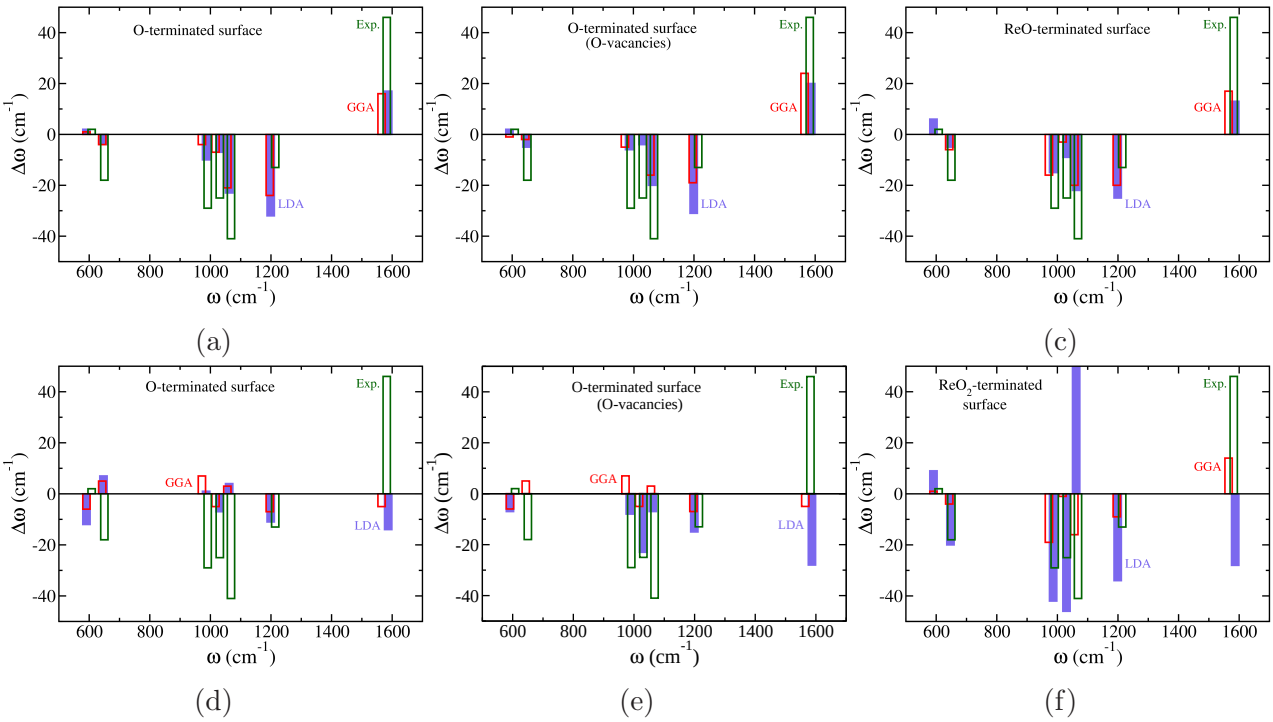

Figure 10.5: Frequencies of phonon modes obtained theoretically and Raman spectral positions obtained experimentally of Py before and after adsorption; positive and negative values of $\Delta\omega$ imply red and blue shifts respectively. Exp., LDA and GGA respectively shows the frequency shift observed experimentally and calculated theoretically using GGA and LDA. The shift in frequency of vertically and horizontally aligned Py on ReO_3 surfaces is shown in the top and bottom panels respectively.

For the horizontally aligned Py over O-terminated surface, we find the softening of C-H in-plane deformation mode and trigonal ring breathing mode using LDA-vdW (Fig. 10.5(d)). The frequency of C-H in-plane deformation mode shifts from 1199 cm^{-1} to 1188 cm^{-1}. and the trigonal ring breathing mode undergoes red shift from

1030 cm^{-1} to 1012 cm^{-1} (Fig. 10.5(d)). The shift of frequencies in the other frequency modes is opposite to that observed experimentally (Fig. 10.5(d)). We get the same trend in frequency shift for this configuration using GGA-vdW (Fig. 10.5(d)). In the configuration with Py aligned over the defect, we notice a red shift in all the modes (Fig. 10.5(e)) using LDA-vdW. GGA-vdW captures the experimental trend of frequency shift for C-H in-plane deformation and trigonal ring breathing modes only in case of Py place horizontally directly above the defect (Fig. 10.5(e)).

In the case of Py adsorption on ReO_2-terminated surface, LDA-vdW predicts the blue shift for ν_{18a,A_1} and red shift for the ring-stretching mode (Fig. 10.5(f)) which is opposite to experimentally observed trend. GGA-vdW captures the experimental trend of the frequency shift (Fig. 10.5(f)) but in this case Py forms a bond with the surface Re atom. We find that the configuration in which Py form a bond with surface atom shows a shift in frequencies as observed experimentally. This further confirms that Py is vertically aligned (slightly tilted towards the surface) forming a bond with ReO_3 surface.

We find that GGA-vdW fails to capture the shift in frequencies for some of the modes adsorbed on ReO_3 surfaces. LDA-vdW captures the frequency shift observed in experiments well. So, we have performed further analysis using LDA-vdW.

10.4.1 Structural and electronic changes during adsorption

Though the dissociated Py on O-terminated surface effectively involves a strong binding between Py and surface, its dissociation is not likely to occur practically, as it has to cross an energy barrier. In the rest of the work here, we have considered the configuration in which N atom of Py bonds to O atom of the O-terminated surface of ReO_3 (Fig. 10.1(b)). In Py adsorption on ReO_2-terminated surface, the configuration with Re atom bonded to N atom of Py (Fig. 10.1(c)) is the most stable configuration and used in the further analysis here.

Table 10.3: Optimized bond distances (in Å) of Py in the gaseous and adsorbed states.

Bonds	Py (gaseous phase)	Py on O-terminated surface	Py on ReO_2-terminated surface
C_2-N	1.33	1.35	1.35
C_2-C_3	1.39	1.37	1.38
C_3-C_4	1.39	1.39	1.39
C_4-C_5	1.39	1.39	1.39
C_5-C_6	1.39	1.38	1.38
C_6-N	1.33	1.34	1.35

From the comparison of optimized bond lengths of Py molecule in the gaseous phase and in the adsorbed state (see Table 10.3), it is clear that there is an increase in C_2-N and C_6-N bond lengths, while parallel C-C bonds of Py decreases after adsorption. This is because of the donation of lone pair electrons of N atom of Py to the ReO_3 surface. We determined the Löwdin charges and estimated the electronic charge transfer δq from Py molecule to the surface using:

$$\delta q = q^{Py}_{ReO_3-Py} - q^{Py}_{frozen} \tag{10.4}$$

where $q^{Py}_{ReO_3-Py}$ is the total electronic charge on Py in ReO_3-Py system and q^{Py}_{frozen} is the total charge on Py in the structural state of adsorption. δq is -0.83 e and -0.15 e for O-terminated and ReO_2-terminated surfaces respectively, which means that a small electronic charge gets transferred from Py molecule to the surface. Detailed analysis of ionic charges shows that the charge is mostly transferred from N atom of Py. In Py adsorption on ReO_2-terminated surface, most of the transferred charge is from the *s* orbital of N. In the adsorption on O-terminated surface on the other hand, we find that bond angle C_2-N-C_6 changes from 117.60° to 123.50°, suggesting a greater shift of the lone pair electrons of N towards oxygen and a weaker electronic repulsive force on Py, and hence increase in the bond angle. We have estimated the

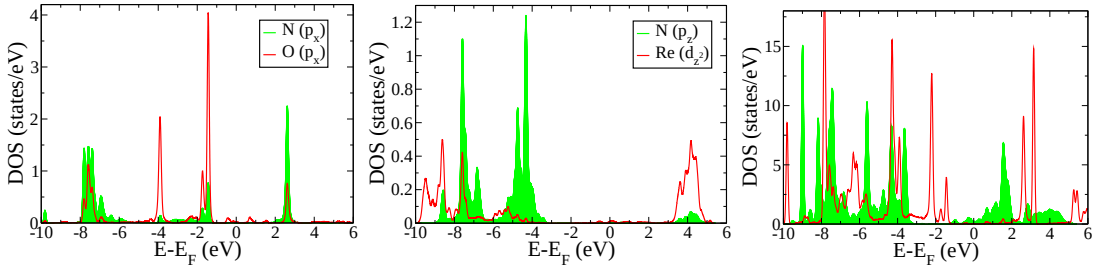

(a) (b) (c)

Figure 10.6: (a) Density of states of N of Py and O atom of O-terminated surface to which N is attached, (b) density of states of N of Py and Re atoms of ReO_2-terminated surface to which N is attached and (c) density of states Py adsorbed on ReO_2-terminated surface (shown in shaded green color) and O-terminated surface (in solid red line).

work function of surfaces using the following relation:

$$\phi = V_{vacuum} - E_{Fermi} \tag{10.5}$$

Where V_{vacuum} is the average potential in the vacuum region and E_{Fermi} is the Fermi level. As a result of the adsorption of Py on O-terminated surface, we estimate a decrease in the work function of ReO_3 surface from 7.8 eV to 6.6 eV. In contrast, there is a relatively smaller change in the work function from 3.8 eV to 3.5 eV of ReO_2-terminated surface upon adsorption. This is consistent with larger Löwdin charge transfer involved in Py adsorption on O-terminated than in ReO_2-terminated surfaces. The transfer of electrons from N to O atom makes the N-O bond polar, resulting in reduced work function of the O-terminated surface. The C_2-N-C_6 bond angle is increased by 2° after adsorption on ReO_2-terminated surface.

From the projected density of states (PDOS) (Fig. 10.6(a)), we note that $2p_x$ orbitals of N in Py form weakly covalent bonds with $2p_x$ states of O atom in the O-terminated surface. Formation of a bond between d_z^2 orbital of Re and p_z orbital of N on ReO_2-terminated surface is clearly seen in Fig. 10.6(b). As a result of the interaction between Py molecule and the surface, broadening of the peaks of molecular electronic states of Py is also evident in PDOS, though they still preserve their strong molecular character (Fig. 10.6(c)). Broadening of peaks in the PDOS of Py on ReO_2-terminated

surface is more pronounced than that of Py on O-terminated surface. This is an indication of stronger covalent bond formation between Py and ReO_2-terminated, consistent with the corresponding binding energy. Due to adsorptive interaction, HOMO of Py shifts to higher energy leading to a reduction in the effective band gap of Py in the structural form of the adsorbed state (shown in Table 10.4), confirming that the chemical interaction between Py and ReO_3 is indeed significant. The larger change in the HOMO-LUMO gap of Py during adsorption on O-terminated surface than that on ReO_2-terminated surface correlates with the greater charge transfer accompanying it.

Table 10.4: The gap between HOMO-LUMO energies Δ, of pyridine in the gaseous phase and adsorbed states. The reduction in gap upon adsorption is central to the chemical mechanism of SERS.

Systems	Δ (eV)
Py (isolated)	3.93
$Py^{frozen}_{O-terminated}$	3.56
$Py^{frozen}_{ReO_2-terminated}$	3.74

We see a charge accumulation around N and O atoms and charge depletion in N-O bond during adsorption on O-terminated surface (shown in Fig. 10.7(a)). The charge accumulation around the O atom suggests large charge transfer as was evident from Löwdin charge analysis. In the adsorption on ReO_2-terminated surface, we see a charge depletion around Re and accumulation around N atom (Fig. 10.7(b)). But there is also a charge accumulation in Re-N bond, indicating the strong polar covalent bond, and hence stronger bonding consistent with the binding energy.

We aligned the Fermi level (E_F) of ReO_3 and HOMO-LUMO of Py with respect to the vacuum level (see Fig. 10.8(a)) to assess the chemical interaction in terms of electronic energies. In the contrasting adsorption on O-terminated surface, E_F is below the HOMO level, which shifts towards the HOMO upon adsorption due to the charge transfer from the HOMO to the surface. In the case of ReO_2-terminated

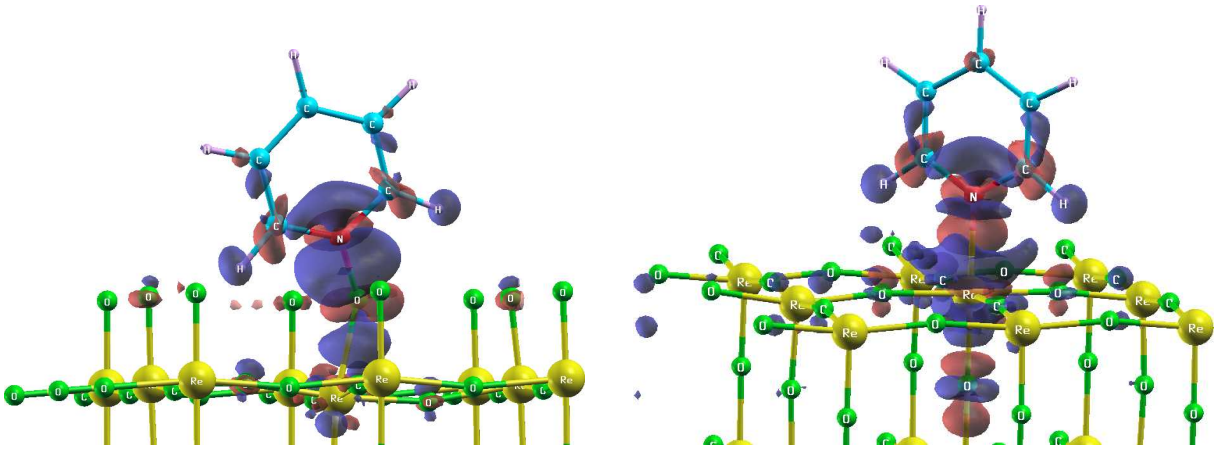

(a) (b)

Figure 10.7: Changes in the charge density during interaction between Py and (a) O-terminated and (b) ReO_2-terminated surfaces, obtained by subtracting the electron densities of surface and molecule from that of the complex. Atomic positions of the surface and molecule have been taken from fully relaxed complex to capture the effects of interaction. Red and blue colors represent the charge accumulation and depletion respectively.

surface, E_F lies between HOMO and LUMO level, and it shifts towards LUMO after adsorption. Ideally, there should be no charge transfer associated with such orbital energy levels, while the Löwdin charge analysis gives an electronic charge effectively transferred from the LUMO to surface. This is because of the intermixing of HOMO and LUMO of Py with surface states (polarizability and covalency giving a polar Re-N covalent bond). As is clearly seen in the PDOS of Py, we have states of LUMO at E_F (Fig. 10.6(c)) in case of ReO_2-terminated surface which is responsible for the effective charge transfer seen in the Löwdin charge analysis.

From the macroscopically averaged electrostatic potentials, our estimate of the electric field in the vicinity of the molecule is of the order of 10^{10} V/m, which is quite large (Fig. 10.8(b)). Thus, both electromagnetic and chemical factors are expected to be relevant to the observed SERS signal in experiments [114], which we discuss in the next section.

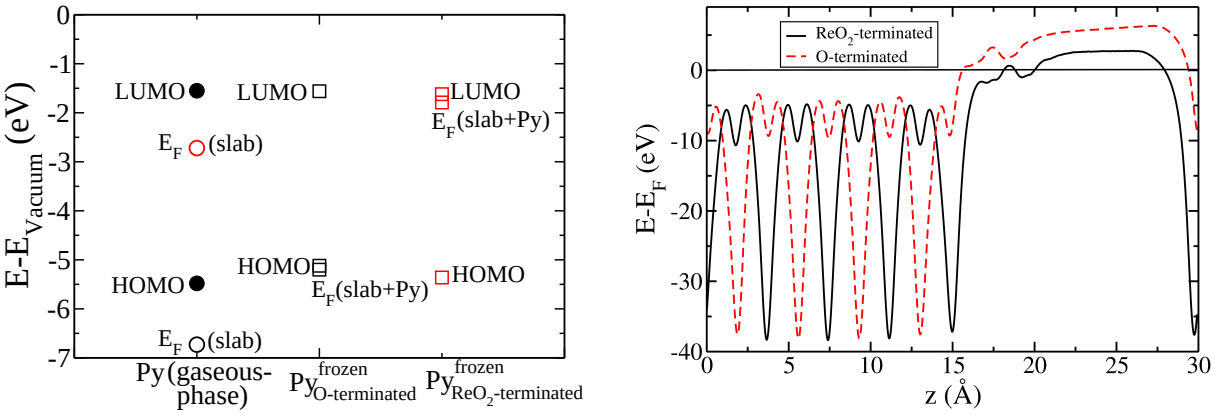

(a) (b)

Figure 10.8: (a) Energies of HOMO-LUMO levels of Py molecule in gaseous and adsorbed states relative to Fermi energies, E_F of O-terminated and ReO_2-terminated surfaces. The energies have been shifted so that vacuum potential is at zero. Fermi energy of O-terminated surface has been shown by black circle and that of ReO_2-terminated surface by red circle, and (b) variation in the planar averaged electrostatic potential in the direction (z) perpendicular to ReO_3 surfaces.

10.5 Discussion

Raman tensors and SERS

Chemical contribution to the enhancement of Raman signal can be thought to arise either from the (i) modification of the polarizability tensor (α_m) of the molecule upon adsorption or (ii) due to change in the polarizability of the surface due to the vibrational motion of adsorbed molecule [248]. This modulated polarizability coupled with the incident field contributes to Raman enhancement. In the first picture of chemical mechanism reduced HOMO-LUMO gap of Py upon adsorption plays an important role. Considering the second picture of the chemical mechanism, the ratio between the SERS cross-section with and without chemical contribution from surface quantifies the enhancement [248]

$$[D\sigma'_{diff}(0)]^2 : [\alpha'_m(0)]^2 \tag{10.6}$$

Where, $\sigma'_{diff}(0)$ and $\alpha'_m(0)$ are respectively the derivatives of the effective cross section of diffusive scattering of metal electrons from the adsorbed molecule and polarizability of the molecule with respect to the normal mode coordinate (Q), and D=$\frac{3v_F}{32\pi\Omega}$ with, v_F and ω are the Fermi velocity and frequency of the incident photon respectively. O-terminated is the stable surface compared to ReO_2-terminated [202], for which we have quantified the chemical enhancement for the Py adsorption on O-terminated surface.

Raman peaks of asymmetric ring breathing, trigonal ring breathing and C-H in-plane deformation modes show significant enhancement due to adsorption on ReO_3 [114]. We freeze these modes, by distorting the molecular structure with their eigen displacements, keeping the surface atoms stationary and obtained the derivative of adsorbate level (E_a) above the Fermi level with respect to the displacement of eigen modes (Q). The resonant state is derived from molecular energy level (E_a) and variation in σ_{diff} is due to the change in E_a with Q. Thus, we get $\sigma'_{diff}(0) = \frac{\sigma_0 E'_a}{(2\hbar\Omega)}$, $\hbar\Omega$ being the energy difference between Fermi energy and the adsorbate induced resonant state, and $\sigma_0 = \frac{64}{3\pi}\frac{\omega_F Q}{n v_F}$ [249], $\hbar\omega_F$ and n are the Fermi energy and carrier concentration respectively. Q is a number whose value depends on the symmetry of resonant state. The resonant state was contributed mainly from p_x states, we have used Q=0.33 [249] in all the considered modes. Considering the zz-component of polarizability tensor of the molecule and using equation 5 we find that the chemical enhancement is of the order 10^3, 10^2 and 10 for asymmetric ring breathing, trigonal ring breathing and C-H in-plane deformation modes respectively. There is a greater shift in the adsorbate level for asymmetric ring breathing with the displacement of atoms compared to trigonal ring breathing and C-H in-plane deformation modes (see Fig. 10.9). We do see a shift in the adsorbate level in trigonal ring breathing mode but there is a negligible change in C-H in-plane deformation modes. So, we get high chemical enhancement in asymmetric ring breathing mode followed by trigonal ring breathing and C-H in-plane deformation modes. Secondly, we see a large shift in E_F-E_{HOMO} level for the modes

which show greater chemical enhancement. Thirdly, asymmetric ring breathing mode involves the movement of N atom towards the surface. This leads to the strong interaction between the molecule and surface, which gives rise to the large chemical enhancement and observed blue shift. These modes also induce the change in charge density, which has been obtained using:

$$\delta\rho = \rho(Q_n) - \rho(0) \tag{10.7}$$

Where Q_n is the n^{th} normal mode coordinate. Visualization of this charge density difference (Fig. 10.9(b) inset) shows that the asymmetric ring breathing mode leads to accumulation of charge in N-O bond and around O atom to which N is attached. We also see an accumulation of a small charge around O atom bonded to Py when trigonal ring breathing mode is frozen (Fig. 10.9(a)). C-H in-plane deformation mode does not influence the distribution of charges on surface atoms (Fig. 10.9(c)), and hence shows a weak chemical enhancement of SERS. Our analysis shows that enhancement in Raman signal of asymmetric and trigonal ring breathing modes is due to both the electromagnetic and chemical effect. Since the interaction between the surface and adsorbate does not affect the C-H bond, we have small chemical enhancement. But due to the polar nature of the C-H bond, the enhancement is mainly electromagnetic in nature.

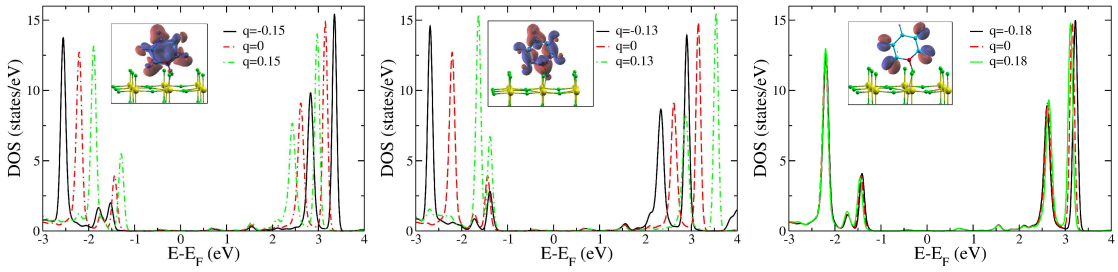

(a) (b) (c)

Figure 10.9: Changes in the projected density of states of Py with normal modes at three amplitudes (a) trigonal, (b) asymmetric ring breathing and (c) C-H in-plane deformation modes. Changes in charge density induced by freezing of these modes are shown in inset. Clearly, the electron-phonon couplings are significant in (a) and (b).

From our analysis, it appears that the observed softening of the Raman modes upon adsorption is basically due to the elongation of the C-N bond length of Py. The asymmetric ring breathing and ring stretching modes involve the displacements of atoms towards the surface, which increase the interaction between adsorbate and surface, hence undergo blue shifts in frequencies. This is consistent with the changes in charge density (Fig. 10.9(b)), where the asymmetric ring breathing modes lead to charge distribution in N-O bond and over surface O atom to which Py is attached.

10.6 Conclusions

Our density functional theory calculations confirm that the observed enhancement in Raman signals of Py adsorbed on ReO_3 nanocrystal has a notable contribution from the chemical mechanism involving the formation of a covalent bond between Py and an atom at the surface of ReO_3 (chemical enhancement), and electronic charge transfer from N to a surface atom in addition to electromagnetic enhancement. Inclusion of vdW leads to stronger energies of binding Py with ReO_3. The chemical interaction between Py and surface leads to a blue shift in asymmetric and trigonal ring breathing mode. The elongation of its C-N bond upon adsorption leads to a red shift in the observed Raman modes. Reduction in the HOMO-LUMO gap of Py upon adsorption and consequent enhanced polarizability, are central to the chemical mechanism relevant to the observed SERS. The enhancement in Raman intensity of asymmetric and trigonal ring breathing modes involves both electromagnetic and chemical mechanisms, whereas that of the C-H in-plane deformation mode originates mostly from an electromagnetic mechanisms.

Part III

Understanding and Predicting Two-Dimensional Materials

Chapter 11

Electron-phonon Coupling in Few Layers of ReX_2 (X = S, Se)

11.1 Introduction

Over the past years, transition metal dichalcogenides (TMDCs) have proven their excellent candidacy in the field of electronics [250, 251], optoelectronics [252–254], valleytronics and spintronics [255–258] due to their various unique properties such as tunable bandgaps [259, 260], high spin-orbit coupling [261] and two dimensional (2D) quantum confinement [262]. According to recent reports, ReS_2 & $ReSe_2$ have proven its worth in high performance transistors and polarization sensitive optoelectronic device applications [263–268]. Amongst TMDCs and other 2D materials, structurally anisotropic materials are very few. ReX_2 (X=S, Se) is a group-VII TMDC possessing distorted $CdCl_2$-type lattice structure with triclinic symmetry [$P\bar{1}$ space group] [269–271]. The ReX_2 crystal is made up of two-dimensional layered stacks with strong covalent bonds between the atoms in each layers and very weak van der Waals bonds between each layer. Each layer has one sheet of rhenium atom sandwiched between two sheets of chalcogen atoms. In each layer, the d^3 electrons in Re atom distorts the octahedral lattice sites by creating Re-Re metal bonds. This bond formation leads

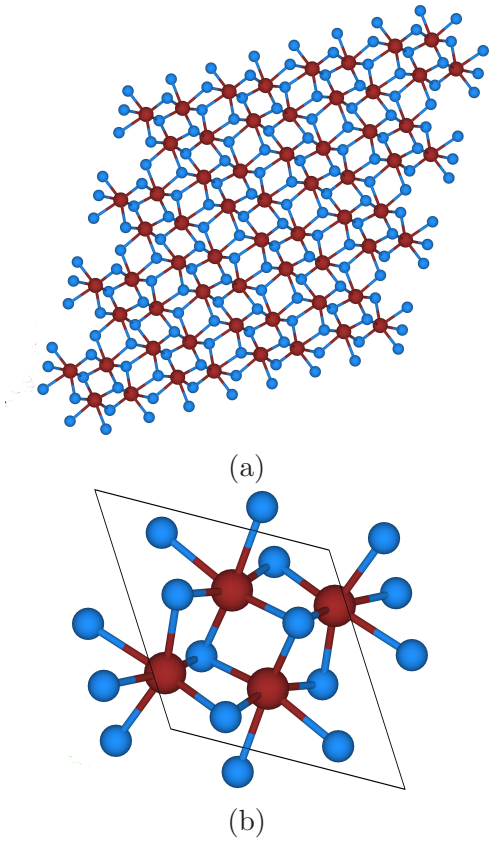

Figure 11.1: Schematic crystal structure of ReX_2 (X=S, Se). (a) Unit cell consists of 4 Re atoms arranged in diamond like structure. (b) Top view along c-axis. Re Chains forms along b axis due to Peierls distortion creating distorted 1T structure.

to a diamond like structure with 4 Re atoms in each vertex along the b axis (Fig. 11.1(a) and (b)). This structure is almost coplanar and distorts the position of the sulfur atomic sites [269–271]. Accordingly, the unit cell of the lattice consists of 4 formula units which give rise to 36 vibrational modes. Amongst these, 18 are Raman active, and 15 are infrared active optical modes [272]. All the Raman modes have A_g symmetry, and the intensity is dependent on the incident excitation polarization [273]. Unlike other TMDCs (e.g., MoS_2), modes cannot be classified strictly according to in-plane (E_g like) or out of plane (A_g like) vibrational [272] eigenvectors.

Raman spectroscopy is a non-invasive analytical tool for studying 2D layered structural material like Graphene [274], phosphorene and TMDCs [275, 276] which has provided useful information about crystal defects [277, 278], crystal structure [279],

lattice orientation [280, 281], crystal stacking order [281, 282] and doping. Few layers of these materials in comparison to monolayer gives relatively intense Raman signal while also providing better electron mobility. By measuring the behavior of phonon peak positions and linewidths, we gain an understanding of the dependence of electron-phonon coupling (EPC) on charge doping in these systems. By measuring EPC in these systems, we gain understanding as in the existence of dopant [283], electrical resistivity [284], thermal conductivity [285] and information about superconductivity [286] to name a few. Experimentally (performed by Subhadip Das from Prof. A. K. Sood's group*), the doping has been done electrically by fabricating a field effect transistor around an atomically thin flake. *In-situ* Raman spectra were recorded at various doping concentrations. For ReS_2, a decrease in phonon energy and linewidth broadening is observed experimentally with increasing electron dope on E_g like modes while A_g like modes are not affected. At high doping, a new mode close to 151 cm^{-1} which has small EPC appears in Raman spectra (shown in Fig. 11.2(a)). In the case of $ReSe_2$ on the contrary, all the 14 Raman modes do not show much phonon softening and line-broadening (Fig. 11.2(b)). This has contrasting behavior of materials with similar electronic and lattice structure. In this chapter, we aim to understand the softening of phonon modes with the electron doping concentrations. Also, to get insight into the different behavior shown by ReS_2 and $ReSe_2$ with electron doping concentrations even if they possess the same lattice structure.

11.2 Computational details

Our first-principles calculations are based on density functional theory (DFT) as implemented in Quantum ESPRESSO package [65]. The exchange-correlation functional has been treated using a Local Density Approximations (LDA) with Perdew-Zunger

*Department of Physics, Indian Institute of Science, Bangalore-560012

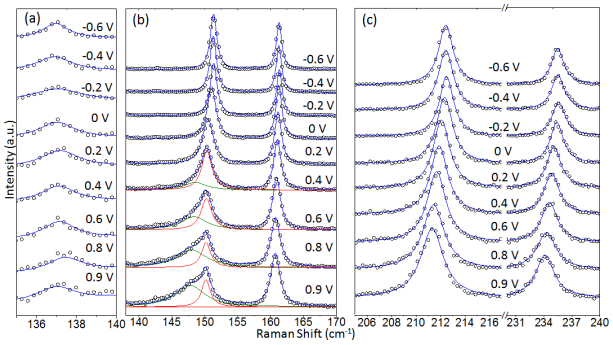

(a)

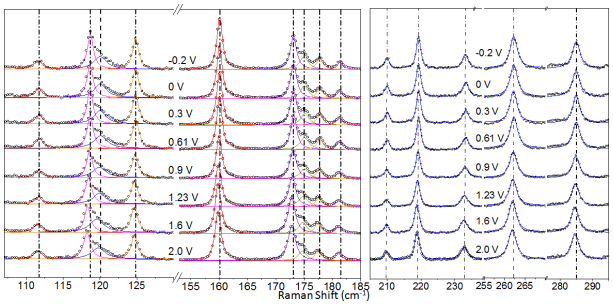

(b)

Figure 11.2: (a) Raman spectral data (black circle) and Lorentzian fit of Raman modes at different top gate voltages for (a) ReS_2, and (b) $ReSe_2$. The peak at 151 cm^{-1} consists of two peaks which starts to separate at higher charge concentration in ReS_2.

functional. Ultrasoft pseudopotentials (USPPs) have been used to model the interaction between valence electrons and ionic cores. We have used fully relativistic ultrasoft pseudopotential to take into the account of spin-orbit coupling (SOC). We used a kinetic energy cut-off of 40 Ry to truncate the plane-wave basis set used to represent Kohn-Sham wavefunctions. The structures have been relaxed to minimum energy until the Hellman-Feynman forces are less than 0.02 eV/Å. In the simulation of a bilayer, we have used a vacuum of 10 Å along z-direction of the periodic cell to keep the interaction between periodic images low. We used uniform meshes of 6×6×6 and 6×6×1 k-points to sample integrations over Brillouin Zone (BZ) of bulk and bilayer ReS_2 respectively. We have used the same parameters for trilayer $ReSe_2$. The zone center phonon frequencies were obtained using the DFT linear response as implemented in the Quantum ESPRESSO package. We have used the same numerical parameters and carried out calculations within a generalized gradient approximation

(GGA) as well for bulk ReS_2.

11.3 Results and discussion

We obtained zone center phonon spectrum of bulk ReS_2 within LDA and GGA flavors of DFT (see methods) and find a good agreement between results of LDA-USPP calculation with experimental values as well as other theoretical results reported earlier [272]. Secondly, the inclusion of vdW interaction does not affect the estimate of frequency notably [272]. In further studies here, we have thus used LDA-USPP based DFT calculations.

While hexagonal rings in ReS_2 structure are not ideal due to the formation of Re chains, we have used the nomenclature of hexagonal high symmetry points in our analysis of its electronic structure. The electronic structure obtained along high symmetry lines (Fig. 11.3(a)) shows an indirect band gap of 1.17 eV. Tongay *et al.* [287] have reported a direct band gap of 1.35 eV at Γ-point of bulk ReS_2 based on GGA calculations. To validate our calculation, we have used a GGA exchange-correlation functional and confirmed a direct band gap of 1.51 eV at Γ-point, and a direct band gap of 1.36 eV at A-point (Fig. 11.3(b)) after covering the entire BZ in the determination of the electronic structure. The band gap at A-point is quite close to that obtained by Tongay *et. al.* [287]. With the inclusion of the spin-orbit coupling (SOC) in LDA-USPP calculations, we get a direct band gap of 1.06 eV at A-point (Fig. 11.3(c)). Similarly, we find an indirect band gap of 0.93 eV and 1.02 eV of $ReSe_2$ based on the calculation with and without the inclusion of SOC. Our results are in good agreement with the earlier theoretical and experimental findings of band gaps of bulk $ReSe_2$ [288, 289].

He *et al.* [281] predicted three stable stacking configuration of bilayered ReS_2. We considered the three stable stacking configuration (stacking configuration 1, 2, 3) with the same relative distances (d) between the two layers as used by He *et al.* [281] and

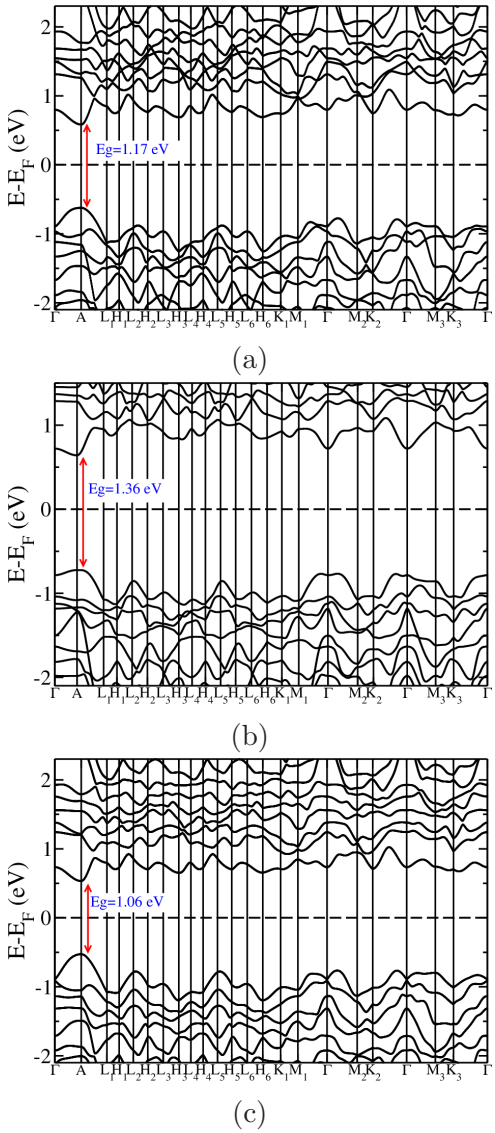

Figure 11.3: Electronic structure of bulk ReS_2 obtained using (a) LDA-USPP, (b) GGA-USPP and (c) LDA-USPP with SOC inclusion.

relaxed them fully. In addition we considered the fourth stacking configuration of bilayer ReS_2 with one monolayer exactly on top of the other ReS_2 monolayer and termed it as a AA stacking (stacking 0). Our results show that AA stacking is clearly the most stable configuration of all (Table 11.1). Secondly, calculated electronic structures of the stacking 0 and stacking 3 configuration show a direct band gap at Γ-point. For bilayer ReS_2 with stacking 0 configuration, we get a direct band gap of 1.20 eV and 1.32 eV respectively for SOC=0 and SOC≠0 (Fig. 11.4(a) and (c)). In the case of bilayer ReS_2 with stacking 3 configuration, there is a slight increase in the

Table 11.1: Energies of stacking configurations (n), (E_n-E_0, n=1,2,3) and relative displacements (d) between the two layers of bilayer ReS_2 with respect to the bottom ReS_2 layer.

Stackings	Energy (meV)	d (Å)
0	0	(-1.80, -0.87, 5.98)
1	54	(-0.008 2.17 6.05)
2	80	(-0.43 -0.11 6.19)
3	49	(0.06 -5.82 6.06)

band gap. We get a direct band gap of 1.23 eV and after inclusion of SOC it gets increased to 1.32 eV (shown in Fig. 11.4(b) and (d)). We do not find a noticeable difference in the electronic structures as a result of these stacking configurations.

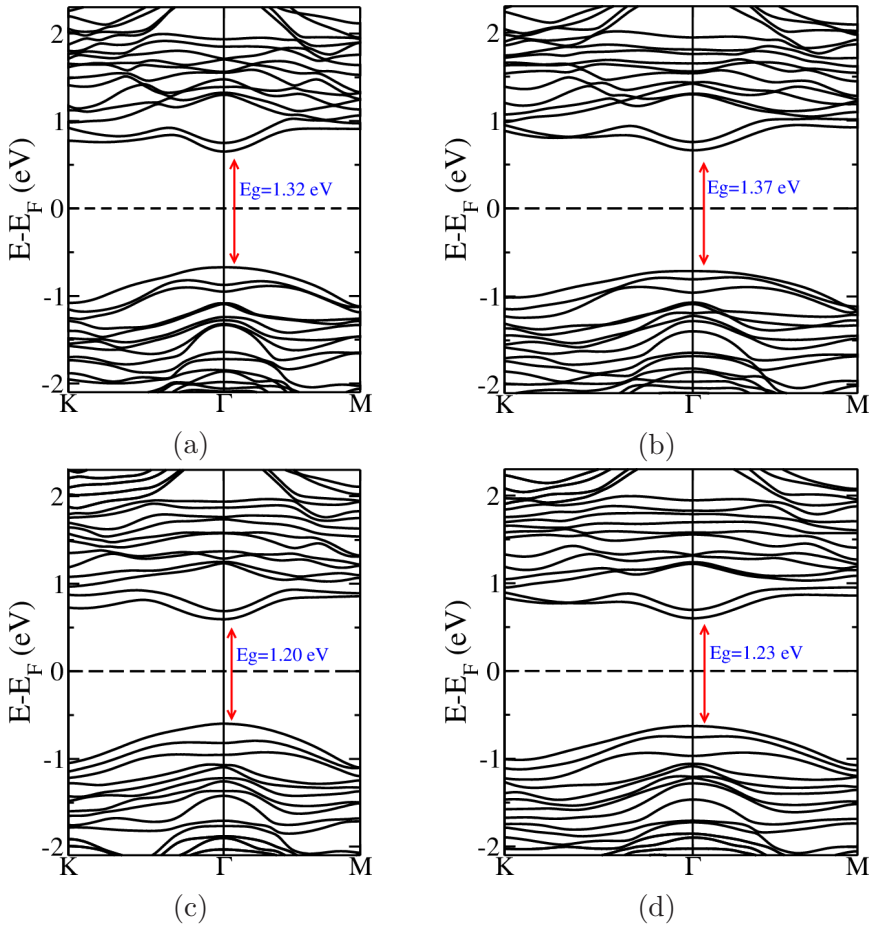

Figure 11.4: Electronic structures of bilayer ReS_2 with stacking 0 (first panel) and stacking 3 (second plane) confguration. Electronic structures in (a) and (b) are obtained with SOC = 0 and in (c) and (d) with SOC $\neq$ 0.

In bilayered ReS_2, we simulated AA-stacking (stacking 0) with an additional electronic

charge equivalent to the experimental concentration of electron doping. The trend

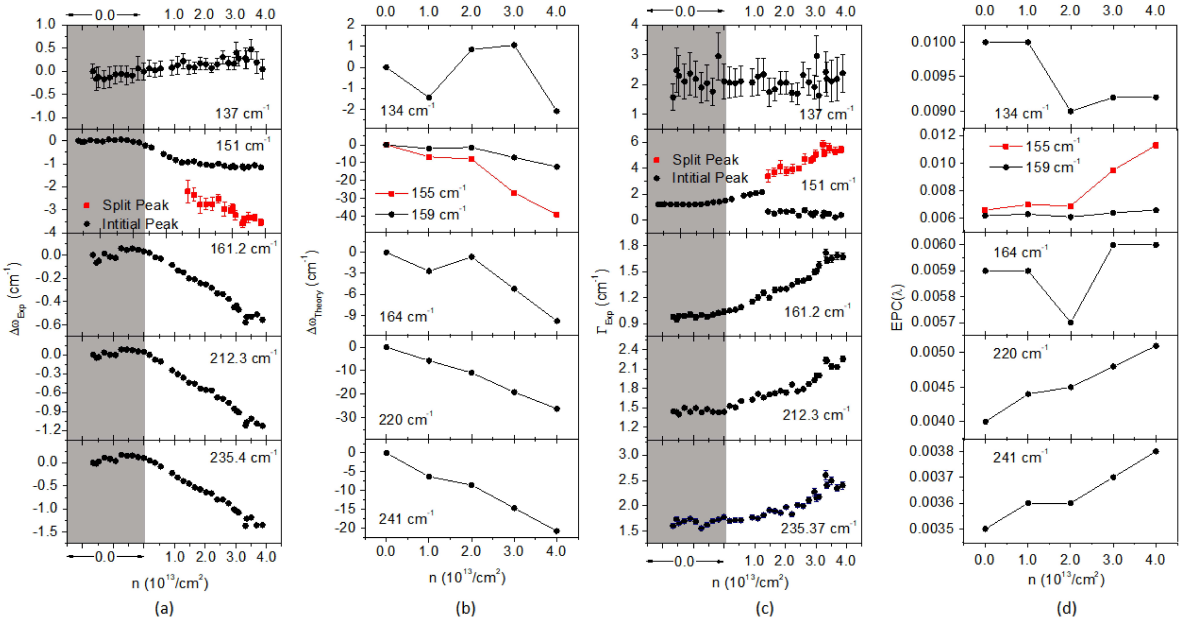

Figure 11.5: (a)-(b) Comparison in changes in phonon frequency ($\omega_{n\neq 0} - \omega_{n=0}$) between experiment and DFT calculations in ReS_2 respectively. (c)-(d) linewidth (Γ) and calculated EPC (λ) are compared as a function of electron doping concentration (n) respectively. Gray region represents zero doping condition. Red square represent experimentally observed split peak at high electron doping.

in changes in phonon frequencies with electron doping concentration qualitatively agrees with the experimental results (Figs. 11.5(a) and (b)). We find that the low frequency (A_{2g}-like) phonon modes do not change much with the electron doping concentration, while there is a significant change in high frequency E_g-like phonon modes. Experimentally, splitting of a peak at 151 cm^{-1} in the Raman spectrum was observed. The difference between our calculated estimates of these two frequencies is 4 cm^{-1} for the undoped case, which is quite small, and may not be resolved in observed Raman spectrum. Interestingly, we find that the two modes respond differently to electron doping, giving rise to an apparent splitting of a peak in the observed Raman spectrum. To understand this we determined the zone center phonon spectrum of monolayer ReS_2. The monolayered ReS_2 also exhibits the two modes at frequencies 155 cm^{-1} and 159 cm^{-1}; however the mode at 159 cm^{-1} has a small Raman-scattering cross-section. Thus, the split peak in the observed Raman spectrum is not due to

the appearance of a new mode but arises from electron doping which changes the frequencies and electron-phonon coupling of these two modes in the opposite manner, leading to two resolved peaks.

From the density of electronic states of bilayer ReS_2 obtained after freezing the modes with maximum atomic displacements of 0.06 Å (see Fig. 11.6), the large shift in VBM and CBM positions are clearly revealed in the modes which couple strongly with the electrons. Evidently, shifts in the CBM and VBM positions are quite weak for higher modes.

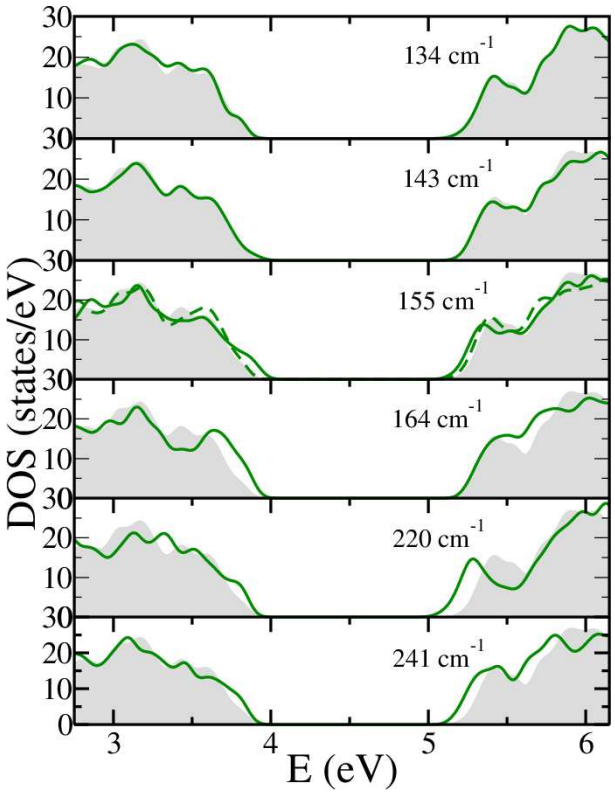

Figure 11.6: Density of states of bilayer ReS_2 (shaded grey) in equilibrium and distorted structures obtained by freezing various phonon modes (in green line). Solid green line is for the frequency 155 cm^{-1} and dotted green line in the same plot is for the frequency 159 cm^{-1}.

The stacking sequence of bilayer TMX_2 is known to influence the shear modes of ReS_2 and $ReSe_2$ [282, 290]. To predict how it affects the behavior of phonon frequencies with electron doping, we obtained zone-centre phonon spectrum for the stacking 3 of bilayer ReS_2. We find that the trend in the changes of frequencies remains the same

(Fig. 11.7). Thus, we conclude that the stacking sequences affect the shear mode but not the other high frequency modes. We do not see any changes in the variation of EPC with electron doping concentration as a result of a change in the stacking sequence (Fig. 11.7).

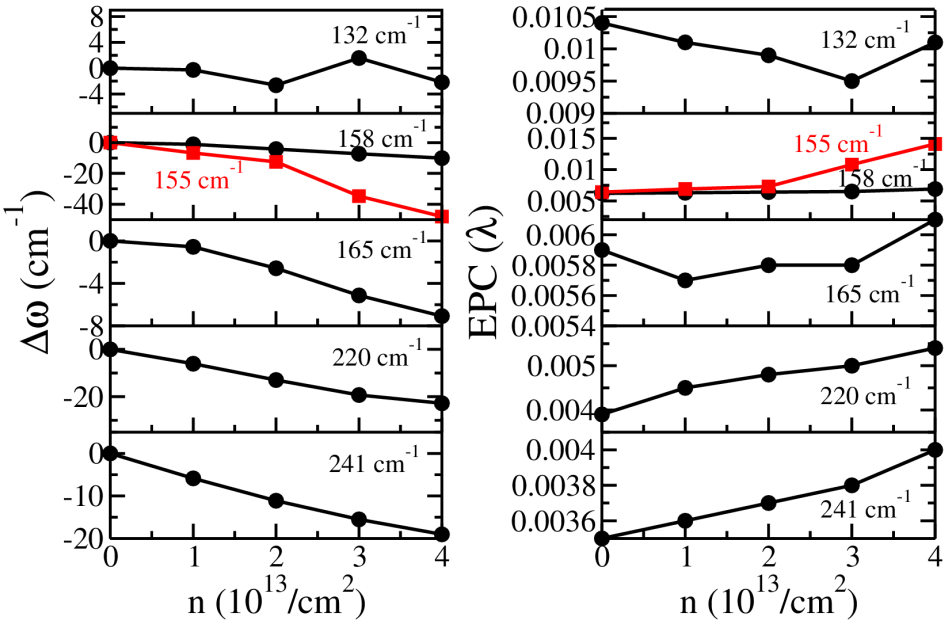

Figure 11.7: Variation in phonon frequencies and electron-phonon coupling (EPC) with electron doping concentration in bilayer ReS_2 (stacking 3), obtained from first-principles DFT calculations.

In trilayer $ReSe_2$, we tried three different ABA stacking configurations. We displaced the middle layer of $ReSe_2$ by three different distances (d) and obtained the relative energy after z-direction relaxation. We find that the AAA stacking is the most stable of all (see Table 11.2), similar to what we found in bilayer ReS_2 (see Table 11.1). For trilayer $ReSe_2$, we see an indirect band gap of 1.12 eV, and VBM is a bit away from Γ-point (Fig. 11.8(a)). After including the SOC in our calculations, we get an indirect band gap of 1.03 eV, with the VBM at Γ-point (Fig. 11.8(b)). We determined the electronic structure of trilayer $ReSe_2$ in the ABA stacking configuration (stacking 2), which has lower energy than the other ABA stacking configuration. We find an indirect band gap of 1.13 eV for ABA stacking of trilayer $ReSe_2$ (Fig. 11.8(c)). Also, the electronic structure does not change much with the stacking sequence. Since,

Table 11.2: Energies of stacking configurations (n), (E_n-E_0, N=1,2) and relative displacements (d) between the middle layer of $ReSe_2$ with respect to bottom layer of trilayer $ReSe_2$.

Stackings	Energy (eV)	d (Å)
0	0	(-0.67, -2.19, 6.35)
1	0.34	(-1.48, -0.77, 6.35)
2	0.02	(-2.30, 0.65, 6.35)

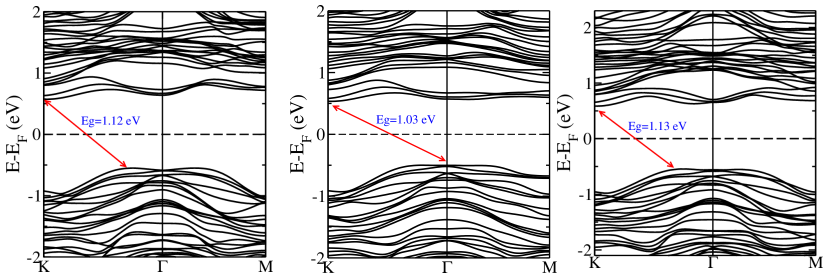

Figure 11.8: Electronic structures of trilayer $ReSe_2$ with (a) SOC = 0, and (b) SOC $\neq$ 0 and (c) stacking 2 of $ReSe_2$ (obtained with SOC=0).

AAA stacking (stacking 0) is the most stable of all, we used it in finding the effects of electron doping. While we see the softening of phonons with electron doping (Fig. 11.9(b) and (d)), the changes are significantly smaller than those in bilayer ReS_2 (Fig. 11.5(b)). Our results qualitatively agree with the contrast seen in the observed effects of doping in ReS_2 and $ReSe_2$.

To understand these observed trends, we obtained the EPC of bilayer ReS_2 and trilayer $ReSe_2$ with the electron doping concentrations. In ReS_2, we noticed that the A_g-like modes couple weakly with electrons, whereas E_g-like modes couple strongly with the electrons (Fig. 11.5(d)). The visualization of eigenvectors of the phonon modes (eigenvectors at zero doping condition shown in Fig. 11.10) reveals that the Re dominated modes with (0, π) (displacements of an atom in adjacent cells are in-phase along x-axis and out-of-phase along y-axis, marked in Fig. 11.10) displacements show significant softening in the frequency and strong coupling with electrons as a result of electron doping. Both Re and S dominated modes involving (0, π) displacement of Re atom show significant softening of the modes. The mode at a frequency of 155 cm^{-1} is

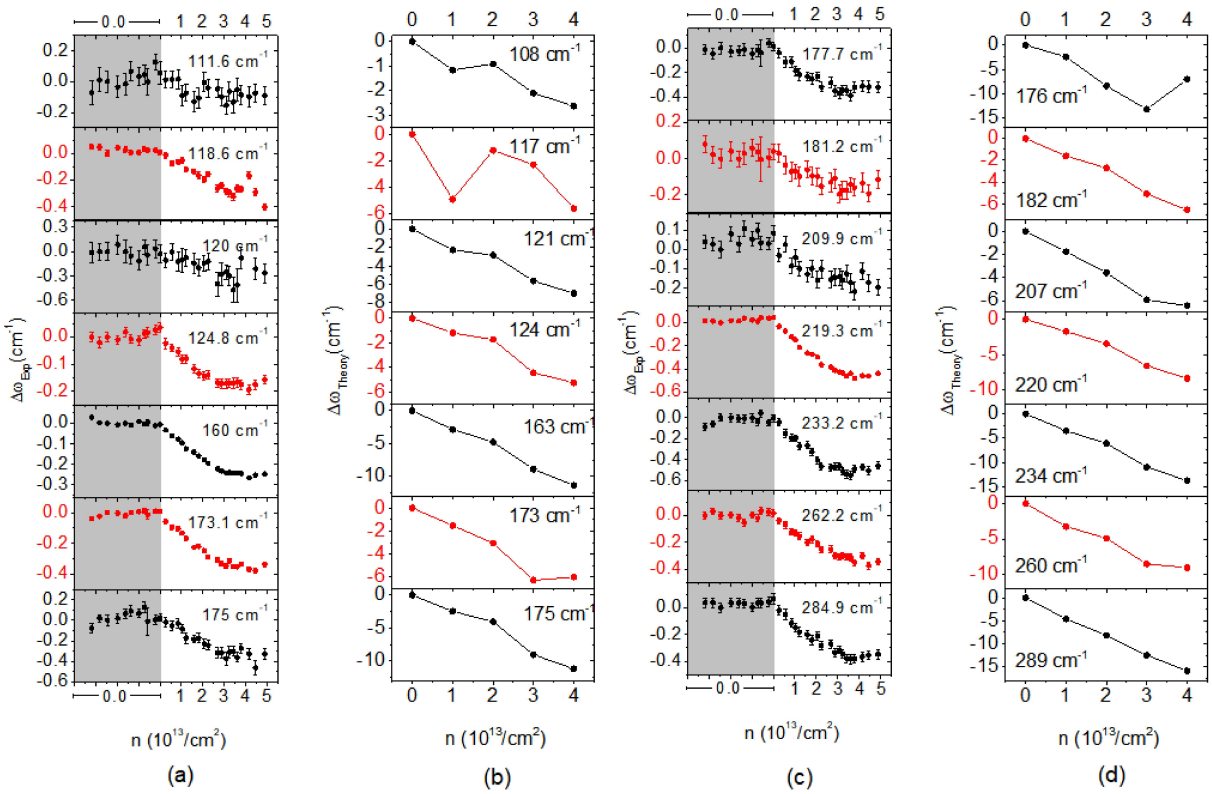

Figure 11.9: (a)-(d)Phonon frequency (ω) from experimental and theoretical calculation of $ReSe_2$. Gray region indicate zero doping condition.

a Re-dominated and involves in-plane (0, π) displacements of Re atoms. On the other hand, the modes at frequencies of 220 cm^{-1} and 240 cm^{-1} involve (π, 0) (displacements of atom in adjacent cells are out-of-phase along x-axis and in-phase along y-axis) in-plane displacements of Re atoms along with the out of plane displacements of S atoms. Hence, the modes of frequencies 155 cm^{-1}, 220 cm^{-1} and 241 cm^{-1} show significant changes in frequency with the electron-doping concentrations due to strong EPC. The mode at a frequency of 159 cm^{-1} is both a Re and S dominated mode. It involves in-plane (π, π) (displacements of an atom in adjacent cells are out-of-phase along x-axis and out-of-phase along y-axis) displacements of Re atoms and hence shows weak dependency on electron doping. The vibrational mode of frequency 164 cm^{-1} involves in-plane (π, 0) displacements but the mode has a significant in-plane displacements of S atoms, hence it does not show significant softening with the electron doping

Table 11.3: Atomic displacements of various phonon modes at zero electron doping and the maximum change in frequency with the electron-doping concentration ($\Delta\omega$). (π, 0) represents out-of-phase displacements of atoms along the x-axis and in-phase displacements of atoms along the y-axis in adjacent unit cell. The in-phase displacement of atoms along x-axis and out-of-phase displacements of atoms along the y-axis in the adjacent unit cell is written as (0, π). (π, π) corresponds to the out-of-phase displacements of atoms along the x and y-axes. See Fig. 11.10 for the schematic representation of atomic displacements of various phonon modes.

Modes (cm^{-1})	Atomic displacements	Description	$\Delta\omega$ (cm^{-1})
134	(π, 0)	Re-dominated	2
155	(0, π)	Re-dominated	39
159	(π, π)	Re and S dominated	12
164	(π, 0)	S dominated	10
220	(π, 0)	Re and S dominated	26
241	(π, 0)	Re and S dominated	21

concentrations. The vibrational mode of frequency 134 cm^{-1} is a Re-dominated mode with the out of plane (π, 0) displacement of Re atoms and hence is not affected much by the electron doping concentrations. We have also summarised the results discussed above in the Table 11.3. From the EPC of trilayer $ReSe_2$, we note that its phonons do not couple strongly with electrons (Fig. 11.11). Hence, $ReSe_2$ trilayer exhibits small or no shifts in frequencies with the electron doping.

The direct band gaps of ReS_2 and $ReSe_2$ at Γ-point are 1.32 eV and 1.22 eV respectively. In contrast to ReS_2, $ReSe_2$ exhibits an indirect band gap of 1.12 eV. The valence band maximum of ReS_2 has the highest density of states at Γ-point while, it is slightly offset from Γ in $ReSe_2$. Phonon frequencies are derived from the interatomic force constants which are linear response functions having a dominant contribution from the phonon mediated coupling between electronic states at the conduction band minimum and valence band maximum. Upon electron doping the valley of conduction band minimum at K-point of $ReSe_2$ gets populated, while that at Γ-point gets populated in ReS_2. As a result, the frontier states at Γ-point are masked from contributing to phonon frequencies in ReS_2 resulting in changes in dominant terms in the interatomic force constant. Hence upon electron doping, a significant change in

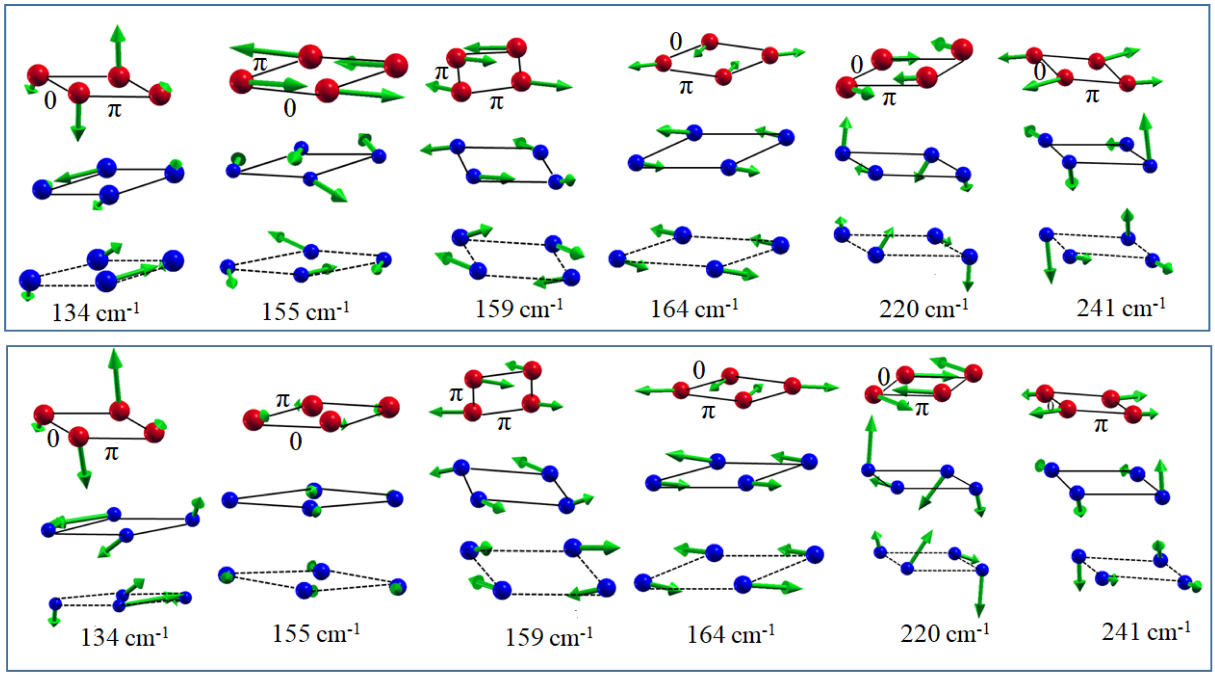

Figure 11.10: Visualisation of phonon vibrational eigenvectors of bilayer ReS_2 at zero doping condition. The two panels are for two different layers of bilayer ReS_2. Re and S atoms are shown by blue and red spheres respectively. The displacements of atoms in the same direction and in opposite directions has been marked respectively as 0 and π in the figure.

phonon frequencies of ReS_2 are observed, while little changes are seen in $ReSe_2$ (see Fig. 11.12).

Dielectric constants of materials are relevant to their electronic, excitonic and trionic properties [291,292]. We determined the electronic contribution to dielectric constants (ϵ^{∞}_{xx} and ϵ^{∞}_{yy}) of bilayer ReS_2 and trilayer $ReSe_2$. ϵ^{∞}_{xx} and ϵ^{∞}_{yy} values of bilayer ReS_2 are 8.61 and 9.06 respectively, whereas they are 11.07 and 10.98 for trilayer $ReSe_2$. Trilayer $ReSe_2$ exhibits a higher dielectric constants than bilayer ReS_2, correlating with its lower band gap. Smaller band gap facilitates greater mixing between the excited states and the ground states with an applied electric field. This results in enhanced polarizability and, hence larger values of dielectric constants.

The Born effective charges (Z^*) are measures of electric polarization in response to atomic displacements ($u_{i,\beta}$) at zero electric field, or equivalently measure of the force

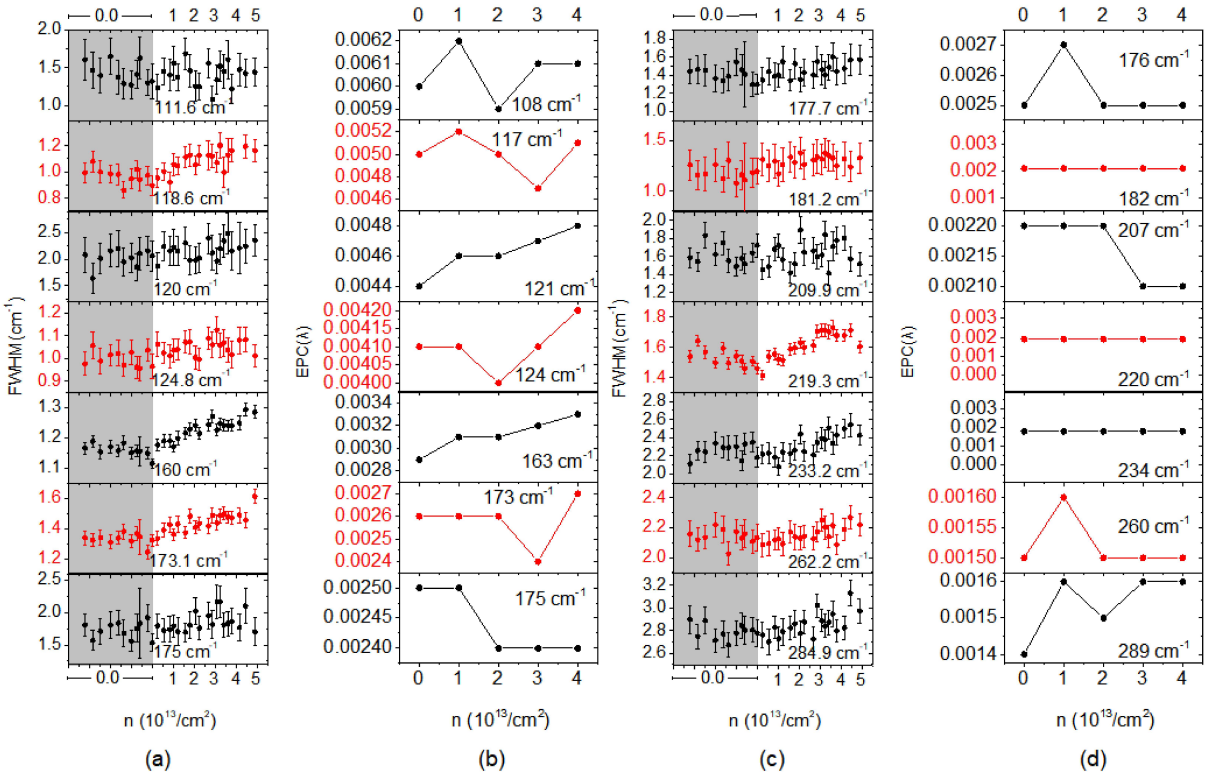

Figure 11.11: (a)-(d) Full width half maxima (Γ) from experiment and calculated EPC (λ) of $ReSe_2$. As before, gray region indicate zero doping condition.

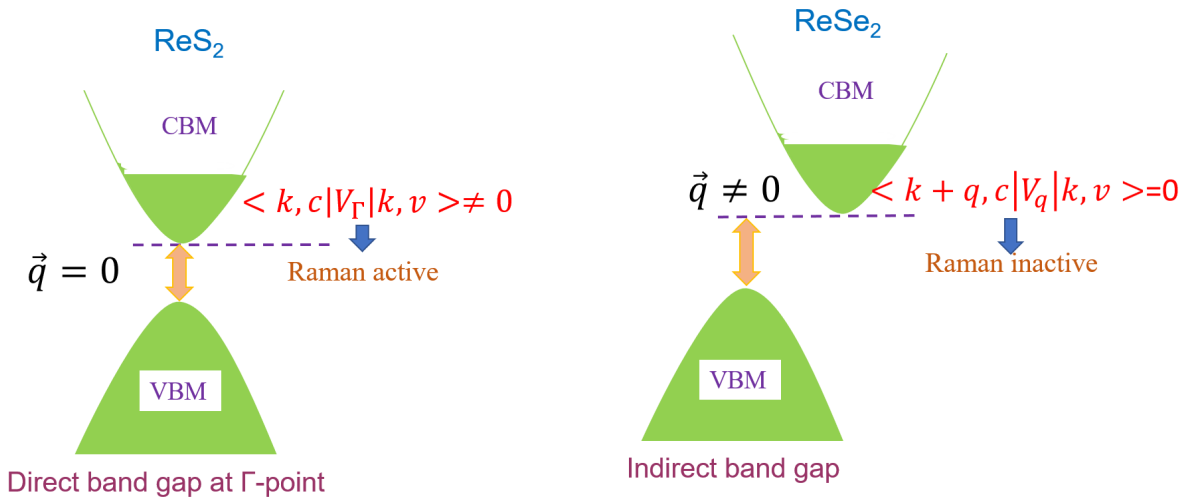

Figure 11.12: Schematic illustration of the coupling of electrons with phonons in ReX_2 (X= S, Se).

exerted on an atom by an electric field and is given by:

$$Z^*_{i,\alpha\beta} = \Omega_0 \frac{\partial F_{i\beta}}{\partial E_\alpha} = \Omega_0 \frac{\partial P_\alpha}{\partial u_{i,\beta}} \tag{11.1}$$

Table 11.4: Born effective charges (Z^*) of Re atoms of bilayer ReS_2 and trilayer $ReSe_2$. Due to symmetry Z^* of top and bottom layer of trilayer $ReSe_2$ are same. Z^* of middle layer $ReSe_2$ have been shown in parentheses.

		Z^*_{xx}	Z^*_{xx}
ReS_2	Re1	-1.285	-0.705
	Re2	-1.366	-0.753
	Re3	0.421	-0.758
	Re4	0.366	-0.635
$ReSe_2$	Re1	-1.320(1.263)	2.555(-2.625)
	Re2	-1.345	-2.714
	Re3	-1.081 (-1.086)	-0.917 (-0.830)
	Re4	-1.186	-0.883

Where, Ω_0 is the volume of the unit cell. P_α is the polarization per unit cell in the direction α (=x,y,z) induced by the displacement of the ith atom in the direction β (=x,y,z). $F_{i\beta}$ is the β component of force acting on the ith atom due to the application of electric field (E) in the direction of α. We find unusually small Born effective charges for Re, S and Se atoms (Table 11.4 and Table 11.5), deviating significantly from their nominal charges of +4, and -2. The xx-component of Z^* of Re atoms (Re3 and Re4 in Table 11.4), diagonally opposite to each other forming a bond have smaller Z^* than Re1 and Re2 atoms in bilayer ReS_2 and trilayer $ReSe_2$. It is quite interesting to note that the signs of Re and Se atoms are opposite to their nominal charges. Such anomalous behavior of Z^* indicates the covalency of its bonds. Similar anomalous behavior has also been observed in MoX_2 (X=S, Se) and WX_2 (X=S, Se) [293]. The large Z^* of trilayer $ReSe_2$ than that of bilayer ReS_2 can be attributed to its smaller band gap.

11.4 Conclusions

In summary, we show that the A_g like modes of ReS_2 couple weakly with electrons while E_g like modes couples strongly. A new mode at 151 cm^{-1} was discovered with low EPC behavior. The stacking order of bilayer ReS_2 and trilayer $ReSe_2$ do not alter

Table 11.5: Born effective charges (Z^*) of S (Se) atoms of bilayer ReS_2 (trilayer $ReSe_2$). Z^* of Se atoms in middle layer $ReSe_2$ have been shown in parentheses.

		Z^*_{xx}	Z^*_{xx}
	S1	0.468	-0.274
	S2	0.44975	0.331
	S3	0.401	0.223
ReS_2	S4	0.299	0.1994
	S5	0.457	0.71797
	S6	0.4699	0.7673
	S7	-0.344	0.111
	S8	-0.3699	0.192
	Se1	0.515 (0.482)	0.492 (0.507)
	Se2	0.473	0.499
	Se3	0.790 (0.689)	1.166 (1.162)
$ReSe_2$	Se4	0.665	1.160
	Se5	0.651 (0.628)	0.587 (0.552)
	Se6	0.655	0.610
	Se7	0.548 (0.534)	1.233 (1.219)
	Se8	0.603	1.285

their electronic properties significantly. The variation in higher phonon frequencies with electron doping does not really depend on the stacking sequence of bilayer ReS_2. Similar behavior can be expected for trilayer $ReSe_2$ also. Phonons of trilayer $ReSe_2$ do not couple strongly with electrons, and hence they exhibit no significant softening of phonon modes. This has been attributed to the indirect band gap of $ReSe_2$ as oppose to direct band gap in ReS_2. We also see anomalous born effective charges in both bilayer ReS_2 and trilayer $ReSe_2$.

Chapter 12

Novel Two-dimensional Alloys from Silicene and Germanene Monolayers

12.1 Introduction

Two-dimensional (2D) materials have been one of the most extensively studied classes of materials recently, due to their exceptional properties that emerge when charge carriers are confined to a plane. While graphene, which is a single atomically thin sheet of graphite, has been investigated extensively by the scientific community, its utilization for some applications, such as field effect transistors (FETs), is limited as it is a zero gap semiconductor with a very weak spin-orbit coupling (SOC). While researchers have tried to open up energy gaps in the electronic structure of graphene through various means like chemical funtionalisation [294], application of electric fields [295, 296] and sublattice symmetry breaking through substrate interaction [297], a newer research direction explores 2D materials beyond graphene [298–300]. Graphene-like monolayered sheets of silicon and germanium (silicene and germanene, respectively) have emerged as a strong contenders in the realm of 2D materials [301–303], due to

their buckled structure and stronger SOC [304, 305].

The main hurdle experienced in realizing silicene and germanene arises from the fact that they do not form layered structures in their bulk phase. As a result, mechanical exfoliation techniques used for fabricating graphene and many other 2D materials [306] do not work. Silicene and Germanene do not exist as freestanding sheets but are typically synthesized as adlayer structures on ordered substrates. Monolayered silicene has been grown epitaxially onto Ag (111) and (110) substrates [307, 308], and high temperature surface reconstruction of hexagonal-$MoSi_2$ nanocrystallites [309]. Few layer germanene has been synthesized under ultra-high vacuum conditions by evaporating germanium onto clean Au (111) surfaces [310,311]. Device applications of these materials were further limited as silicene was not expected to withstand isolation from its metallic template or exposure to ambient air [312–314]. This challenge has been overcome by using a synthesis–transfer–fabrication process known as silicene encapsulated delamination with native electrodes (SEDNE) [315], paving the way for silicene and germanene as replacements for silicon in the electronics industry.

An interesting question, then, is if new materials can be created by incorporating Ge substitutionally into the silicene lattice and vice versa. This would be analogous to the study of three-dimensional Si-Ge alloys with superior thermoelectric properties [316]. A novel 2D honeycomb framework with half of the Si atoms in silicene replaced by Ge has been theoretically studied and predicted to be energetically more stable than a germanene monolayer while also retaining the linear energy-momentum relationship characterized by Dirac cones [317, 318].

In this chapter, we explore the structure, stability and electronic properties of novel two-dimensional alloys of silicon and germanium ($Si_{1-x}Ge_x$) with the honeycomb lattice at the entire range of concentration x $\in$ [0, 1], using first-principles Density Functional Theory (DFT) calculations. For a range of concentrations, we find the equilibrium lattice constant varies linearly with increasing germanium concentration, consistent with the Vegard's law. We show that Ge atoms can be incorporated into the

silicene lattice and form dynamically stable 2D Si-Ge alloys. Their electronic structure near the Fermi level can be characterized by Dirac cones at all concentrations studied here. However, the inclusion of spin-orbit coupling introduces a small (∼10 meV) band gap in all structures which can be modulated with the Si:Ge ratio. The lowest energy configurations at each concentration consists of like atoms occupying the adjacent positions. Phonon calculations reveal softening of phonon frequencies as a function of increasing Ge concentration.

12.2 Computational details

Our first-principles calculations are based on the DFT as implemented in the Quantum ESPRESSO (QE) package [65]. We represent the interaction between the ionic cores and valence electrons using norm-conserving pseudopotentials. We use a kinetic energy cut off of 50 Ry to truncate the plane wave basis sets. The exchange-correlation energy of electrons has been treated with a generalized gradient approximation (GGA) with Perdew-Burke-Ernzerhof (PBE) parametrized form [103]. In the simulation of the two-dimensional structure, we use a periodic supercell with a vacuum of about 15 Å in order to weaken any interaction between their periodic images. We substitute Ge atoms in silicene using 2×2 supercells to obtain 2D $Si_{1-x}Ge_x$ alloys. We use a uniform k-point mesh of 6×6×1 for sampling the integrations over Brillouin zone. Raman spectroscopy is one of the most commonly used optical techniques for the characterization of 2D materials like graphene. Important structural features can be derived from the analysis of the Raman spectra, e.g., the shift in frequency of the Raman peaks have been successfully used to not only quantify the number of layers in 2D materials [319], but also to estimate carrier concentration and the quality of the graphene sheets [320]. We determined phonon dispersion using Fourier interpolation of the dynamical matrices obtained at q points on a uniform 3×3×1 mesh with DFT linear response method as implemented in QE.

12.3 Results and discussion

As there are a large number of configurations for each concentration (x) of $Si_{1-x}Ge_x$, we use the site-occupancy disorder (SOD) technique [68] to determine the symmetry-inequivalent configurations. The two configurations are considered equivalent if any one of the geometric operations like translations, rotations, reflections can convert one structure into the other. A list of possible isometric transformations (which are geometric transformations in this case) are provided on the basis of symmetry of parent crystal structure and all the inequivalent configurations are generated via atomic substitution.

For each of the configurations at various concentrations, we further calculate the alloy formation energies per atom, E_f:

$$E_f = \frac{E_{Si_{1-x}Ge_x} - (1-x)E_{Si} - xE_{Ge}}{N} \tag{12.1}$$

Where E_{Si} and E_{Ge} are the energies of monolayer silicene and germanene and N is the total number of atoms. Relatively low alloy formation energies, as compared to room temperature (26 meV), suggest that high temperature synthesis routes can be used to grow these alloys (Fig. 12.1(a)). The difference in the alloy formation energies of the lowest and highest energy configurations ranges from ∼5 meV/atom at x = 0.25 and 0.75 to ∼15 meV/atom at x = 0.5 (see Fig. 12.1(a)). The lattice constant of the lowest energy configurations increase linearly with Ge concentration, consistent with Vegard's law, as shown in Fig. 12.1(b). For a particular Ge concentration, we do not see a significant variation in the lattice constant on the basis of ordering of Ge atoms. We find that in each concentration like atoms prefer to occupy the adjacent positions in the lowest energy structure (Fig. 12.1(c)-(i)). The highest energy structures are most disordered with respect to site occupancy by Si and Ge atoms. The lowest energy structure of silicene (x = 0) and germanene (x = 1) is buckled with a buckling characterized by Δ = 0.45 Å and 0.69 Å respectively, consistent with the earlier

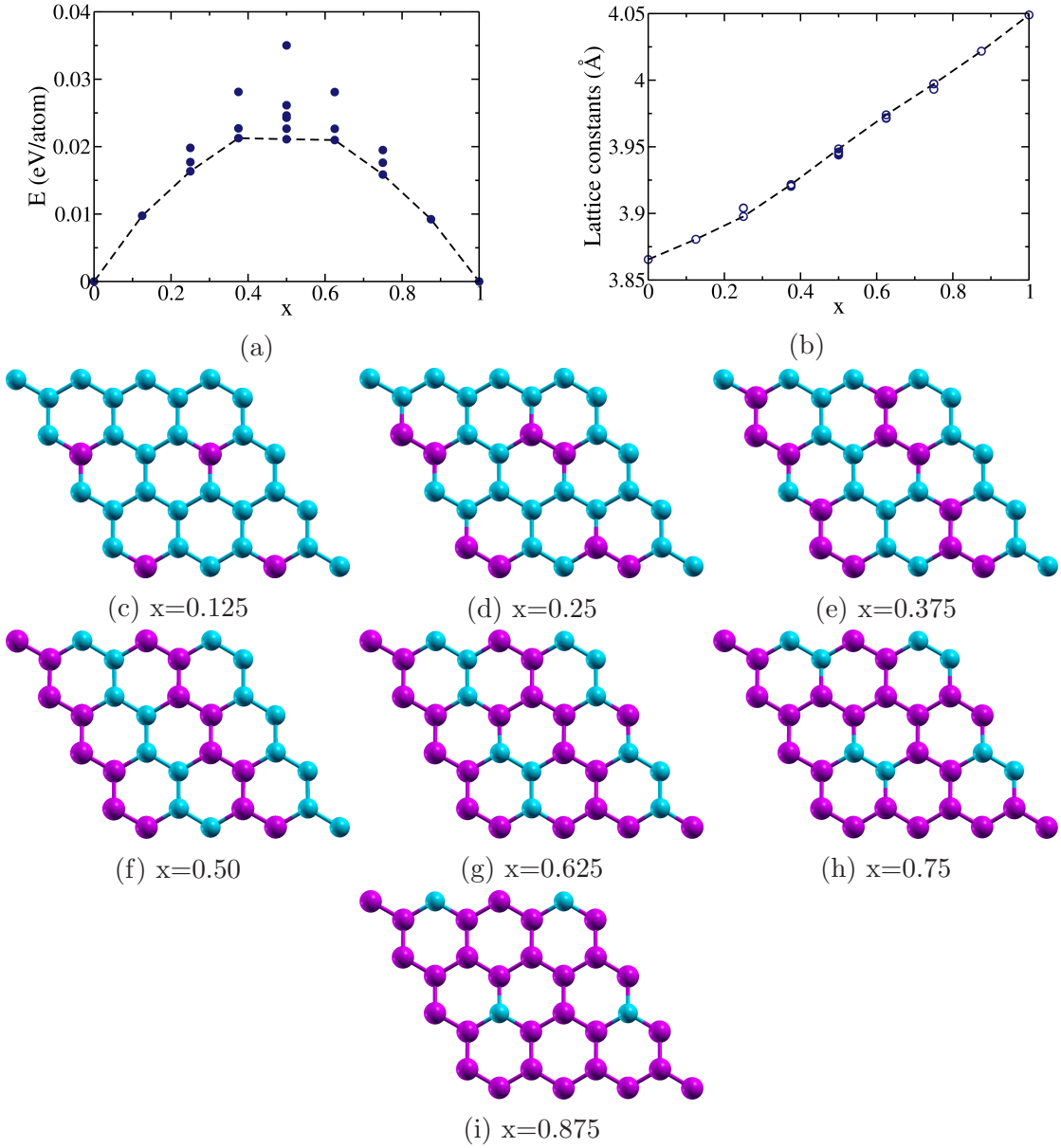

(a) (b)

(c) x=0.125 (d) x=0.25 (e) x=0.375

(f) x=0.50 (g) x=0.625 (h) x=0.75

(i) x=0.875

Figure 12.1: (a) Alloy formation energies, and (b) lattice constants of symmetry inequivalent configurations of 2D monolayers $Si_{1-x}Ge_x$. Dashed line in (a) connects the lowest energy at each concentration. Lowest energy configurations for x=0.25 to 0.875 has been shown in Figs. (c)-(i).

reports [321, 322]. We have obtained the buckling (Δ) of atoms for x > 0 and x < 1 using:

$$\Delta_\mu = \frac{z_i + z_j + z_k}{3} - z_\mu \tag{12.2}$$

Where, z_i, z_j, and z_k are the z-coordinates of a neighboring atom of μ, and i, j, k, and μ are the atomic indices. It is evident from Fig. 12.2(a) that with the increase

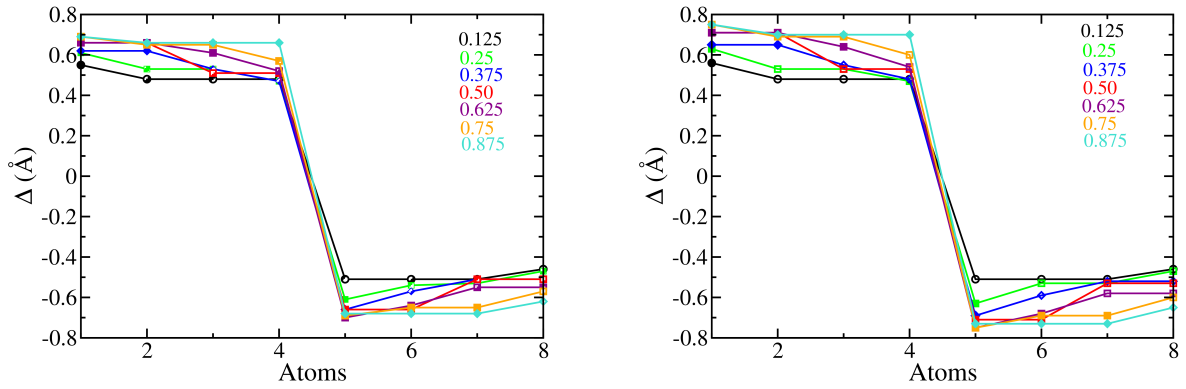

(a) (b)

Figure 12.2: Buckling of atoms in $Si_{1-x}Ge_x$ at various Ge concentrations, x ∈ [0, 1] with (a) SOC=0, and (b) SOC≠0. The indices of Si/Ge atoms are shown on the x-axis. Open and solid symbols show the buckling of Si and Ge atoms respectively.

in Ge concentration there is an increase in buckling. After the inclusion of SOC, the magnitude of bucklings got increased, but the trends remain the same (Fig. 12.2(b)).

The calculated electronic structure of these alloys (shown in Fig. 12.3(a)) reveals that the general features of band dispersion are similar to silicene and germanene, where the π bonding and antibonding bands originating from the p_z orbitals of Ge and Si atoms cross at the K-point at the Fermi energy. Around the crossing point, the two bands are linear and can be characterized as Dirac cones. Fermi velocity, the slope of the electronic band dispersion curves at the K-point, does not appear to be significantly impacted by the alloying process. Silicene and germanene are semi-metallic with the Dirac cone at K-point. With the introduction of the spin-orbit coupling (SOC), we get a band gap of 2 meV and 25 meV for silicene and germanene respectively. We note that the inclusion of SOC has a significant effect on the properties of germanene as expected from its heavier nucleus.

As a result of the increase in Ge concentration in $Si_{1-x}Ge_x$, we notice an increase in the band gap upto Ge concentration of x = 0.25. For concentration, x > 0.25, there is an oscillations in the band gaps (Fig. 12.4(a)). The odd number of Ge atoms in $Si_{1-x}Ge_x$ breaks the lattice symmetry and hence we notice a decrease in the band gap for the Ge concentrations, x = 0.375, 0.625, and 0.875. For these concentrations, Dirac cone

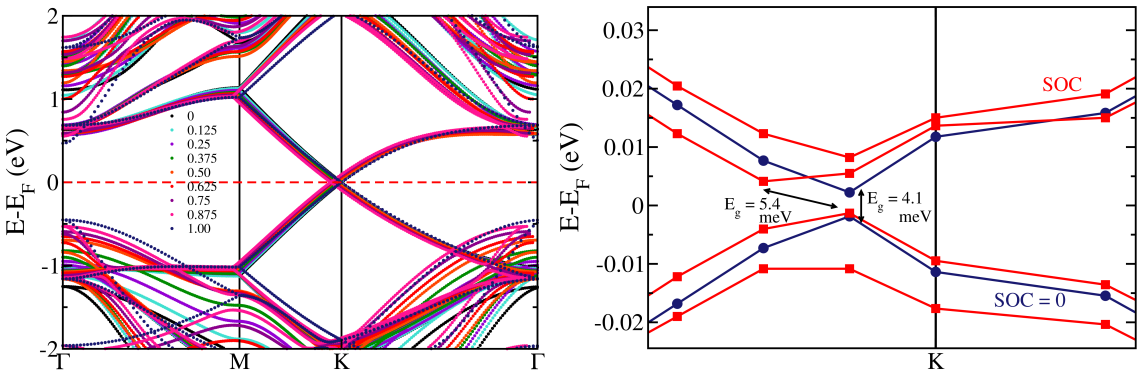

(a) (b)

Figure 12.3: Electronic structures of $Si_{1-x}Ge_x$ as (a) x varies from 0 to 1, and (b) zoomed-in band structures for x=0.375 with SOC = 0 (in blue) and SOC $\neq$ 0 (in red).

shifts away from K-point and we get a direct band gap along M-K direction. With the inclusion of SOC, we notice an increase in the band gap for all the Ge concentrations considered here. For x=0.375, we get an indirect band gap of 5.4 meV along M-K, but for other Ge concentrations we still get a direct band gap with SOC $\neq$ 0 (shown in Fig. 12.3(b)). For x = 0.125 and x = 0.875, the gaps are observed at the high symmetry K-point but the Fermi level lies closer to the valence band than the conduction band with SOC $\neq$ 0.

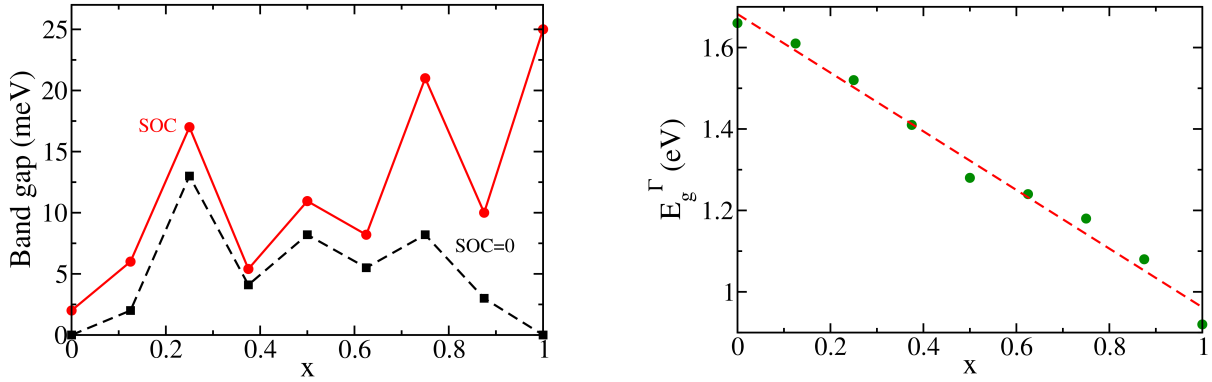

(a) (b)

Figure 12.4: (a) Band gap of $Si_{1-x}Ge_X$ obtained using SOC = 0 and SOC $\neq$ 0, and (b) at Γ-point as a function of Ge concentrations obtained using SOC = 0.

We have obtained the density of states for x = 0.375 and x = 0.75 (shown in Fig. 12.5.) for all the possible configurations at a particular Ge concentrations. The electronic density of states reveals that the states near the Fermi energy, are not affected by the

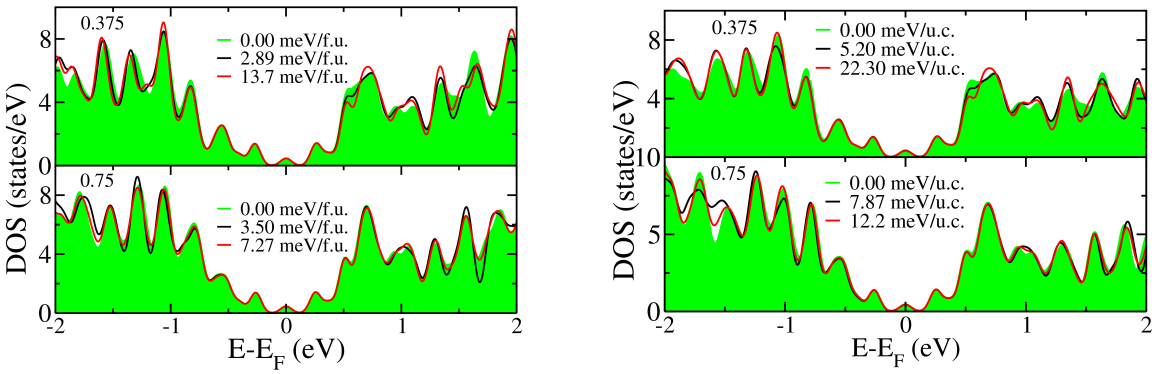

(a) (b)

Figure 12.5: Density of states of $Si_{1-x}Ge_x$ at x = 0.375 and 0.75 Ge concentrations with (a) SOC=0, and (b) SOC≠0.

concentrations or configurations (as shown in Fig. 12.5(a)). The states at E $\sim \pm$ 0.5 eV from the Fermi energy, corresponding to the σ bonding and antibonding states are significantly impacted by Ge concentration. The low energy bands near the Γ-point become closer as the Ge concentration is increased, resulting in an almost linear variation of the gap between the states at Γ-point (Fig. 12.4(b)). This is possibly due to the weakening of the π bonding with alloying, resulting in an sp^3 bond character. With the inclusion of SOC, we get the same behavior (Fig. 12.5(b)) in the electronic density of states. The observation is also consistent with an increase in the buckling with increasing Ge concentration.

We determined the phonon dispersion along the high symmetry points in the Brillouin zone, shown in Fig. 12.6. The phonon spectra of $Si_{1-x}Ge_x$ are very similar to that of silicene. We observe a general softening of the phonon modes with alloying, which may be attributed to the higher strength of the Si-Si bonds as compared to the Ge-Ge bonds. For the lowest energy configurations of $Si_{1-x}Ge_x$, the optical and acoustical branches are well separated. Out of plane polarized acoustic (ZA) phonon modes are weakly unstable (Fig. 12.7(a)) which essentially means that these alloys should show long-length scale buckling/ripples in addition to only atomic scale buckling in pure silicene and germanene. Thus the alloy structures are locally stable, but for these ripples. These have also been reported for monolayered germanene [305].

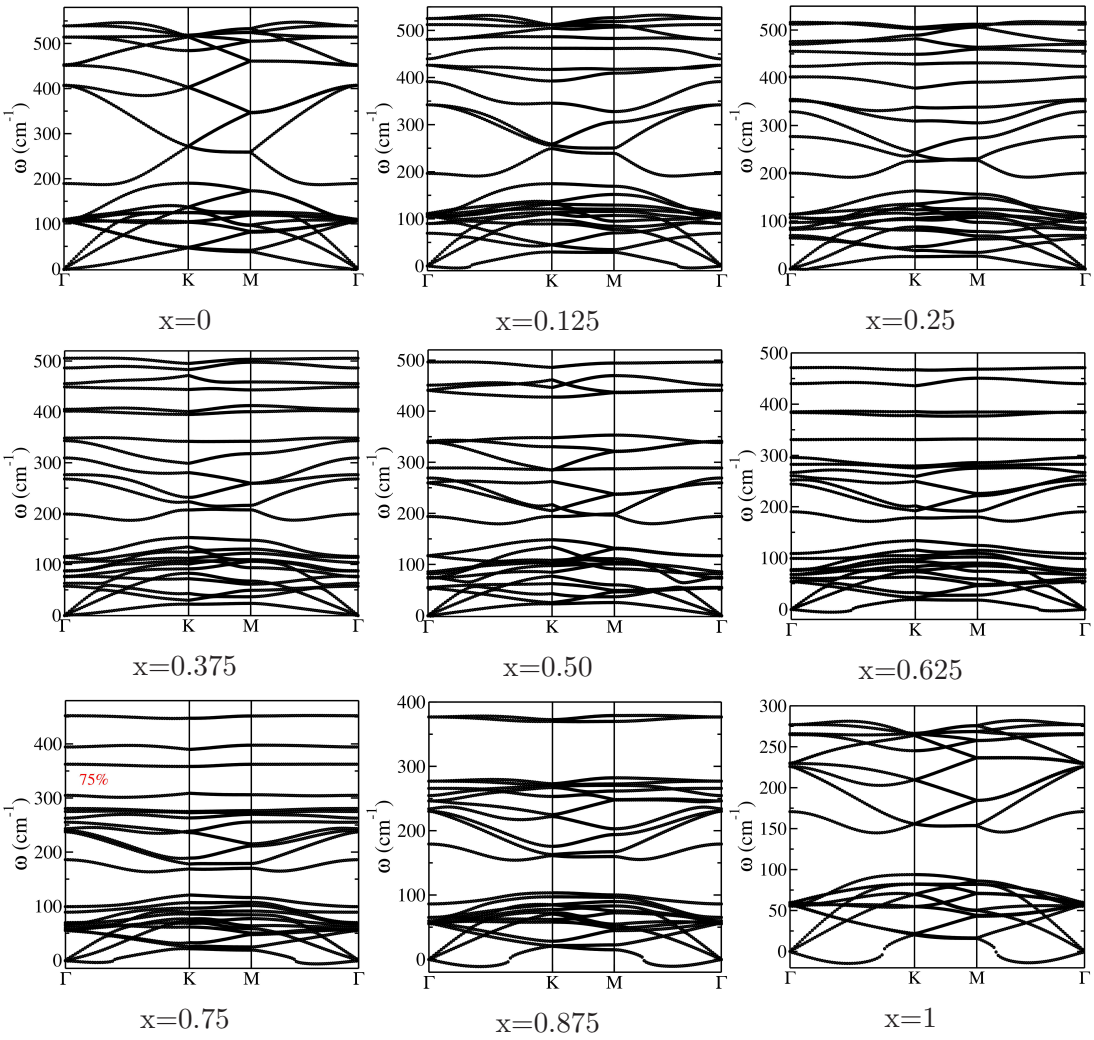

Figure 12.6: Phonon dispersion of 2D monolayers of $Si_{1-x}Ge_x$ for x ∈ [0, 1].

The buckling of atoms in the z-direction breaks the mirror symmetry that exists for graphene, leading to hybridization of the out of plane acoustic (ZA) and optical (ZO) modes with the other modes.

The out of plane optical (ZO) vibrational mode, which is flat for silicene, starts to show a bump near the Γ-point and flattening near the K-point, as Si is substituted by Ge in the lattice (Fig. 12.7(b)). It is of interest to note that there is an increase in ZO frequency for x = 0.125 and x = 0.25 Ge concentrations. For the x > 0.25 there is a softening of modes at Γ-point. ZO mode frequencies show weak dependency on Ge concentration in $Si_{1-x}Ge_x$. Graphene exhibits a Raman active G-peak at 1584 cm^{-1} [323] corresponding to the in-plane transverse optical (TO) and longitudinal

optical (LO) modes at the Γ-point. The frequency of the LO and TO branches for silicene is 539 cm^{-1}. We note that while this frequency is comparable to the mode in bulk silicon (521 cm^{-1}), it is lower than earlier reports on silicene (570 cm^{-1} and 540 cm^{-1} [305]). The degeneracy of the LO and TO modes is lifted for x >0.125. The modes become degenerate at x = 0.875, as shown in Fig. 12.7(c).

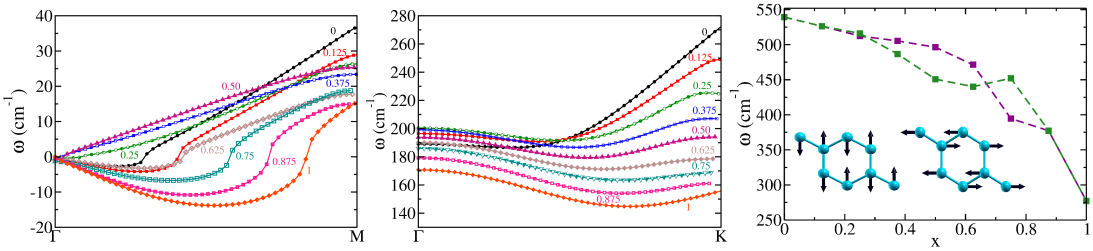

Figure 12.7: Out of plane (a) acoustic, and (b) optical modes for various Ge concentrations, (c) transverse and logitudinal optical phonon modes as a functon of Ge concentrations. Atomic displacements associated with LO and TO modes have been shown in the inset in Fig. (c).

12.4 Conclusions

We predict stable 2D alloys of silicon and germanium ($Si_{1-x}Ge_x$), obtained by substitution at the entire range of concentration x ∈ [0, 1]. The electronic structure near the Fermi level can be characterized by Dirac cones at all concentrations studied here. Lowest energy configurations at each concentration consists of like atoms occupying the adjacent positions, indicating segregation in the lattice. As a result of substitution, the Dirac cone shifts away from K-point for x = 0.375, 0.50, and 0.625 Ge concentrations. We get an indirect band gap for the Ge concentration x = 0.375 along M-K with SOC ≠ 0. There is a softening of mode due to Ge substitution and $Si_{1-x}Ge_x$ is expected to show long length scale buckling as opposed to the atomic scale buckling in silicene/germanene.

Chapter 13

Summary

The main objective of this dissertation is to explore and develop the understanding of properties of materials at various length scales ranging from the bulk to the atomistic level. We have shown that the electronic properties of the materials can be tuned by substitutional alloying and defects for example, leading to better catalytic activity. Also, we demonstrate that external fields like pressure and electron doping can be used to induce an unusual phenomenon governed by fascinating physics.

Aliovalent anion substitution gives rise to marked changes in electronic structure and properties, and also reduce the defect concentration. We determined the effects of aliovalent anion co-substitution of N, F in TiO_2 and N, Cl in ZnO on their electronic, and structural properties. We find that in both cases N-2p states give rise to isolated sub-band at the top of valence states leading to a notable reduction in their band gaps. The complete substitution of O atoms of TiO_2 by N, F leads to the formation of dark-colored TiNF. TiNF is an indirect band gap semiconductor, with a band gap close to that of TiO_2. We find anamolous Born effective charges (Z^*) in TiNF, which show a strong covalent p-d hybridization and interaction between anions and Ti. Predominant dependence of its static dielectric constants ε^0 on relatively high frequency modes suggests that they are expected to be weakly dependent on temperature and pressure. Based on the analysis of conduction and valence band edges, we

predict TiNF to be suitable for photocatalytic water splitting reaction. The transition from N-2p in the valence band to Ti^{3+} states in the conduction band is responsible for the dark or black color of TiNF. The complete substitution of O by ZnO results in the orthorhombic crystal structure of Zn_2NCl. Short Zn-N bonds cause stronger hybridization, and the conduction bands with antibonding character are also consequently affected. This results in the enhanced stability and band gap of Zn_2NCl. Whereas, complete substituion of O by N, F in CdO results in the formation of Cd_2NF with a rock-salt structure similar to that of CdO, with its valence bands consisting primarily of N-2p states. These works have been carried out in close interaction with experimentalists.

$Cd_4As_2Br_3$ and $Cd_4Sb_2I_3$ are the analogous compounds to CdSe and CdTe, where anions are substituted by As, Br and Sb, I respectively. Complete replacement of S^{2-} by P and X (X = Cl, Br, I) gives a new class of compounds of $Cd_4P_2X_3$ (X = Cl, Br, I) with good stability and catalytic activity. We report that their conduction bands are aligned favorably with respect to the redox potential of HER, and hence can be useful in photocatalysis of HER. We also find the suitable alignment of the conduction band position of $Cd_4P_2X_3$ (X = Cl, Br, I) compounds in relation to CO_2 redox potentials to perform CO_2 reduction. We show that Cl and Br vacancies in $Cd_4P_2Cl_3$ and $Cd_4P_2Br_3$ give rise to defect peaks in the gap and inhibit the electron-hole recombination leading to a better photocatalytic HER activity than that of $Cd_4P_2I_3$.

We developed an understanding of pressure-induced structural phase transitions observed in ReO_3 at low pressure (from *Pm3m* to *Im3* phase). We have shown that the softening and anharmonicity of the M_3 phonon modes are relevant to the low-pressure phase transitions in ReO_3. We find that the transition has a weakly first-order character, and is caused by a third-order anharmonic coupling between M_3 and acoustic modes.

We presented studies of the catalytic activity of intermetallic (Pd_2Ge) and metallic phosphides ($Ni_{0.2}Co_{0.8}P$, Ni substituted CoP) for ethanol oxidation reaction and

water splitting reactions respectively. We find that the perfect balance between the adsorption energies of CH_3CO and OH on the Pd_2Ge surfaces dictates its superior electrocatalytic activity of ethanol oxidation reaction as compared to Pd. Ni substituted CoP shows better catalytic activity compared to Ni_2P and CoP due to the optimal binding of reaction intermediates on its surface, with ΔG values quite close to zero. Also, it has more than one catalytically active sites which facilitate further reactions.

Physical and chemical properties of transition metal oxides are central to the emerging field of oxide electronics. However, they are greatly influenced by defects, particularly, oxygen vacancies, which are always present in oxides. In this, we show how the control of oxygen vacancies at (001) surface of ReO_3 can be used to tune its work function remarkably from 7 to 3 eV. Our results highlight how significantly oxygen vacancies alter the frontier states of a metallic oxide and have important consequences to the development of electronic devices and catalysts based on oxide heterostructures.

ReO_3 in its nanocrystalline form is known to show surface-enhanced Raman scattering (SERS) in pyridine, pyrimidine, and pyrazine. We developed an understanding of the chemical mechanism contributing to SERS observed experimentally. Our analysis demonstrates how the chemical interaction between a molecule and a surface captured by first-principles calculations can be used to quantify the chemical contribution to the enhancement factor of SERS. Taking pyridine adsorbed on ReO_3 (an unusual metal) as an example, we find that SERS of certain modes of pyridine have a significant contribution from the chemical mechanisms, and explain the SERS experiments reported.

ReS_2 and $ReSe_2$ possess the same lattice structure in their two-dimensional forms, though phonons in $ReSe_2$ couple weakly with electrons as compared to ReS_2. We show that 2D ReS_2 is a direct band semiconductor with conduction band minimum at Γ-point, and 2D $ReSe_2$ is an indirect band gap semiconductor with its CBM at K-point. Upon electron doping, the valley of conduction band minimum at K-point of

$ReSe_2$ gets populated while that at Γ-point gets populated in ReS_2. As a result, the frontier states at Γ-point are masked from contributing to phonon frequencies in ReS_2 upon doping leading to notable changes in the dominant terms in the perturbative expansion of the interatomic force constant. Hence, upon electron doping, significant changes in phonon frequencies of ReS_2 are observed, while little changes are seen in $ReSe_2$ (observed experimentally).

We have predicted novel two-dimensional alloys ($Si_{1-x}Ge_x$) by substituting Ge atoms in silicene. We present a detailed analysis of stability, electronic and vibrational properties of $Si_{1-x}Ge_x$ at the entire range of concentration x ∈ [0,1]. We show that the spin-orbit coupling introduces a small (∼10 meV) band gap in all structures which can be modulated by varying the dopant concentrations. Lowest energy configuration at each concentration consists of like atoms occupying adjacent positions. We demonstrate their structural stability through phonon dispersion which contains no unstable modes and reveals softening of phonon frequencies as a function of increasing Ge concentration.

We summarize our work presented in this thesis in a schematic diagram (see Figure 13.1) which expresses the central theme of topics covered. In summary, we highlighted how the substitutional alloying, defects and pressures tune smart functional and catalytic properties of materials of various dimensionality.

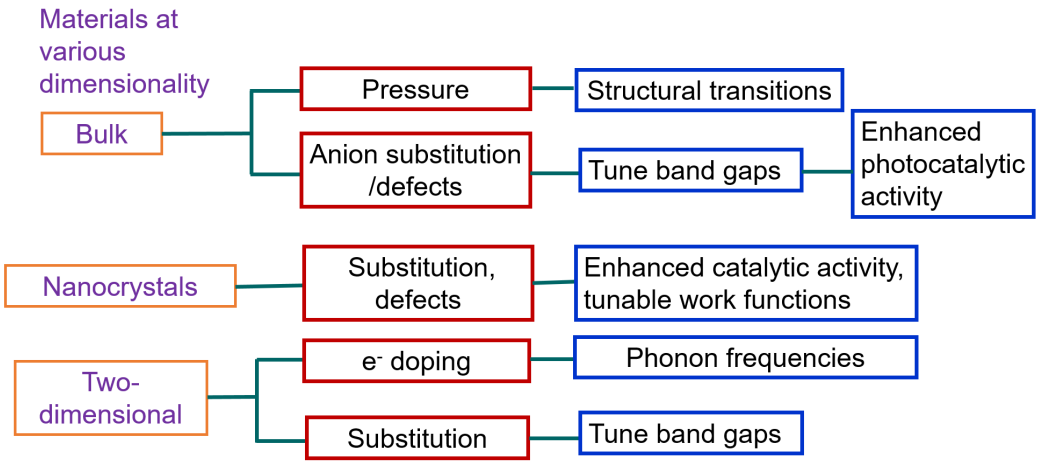

Figure 13.1: Schematic summarizing the work presented in the thesis.

Bibliography

[1] A. Russell and K. L. Lee, *Structure-Property Relations in Nonferrous Metals* (Wiley-interscience, United States of America, 1976).

[2] S. T. Pantelides, Rev. Mod. Phys. **50**, 797 (1978).

[3] Z. Zhao *et al.*, Nano Research **8**, 4061 (2015).

[4] C. E. Ekuma, The Journal of Physical Chemistry Letters **9**, 3680 (2018).

[5] A. Mansouri Tehrani and J. Brgoch, Chemistry of Materials **29**, 2542 (2017).

[6] A. Kaschner *et al.*, Applied Physics Letters **80**, 1909 (2002).

[7] L. L. Kerr, X. Li, M. Canepa, and A. J. Sommer, Thin Solid Films **515**, 5282 (2007).

[8] N. Varghese *et al.*, Materials Research Bulletin **42**, 2117 (2007).

[9] H. Qin, W. Li, Y. Xia, and T. He, ACS Applied Materials & Interfaces **3**, 3152 (2011).

[10] Z. Zhang *et al.*, RSC Adv. **3**, 7215 (2013).

[11] E. Antolini, Journal of Power Sources **170**, 1 (2007).

[12] A. J. Medford *et al.*, Journal of Catalysis **328**, 36 (2015), special Issue: The Impact of Haldor Topse on Catalysis.

[13] H.-F. Wang and Z.-P. Liu, The Journal of Physical Chemistry C **111**, 12157 (2007).

[14] Z. Liang, T. Zhao, J. Xu, and L. Zhu, Electrochimica Acta **54**, 2203 (2009).

[15] C. Lamy, E. Belgsir, and J.-M. Léger, Journal of Applied Electrochemistry **31**, 799 (2001).

[16] W. Zhou *et al.*, Applied Catalysis B: Environmental **46**, 273 (2003).

[17] S. C. S. Lai and M. T. M. Koper, Phys. Chem. Chem. Phys. **11**, 10446 (2009).

[18] G. Camara and T. Iwasita, Journal of Electroanalytical Chemistry **578**, 315 (2005).

[19] L. Chen *et al.*, Nature Communications **8**, 14136 (2017).

[20] Y.-Y. Yang *et al.*, ACS Catalysis **4**, 798 (2014).

[21] K. Takanabe, ACS Catalysis **7**, 8006 (2017).

[22] N. Mahmood *et al.*, Advanced Science **5**, 1700464 (2018).

[23] Y. Zheng, Y. Jiao, A. Vasileff, and S.-Z. Qiao, Angewandte Chemie International Edition **57**, 7568 (2018).

[24] M. Gong *et al.*, Nano Research **9**, 28 (2016).

[25] J. Wei *et al.*, Nano-Micro Letters **10**, 75 (2018).

[26] N.-T. Suen *et al.*, Chem. Soc. Rev. **46**, 337 (2017).

[27] C. N. R. Rao and B. Raveau, *Transition Metal Oxides: Structure, Properties and Synthesis of Ceramic Oxides* (Wiley-VCH, New York/Weinheim, 1998).

[28] J. Klarbring and S. I. Simak, Phys. Rev. B **97**, 024108 (2018).

[29] K. K. Kim *et al.*, Nano Letters **12**, 161 (2012).

[30] D. Kong *et al.*, Nano Letters **10**, 2245 (2010).

[31] D. Liu *et al.*, Nature Communications **3**, 931 (2012).

[32] S. Susarla *et al.*, Chemistry of Materials **29**, 7431 (2017).

[33] H.-P. Komsa and A. V. Krasheninnikov, The Journal of Physical Chemistry Letters **3**, 3652 (2012).

[34] A. Das *et al.*, Nature Nanotechnology **3**, 210 (2008).

[35] B. Chakraborty *et al.*, 2D Materials **3**, 015008 (2016).

[36] J. Heyd, G. E. Scuseria, and M. Ernzerhof, The Journal of Chemical Physics **118**, 8207 (2003).

[37] O. K. Andersen, Phys. Rev. B **12**, 3060 (1975).

[38] J. C. Slater, Phys. Rev. **51**, 846 (1937).

[39] J. C. Slater, Phys. Rev. **81**, 385 (1951).

[40] A. D. Corso and A. M. Conte, Phys. Rev. B **71**, 115106 (2005).

[41] S. Grimme, Journal of Computational Chemistry **27**, 1787 (2006).

[42] A. Tkatchenko and M. Scheffler, Phys. Rev. Lett. **102**, 073005 (2009).

[43] G. J. Ackland, M. C. Warren, and S. J. Clark, Journal of Physics: Condensed Matter **9**, 7861 (1997).

[44] S. Baroni, P. Giannozzi, and A. Testa, Phys. Rev. Lett. **58**, 1861 (1987).

[45] S. Baroni, P. Giannozzi, and A. Testa, Phys. Rev. Lett. **59**, 2662 (1987).

[46] C. N. R. Rao, The Journal of Physical Chemistry Letters **6**, 3303 (2015).

[47] C. Fang, K. Ramanujachary, H. Hintzen, and G. de With, Journal of Alloys and Compounds **351**, 72 (2003).

[48] R. Saha *et al.*, ChemPhysChem **14**, 2672 (2013).

[49] S. R. Lingampalli and C. N. R. Rao, J. Mater. Chem. A **2**, 7702 (2014).

[50] S. R. Lingampalli *et al.*, Journal of the American Chemical Society **138**, 8228 (2016).

[51] S. Kouser *et al.*, Angewandte Chemie **127**, 8267 (2015).

[52] R. Asahi *et al.*, **293**, 269 (2001).

[53] D. Li *et al.*, Chemical Physics Letters **401**, 579 (2005).

[54] Y. Liu, Z. Wang, W. Wang, and W. Huang, Journal of Catalysis **310**, 16 (2014).

[55] O. Ola and M. Maroto-valer, Journal of Photochemistry and Photobiology C: Photochemistry Reviews **24**, 16 (2015).

[56] L. Pan, X. Zhang, L. Wang, and J.-J. Zou, Materials Letters **160**, 576 (2015).

[57] J. Schneider *et al.*, Chemical Reviews **114**, 9919 (2014).

[58] R. Li *et al.*, Energy Environ. Sci. **8**, 2377 (2015).

[59] A. Burke *et al.*, Nano Letters **8**, 977 (2008).

[60] K. H. Ko, Y. C. Lee, and Y. J. Jung, Journal of Colloid and Interface Science **283**, 482 (2005).

[61] V. Aravindan, Y.-S. Lee, R. Yazami, and S. Madhavi, Materials Today **18**, 345 (2015).

[62] C. Burda *et al.*, Nano Letters **3**, 1049 (2003).

[63] S. I. Shah *et al.*, Proceedings of the National Academy of Sciences **99**, 6482 (2002).

[64] M. M. Ayyub *et al.*, ChemPhysChem **19**, 3410 (2018).

[65] P. Giannozzi *et al.*, Journal of Physics: Condensed Matter **21**, 395502 (2009).

[66] S. F. Matar, Journal of Solid State Chemistry **185**, 25 (2012).

[67] C. Wstefeld *et al.*, Angewandte Chemie International Edition in English **27**, 929 (1988).

[68] R. Grau-Crespo, S. Hamad, C. R. A. Catlow, and N. H. de Leeuw, Journal of Physics: Condensed Matter **19**, 256201 (2007).

[69] J. Bhattacharjee and U. V. Waghmare, Phys. Chem. Chem. Phys. **12**, 1564 (2010).

[70] M. Mikami, S. Nakamura, O. Kitao, and H. Arakawa, Phys. Rev. B **66**, 155213 (2002).

[71] P. Ghosez, J.-P. Michenaud, and X. Gonze, Phys. Rev. B **58**, 6224 (1998).

[72] A. Malashevich, M. Jain, and S. G. Louie, Phys. Rev. B **89**, 075205 (2014).

[73] I. Tanaka *et al.*, Materials Transactions **43**, 1426 (2002).

[74] R. Bès *et al.*, Phys. Rev. B **87**, 024104 (2013).

[75] A. Paris and S. Taioli, The Journal of Physical Chemistry C **120**, 22045 (2016).

[76] K. Manjunath, S. Prasad, U. V. Waghmare, and C. N. R. Rao, Dalton Trans. **47**, 9303 (2018).

[77] P. E. Blöchl, Phys. Rev. B **50**, 17953 (1994).

[78] G. Kresse and J. Furthmller, Computational Materials Science **6**, 15 (1996).

[79] F. P. Koffyberg, Phys. Rev. B **13**, 4470 (1976).

[80] S. R. Lingampalli *et al.*, European Journal of Inorganic Chemistry **2017**, 2377 (2017).

[81] N. Kumar *et al.*, Inorganic Chemistry **52**, 10512 (2013).

[82] H. Xie *et al.*, Semiconductor Science and Technology **27**, 125008 (2012).

[83] F. Stavale, L. Pascua, N. Nilius, and H.-J. Freund, The Journal of Physical Chemistry C **118**, 13693 (2014).

[84] A. K. Rumaiz *et al.*, Applied Physics Letters **95**, 262111 (2009).

[85] Wen, J. *et al.*, Eur. Phys. J. B **80**, 25 (2011).

[86] X. Liu, C. Wessel, F. Pan, and R. Dronskowski, Journal of Solid State Chemistry **203**, 31 (2013).

[87] J. P. Perdew and A. Zunger, Phys. Rev. B **23**, 5048 (1981).

[88] M. Usuda, N. Hamada, T. Kotani, and M. van Schilfgaarde, Phys. Rev. B **66**, 125101 (2002).

[89] J. Wróbel *et al.*, Phys. Rev. B **80**, 155124 (2009).

[90] K. Wu and T. Lian, Chem. Soc. Rev. **45**, 3781 (2016).

[91] Z. Yu *et al.*, Dalton Trans. **42**, 4633 (2013).

[92] J. F. Reber and M. Rusek, The Journal of Physical Chemistry **90**, 824 (1986).

[93] Y. Xie *et al.*, J. Mater. Chem. C **4**, 6483 (2016).

[94] K. Wang *et al.*, RSC Adv. **4**, 15702 (2014).

[95] Y. Wang *et al.*, Journal of Nanoscience and Nanotechnology **10**, 433 (2010).

[96] C. Wu *et al.*, Nanotechnology **21**, 505203 (2010).

[97] H. Luo *et al.*, The Journal of Physical Chemistry C **119**, 10749 (2015).

[98] Y. Proskuryakov *et al.*, Solar Energy Materials and Solar Cells **93**, 1572 (2009).

[99] T. Okamoto *et al.*, Japanese Journal of Applied Physics **51**, 10NC12 (2012).

[100] H. Zhao *et al.*, in *Conference Record of the IEEE Photovoltaic Specialists Conference* (IEEE, San Diego, CA, USA, 2008).

[101] A. Kudo and Y. Miseki, Chem. Soc. Rev. **38**, 253 (2009).

[102] A. Roy *et al.*, Solid State Communications **255-256**, 5 (2017).

[103] J. P. Perdew, K. Burke, and M. Ernzerhof, Phys. Rev. Lett. **77**, 3865 (1996).

[104] A. Roy *et al.*, ACS Applied Materials & Interfaces **10**, 2526 (2018).

[105] F. Dong *et al.*, Phys. Chem. Chem. Phys. **17**, 16058 (2015).

[106] H. Tan *et al.*, ACS Applied Materials & Interfaces **6**, 19184 (2014).

[107] D. V. S. Muthu *et al.*, Phys. Rev. B **91**, 224308 (2015).

[108] P. Ghosez, E. Cockayne, U. V. Waghmare, and K. M. Rabe, Phys. Rev. B **60**, 836 (1999).

[109] J. E. Schirber and B. Morosin, Phys. Rev. Lett. **42**, 1485 (1979).

[110] J.-E. Jørgensen *et al.*, Phys. Rev. B **33**, 4793 (1986).

[111] T. Chatterji and G. McIntyre, Solid State Communications **139**, 12 (2006).

[112] J.-E. Jørgensen, J. Staun Olsen, and L. Gerward, Journal of Applied Crystallography **33**, 279 (2000).

[113] E. Suzuki, Y. Kobayashi, S. Endo, and T. Kikegawa, Journal of Physics: Condensed Matter **14**, 10589 (2002).

[114] K. Biswas, S. V. Bhat, and C. N. R. Rao, J. Phys. Chem. C **111**, 5689 (2007).

[115] J. Purans, A. Kuzmin, E. Cazzanelli, and G. Mariotto, Journal of Physics: Condensed Matter **19**, 226206 (2007).

[116] P. B. Allen and W. W. Schulz, Phys. Rev. B **47**, 14434 (1993).

[117] M. G. Stachiotti, F. Cora, C. R. A. Catlow, and C. O. Rodriguez, Phys. Rev. B **55**, 7508 (1997).

[118] U. D. Wdowik *et al.*, Phys. Rev. B **82**, 104301 (2010).

[119] D. Vanderbilt, Phys. Rev. B **41**, 7892 (1990).

[120] A. M. Rappe, K. M. Rabe, E. Kaxiras, and J. D. Joannopoulos, Phys. Rev. B **41**, 1227 (1990).

[121] P. Blaha *et al.*, *WIEN2K, An Augmented Plane Wave + Local Orbitals Program for Calculating Crystal Properties* (Karlheinz Schwarz, Techn. Universität, Wien, Austria, 2001).

[122] A. Togo, F. Oba, and I. Tanaka, Phys. Rev. B **78**, 134106 (2008).

[123] M. Ishii, T. Tanaka, T. Akahane, and N. Tsuda, Journal of the Physical Society of Japan **41**, 908 (1976).

[124] U. V. Waghmare and K. M. Rabe, Phys. Rev. B **55**, 6161 (1997).

[125] S. Sarkar *et al.*, Chemistry of Materials **27**, 7459 (2015).

[126] W. X. Chen, J. Y. Lee, and Z. Liu, Chem. Commun. 2588 (2002).

[127] V. T. Thanh Ho *et al.*, Energy Environ. Sci. **4**, 4194 (2011).

[128] E. Antolini, J. R. Salgado, and E. R. Gonzalez, Journal of Power Sources **160**, 957 (2006).

[129] B. Lim *et al.*, Science **324**, 1302 (2009).

[130] D. Wang *et al.*, Nature Materials **12**, 81 (2013).

[131] Y. Kang *et al.*, ACS Nano **6**, 2818 (2012).

[132] B. Y. Xia, H. B. Wu, X. Wang, and X. W. D. Lou, Journal of the American Chemical Society **134**, 13934 (2012).

[133] H. Qiu *et al.*, Nature Communications **4**, 2642 (2013).

[134] Journal of Power Sources **164**, 527 (2007).

[135] R. C. McMurry, J. E.; Fay, *Chemistry* (Pearsons Publications, ADDRESS, 2008).

[136] S. Meenakshi, P. Sridhar, and S. Pitchumani, RSC Adv. **4**, 44386 (2014).

[137] J. Bagchi and S. K. Bhattacharya, Journal of Power Sources **163**, 661 (2007).

[138] M. Wang, D. jun Guo, and H. lin Li, Journal of Solid State Chemistry **178**, 1996 (2005).

[139] Journal of Power Sources **162**, 1077 (2006).

[140] C. Xu, Z. Tian, P. Shen, and S. P. Jiang, Electrochimica Acta **53**, 2610 (2008).

[141] H. T. Zheng, Y. Li, S. Chen, and P. K. Shen, Journal of Power Sources **163**, 371 (2006).

[142] C. Xu, Z. Tian, P. Shen, and S. P. Jiang, Electrochimica Acta **53**, 2610 (2008).

[143] D. Chu *et al.*, Catalysis Communications **10**, 955 (2009).

[144] Z.-P. Sun *et al.*, Journal of Power Sources **185**, 801 (2008).

[145] Z. Zhang, L. Xin, K. Sun, and W. Li, International Journal of Hydrogen Energy **36**, 12686 (2011), 3rd Iranian Fuel Cell Seminar.

[146] S.-C. Lin, J.-Y. Chen, Y.-F. Hsieh, and P.-W. Wu, Materials Letters **65**, 215 (2011).

[147] L. Shi *et al.*, European Journal of Inorganic Chemistry **2012**, 2700 (2012).

[148] Q. Yi *et al.*, Electroanalysis **23**, 2232 (2011).

[149] T. Herranz *et al.*, ChemElectroChem **1**, 885 (2014).

[150] W. Du *et al.*, ACS Catalysis **2**, 287 (2012).

[151] R. Kodiyath *et al.*, Energy Environ. Sci. **8**, 1685 (2015).

[152] L. Rao *et al.*, Phys. Chem. Chem. Phys. **16**, 13662 (2014).

[153] W. Hong, J. Wang, and E. Wang, ACS Applied Materials & Interfaces **6**, 9481 (2014).

[154] J. P. Perdew and A. Zunger, Phys. Rev. B **23**, 5048 (1981).

[155] P. Sabatier, Berichte der deutschen chemischen Gesellschaft **44**, 1984 (1911).

[156] Z. Liang, T. Zhao, J. Xu, and L. Zhu, Electrochimica Acta **54**, 2203 (2009).

[157] B. Hammer and J. Nrskov, Surface Science **343**, 211 (1995).

[158] E. Gonzalez *et al.*, physica status solidi (b) **246**, 1275 (2009).

[159] F. Calle-Vallejo *et al.*, Angewandte Chemie International Edition **53**, 8316 (2014).

[160] R. A. Nickell *et al.*, Journal of Power Sources **161**, 1217 (2006).

[161] H. B. Gray, Nature Chemistry **1**, 7 (2009).

[162] M. G. Walter *et al.*, Chemical Reviews **110**, 6446 (2010).

[163] T. R. Cook *et al.*, Chemical Reviews **110**, 6474 (2010).

[164] Y. Lee *et al.*, The Journal of Physical Chemistry Letters **3**, 399 (2012).

[165] M. E. G. Lyons and S. Floquet, Phys. Chem. Chem. Phys. **13**, 5314 (2011).

[166] D. Voiry *et al.*, Nature Materials **12**, 850 (2013).

[167] D. Merki and X. Hu, Energy Environ. Sci. **4**, 3878 (2011).

[168] S. Anantharaj *et al.*, ACS Catalysis **6**, 8069 (2016).

[169] J. Suntivich *et al.*, **334**, 1383 (2011).

[170] D. Li, H. Baydoun, C. N. Verani, and S. L. Brock, Journal of the American Chemical Society **138**, 4006 (2016), pMID: 26972408.

[171] Y. Zhao *et al.*, Nature Communications **4**, 2390 (2013).

[172] I. C. Man *et al.*, ChemCatChem **3**, 1159 (2011).

[173] M. S. Burke *et al.*, Chemistry of Materials **27**, 7549 (2015).

[174] M. Garca-Mota *et al.*, The Journal of Physical Chemistry C **116**, 21077 (2012).

[175] Y. Zhao *et al.*, Journal of the American Chemical Society **138**, 6517 (2016).

[176] M. Gong *et al.*, Journal of the American Chemical Society **135**, 8452 (2013).

[177] M. S. Burke *et al.*, Journal of the American Chemical Society **137**, 3638 (2015).

[178] L. Trotochaud, S. L. Young, J. K. Ranney, and S. W. Boettcher, Journal of the American Chemical Society **136**, 6744 (2014).

[179] Y. Li *et al.*, Journal of the American Chemical Society **133**, 7296 (2011).

[180] V. Kiran, D. Mukherjee, R. N. Jenjeti, and S. Sampath, Nanoscale **6**, 12856 (2014).

[181] C. Di Giovanni *et al.*, ACS Catalysis **4**, 681 (2014).

[182] A. T. Swesi, J. Masud, and M. Nath, Energy Environ. Sci. **9**, 1771 (2016).

[183] J. Masud, A. T. Swesi, W. P. R. Liyanage, and M. Nath, ACS Applied Materials & Interfaces **8**, 17292 (2016).

[184] T. Liu *et al.*, Chem. Commun. **51**, 16683 (2015).

[185] P. Chen *et al.*, Inorg. Chem. Front. **3**, 236 (2016).

[186] P. Chen *et al.*, Angewandte Chemie (International ed. in English) **54**, 1471014714 (2015).

[187] K. Xu *et al.*, Journal of the American Chemical Society **137**, 4119 (2015).

[188] E. J. Popczun *et al.*, Journal of the American Chemical Society **135**, 9267 (2013).

[189] S. Anantharaj, P. N. Reddy, and S. Kundu, Inorganic Chemistry **56**, 1742 (2017).

[190] A. Dutta *et al.*, ACS Energy Letters **1**, 169 (2016).

[191] L.-A. Stern, L. Feng, F. Song, and X. Hu, Energy Environ. Sci. **8**, 2347 (2015).

[192] C.-C. Hou, S. Cao, W.-F. Fu, and Y. Chen, ACS Applied Materials & Interfaces **7**, 28412 (2015).

[193] X.-Y. Yu *et al.*, Energy Environ. Sci. **9**, 1246 (2016).

[194] J. Yu *et al.*, ACS Applied Materials & Interfaces **8**, 27850 (2016).

[195] P. Xiao, W. Chen, and X. Wang, Advanced Energy Materials **5**, 1500985 (2015).

[196] J. Kibsgaard *et al.*, Energy Environ. Sci. **8**, 3022 (2015).

[197] A. Dutta and N. Pradhan, The Journal of Physical Chemistry Letters **8**, 144 (2017).

[198] Y. Feng, X.-Y. Yu, and U. Paik, Chem. Commun. **52**, 1633 (2016).

[199] S. Fu *et al.*, ACS Energy Letters **1**, 792 (2016).

[200] Journal of the Electrochemical Society **152**, .

[201] J. Rossmeisl *et al.*, Journal of Electroanalytical Chemistry **607**, 83 (2007).

[202] Suchitra, J. Pan, and U. V. Waghmare, Journal of Applied Physics **116**, 034304 (2014).

[203] M.-G. Kim, M. G. Kanatzidis, A. Facchetti, and T. J. Marks, Nat. Mater. **10**, 382 (2011).

[204] M. J. Rozenberg *et al.*, Phys. Rev. B **81**, 115101 (2010).

[205] J. Meyer *et al.*, Advanced Materials **24**, 5408 (2012).

[206] M. T. Greiner and Z.-H. Lu, NPG Asia Mater **5**, 1 (2013).

[207] S. D. Ha and S. Ramanathan, Journal of Applied Physics **110**, (2011).

[208] T. Choi *et al.*, Science **324**, 63 (2009).

[209] A. Ohtomo and H. Y. Hwang, Nature **427**, 423 (2004).

[210] N. Nakagawa, H. Y. Hwang, and D. A. Muller, Nat. Mater. **5**, 204 (2006).

[211] J. A. Bert *et al.*, Nat. Phys. **7**, 767 (2011).

[212] R. V. K. Mangalam *et al.*, Solid State Commun. **149**, 1 (2009).

[213] Z. Zhong, P. X. Xu, and P. J. Kelly, Phys. Rev. B **82**, 165127 (2010).

[214] G. Herranz *et al.*, Phys. Rev. Lett. **98**, 216803 (2007).

[215] Y. Li *et al.*, Phys. Rev. B **84**, 245307 (2011).

[216] M. T. Greiner *et al.*, Adv. Funct. Mater. **22**, 4557 (2012).

[217] E. Cho and S. Han, Microelectron. Eng. **88**, 3407 (2011).

[218] N. Tsuda and A. Fujimori, J. Catal. **69**, 410 (1981).

[219] Y. Yuan and Y. Iwasawa, J. Phys. Chem. B **106**, 4441 (2002).

[220] S. Ling, D. Mei, and M. Gutowski, Catal. Today **165**, 41 (2011).

[221] K. Biswas *et al.*, Journal of Physics: Condensed Matter **19**, 436214 (2007).

[222] J.-E. Jorgensen, J. Staun Olsen, and L. Gerward, J. Appl. Cryst. **33**, 279 (2000).

[223] B. Houser and R. Ingalls, Phys. Rev. B **61**, 6515 (2000).

[224] J. E. Schirber *et al.*, Phys. Rev. B **29**, 4150 (1984).

[225] T. Chatterji and G. McIntyre, Solid State Commun. **139**, 12 (2006).

[226] M. Tsukada, N. Tsuda, and F. Minami, J. Phys. Soc. Jpn. **49**, 1115 (1980).

[227] J. Neugebauer and M. Scheffler, Phys. Rev. B **46**, 16067 (1992).

[228] Y. X. Wang, M. Arai, T. Sasaki, and C. L. Wang, Phys. Rev. B **73**, 035411 (2006).

[229] C. Cheng, K. Kunc, and M. H. Lee, Phys. Rev. B **62**, 10409 (2000).

[230] J. Padilla and D. Vanderbilt, Phys. Rev. B **56**, 1625 (1997).

[231] E. Heifets *et al.*, Surf. Sci. **513**, 211 (2002).

[232] N. Li *et al.*, J. Appl. Phys. **107**, 123704 (2010).

[233] F. Cora, M. G. Stachiotti, C. R. A. Catlow, and C. O. Rodriguez, J. Phys. Chem. B **101**, 3945 (1997).

[234] M. G. Stachiotti, F. Cora, C. R. A. Catlow, and C. O. Rodriguez, Phys. Rev. B **55**, 7508 (1997).

[235] K. Biswas and C. N. R. Rao, J. Phys. Chem. B **110**, 842 (2006).

[236] Y. Luo, A. Aubry, and J. B. Pendry, Phys. Rev. B **83**, 155422 (2011).

[237] H. Xu, J. Aizpurua, M. Käll, and P. Apell, Phys. Rev. E **62**, 4318 (2000).

[238] J. P. Camden *et al.*, Journal of the American Chemical Society **130**, 12616 (2008).

[239] P. L. Stiles, J. A. Dieringer, N. C. Shah, and R. P. V. Duyne, Annual Review Analytical Chemistry **1**, 601 (2008).

[240] S. M. Morton, E. Ewusi-Annan, and L. Jensen, Phys. Chem. Chem. Phys. **11**, 7424 (2009).

[241] L. Tong, T. Zhu, and Z. Liu, Chem. Soc. Rev. **40**, 1296 (2011).

[242] R. Olivares-Amaya *et al.*, The Journal of Physical Chemistry C **116**, 15568 (2012).

[243] L. Jensen, C. M. Aikens, and G. C. Schatz, Chem. Soc. Rev. **37**, 1061 (2008).

[244] J. P. Perdew *et al.*, Phys. Rev. B **46**, 6671 (1992).

[245] S. Grimme, Journal of Computational Chemistry **27**, 1787 (2006).

[246] P. Johansson, Phys. Chem. Chem. Phys. **7**, 475 (2005).

[247] M. Castell-Ventura, Y. Akacem, and E. Kassab, The Journal of Physical Chemistry C **112**, 19045 (2008).

[248] B. N. J. Persson, K. Zhao, and Z. Zhang, Phys. Rev. Lett. **96**, 207401 (2006).

[249] B. Persson, Surface Science **281**, 153 (1993).

[250] Q. H. Wang *et al.*, Nature nanotechnology **7**, 699 (2012).

[251] B. Liu *et al.*, ACS nano **10**, 5153 (2016).

[252] I. B. Amara, E. B. Salem, and S. Jaziri, Journal of Applied Physics **120**, 051707 (2016).

[253] K. F. Mak and J. Shan, Nature Photonics **10**, 216 (2016).

[254] S. Yang *et al.*, Nanoscale **6**, 7226 (2014).

[255] T. Cao *et al.*, Nature communications **3**, 887 (2012).

[256] H. Zeng *et al.*, Nature nanotechnology **7**, 490 (2012).

[257] K. F. Mak, K. He, J. Shan, and T. F. Heinz, Nature nanotechnology **7**, 494 (2012).

[258] H. Ochoa and R. Roldán, Physical Review B **87**, 245421 (2013).

[259] T. Chu *et al.*, Nano letters **15**, 8000 (2015).

[260] J. O. Island *et al.*, Nanoscale **8**, 2589 (2016).

[261] J. Reyes-Retana and F. Cervantes-Sodi, Scientific reports **6**, 24093 (2016).

[262] K. He *et al.*, Physical review letters **113**, 026803 (2014).

[263] Y.-C. Lin *et al.*, ACS nano **9**, 11249 (2015).

[264] E. Zhang *et al.*, Advanced Functional Materials **25**, 4076 (2015).

[265] C. M. Corbet *et al.*, ACS nano **9**, 363 (2014).

[266] E. Liu *et al.*, Nature communications **6**, 6991 (2015).

[267] S. Yang *et al.*, Scientific reports **4**, 5442 (2014).

[268] E. Zhang *et al.*, ACS nano **10**, 8067 (2016).

[269] C. Ho, Y. Huang, P. Liao, and K. Tiong, Journal of Physics and Chemistry of Solids **60**, 1797 (1999).

[270] J. Wildervanck and F. Jellinek, Journal of the Less Common Metals **24**, 73 (1971).

[271] H.-J. Lamfers, A. Meetsma, G. Wiegers, and J. De Boer, Journal of alloys and compounds **241**, 34 (1996).

[272] Y. Feng *et al.*, Physical Review B **92**, 054110 (2015).

[273] D. A. Chenet *et al.*, Nano letters **15**, 5667 (2015).

[274] A. Ferrari *et al.*, Physical review letters **97**, 187401 (2006).

[275] A. Berkdemir *et al.*, Scientific reports **3**, 1755 (2013).

[276] H. Li *et al.*, Advanced Functional Materials **22**, 1385 (2012).

[277] M. Kitajima, Critical reviews in Solid state and Material Sciences **22**, 275 (1997).

[278] M. D. Fontana and P. Bourson, Applied Physics Reviews **2**, 040602 (2015).

[279] J. Champarnaud-Mesjard *et al.*, Journal of physics and chemistry of solids **61**, 1499 (2000).

[280] J. Wu *et al.*, Angewandte Chemie **127**, 2396 (2015).

[281] R. He *et al.*, Nano letters **16**, 1404 (2016).

[282] X.-F. Qiao *et al.*, Nanoscale **8**, 8324 (2016).

[283] A. Das *et al.*, Nature nanotechnology **3**, 210 (2008).

[284] O. Rapp, J. Jackle, and K. Frobose, Journal of Physics F: Metal Physics **11**, 2359 (1981).

[285] C. Yung, D. Schmidt, and A. Cleland, Applied physics letters **81**, 31 (2002).

[286] X. Xi *et al.*, Nature nanotechnology **10**, 765 (2015).

[287] S. Tongay *et al.*, Nature communication **5**, 3253 (2014).

[288] D. Wolverson *et al.*, Acs Nano **8**, 11154 (2014).

[289] H. Zhao *et al.*, Nano Research **8**, 3651 (2015).

[290] E. Lorchat, G. Froehlicher, and S. Berciaud, ACS nano **10**, 2752 (2016).

[291] C. Steinke *et al.*, Physical Review B **96**, 045431 (2017).

[292] M. Kumagai and T. Takagahara, Physical Review B **40**, 12359 (1989).

[293] A. Singh, S. N. Shirodkar, and U. V. Waghmare, 2D Materials **2**, 035013 (2015).

[294] V. Georgakilas *et al.*, Chemical Reviews **112**, 6156 (2012).

[295] Y. Zhang *et al.*, Nature **459**, 820 (2009).

[296] K. F. M. E. C. Chun Hung Lui, Zhiqiang Li and T. F. Heinz, Nature Physics **7**, 944947 (2011).

[297] M. S. Nevius *et al.*, Phys. Rev. Lett. **115**, 136802 (2015).

[298] S. Z. Butler *et al.*, ACS Nano **7**, 2898 (2013).

[299] A. H. C. Neto and K. Novoselov, Materials Express **1**, 10 (2011).

[300] A. Azizi *et al.*, ACS Nano **9**, 4882 (2015).

[301] A. Kara *et al.*, Surface Science Reports **67**, 1 (2012).

[302] M. Houssa *et al.*, Applied Physics Letters **98**, 223107 (2011).

[303] P. Vogt *et al.*, Phys. Rev. Lett. **108**, 155501 (2012).

[304] S. Cahangirov *et al.*, Phys. Rev. Lett. **102**, 236804 (2009).

[305] N. J. Roome and J. D. Carey, ACS Applied Materials & Interfaces **6**, 7743 (2014).

[306] M. Yi and Z. Shen, J. Mater. Chem. A **3**, 11700 (2015).

[307] B. Aufray *et al.*, Applied Physics Letters **96**, 183102 (2010).

[308] B. Feng *et al.*, Nano Letters **12**, 3507 (2012).

[309] C. Volders, E. Monazami, G. Ramalingam, and P. Reinke, Nano Letters **17**, 299 (2017).

[310] M. Derivaz *et al.*, Nano Letters **15**, 2510 (2015).

[311] M. E. Dvila and G. L. Lay, Scientific Reports **6**, 20714 (2016).

[312] A. Molle *et al.*, Advanced Functional Materials **23**, 4340 (2013).

[313] H. Zandvliet, Nano today **9**, 691 (2014).

[314] A. K. Geim and I. V. Grigorieva, Nature **499**, 419425 (2013).

[315] L. Tao *et al.*, Nature Nanotechnology **10**, 227 (2015).

[316] J. J. Pulikkotil and S. Auluck, AIP Advances **5**, 037145 (2015).

[317] P. Jamdagni *et al.*, Materials Research Express **2**, 016301 (2015).

[318] H. Zhou *et al.*, Journal of Physics: Condensed Matter **25**, 395501 (2013).

[319] C. Lee *et al.*, ACS Nano **4**, 2695 (2010).

[320] A. C. Ferrari, Solid State Communications **143**, 47 (2007).

[321] X. Li *et al.*, Phys. Rev. B **87**, 115418 (2013).

[322] A. Nijamudheen, R. Bhattacharjee, S. Choudhury, and A. Datta, The Journal of Physical Chemistry C **119**, 3802 (2015).

[323] A. Jorio *et al.*, Physica Status Solidi (b) **247**, 2980 (2010).